Surface Modification of Electrode Surfaces for Water Treatment and Sensing Applications

BY

Pralay Gayen

Submitted in partial fulfillment of the requirements

For the degree of Doctor of Philosophy in Chemical Engineering in the Graduate College of the

University of Illinois at Chicago, 2018

Chicago, Illinois

Defense Committee:
Dr. Brian P. Chaplin, Chair and Advisor, Department of Chemical Engineering
Dr. Vikas Berry, Department of Chemical Engineering
Dr. Alan D. Zdunek, Department of Chemical Engineering
Dr. Sangil Kim, Department of Chemical Engineering
Dr. Jeremiah Abiade, Department of Mechanical and Industrial Engineering

This thesis work is dedicated to my wife, Rumki, who has always supported me in each and every challenge in PhD study as well as in life. I would also like to dedicate my thesis to my parents, Paritosh and Sova who has been always there for me and source of immense inspiration and support towards the successful completion of every hurdle in life.

ACKNOWLEDGEMENTS

I would like to express my sincere gratitude and appreciation to the University of Illinois at Chicago (UIC) for having me as a PhD candidate. I am highly excited and honored to have such a wonderful time as a PhD candidate at UIC due to its friendly nature and diverse culture. I would also like to acknowledge few people who played an important role towards the progress and success I have achieved. First, I would like to extend my gratitude and appreciation to my advisor, ***Dr. Brian P. Chaplin***, for allowing me to work as a graduate student under his supervision. I would like to greatly appreciate his consistent guidance, advice, problem solving ability, writing skill and quick communication skill which highly expedited my projects forward. I can confidently say that my writing skill regarding publications and thinking about new ideas or strategies have been highly improved due to his critical guidance. I would like to appreciate my thesis committee members, ***Dr. Vikas Berry, Dr. Sangil Kim, Dr. Alan D. Zdunek and Dr. Jeremiah Abiade*** for their valuable time, meaningful suggestions, constructive comments and critical insights. I would also like to thank all the lab members of the Chaplin's lab for meaningful discussion, coordinating the use of lab instruments and sharing their ideas which have helped a lot in the rigorous journey. First ***Yin Jing,*** a former PhD candidate who helped me a lot by discussing results and providing meaningful insight in my project. Second ***Jason Spataro***, an undergraduate researcher who helped me a lot by performing experiments during my busy schedule which accelerated my progress. I would like to thank ***Saurabh Misal, Samuel Plunkett, Meng-Hsuan Lin, Lun Guo***, ***Sarath Kumar Sekar***, ***Bilal Mehmood***, ***Soroush Almassi, and Sasmita Nayak*** for making my life and work highly enjoyable and exciting in the lab. I will really miss the group and the environment in the lab.

I would like to acknowledge and express my sincere gratitude to my family. I would like to thank my wife, ***Rumki*** who made my life in United States very smooth, enjoyable and exciting with her support, mental strength and love. I still can remember the first few days struggle in the USA which I could not withstand without her. I would like to appreciate my parents, ***Paritosh and Sova*** for continuous support, unconditional love, and providing resources when I needed those most. They were always there for me from the beginning of my life with their affection, love, courage and support when I am stressed, nervous, confused and scared. I know that my family will always be my support if I fall, be there if I need to discuss, and soothe me if I am in stress.

At the end I would like to thank National Science Foundation (NSF) for funding the research projects.

CONTRIBUTION OF AUTHORS

Research objective, introduction, background and thesis outline have been discussed in Chapter 1. Chapter 2 represents literature review and state of knowledge of the research projects. Chapter 3 discusses a published work (full citation added) in *ACS Applied Materials and Interfaces* regarding the use modified electrodes for electrochemical detection of antibiotics in wastewater matrix. For this work I was the first author, primary and major contributor and my research advisor, **Dr. Brian P. Chaplin** supervised the project, performed critical discussion, provided insights and revised manuscript. Chapter 4 shows another published work (full citation added) in *ACS Applied Materials and Interfaces* which discusses surface modification of electrode surfaces for perchlorate (carcinogenic) formation inhibition with significant organic oxidation. For this work I was the first author, primary and major contributor and **Dr. Brian P. Chaplin** supervised the project, performed critical discussion, provided insights and revised manuscript. An unpublished work regarding nitrate reduction using palladium based catalyst deposited reactive electrochemical membrane (REM) has been discussed in Chapter 5. For this work I was the first author and main contributor whereas **Jason Spataro** performed few experiments and **Sumant Avasarala, Abdul-Mehdi Ali and Dr. José M. Cerrato** performed inductive coupled plasma with optical emission spectroscopy (ICP-OES), scanning electron microscope combined with energy dispersive spectroscopy (SEM/EDS) and SEM with microprobe mapping on catalyst deposited REMs. **Dr. Brian P. Chaplin** supervised the project, performed critical discussion, provided insights and revised manuscript. Chapter 6 represents another manuscript regarding catalyst (bismuth doped tin oxide) deposited REMs for excellent organic oxidation and removal from water matrices. For this work I was the first author and primary contributor and **Chen Chen and Dr. Jeremiah Abiade** performed pulsed laser deposition (PLD) for the catalyst deposition on the REMs. **Dr. Brian P. Chaplin** supervised the project, performed critical discussion, provided insights and revised manuscript. Chapter 7 presents the conclusion of the thesis and shows the future possibility of the work.

TABLE OF CONTENT

1. Introduction……..1

1.1 Background……1

1.2 Research Objectives/Motivation……5

1.3 Outline……8

2. Literature Review…….....9

2.1 Synthesis and properties of non-porous boron-doped diamond (BDD) electrodes…...9

2.1.1 Synthesis of boron-doped diamond (BDD) electrodes……..9

2.1.2 Properties of boron-doped diamond (BDD) electrodes……...11

2.2 Different modification of BDD electrode surfaces……..13

2.2.1 Modification of BDD electrode surfaces for water treatment application…..17

2.2.2 Modification of electrode surfaces for sensing applications…….…….20

2.3 Synthesis and Modification of Porous Conductive Sub-stoichiometric and Doped TiO_2 Membrane Electrode for Water Treatment Application…….25

2.4 Electrocatalysts for Nitrate Reduction and OH• Production……...26

3. Selective Electrochemical Detection of Ciprofloxacin with a Porous Nafion/Multi-Walled Carbon Nanotube Composite Film Electrode……30

3.1 Abstract……30

3.2 Introduction……..31

3.3 Experimental……33

3.3.1 Reagents……...33

3.3.2 Fabrication of Porous-Nafion-MWCNT/BDD electrode…….33

3.3.3 Oxidation of MWCNT…….35

3.3.4 Characterization……...35

3.3.5 CFX detection experiments…….……35

3.3.6 Capacitance measurements…….….36

3.3.7 Adsorption experiments and CFX analysis…….….37

3.4 Results and Discussion……38

3.4.1 Physical and chemical characterization……...38

3.4.2 Electrochemical characterization…….43

3.4.3 Electrochemical detection of CFX……...46

3.4.4 Effect of pH and scan rate (ν) on CFX detection…….……48

3.4.5 CFX detection at porous-Nafion-MWCNT/BDD……50

3.4.6 CFX detection in the presence of non-target water constituents…….54

3.4.7 Detection of CFX on porous-Nafion-MWCNT/BDD in wastewater effluent (WWE)…….55

3.4.8 Elucidation of adsorption sites for CFX detection……...57

3.4.9 Fouling and regeneration of the sensor……61

3.5 Conclusion……...64

3.6 Acknowledgement……...64

4. Fluorination of Boron-doped Diamond Film Electrodes for Minimization of Perchlorate Formation……...65

4.1 Abstract……65

4.2 Introduction……..66

4.3 Materials and Methods…….68

4.3.1 Reagents……...68

4.3.2 Electrode preparation……...68

4.3.3 Electrode fluorination experiments……..69

4.3.4 Electrode oxidation experiments……..70

4.3.5 Electrode ageing experiments……..71

4.3.6 Electrochemical characterization methods……..71

4.3.7 Analytical methods……..72

4.3.8 Quantum mechanical simulations……73

4.4 Results and Discussion……73

4.4.1 Physical characterization……73

4.4.2 Electrochemical characterization……77

4.4.3 Perchlorate formation rates……..80

4.4.4 Organic compound oxidation……...86

4.4.5 Electrode stability……88

4.4.6 Mechanism…….…..92

4.5 Conclusions…….……93

5. Electrocatalytic Reduction of Nitrate using Magnéli Phase TiO_2 Reactive Electrochemical Membranes Doped with Pd-based Catalysts……..95

5.1 Abstract…….……...95

5.2 Introduction…….…….96

5.3 Materials and Methods…….98

5.3.1 Reagents…….…..98

5.3.2 Catalyst Loaded Magnéli Phase Powder Preparation……...…..98

5.3.3 Catalyst Loaded REM Preparation……..99

5.3.4 Batch Nitrate Reduction Experiments……..…..99

5.3.5 Flow-through Nitrate Reduction Experiments……...100

5.3.6 Membrane Characterization……...…101

5.3.7 Analytical Methods……103

5.3.8 Product Selectivity, Current Efficiency, and Energy Calculations……103

5.4 Results and Discussion…….……...…..104

5.4.1 Materials Characterization…….....104

5.4.2 Catalytic Nitrate Reduction……111

5.4.3 Electrocatalytic Nitrate Reduction…….112

5.4.3.1 Effect of Flow Direction……..114

5.4.3.2 Effect of Solution Conditions……....……..120

5.4.3.3 REMs in Series……....……121

5.4.4 Reactivity Characterization……122

5.4.5 Technological and Environmental Implications……...…125

5.5 Conclusions…….…...127

5.6 Acknowledgement…….……..…..128

6. Electrochemical Oxidation and Mineralization of Organic Compounds using Bismuth-doped Tin Oxide deposited Reactive Electrochemical Membranes……129
6.1 Abstract……..129

6.2 Introduction……130

6.3 Materials and Methods……...134

6.3.1 Reagents…….134

6.3.2 Catalyst Loaded REM Preparation……134

6.3.3 Batch Organics Oxidation Experiments…….136

6.3.4 Flow-through Organics Oxidation Experiments……136
6.3.5 Membrane Characterization……...137
6.3.6 Electrochemical Characterization Methods……...…138
6.3.7 Analytical Methods……139
6.3.8 Quantum Mechanical Simulations……139
6.3.9 Current Efficiency and Energy Consumption Calculations……..140
6.4 Results and Discussion……..141
6.4.1 Material Characterization……..141
6.4.2 Flow-Through REM Oxidation Experiments……148
6.4.2.1 TA Oxidation Experiments……148
6.4.2.2 Organics Oxidation Experiments……153
6.4.3 Voltammetric Results……155
6.4.4 DFT Simulation……...……..156
6.4.5 Technical and Environmental Significance ……...……..157
6.5 Acknowledgement…….158
7. Conclusion……...160
Appendices…….164
Appendix A……164
Appendix B……172
Appendix C……182
Appendix D…….……...197
Appendix E……202
References……..204

LIST OF FIGURES

Figure 3-1. SEM images of (a) bare BDD, (b) porous-nafion/BDD and (c, d) porous-nafion-MWCNT/BDD. TEM images of (e, f) unsupported porous-nafion-MWCNT……..……40

Figure 3-2. CV curves of bare BDD, Nafion/BDD, porous-Nafion/BDD, Nafion-MWCNT/BDD, and porous-Nafion-MWCNT/BDD in (a) 0.1 M KH_2PO_4 electrolyte containing 5mM $K_3Fe(CN)_6/K_4Fe(CN)_6$ and (b) 0.1M $HClO_4$ electrolyte containing 5mM $Fe(ClO_4)_2/Fe(ClO_4)_3$……..…46

Figure 3-3. DPV curves of 50 µM CFX on BDD, Nafion/BDD, porous-Nafion/BDD, Nafion-MWCNT/BDD, and porous-Nafion-MWCNT/BDD electrodes in 0.1 M KH_2PO_4 solution (pH = 4.50)……...47

Figure 3-4. (a) Effect of pH on the peak currents of 100 µM CFX in 0.1 M KH_2PO_4. (b) Linear relationship of peak current (I_p) vs scan rate (ν) in 0.1 M KH_2PO_4 with 50 µM CFX……50

Figure 3-5. (a) DPV curves of porous-Nafion-MWCNT/BDD at different concentrations of CFX in 0.1 M KH_2PO_4 (b) The corresponding calibration graph of CFX……..53

Figure 3-6. DPV curves before fouling (25 µM CFX), fouling with 1mM ABA, after fouling (25 µM CFX), and after cleaning (25 µM CFX): (a) with cathodic treatment (-1 V vs SHE for 60 sec) in 0.1M KH_2PO_4 solution (b) with cathodic treatment (-1 V vs SHE for 60 sec) in 0.1 M NaCl solution and (c) with base wash (0.01 M NaOH)……..63

Figure 4-1. XPS spectra of a) BDD-O b) BDDF-plasma, c) BDDF-PFOA, d) BDDF-aromatic and e) BDDF-aliphatic……...74

Figure 4-2. CV scans of 5mM a) $Fe(CN)_6^{3-/4-}$ and b) $Fe^{3+/2+}$ for BDD-O, BDDF-aliphatic and BDDF-aliphatic-aged; c) BDDF-aliphatic-aged: 5 mM $Fe(CN)_6^{3-/4-}$; d) BDDF-aliphatic-aged: 5 mM $Fe^{3+/2+}$ in 100mM $NaClO_4$ (for $Fe(CN)_6^{3-/4-}$) and 100mM $HClO_4$ (for $Fe^{3+/2+}$)……..79

Figure 4-3. Perchlorate formation rates on BDD-O, BDDF-plasma, BDDF-PFOA, BDDF-aromatic, and BDDF-aliphatic. The data for perchlorate formation were normalized according to corresponding BDD-O as different oxygenated BDD electrodes (BDD-O) were used for each of the different modifications [$BDDF_{i\text{-}normalized}$ = ($BDDF_{i\text{-}experimental}/BDD\text{-}O_{i\text{-}experimental}$)*BDD-O, where i = aliphatic, aromatic, PFOA or plasma]……...82

Figure 4-4. Total, free chlorine, chlorate, perchlorate and chloride mole balances for a) BDD-O without phenol, b) BDDF-aliphatic without phenol, c) BDD-O with 1 mM phenol and d) BDDF-aliphatic with 1 mM phenol. Experimental parameters: Supporting electrolyte = 10 mM NaCl; current density = 10 mA cm^{-2}; T = 22^o C……...85

Figure 4-5. Perchlorate formation rates on BDD-O and BDDF-aliphatic (Cycle 1 – Cycle 16). Inset shows DFT calculated geometry of the BDDF-aliphatic electrode surface……90

Figure 4-6. Schematic of the proposed mechanism for the inhibition of chlorate oxidation in the presence of phenol oxidation on a BDDF-aliphatic electrode. Atom key: C (grey); F (teal); O (red); H (white); Si (blue-grey); Cl (green). See online version for colors……..……93

Figure 5-1. XRD data for 1) Ti_nO_{2n-1} powder, 2) REM, 3) Pd-Cu/REM and 4) Pd-In/REM. The locations of the characteristic peaks for Ti_4O_7, Ti_6O_{11}, In, Pd, and Cu are represented by the vertical dashed lines. a) 2Θ = 20-38 deg and b) 2Θ = 38-52 deg……106

Figure 5-2. SEM image of REM surface.....108

Figure 5-3. Scanning electron microscope images of the a) Pd-Cu/REM and f) Pd-In/REM surface. SEM/EDS elemental mapping of b) Ti; c) O; d) Pd; and e) Cu on the Pd-Cu/REM surface and g) Ti; h) O; i) Pd; and j) In on the Pd-In/REM surface……109

Figure 5-4. Scanning electron microscope and microprobe image of the vertical cross-section of a) Pd-Cu/REM and f) Pd-In/REM. Scanning electron microscope and microprobe mapping of the vertical cross-section: b) Ti, c) O, d) Pd, and e) Cu in Pd-Cu/REM; and g) Ti, h) O, i) Pd, and j) In in Pd-In/REM. Top surface of the pellet is the left side of the image. Solid black lines on panels d, e, i, and j are estimated penetration depths of the catalyst metals……110

Figure 5-5. Schematic showing REM flow-through reactor with a) anode-cathode flow mode (upstream counter electrode) and b) cathode-anode flow mode (downstream counter electrode)……..113

Figure 5-6. a) Nitrate and b) nitrite concentration profiles for REM and Pd-Cu/REM at different potentials in the anode-cathode flow mode under different solution conditions. c) Nitrate and d) nitrite concentration profiles for REM and two Pd-Cu/REM in series at different potentials in anode-cathode mode……115

Figure 5-7. a) Nitrate and b) nitrite concentration profiles for catalyst-free REM, Pd-Cu/REM and Pd-In/REM in cathode-anode flow mode…….116

Figure 5-8. Electrocatalytic and catalytic NO_3^- reduction in the Pd-Cu/REM flow-through reactor. a) k_{obs} values versus J, b) NO_3^- concentration versus J. The solid lines are the model fits using equations 5-16 and 5-17 and the dashed horizontal line represents the MCL for NO_3^-…123

Figure 6-1. XRD data for REM and REM/BDTO/EDT with Ti_4O_7, Ti_5O_9, Ti_6O_{11}, SnO_2, SnO and Bi_2O_3 characteristic peaks…….143

Figure 6-2. SEM images of a) REM and b) REM/BDTO/EDT. EDS of c) REM surface, d) REM/BDTO/EDT surface and e) REM/BDTO/EDT cross section……145

Figure 6-3. XPS of REM, REM/BDTO/EDT and REM/BDTO/PLD20 at a) 0-1350 eV and b) 100-520 eV……..147

Figure 6-4. Schematic of reverse dead end flow mode……...……148

Figure 6-5. a) TA, b) HTA, c) ATZ and d) CDN concentration profiles for REM, REM/BDTO/EDT and REM/BDTO/PLD20 at different potentials in the cathode-anode flow mode……...……..150

Figure 6-6. DFT determined E_a with electrode potential for ATZ and CDN ……...……..157

Figure S-3-1. XPS of (a) MWCNT and (b) MWCNT-O (oxidized sample). **Legend**: C1: C=C; C2: C-C; C3: -C-OH; C4: -C=O; C5: -COOH; C6: -CO_3; C7: π-π*……...164

Figure S-3-2. (a) Calibration graphs at different concentration of CFX with (slope= 0.69±0.034) and without (slope= 2.08±0.085) 1mM Ca^{2+} in 0.1M KH_2PO_4 (LOD= 0.005µM, linear ranges (µM)= 0.05-1, 1-15), (b) Calibration graphs at different concentration of CFX without (y =1.6768±0.11 x + 7.0689±0.911, R^2 = 0.9831), with (y = 0.1543±0.03 x + 0.3286±0.341, R^2 = 0.9119), pH (4.5) adjusted (y = 0.3158±0.007 x + 1.7424±0.059, R^2 = 0.998 and both pH (4.5) and conductivity (0.1 M electrolyte) adjusted (y = 1.0492±0.07 x + 3.5865±0.636, R^2 = 0.9868) wastewater effluent matrix……...…165

Figure S-3-3. DPV curves of porous-Nafion-MWCNT/BDD at different concentrations of CFX with WWE (pH= 7.80)…….166

Figure S-3-4. DPV curves of porous-Nafion-MWCNT/BDD at different concentrations of CFX with WWE (pH= 4.50)…….166

Figure S-3-5. DPV curves of porous-Nafion-MWCNT/BDD at different concentrations of CFX with WWE (pH = 4.50 & 0.1 M KH_2PO_4)……...…167

Figure S-3-6. DPV curves of porous-Nafion-MWCNT/BDD at different concentrations of CFX in 0.1 M KH_2PO_4 without organics…….…….167

Figure S-3-7. DPV curves of porous-Nafion-MWCNT/BDD at different concentrations of CFX in 0.1 M KH_2PO_4 with 1:1 HBA…….…….168

Figure S-3-8. DPV curves of porous-Nafion-MWCNT/BDD at different concentrations of CFX in 0.1 M KH_2PO_4 with 1:1 ABA……..168

Figure S-3-9. DPV curves of porous-Nafion-MWCNT/BDD at different concentrations of CFX in 0.1 M KH_2PO_4 with 1:1 SA……169

Figure S-3-10. Calibration graphs of CFX at different concentration without organics (blank/CFX only) (y = 0.920±0.03 x + 8.38±0.249, R^2 = 0.996), with equimolar ABA (y = 0.854±0.012 x + 7.328±0.105, R^2 = 0.99), equimolar HBA (y = 0.72±0.052 x + 6.144±0.112, R^2 = 0.999) and equimolar SA (y = 0.782±0.005 x + 6.723±0.046, R^2 = 0.998)…….169

Figure S-3-11. Adsorption isotherms of ciprofloxacin on MWCNT and MWCNT-O at 20^O C fitted with two models (Freundlich and Langmuir model)……..170

Figure S-3-12. Calibration graphs of CFX with porous-Nafion-MWCNT/BDD (y = 1.9379±0.049x + 5.995±0.300, R^2= 0.9981, and porous-Nafion–MWCNT-O/BDD (y=1.8036±0.13 x+5.341±0.784, R^2 = 0.9852)……....170

Figure S-4-1. Deconvoluted results of C 1s XPS spectra of a) BDD-O, b) BDDF-plasma, c) BDDF-PFOA, d) BDDF-aliphatic, e) BDDF-aromatic, f) BDDF-PFOA-aged and g) BDDF-aliphatic-aged. Legend: C1: =C=C=; C2: ≡C-C≡; C3: ≡C-OH; C4: =C=O; C5: ≡C-F; C6: -COOH; C7: $=CF_2$; C8: $-CF_3$……....173

Figure S-4-2 CV scans of: a) BDD-O and BDDF-plasma: 5 mM $Fe(CN)_6^{3-/4-}$; b) BDD-O and BDDF-plasma: 5 mM $Fe^{3+/2+}$; c) BDDF-PFOA and BDDF-PFOA-aged: 5mM $Fe(CN)_6^{3-/4-}$; d) BDDF-PFOA and BDDF-PFOA-aged: 5mM $Fe^{3+/2+}$; e) BDD-O and BDDF-aromatic: 5mM $Fe(CN)_6^{3-/4-}$; f) BDD-O and BDDF-aromatic: 5mM $Fe^{3+/2+}$; ……..…177

Figure S-4-3. DFT optimized structures of different fluorinated groups on a 10 carbon atom cluster that represents the BDD surface. Atom key: C (grey); F (teal); O (red); H (white); Si (blue-grey)……179

Figure S-4-4. Duplicate experiment to that shown in the main manuscript. Total, free chlorine, chlorate, perchlorate, and chlorine mole balance for a) BDD-O without phenol; b) BDDF-aliphatic without phenol; c) BDD-O with phenol; and d) BDDF-aliphatic with phenol…….180

Figure S-4-5. Bulk oxidation of a) 1mM phenol and b) 0.1mM TA for BDD-O, BDDF-PFOA and BDDF-aliphatic at 22^0C……181

Figure S-4-6. Perchlorate formation rates for BDD-O, BDDF-PFOA and BDDF-PFOA-aged……..181

Figure S-5-1. Schematic of the experimental flow-through reactor setup: a) anode-cathode and b) cathode-anode flow mode……182

Figure S-5-2. Experimental measurements of flow velocity (u) with pressure drop (ΔP) for REM and Pd-M/REMs……..183

Figure S-5-3. a) Nitrate, b) nitrite, and c) ammonium concentration profiles, and d) first-order fit for initial (50%) nitrate reduction for Pd-Cu/TiO_2, Pd-Cu/Ti_nO_{2n-1}, and Pd-In/ Ti_nO_{2n-1} in batch mode……184

Figure S-5-4. Anode-cathode flow mode. a) LSV scans of solutions with 5 mM $NaNO_3$ in 100 mM $NaHCO_3$ for REM, Pd-Cu/REM, and Pd-In/REM. b) Background subtracted LSV scans for Pd-Cu/REM and Pd-In/REM……...185

Figure S-5-5. a) Nitrate and b) nitrite concentration profiles for REM and Pd-In/REM at different applied potential in the anode-cathode mode and under different solution conditions.186

Figure S-5-6. LSV scans of 5 mM $NaNO_3$ in a 100 mM $NaHCO_3$ electrolyte for Pd-Cu/REM under air and argon purging……..……...187

Figure S-5-7. Nitrate and nitrite concentration (C/C_0) profile with flux for chemical and electrochemical reaction methods……188

Figure S-6-1. Concentration profiles for oxidation of a) ATZ at 1.5 V/SHE, c) ATZ at 1.8 V/SHE, e) CDN at 1.14 V/SHE and g) CDN at 1.5 V/SHE at 20, 30 and 40 ^{0}C. Arrhenius plot for oxidation of b) ATZ at 1.5 V/SHE, d) ATZ at 1.8 V/SHE, f) CDN at 1.14 V/SHE and h) CDN at 1.5 V/SHE……...198

Figure S-6-2. Schematic of the flow-through reactor setup: anode-cathode flow mode……199

Figure S-6-3. Flow velocity (u) with pressure drop (ΔP) for REM, REM/BDTO/EDT and REM/BDTO/PLD20……...…….200

Figure S-6-4. Deconvoluted XPS of a) Sn 3d and b) Bi 4f spectra of REM/BDTO/EDT and c) Sn 3d spectra of REM/BDTO/PLD20…….200

Figure S-6-5. LSV of background electrolyte (100 mM KH_2PO_4), 10 µM of ATZ and CDN in 100 mM KH_2PO_4 for a) BDD and b) REM/BDTO…….201

Figure S-6-6. Peak current (i_p, mA) with a) scan rate (ν) and b) square root of scan rate (√ν) for ATZ and CDN oxidation with REM/BDTO
(scan rates = 10, 20, 40, 60, 80 and 100 mV sec^{-1})…….201

LIST OF TABLES

Table 2-1. Electrochemical methods for the determination of different antibiotics……22

Table 3-1. Deconvolution results of C1s XPS spectra for MWCNT and MWCNT-O (values given in atomic percent)…….42

Table 3-2. Double layer capacitances for different modified electrodes…….45

Table 3-3. The comparison of different methods for the determination of Ciprofloxacin……..52

Table 3-4. Determination of CFX in the presence of different interferences. Errors on estimates represent the standard errors……..56

Table 3-5. The comparison of normalized slopes for CFX calibration with porous-Nafion-MWCNT/BDD and porous-Nafion- MWCNT-O/BDD……60

Table 3-6. Results of adsorption isotherm models fitting to adsorption data of CFX on MWCNT and MWCNT-O…….61

Table 4-1. Atomic Concentrations of C, O, F, and Si determined by XPS for different surface modifications (values given in atomic percent)…….75

Table 4-2. Deconvoluted XPS results for C 1s spectra for BDD-O, BDDF-plasma, BDDF-PFOA, BDDF-aliphatic, BDDF-aromatic, BDDF-PFOA-aged, and BDDF-aliphatic-aged electrodes (values given in atomic percent). Functional groups: C1 (284.5 eV): =C=C=; C2 (285.3±0.2 eV): ≡C-C≡; C3 (286.3±0.3 eV): ≡C-OH; C4 (287.0±0.1 eV): =C=O; C5 (287.6±0.04 eV): ≡C-F; C6 (288.5±0.2 eV): -COOH; C7 (290.5±0.3 eV): $=CF_2$; C8 (292.8±0.5 eV): $-CF_3$……....75

Table 4-3. Phenol and TA Oxidation Rates for Different Fluorinated Electrodes**.** The data for organic compound oxidation are normalized according to BDD-O as different oxygenated BDD electrodes (BDD-O) were used for each of the different modifications……...87

Table 5-1. Water quality data of the surface water sample…….113

Table 5-2. Summary of results for nitrate reduction with a Pd-Cu/REM at a cathodic potential of -2.5 V/SHE……...118

Table 6-1. Atomic concentrations (atomic %) of Ti, O, Sn and Bi determined by XPS for REM, REM/BDTO/EDT and REM/BDTO/PLD20……..……146

Table 6-2. Summary of experimental data for all flow-through organics oxidation experiments……..151

Table 6-3. Energy Requirement (E_{EO}, kWh m^{-3}) and Current Efficiency (CE, %) for TA, ATZ and CDN oxidation with REM, REM/BDTO/EDT and REM/BDTO/PLD20 electrodes……..159

Table S-3-1. Determination of CFX in the presence of different interferences (LDRs including LODs). Errors on estimates represent the standard errors……...171

Table S-4-1. Comparison of Atomic Ratios (F:Si, F:C and Si:CF_2:CF_3) of an Aliphatic Silane molecule with BDDF-aliphatic (from XPS) and BDDF-aliphatic-aged (from XPS) and Si:CF of an Aromatic Silane molecule with BDDF-aromatic (from XPS)……174

Table S-4-2. CV data of BDD-O, BDDF-plasma, BDDF-PFOA, BDDF-aliphatic, BDDF-aromatic, BDDF-aliphatic-aged and BDDF-PFOA-aged with $Fe(CN)_6^{3-/4-}$ and $Fe^{2+/3+}$ redox couple……...……178

Table S-5-1. Summary of experiment data for all flow-through experiments……189

Table S-5-2. Total N Data for REM, Pd-In/REM, and Pd-Cu/REM under different solution conditions…….192

Table S-5-3. Nitrite Concentration and Selectivity for Both Electrocatalytic (-2.5 V/SHE) and Catalytic NO_3^- Reduction at Different Fluxes…….194

Table S-5-4. Energy Requirements (kWh mol^{-1}), E_{EO} (kWh m^{-3}), Current Efficiency (CE, %) for REM, Pd-Cu/REM and Pd-In/REM in All Solution Conditions and for Pd-Cu/REM with 10 and 100 mM NO_3^- Under Air Purging with Anode-Cathode Flow Mode……..195

ABBREVIATIONS

REM - Reactive electrochemical membrane

ICP-OES - Inductive coupled plasma with optical emission spectroscopy

SEM/EDS - Scanning electron microscope combined with energy dispersive spectroscopy

PLD - Pulsed laser deposition

BDD - Boron-doped diamond

WWE - Wastewater effluent

CFX – Ciprofloxacin

BDTO – Bismuth doped tin oxide

XPS - X-ray photo electron spectroscopy

TEM - Transmission electron microscopy

DPV - Differential pulse voltammetry

EAOP - Electrochemical advanced oxidation process

PFOA - Perfluorooctanoic acid

DFT - Density function theory

EPA - Environmental protection agency

MCL - Maximum contaminant levels

XRD - X-ray diffraction

COD - Chemical oxygen demand

EU - European union

DET - Direct electron transfer

EIS – Electrochemical impedance spectroscopy

GCE – Glassy carbon electrode

CPE – Carbon paste electrode

CVD - Chemical vapor deposition

MCD - Microcrystalline diamond

NCD - Nanocrystalline diamond

RDS - Rate determining step

MIP - Molecularly imprinted polymer

MWCNT - Multi-walled carbon nanotubes

EDA - Electron donor-acceptor mechanism

CAHB - Charge assisted H-bond

SHE - Standard hydrogen electrode

SDBS - Sodium dodecylbenzenesulfonate

HBA - 4-hydroxybenzoic acid

ABA - 4-aminobenzoic acid

HPLC - High performance liquid chromatography

LOD - Limit of detection

RSD - Relative standard deviation

SDBS - Sodium dodecyl benzene sulfonate

SAM - Self-assembled monolayer

NEXAFS - Near-edge X-ray absorption fine structure spectroscopy

RF - Radio frequency

SCCM - Standard cubic centimeters per minute

RDE - Rotating disc electrode

PDA - Photodiode array detector

WHO - World Health Organization

DOM - Dissolved organic matter

IC - Ion chromatography

PEEK - Polyether ether ketone

EDT - Electrodeposition followed by thermal oxidation

LSV - Linear scanning voltammetry

OEP - Oxygen evolution potential

ORR – Oxygen reduction reaction

SUMMARY

This dissertation summarizes different modifications of porous and non-porous electrode surfaces for electrochemical water and wastewater treatment and sensing applications. Specifically, the research is focused on the preparation of porous substoichiometric TiO_2 electrodes (Ti_nO_{2n-1}, n = 4 - 10), modification of Ti_nO_{2n-1} and non-porous boron-doped diamond (BDD) electrodes, electrode characterization using analytical and electrochemical techniques, and their use for trace contaminant detection, oxidation and reduction of organic and inorganic contaminants from water matrices. The major objectives of the research are: 1) to study the electrochemical detection of antibiotics in wastewater matrices with high sensitivity and selectivity using modified electrodes, 2) to investigate the effects of different surface fluorination methods on perchlorate (carcinogenic) formation inhibition and organic contaminant oxidation during electrochemical water treatment, 3) to investigate the use of bimetallic catalysts for electrocatalytic nitrate reduction in water matrices, and 4) to determine the effect of doped metal oxide (bismuth doped tin oxide) catalysts for the enhancement of hydroxyl radical production to enhance the electrochemical oxidation of organic contaminants.

This dissertation reports on the successful fulfilment of the research objectives as follows:

The overuse and presence of ciprofloxacin (CFX), a second generation fluoroquinolone, an antibiotic for treating diseases associated with gram-positive and gram-negative bacteria and can cause the emergence of potential drug resistant bacteria. Electrochemical techniques are the most extensively used methods compared to other analytical techniques as they are cost effective, energetically viable, robust, highly sensitive, quick and easy to use. They have been mainly used for CFX detection in urine sample, milk, serum and tablets. However, CFX detection in natural

or wastewater matrices has not been investigated. In this work an electrochemical sensor was fabricated by modifying the boron-doped diamond (BDD) electrode surface with a porous nafion multi-walled carbon nanotube composite film. X-ray photo electron spectroscopy (XPS), scanning electron microscopy (SEM) and transmission electron microscopy (TEM) were utilized to characterize the sensor. The sensors were able to detect CFX using differential pulse voltammetry (DPV) in the presence of other antibiotics (i.e., amoxicillin), other non-target water components and several commonly present organic compounds. The sensor was capable of CFX detection in the presence of WWE matrix with excellent sensitivity and selectivity. Different concentration of different organic compounds can foul the sensor but the fouling was easily removed using short cathodic current confirming its effectiveness for contaminant detection in diverse water matrices.

Electrochemical advanced oxidation process (EAOPs) has been widely used for organic compound oxidation in various water matrices. However, the use of EAOPs are limited by perchlorate formation, which is a carcinogenic byproduct formed via extended electrolysis of chloride ions present in solution. To address this problem, fluorination was performed on BDD electrodes using radio frequency (RF) plasma in the presence of H_2 and CF_4, perfluorooctanoic acid (PFOA) electrochemical oxidation, and silanization using aliphatic and aromatic silane. XPS was performed to characterize the effectiveness of the fluorination methods. Chronoamperometry experiments were used to monitor perchlorate production and organic compound oxidation as a function of electrode coating. The most effective method to prevent perchlorate production was modification of the BDD electrode with an aliphatic silane (1H, 1H, 2H, 2H perfluorodecyltrichlorosilane) self-assembled monolayer (SAM). The SAM was able to completely inhibited perchlorate formation with only minor effects on organic compound

oxidation. The surface coverage, thickness the blocking layer and steric effect hindered the electron transfer rate and the result was supported by XPS and density function theory (DFT) simulations determined film length.

Nitrate (NO_3^-) is one of the most common pollutants in the natural environment. Therefore the US Environmental Protection Agency (EPA) has set maximum contaminant levels (MCLs) for NO_3^- and NO_2^- of 700 and 70 μM, respectively. Destructive methods for NO_3^- removal have been extensively researched over the years. Catalytic and electrocatalytic nitrate reduction using bimetallic catalysts have shown promise, but these methods are limited by storage and delivery of an external electron donor (e.g., H_2) and formation of high concentrations of undesired NO_2^- and NH_3, respectively. In this study two different bimetallic catalysts (e.g. Pd-Cu and Pd-In) were used to modify reactive electrochemical membranes (REMs) using the incipient wetness method and the modified REMs were characterized by X-ray diffraction (XRD), SEM/EDS, and ICP-OES. Electrocatalytic nitrate reduction was performed with respect to electrode placement, flow rate, electrode potential, NO_3^- concentration, and under various solution conditions using chronoamperometry in flowthrough mode. This study showed that NO_3^- was reduced from a 1 mM feed concentration to below the EPA's regulatory MCL (700 μM) in a single pass through the REM (residence time ~ 2 s), with low product selectivity (<2 %) of NO_2^-/NH_3, high current efficiency (105 ± 5.4%), and low energy consumption (1.1 to 1.3 kWh mol^{-1}). Nitrate reduction was not affected by dissolved oxygen and carbonate species and only slightly decreased in a surface water sample due to Ca^{2+} and Mg^{2+} scaling.

Research has shown that REMs composed of Ti_nO_{2n-1} are very effective for EAOPs. However, at high membrane fluxes the removal of contaminants can become kinetically limited. This work showed that the deposition of bismuth doped tin oxide (BDTO) catalysts to REMs

could enhance the hydroxyl radical and thus increase electrochemical oxidation rates. The catalysts were deposited by pulsed electrodeposition and pulsed laser deposition techniques and characterized using XPS, XRD, SEM/EDS, TEM, linear scan voltammetry (LSV), and ICP-OES. Terephthalic acid (TA) was used as a hydroxyl radical probe, whereas atrazine (ATZ) and clothianidin (CDN) were chosen as potential harmful herbicide and pesticide, respectively. TA, ATZ, and CDN oxidation rate constants increased upon BDTO deposition. At the highest applied potential (3.5 V/SHE), TA, ATZ and CDN concentrations were below the detection limit in the permeate for REM/BDTO electrodes. Chemical oxygen demand (COD) analysis of TA and total N analysis of ATZ and CDN showed complete mineralization of the compounds at the highest applied potential. DFT simulations provided potential dependent activation energies for ATZ and CDN, which were supported by experimental data.

The dissertation showed modification of porous and non-porous electrodes for excellent sensitivity and selectivity for antibiotics detection in water matrices, minimization of perchlorate formation, nitrate reduction and subsequent removal from water matrices and excellent organics oxidation and mineralization. The results of the dissertation have opened several new research directions. The modification of BDD electrodes can be performed using selectively edge functionalized (-COOH) vertically aligned carbon nanotubes and porous nafion composite film which may increase the selectivity and sensitivity. Due to the toxicity of fluorocarbons, electrodes can be modified using metal oxide materials (Al_2O_3, ZrO_2, TiO_2) for perchlorate formation inhibition with significant organics oxidation by creating a blocking layer. A series of bimetallic catalyst deposited REMs can be used for highly concentrated nitrate reduction and removal in reverse osmosis and ion exchange brine solution. Bimetallic catalyst deposited REM

and bismuth doped tin oxide catalyst deposited REM can be used as cathode and anode, respectively for nitrate reduction and organics oxidation simultaneously in a single setup.

1. Introduction

1.1 Background

Water covers about 71 % of earth's surface among which 96.5 % is held by ocean [1,2]. Only 2.5 % of the total water is fresh water and 70 % of it is held by icecaps, icebergs etc. Therefore clean, fresh and drinkable water that are in the form of surface water and groundwater are concentrated in certain regions and highly necessary for life on earth [2–4]. Due to uneven distribution of drinking water in the form of groundwater and surface water, a high population on earth does not have adequate access to drinking water [3–5]. Due to increased demand of fresh water for agricultural, industrial, domestic, and commercial use, the drinking water scarcity situation is becoming worse [2,3,5]. Due to lack of effective water treatment technologies, increased population, and mismanagement of drinking water sources, the water supplies have been contaminated with trace organic contaminants, heavy metals, inorganic contaminants, pathogens, and disinfection byproducts that can cause acute and chronic illness in human being [6–9]. Several contaminants present in water matrices are of concern because they can cause serious health risks and therefore have prompted government agencies, such as the US Environmental Protection Agency (EPA) and European Union (EU) to set maximum concentration limits in drinking water [10–12].

Water treatment and sensing technologies should be energy efficient, low cost, quick, easy to use, and have high sensitivity and selectivity. Several different physical, biological, and chemical treatment techniques have been used as destructive treatment methods to remove recalcitrant contaminants from water. Physical separation techniques mainly used coagulation, evaporation, liquid-liquid extraction, distillation, ion exchange, adsorption, reverse osmosis, and membrane

filtration to remove a wide range of contaminants from water [13–22]. Physical techniques suffer from several disadvantages such as fouling, incomplete removal, concentrated brine formation, and chemical addition. For example, membrane filtration depends exclusively on size of the contaminants for effective separation and removal, suffers from membrane fouling and associated physical and chemical cleaning cost and time. Membrane filtration is often coupled with other processes such as coagulation and flocculation, advanced oxidation processes, and ozonation to achieve effective removal of contaminants, which have additional disadvantages such as pH adjustment, sludge production and removal, and cost associated with chemical addition [23–27]. Another water treatment method is biological treatment, which uses different types of bacteria and microorganism to degrade contaminants [28–32]. However, the application of biological treatment suffers from high sludge production, bacterial contamination, and sometimes low removal efficiency [33–36]. The photochemical techniques utilize UV light in the presence of a photocatalysis (e.g. TiO_2) or oxidizing chemicals (e.g. O_3, H_2O_2) to produce highly active in-situ reactive oxygen species for effective removal of contaminants [37–39]. The photochemical treatment suffers from the requirement of a UV light source, addition of chemicals, formation of reaction byproducts, and low process efficiency [40]. The chemical treatments are chlorination, fenton and ozonation process that require the addition of bleach, Fe(II), H_2O_2, and O_3 for contaminant degradation [41–44]. The chemical treatments suffer from formation of hazardous reaction byproducts and associated treatment cost, treatment of downstream slurries, and high cost due to the addition of the chemicals [45,46].

Electrochemical advanced oxidation processes (EAOPs) have emerged as an effective water and wastewater treatment technology [47–57]. The widely used materials for EAOPs are doped-SnO_2, PbO_2, boron-doped diamond (BDD), and substoichiometric- and doped-TiO_2 [47–57]. EAOPs

have certain advantages over the conventional methods discussed above, such as high current efficiency, low cost, no requirement of chemical addition, and are pathogen free [58–61]. EAOP involves direct electron transfer (DET) and the production of $OH^{\bullet}$ at an appropriate anode surface. The formation of $OH^{\bullet}$ is very effective for contaminant removal because it reacts unselectively with several organic compounds at diffusion-limited rates without leaving a residual in the treated water [62].

The application of EAOPs is limited by the formation of perchlorate (ClO_4^-) from chloride via extended electrolysis. The formation of ClO_4^- is unwanted as it is carcinogenic and EPA has set a health advisory level of 15 ppb [63]. Therefore modification of electrodes or treatment strategies is necessary to reduce or inhibit perchlorate formation without affecting the rates of organic contaminant oxidation.

EAOPs with non-porous electrodes and in batch or flow-by configurations suffer from low surface area, low mass transfer rate constants, and thus require extended contact times to achieve water treatment goals. To address these challenges, reactive electrochemical membranes (REM) made of conductive ceramic materials have been introduced. Recent work showed REMs have high mass transfer rate constants due to the flow-through mode operation [64]. However, previous results showed that rate constants for some contaminants became kinetically limited at higher membrane fluxes [64]. To minimize the kinetic limitation, modification of REMs using catalysts is necessary, which is mainly focused on increasing the hydroxyl radical production rate.

EAOPs are very useful for organic and inorganic contaminant oxidation. However nitrate cannot be oxidized as N in nitrate is already present in maximum oxidation state. The consumption of NO_3^- and NO_2^- has serious health risks [65–67]. Several physical separation

techniques such as electrodialysis, ion exchange, and reverse osmosis have been used for NO_3^- removal, but they are nonselective and produce concentrated NO_3^- brines, which require costly post-treatment or disposal [68,69]. Previous studies have also shown destructive NO_3^- removal from water via catalytic and electrocatalytic reduction [70–80]. Chemical and electrochemical reduction suffers from storage and delivery of an external electron donor (e.g. H_2) and formation of high concentration of NO_2^- and NH_3, respectively [70,74,75,81–83]. Therefore, continuous NO_3^- reduction and removal without brine formation, lowering the selectivity towards NO_2^- and NH_3, and elimination of post treatment and disposal costs are highly necessary.

Once water is treated, it must be continuously monitored to determine if treatment objectives have been obtained. Antibiotics are important class of compounds that enter the environment from livestock operations and incomplete removal during wastewater treatment. The overuse of antibiotics can cause the emergence of potential drug resistant bacteria. Different analytical techniques were extensively utilized for the detection of antibiotics, which include capillary electrophoresis, liquid chromatography—mass spectroscopy, spectrophotometry, high-performance liquid chromatography, immunoassay, chemiluminescence, spectrofluorimetry and electrochemical techniques [84–93]. Electrochemical techniques (impedance spectroscopy, voltammetry) are the most extensively used methods compared to other analytical techniques as they are cost effective, energetically viable, robust, highly sensitive, quick and easy to use. Studies have been performed on the fabrication of electrochemical sensors for the sensing antibiotics mainly in serum, urine, and tablets. However electrochemical sensors were not used for the determination of antibiotics in water matrices [94–109]. Therefore detection of antibiotics in water and wastewater matrix is highly necessary.

1.2 Research Objectives/Motivation

The overall motivation of this work is to modify different porous and non-porous electrode surfaces for water and wastewater treatment and sensing applications. Non-porous BDD electrode surfaces were modified using different materials to detect antibiotics (CFX) in wastewater solutions and to inhibit perchlorate formation without significantly affecting organics oxidation. Porous electrodes were modified using metal and metal oxide catalysts for nitrate reduction and organic compound oxidation, respectively from water matrices. The specific research objectives are as follows:

1) *Electrochemical Detection of Antibiotics (Ciprofloxacin) with a Modified BDD Electrode*

Ciprofloxacin (CFX) has been used to treat the diseases associated with gram-positive and gram-negative bacteria. As it is not fully metabolized CFX can be found in natural and groundwater which is highly influenced by domestic, industrial wastewater, and agricultural runoff. The presence of CFX in water matrices can cause emergence of drug resistant bacteria. Electrochemical techniques have been the most widely used method for CFX detection among several analytical techniques due to low energy requirement, low cost, ease of use, and the short time requirement. Electrochemical techniques have been mainly used for CFX detection in urine samples, serum, milk, and tablets. However electrochemical CFX detection in natural or wastewater matrices has not been investigated. The previously studied electrochemical sensors for CFX detection was also limited by low sensitivity and selectivity. However high sensitivity and selectivity of the sensor is required, as CFX is generally present in trace quantities and with several other non-target water constituents. Therefore, modification of electrodes is needed to increase the selectivity and sensitivity of the sensor for CFX detection in water matrices. The BDD electrodes were modified using a solution mixture of MWCNT, Nafion, and salt. DPV was

used to detect CFX in the presence of different constituents to determine selectivity and sensitivity of the sensor. Sensors can also be fouled in the presence of different contaminants in water matrices. Therefore regeneration of the sensor is necessary for continuous detection of CFX with excellent sensitivity, selectivity, and long term use. An electrochemical technique has also been introduced to fully regenerate the sensor.

2) Modification of BDD Electrode Surfaces for Minimization of Perchlorate Formation

Electrochemical advanced oxidation processes (EAOPs) have been widely used for organic compound oxidation from water matrices due to high current efficiency, low cost, no chemical addition, no pathogen contamination and no or less by-product formation. However the use of EAOP is limited by toxic perchlorate formation (EPA health advisory level = 15 ppb). The perchlorate has been formed via extended electrolysis of chloride present in water matrices. The perchlorate formation strongly depends on the electrode surface functional groups. Fluorination of electrode surface with thin blocking films can be effective for preventing perchlorate formation by limiting the probability of electron tunneling. In this study, BDD electrodes were modified using fluorination techniques such as radio frequency (RF) plasma in the presence of H_2 and CF_4 gases, perfluorooctanoic acid (PFOA) electrochemical oxidation, and silanization using aliphatic and aromatic silane.. The different fluorination methods may incorporate different thicknesses and areal coverages of fluorinated groups on the BDD surface. Chronoamperometry was used to monitor perchlorate formation and organic compound oxidation on the modified electrodes, to determine the most effective and stable electrode modification method.

3) Modification of REM Electrode Surfaces for Nitrate Reduction

Nitrate is one of the most common pollutants present in natural waters. Nitrate and nitrite both have potential health risks and therefore the USEPA has set maximum contamination levels

(MCLs) for NO_3^- and NO_2^- as 700 and 70 μM, respectively, in drinking water. Catalytic and electrocatalytic nitrate reduction methods are limited by storage and delivery of an external electron donor (e.g., H_2) and formation of high concentrations of undesired NO_2^- and NH_3, respectively. Bimetallic catalysts composed of a noble metal (e.g., Pd, Pt) for H adsorption and a promoter metal (e.g., Cu, Sn, In) for nitrate reduction are needed. In this study, two different bimetallic catalysts (e.g., Pd-Cu and Pd-In) were deposited on the REM surface using the incipient wetness method and the modified electrodes were used for electrocatalytic nitrate reduction. Various operational parameters were investigated, including counter electrode placement, flow rate, electrode potential, NO_3^- concentration, and effect of various solution conditions.

4) *Modification of REM Electrode Surfaces for Improved Electrocatalytic Organics Oxidation and Removal*

The use of non-porous electrodes to oxidize water contaminants using EAOPs is limited by low surface area and low mass transfer rate constants, requiring long contact times to achieve treatment goals. REMs made of substoichiometric TiO_2 (Ti_nO_{2n-1}, n = 4 – 10) are very effective for electrochemical oxidation of organic compounds due to their high specific surface area, low cost, high mass transfer rate constants, and ability to generate hydroxyl radicals. Previous work indicated that the fast mass transfer rates achieved in the REM system caused kinetic limitations. To overcome these kinetic limitations, electrode modification is necessary. Doped tin oxide is another material that is an effective EAOP electrode material. Bismuth doped tin oxide (BDTO) catalysts were deposited on REMs using pulsed laser deposition (PLD) and pulsed electrodeposition methods. The formation of hydroxyl radicals on this modified REMs was investigated using terephthalic acid as a hydroxyl radical probe, and atrazine and clothianidin as

model herbicide and pesticide contaminants, respectively. Chronoamperometry flow-through oxidation experiments were performed as a function of potential and flow rate were to determine the effectiveness of these electrodes for water treatment of agricultural waters.

1.3 Outline

The dissertation is organized in the following manner. Chapter 2 presents the literature review and state of knowledge on the 1) synthesis of non-porous BDD and porous, substoichiometric TiO_2 REM electrodes, 2) modification of non-porous electrode surfaces for water treatment and sensing application, 3) modification of porous REM electrode surfaces for water treatment application and 4) electrocatalysts for nitrate reduction and hydroxyl radical production. Chapter 3 contains a study focused on sensor fabrication and electrochemical detection of antibiotics in water matrices, which was published in ACS Applied Materials and Interfaces as "Selective Electrochemical Detection of Ciprofloxacin with a Porous Nafion/Multi-Walled Carbon Nanotube Composite Film Electrode". This paper fulfills research objective 1. Chapter 4 contains a study focused on the modification of BDD electrode surfaces for inhibition of perchlorate formation, which was published in ACS Applied Materials and Interfaces as "Fluorination of Boron-doped Diamond Film Electrodes for Minimization of Perchlorate Formation". This publication fulfills research objective 2. Chapter 5 contains a study focused on the modification of porous REM electrode surfaces using bimetallic catalysts for nitrate reduction. This work fulfills research objective 3. Chapter 6 contains a study focused on the modification of porous REM electrode surfaces using doped metal oxide catalysts to enhance the oxidation rates of organic contaminants. This work addresses research objective 4. Chapter 7 summaries the major findings of the dissertation and discusses future related research directions.

2. Literature Review

This section communicates the state of knowledge of the 1) synthesis of non-porous BDD and porous Magnéli phase TiO_2 electrodes, 2) modification of BDD electrode surfaces for water treatment and sensing applications, 3) modification of porous REM electrode surfaces for water treatment applications and 4) electrocatalysts for nitrate reduction and hydroxyl radical production. BDD electrodes are more useful for water treatment and sensing applications compared to other conventional electrodes (e.g., GCE, CPE), due to their large potential window, low background current density, high stability, and resistance to fouling [52,53,110–113]. Due to the large potential window of BDD, numerous analytes (e.g., antibiotics, organics and heavy metals) can be detected using modified BDD electrodes. The conductive Magnéli phase sub-stoichiometric TiO_2, and doped-TiO_2 are also very promising electrode materials to prepare porous REMs that function as both an EAOP electrode as well as a water treatment filtration membrane [50,54,64,114]. BDD and Ti_4O_7 electrodes oxidize and remove recalcitrant compounds from wastewater by the production of hydroxyl radicals (OH•) (equation 2-1) and direct electron transfer (DET) reactions (equation 2-2) [55,113,115–118]:

$$H_2O \rightarrow OH^{\bullet} + H^{+} + e^{-} \quad (2\text{-}1)$$

$$R \rightarrow (R^{\bullet})^{+} + e^{-} \quad (2\text{-}2)$$

The synthesis, properties, different modification methods for BDD and Ti_4O_7 electrodes, and their use for wastewater treatment and sensing applications are discussed below.

2.1 Synthesis and Properties of Non-porous Boron-doped Diamond (BDD) Electrodes

2.1.1 Synthesis of Boron-doped Diamond (BDD) Electrodes

Un-doped diamond is an insulating material due to its large band gap (> 5 eV). It has a high resistivity on the order of 10^{20} ohm-cm. To make the diamond conductive, a dopant (e.g.,

boron (p-dopant), phosphorus (n-dopant)) is added to decrease the band gap. The n-type semiconductor can be prepared by incorporating nitrogen, phosphorus, antimony, or another group V element [119–123]. A p-type semiconductor can be prepared by doping with boron (to form BDD) or other group III element, which has low charge carrier density and an activation energy of 0.37 eV to form BDD [119–123]. BDD film deposition on a substrate is usually performed by chemical vapor deposition (CVD) method. BDD electrodes have been mainly synthesized as microcrystalline and nanocrystalline materials [122,124–127]. The CVD methods use hot filaments [128–131] or microwave radiation [132–136] to activate the gases at ~ 2000 ^{o}C. The pressure used for CVD is typically in the range of 10-50 mbar and the gas phase consists of 0.5-3.0 % methane in a hydrogen carrier gas. The boron dopant source used is usually diborane (~ 0.0015%) [129,131,137,138], trimethyl borate [128,139], B_2O_3 [140–142], or trimethoxy borane [133].

Different self-passivating metals (e.g. Ti, Ta, W, Mo, Nb) and polycrystalline silicon have been used as substrates for BDD. Due to the fragility of Si, it is not an ideal substrate for industrial applications. However, it is highly compatible for BDD deposition, due to the formation of a self-limiting oxide and its low electrochemical activity [143]. Diamond films deposited by CVD methods are usually microcrystalline diamond (MCD) and have grain sizes of 2-5 µm. Nanocrystalline diamond (NCD) can be deposited by $Ar/H_2/CH_4$ plasma with a higher argon content. NCD (grain size= 3-5 nm) has higher conductivity than MCD as it has higher content of sp^2 hybridization and graphitic carbon phase [127,144,145]. Raman spectroscopy has been generally used to characterize the diamond film. A single sharp peak at 1332 cm^{-1} is assigned to the diamond (sp^3 bonding) peak [146,147].

2.1.2 Properties of Boron-doped Diamond (BDD) Electrodes

The electrochemical properties of BDD electrodes depend on different parameters such as doping level, surface termination, and type of pretreatment (annealing, cathodic, anodic). The various parameters responsible for different BDD electrode performance and properties are discussed below.

2.1.2.a Effect of Doping Level

The most common dopant is boron that has been extensively used to make the diamond a p-type semiconductor. At low doping levels (10^{18} atoms/cm^3), the doped diamond shows semiconducting behavior, but at high doping levels (10^{20} atoms/cm^3) the doped diamond exhibits semi-metallic behavior [144]. The different doping levels (10^{18} (lightly doped) and 10^{20} (heavily doped) cm^{-3}) show different hydrophobicity, reversibility, and working potential window. Raman spectra showed that for low doping levels only a single peak was observed at 1332 cm^{-1}, which was a confirmation of diamond phase formation [148], whereas for higher doping levels another peak was observed at 500 cm^{-1}, that might be due to Fano interference between phonon state and the electronic continuum [141]. XPS data showed that the O1s/C1s increased from 1.2 (lightly doped, contact angle- 106^0) to 2.7% (heavily doped, contact angle- 84^0) which was in accordance with the wetting behavior. After hydrogen plasma treatment of moderately boron doped diamond (10^{19} atom cm^{-3}) the electrode behaves as an insulator, which suggests a strong decrease of the free carrier density due to passivation of free charge carriers by hydrogen trapping of the dopant [137].

2.1.2.b Effect of Different Pretreatment Methods

Annealing, anodic treatment, and anodic with subsequent cathodic treatments have different effects on the electrode performance [149,150]. Different redox couples were used with cyclic voltammetry experiments (CV) to characterize the electrodes after pretreatment. The peak separation in CVs ($Ce^{4+/3+}$ and $Fe(CN)_6^{4-/3-}$) [151] increased after anodic treatment (+3V for 30 min) & annealing (400 ^{0}C for 30 min in O_2 atmosphere) but decreased after cathodic treatment (-3V for 30 min) due to the presence of small amounts of sp^2 carbon as a surface impurity in cathodically pretreated BDD [150]. The differences in redox couple measurements may be due to surficial property, which may be due to change in the surface functionalization of the BDD film which became H-terminated. XPS confirmed the result showing an increase in superficial oxygen content (mainly C-O or C-O-C and C=O group) [139]. From Mott-Schottky analysis it was found that the apparent doping density increased after combined cathodic and anodic treatment which was derived from the slope of the Mott-Schottky plot, and a positive shift of flat-band potential occurred after only anodic treatment [149]. The flat band potential increased (positive shift) after anodic treatment but decreased (negative shift) after subsequent cathodic treatment as well as for annealed electrode [149]. For as-deposited electrode all the results were explained by valence band edge position close to $Ce^{4+/3+}$ redox level but for annealed samples it was suggested that a new superficial conductive layer was formed after cathodic and anodic steps. The ascending order of reversibility was: as-deposited < anodically pre-treated < thermally pre-treated < cathodically pre-treated. The effect of application of different current densities on surface termination was also studied [151].

2.2 Different Modification of BDD Electrode Surfaces

Different modification methods are used on BDD electrodes to allow them to function for water treatment and sensing applications. These methods are discussed in the proceeding sections.

2.2.a Formation of O-terminated Surface

O-terminated surface can be prepared by electrochemical oxidation [149,151–153], high-temperature acid treatment [128,134,152], thermal treatment (400^0C) [152], oxygen plasma treatment [142,154], electroless oxidation (Ce^{4+}, MnO_4^- etc) [155,156], and UV treatment in O_2 [157], air [158], and O_3 [154]. The oxidation of BDD can produce different surface functional groups –C-OH, -C=O, -COOH and C-O-C, as determined by XPS [159].

XPS data compared the different oxidation methods which indicated that the electrochemical oxidation method was best for production of hydroxyl group termination, UV/ozone method was best for hydroxyl group termination when it was applied for 15 min but plasma method was not suitable as it graphitized the surface [154]. The contact angle measurement confirmed the presence of oxygenated group on the surface. The water contact angle was decreased from higher value (92.5deg) (H-termination) to a lower value (1.6deg) (O-termination) confirming lower hydrophobicity of O-terminated BDD [160,161]. The contact angle is dependent on surface energy, which is a combination of dispersive (σ_d) component and polar component (σ_p). The data of dispersive component which is an indication of roughness showed almost no change confirming that decrease of contact angle was attributed to oxygenated surface only (change in σ_p) and not by roughness [155,156].

2.2.b Formation of F-terminated Surface

Fluorine-termination of the BDD surface was mainly accomplished by using RF plasma treatment in either CF_4 [162–164], F_2, [165] or XeF_2 [166] gas. Fluorine termination was also fabricated by using electrochemical oxidation of perfluorooctanoic acid (PFOA) [167]. Plasma treatment caused etching of the crystals and roughness was reduced, which was evidenced by SEM and AFM analyses [162]. The C1s core spectra shifted to higher bond energy (+1.5eV) after fluorination. After keeping it in an ultra-high vacuum for 3 weeks XPS showed a decrease in intensity of the peaks, which suggested that fluorination process was not stable. The potential window increased after fluorination from about 3 V to 5 V [162,165]. Results concluded that fluorination took place not only at BDD surface but also at underlying region and also rearrangement of the surface was speculated [162]. Fluorination made the surface hydrophobic and decreased the interaction between hydrophobic surface and hydrophilic compounds (e.g., water), which eventually increased the potential window. Contact angle measurements confirmed that after fluorination (106.3 deg) the surface was more hydrophobic than as-deposited BDD (85.9 deg). Different redox couples were used to characterize the surface terminations and the results of CV scans with the $Fe(CN)_6^{3-/4-}$ redox couple showed a decrease in current response and an increase in peak separation for fluorinated BDD relative to oxidized BDD [168]. Electrostatic or dipole-dipole interaction between redox couple and F atoms present on electrode was responsible for the decrease in current. It was also seen that redox reaction with $Ru(NH_3)_6^{2+/3+}$ redox couple was not influenced by surface termination of BDD electrodes as electrical passivation was not caused by the plasma and the reactivity of this redox couple was not highly dependent on surface termination as observed for $Fe(CN)_6^{3-/4-}$ and $Fe^{2+/3+}$ [168]. It was concluded that $Fe^{2+/3+}$ and

$Fe(CN)_6^{3-/4-}$ had lower rate constants after fluorination as the reactions were highly dependent on surface termination. BDD surface was fluorinated also via electrochemical reactions [165]. The fluorination was accomplished by electrochemical oxidation of the BDD surface by applying 2.3 V/SHE in the presence of perfluorooctanoic acid (PFOA) [165]. Fluorinated BDD surface was analyzed by XPS and results indicated that the fluorinated diamond contained the following element: carbon (83.3%), fluorine (8.6%), and oxygen (7.3%) which confirmed the successful incorporation of F on to the BDD surface [165]. At lower binding energies (284.24 - 288.09 eV) the observed peaks may be due to the C-C, C=C, -C-OH, -C=O and –COOH. However at the higher binding energies (290.67 - 293.09 eV) the observed peaks at might be due to CF_2 and CF_3 functional groups [165]. The contact angle increased form 43.5deg (untreated) to 115.2deg (fluorinated) showing higher hydrophobicity which was due to the incorporation of fluorinated groups on BDD surface. BDD electrode was also fluorinated in RF barrel reactor (100mTorr, 100W, 2min) [163,164]. XPS data showed an additional peak at 288.5eV associated to C-F bonds along with CF_2 functional group at 291.4 eV [163,164]. The results confirmed that fluorination using different methods were able to incorporate different fluorinated functional groups on the BDD electrode surface which increased hydrophobicity of the surface. Chlorate and organics oxidation was done on both electrode to show the effect of functionalization using fluorine on both the oxidation rates [167]. Perchlorate formation rate was much higher for the oxidized BDD electrode than that for the fluorinated BDD electrode, suggesting that the fluorinated electrode was able to lower the formation of ClO_4^- [167]. The lower ClO_4^- formation for fluorinated BDD electrodes may be due to the hydrophobic interactions and/or dipole-dipole interactions. The increase in the reaction distance of ClO_3^- from the electrode surface due to the interactions decreased the chances of

DET (electron tunneling) which subsequently decreased the perchlorate formation [167].

2.2.c Formation of H-terminated Surface

The as-deposited BDD is mainly H-terminated. H-terminated surface can be prepared from O-terminated surface by using hydrogen plasma [137,140]. During preparation of BDD, hydrogen flow is continued after the flow of methane is stopped in the CVD process and which results in a H-terminated surface [142]. Hydrogen plasma was applied by radio-frequency plasma (320W, power density between electrodes 0.4 W cm^{-2}, 500^0C, 3-6 hours) [137], microwave hydrogen plasma (800^0C, 300 sccm hydrogen, 1200W, 50Torr, 30 min) [128], hydrogen plasma CVD (1kW, 60Torr for 10min) [169], annealing (800^0C, 40 min, 0.02 Mpa, hydrogen atmosphere) [133] and electrochemical (-35 V vs a platinum counter electrode in 2M H_2SO_4) [134]. Different boron concentration (10^{19} and 10^{20} cm^{-3}) and hydrogen plasma (0.4 W cm^{-2}, 500^0C, 6 hours) were used to check the effect of hydrogen plasma [137]. Mott-Schottky analysis and CVs (redox couple: $Ce^{4+/3+}$) were performed on the hydrogenated electrode to check the effect of the hydrogenation on surface properties. Mott-Schottky analysis between before and after plasma treatment showed significant difference for moderately doped (10^{19} cm^{-3}) electrode and almost no difference for on highly (10^{20} cm^{-3}) doped electrode. After hydrogen plasma treatment of moderately boron-doped diamond, the electrode behaved as an insulator which was revealed from the flat Mott-Schottky plot. The result suggested strong decrease of free carrier (Boron) density and eventually conductivity due to passivation of free charge carrier by hydrogen trapping on dopant and forming B-H bond [137]. For highly doped electrode the charge transfer was not disturbed by hydrogen plasma [137]. The change in surface termination also changed the bulk properties of superconducting diamond [133].

2.2.1 Modification of BDD Electrode Surfaces for Water Treatment Application

Various advanced water treatment applications are being researched using BDD electrodes such as: industrial wastewater treatment, electrochemical disinfection of cooling tower waters, and drinking and wastewater treatment [52,118,170–172,172–186]. Due to the unique characteristics, such as the high potential window, high overpotential for oxygen evolution and the ability to use EAOP electrodes with high current efficiency, BDD is especially used for the sensing, destruction and removal of organic pollutants from water matrices. Oxidation and removal of different types of organic pollutants mainly phenolic compounds and aliphatic acids using BDD is reviewed below because they are abundant in different wastewater streams, highly hazardous, and not removed by conventional water treatment technologies [52,118,170–172,172–186].

2.2.1.a Oxidation of Organic Pollutants

BDD electrodes are very effective at oxidizing recalcitrant compounds via DET reactions and OH• production. It was seen that BDD was useful for mineralization of different organics (phenol, benzoquinone, oxalic acid, aromatic amines, N-nitrosodimethylamine, and perfluorooctane sulfonate) via the formation of hydroxyl radical and direct electron transfer (DET) [52,118,170–172,172–186]. The electrochemical mineralization was partly attributed to the DET and partly to hydroxyl radical reaction. The extent of DET decreased with increasing potential due to competing hydroxyl radical reactions.

Phenolic compounds are very common in industrial wastewater and are not removed by conventional treatment techniques such as biological, filtration, ion exchange and reverse osmosis [118,170–172,172–175]. EAOP method is found to be very useful to degrade and

mineralize phenolic compounds in water matrices [118,170–172,172–175]. Three different mechanisms for phenolic compound oxidation via EAOP methods were proposed. First mechanism is the oxidation of phenolic compounds via DET, formation of phenoxy radical and subsequent polymerization at lower potentials where $OH^{\bullet}$ production is not occurring, second mechanism is the DET of the phenoxy radical, reaction of the product with water and formation of p-benzoquinone, and third mechanism is the reaction of phenolic compounds with $OH^{\bullet}$ at higher potentials, formation of organic acids as intermediates and carbon dioxide and water as the final products [159]. The aliphatic acids are the byproducts of AOP and EAOP methods and they do not degrade, due to slow reaction kinetics towards $OH^{\bullet}$. EAOP using BDD electrodes can be very useful as the acids are prone to DET oxidation and they form carbon dioxide and water as final products [182–187].

2.2.1.b By-product Formation (Perchlorate)

When drinking water is subjected to treatment by electrochemical oxidation, toxic by-products can be formed from the oxidation of the chloride ion. BDD electrodes can remove contaminants by direct and indirect electrochemical oxidation. These indirect oxidation mechanisms can result in perchlorate and chlorinated byproduct formation [187–190]. BDD electrode has been shown to oxidize chloride to perchlorate in the following pathway [190]:

$$Cl^- \rightarrow OCl^- \rightarrow ClO_2^- \rightarrow ClO_3^- \rightarrow ClO_4^- \qquad (2\text{-}3)$$

The fourth reaction step (formation of perchlorate from chlorate) was proved to be the slowest step and was considered as rate determining step (RDS).

Perchlorate found in drinking water has carcinogenic potential. The USEPA has fixed a

health advisory level for perchlorate of 15 ppb in drinking water matrices. California and Massachusetts have fixed the limiting concentrations of 6 and 2 ppb respectively, for perchlorate in drinking water. Formation of this by-product can limit the use of BDD electrodes for water treatment applications [63,192–195].

2.2.1.c Perchlorate Formation Mechanism

Due to the high health risk of perchlorate formation during anodic oxidation of chloride containing waters with BDD electrodes, reactions that form perchlorate must be suppressed. Previous research showed that the oxidation of chlorate to perchlorate was the rate-determining step in the process [84], and the formation of perchlorate from chlorate involved a two-step process, which is stated below [85]:

$$ClO_3^- \rightarrow ClO_3^{\bullet} + e \qquad (2\text{-}4)$$

$$ClO_3^{\bullet} + OH^{\bullet} \rightarrow HClO_4 + e \qquad (2\text{-}5)$$

The first step (equation 2-4) involved the oxidation of chlorate ion to chlorate radical via DET and in the second step (equation 2-5) chlorate radical reacted with hydroxyl radical in the diffusion layer to form perchlorate [195]. High concentration of competitive ions (e.g Cl^-) inhibits the formation of perchlorate as chloride ion is adsorbed faster than chlorate and stops the chlorate oxidation to perchlorate [195]. BDD can form bonds with intermediate chlorate radicals, thus increasing their lifetimes and probability of reacting with hydroxyl radicals. The formation of chlorate radical from chlorate ion went through direct electron transfer mechanism determined by DFT modeling [195]. It indicated that chlorate radical did not chemisorb to ≡CH or =C=O sites but formed complexes with ≡C· and ≡C-O·. Also chlorate radical adsorbed at this

site supported the result showing that low concentration of chlorate ion blocked water oxidation [195]. The chlorate radical chemisorbed to the ≡C· site by both oxygen and chlorine atom. The activation energy for the reaction of hydroxyl radical and chlorate radical was significantly low confirming the possibility of this reaction at room temperature. Also chlorate radical could react with ≡C-O· and =CHO· sites but reaction with =CHO· was not possible at room temperature due to its high activation energy. The binding of chlorate with the other site could limit chlorate ion formation [195]. A linear increase of perchlorate formation with current density was not observed due to oxygen formation or reaction of chlorate radical with electrode surface. The presence of organic compounds inhibited perchlorate formation compared to the blank electrolyte which may be due to the competition between chlorate ion and organics or the reaction between organics and chlorinated compounds [196]. Hydrophobicity had no influence in inhibition of perchlorate formation values [196]. At lower current densities primary reaction was between hydroxyl radical and organics at kinetic limited conditions. At higher current densities the perchlorate formation inhibition decreased as the reaction was mass transfer limited [196]. All the previous results confirmed that surface modification and surface functional groups play an important role towards organics oxidation and perchlorate formation.

2.2.2 Modification of Electrode Surfaces for Sensing Applications

Sensors have been used for detection of a wide variety of components in different matrices, including toxic gas sensors; sensors to detect heavy metals, toxic organics and antibiotics in water matrices. Many different analytical techniques have been used to detect CFX and other antibiotics in different matrices [84–93]. Though there are several analytical techniques present the electrochemical techniques are the most extensively used the most extensively used methods

compared to other analytical techniques as they are cost effective, energetically viable, robust, highly sensitive, quick and easy to use (Table 2-1).

Table 2-1 - Electrochemical methods for the determination of different antibiotics

Electrode	Method	Material Used	Linear Range (μM)	LOD (μM)	Antibiotics	Refs.
GCE	DPV	MWCNT/SnO_2	1 - 9.9	0.2	Levofloxacin	[197]
GCE	DPV	MIP/G-Au	1 - 100	0.53	Levofloxacin	[198]
CPE	CV	Nickel oxide	250 - 6980	25.4	Choline	[199]
GCE	DPV	PAR/EGR	0.04 - 120	0.01	Ciprofloxacin	[96]
GCE	CV	GO-MWCNT	0.1-10	0.07	Azithromycin	[200]
GCE	CV	MWCNT/DNA	2.41 – 290	1.0	Ciprofloxacin	[201]
CPE	CV	P-β-CD-l-arg	0.05–100	0.01	Ciprofloxacin	[97]
CPE	CV	PVC	10 -10^4	10	Ciprofloxacin	[202]
CNT	CV	Antibody	0.01 -10^3	0.01	Norfloxacin	[92]
GCE	DPV	PoAP/MWCNT	3-200	1.0	Levofloxacin	[93]
GCE	CV	CNT/$MgFe_2O_4$	0.10 – 1000	0.01	Ciprofloxacin	[203]
GCE	CV	SWNT	5 - 100	0.5	Roxithromycin	[204]
GCE	CV	Cyt-C/CNTs/CF	2 - 78	1.0	Ciprofloxacin	[205]
GCE	CV	MWCNT	40–1000	6.0	Ciprofloxacin	[101]
GCE	DPV	MWCNT/Nafion	0.1–100	0.05	Norfloxacin	[206]
GCE	CV	DNA	0.5 - 5	0.1	Levofloxacin	[91]

* MWCNT/SnO_2 = Multi-walled carbon nanotubes modified with SnO_2 rods, MIP/G-Au = Molecularly imprinted polymer (MIP) constructed with graphene–Au nanoparticles, PAR/EGR = poly(alizarin red) and electrodeposited graphene, GO-MWCNT = graphene oxide and multi-walled carbon nanotubes, MWCNT/DNA= Multi-walled carbon nanotubes and Deoxyribonucleic acid, P—β-CD-l-arg= polymerized β-cyclodextrin (β-CD) and L-arginine (L-arg), PVC= Polyvinyl chloride, PoAP/MWCNT= poly(o-aminophenol)/multi-walled carbon nanotubes composite, $MgFe_2O_4$/ MWCNT= $MgFe_2O_4$ nanoparticles and multi-walled carbon nanotubes composite, SWNT= single walled carbon nanotubes, Cyt-C/MWCNTs/CF= cytochrome C, Multi-walled carbon nanotubes and ciprofloxacin composite film.

The use of different materials (e.g. polymer, CNTs, and nanoparticles) to modify electrodes (e.g BDD, GCE and CPE) has been used by electrochemical methods (e.g. voltammetry, impedance spectroscopy) to detect antibiotics. Nanostructured carbon compounds, especially carbon nanotubes (CNTs), have merged as a robust material for surface modification of electrodes, due to their unique properties. CNTs have gained attention due to the following properties: high specific surface area, thermal and chemical stability, conducting behavior, and the presence of functional groups formed on the CNT surface [207–211]. Different functional groups can be incorporated by different treatment methods. For example, CNTs were reacted with a mixture of nitric acid and sulfuric acid to create acid groups on the surface [212–214]. The formation of the functional groups on CNTs changes the properties (hydrophobic nature, conductivity, H-bond, and π-π* electron donor-acceptor mechanism) of CNTs [207–209,212–214]. The oxidized CNTs can interact with different compounds (e.g. organics, antibiotics, surfactants, dyes and heavy metals) via hydrophobicity, H-bond, π-π* electron donor-acceptor mechanism (EDA), charge assisted H-bond (CAHB) [208,213,215,216].

Various modified electrodes were used to detect antibiotics due to their high selectivity and sensitivity (Table 2-1) [91-93,96,97,198–207]. As highly selective recognition elements (fluoroquinolones), molecularly imprinted polymers (MIPs) were used for the development of various sensors, via electro-polymerization. The prepared G-AuNPs were dispersed in water and the glassy carbon electrode (GCE) surface was coated with G-AuNPs suspension and dried under infrared lamp to obtain G-AuNPs/GCE [198]. Graphene has some unique properties such as large surface area (2630 m^2 g^{-1} for single-layered graphene), high concentration of edge-planes/defects, excellent electron transfer, strong mechanical strength and both excellent thermal and electrical conductivities. The excellent conductivity and the large surface area of graphene

and the oxygen-related defects of the reduced graphene oxide, (RGO)/nickel hydroxide nanoparticles, (electrodeposited graphene) EGR/PAR (polyalizarin red) and MIP/Graphene-Au provided a simple and novel method for the development of voltammetric sensors for the accurate determination of trace amount of antibiotics [96,199,200]. Another method comprising of DNA and MWCNTs was also used to modify sensors to detect antibiotics (ciprofloxacin and levofloxacin). A stable suspension of MWCNT in DMF solution was added to the DNA solution and the resulting suspension was kept in an ice–water bath. The suspension of MWCNT/DNA was drop casted on GCE, which was dried in air and the resulting electrode was called MWCNT/DNA/GCE [201]. A major problem for developing CNT-based sensor is how to immobilize CNT onto the electrode with high stability. Another method was introduced using PoAP/MWCNTs composite film on GCE as sensor. The PoAP/MWCNTs/GCE was prepared by performing cyclic voltammetry in the potential range from −0.20 to 0.84 V for 10 cycles. The polymer/MWCNT composite films deposited electrodes were effective for antibiotics detection due to high stability, repeatability, reproducibility, film homogeneity and high electroactive surface area [93]. BDD was also used as substrate to prepare sensors for antibiotics. The MIP film was prepared by electro-polymerizing pyrrole on the surface of the BDD electrode via a cyclic voltammetry (CV) process in phosphate buffer solution (PBS) with the antibiotic as template molecule and BDD/PPY sensor was prepared [217]. Different materials like nickel oxide, GO-MWCNT, MWCNT/SnO_2, P-β-CD-L-arg/CPE, PVC, antibody, $MgFe_2O_4$/MWCNT, SWNT, MWCNT/Nafion, and Cyt-C/MWCNTs/CF were also used to prepare sensors to detect different antibiotics (Table 2-1).

Although several different techniques, substrates, and materials were used to prepare sensors to detect antibiotics in serum, urine and tablet samples, electrochemical sensors has not

been highly applied for the determination of CFX in water matrices. The underlying detailed mechanism of antibiotics detection using electrochemical techniques has also not been investigated thoroughly. Obtaining a lower detection limit will be also useful to monitor trace amount of antibiotics in wastewater matrix.

2.3 Synthesis and Modification of Porous Conductive Substoichiometric and Doped TiO_2 Membrane Electrode for Water Treatment Application

The Magnéli phase titanium suboxides (Ti_nO_{2n-1}, n = 4 to 10), and doped-TiO_2 are very useful electrode materials for water treatment application due to high porous structure, ability to use EAOP, high chemical stability, and low fabrication cost. Titanium dioxide (TiO_2) is an insulator (conductivity = 10^{-9} $\Omega^{-1}cm^{-1}$) [218], but can be made conductive by partially reducing (oxygen deficiency in the lattice structure) at 900 ^{0}C in the presence of H_2 or incorporating n-type dopant (Nb, V or Ta) creating n-type semiconductor behavior [159]. Ti_4O_7 (conductivity= 166 $\Omega^{-1}cm^{-1}$) and Ti_5O_9 are the most important Magnéli phases as they are the most conductive [219]. Reduction methods and parameters have been optimized to synthesize mainly Ti_4O_7 [218].

Ti_4O_7 electrodes have been widely used for cathodic protection of metal structures, battery electrodes, fuel cell supports, photocatalysts, electrodes for electrochemical oxidation and reduction of water contaminants due to their unique chemical, electrical, and electrochemical properties [54,220–223]. The OH• produced on Ebonex® (commercially available Ti_4O_7) are less abundant but more reactive than those formed on BDD [50,64]. A passivation layer of TiO_2 can be formed on Magnéli phases via anodic polarization at 1.6V vs SHE due to the introduction of oxygen in the lattice structure [223,224]. However researches showed that the passivation can be reversible or irreversible [223,224] and a conclusion cannot be made depending on the

literature. Nb doped oxide, $Ti_{0.9}Ni_{0.1}O_2$ (general formula= $Ti_{1-x}Nb_xO_2$ ($0 \leq x \leq 0.8$)) has been shown to have the similar conductivity as Ti_4O_7 [223]. The Nb doped TiO_2 is more resistant to oxidation than Ti_4O_7 as it has lower oxygen deficiencies than Ti_4O_7 [225]. Substoichiometric titanium oxides have been recently utilized for reactive electrodchemical membrane (REM) fabrication because they can be prepared as porous monolithic structures at low cost (compared to BDD) and are reported to produce OH• via water oxidation which can degrade recalcitrant compounds [64,226–228]. A recent study showed large improvement in permeates flux at low transmembrane pressures [64]. At high fluxes the heterogeneous rate constant plateaued, which suggested a kinetic limitation [64]. To increase the kinetic rate constants of organic compound oxidation, with the advantage of the fast mass transport associated with the submicron pores, further modification with nanoparticles or catalysts will be performed on the REMs.

2.4 Electrocatalysts for Nitrate Reduction and OH• Production

Nitrate is one of the most common pollutants in ground and surface water due to the excessive use of nitrogen rich fertilizers [229–234]. Nitrate poses serious health hazards as it can be biologically reduced to nitrite which can cause blue baby syndrome and can form carcinogenic nitrous amines [65–67,235]. Conventional removal technologies such as ion exchange, reverse osmosis, and electrodialysis only separate nitrate and create concentrated nitrate brine which again requires additional cost for the post treatment processes [68,69]. However catalytic and electrocatalytic nitrate reduction/hydrogenation has emerged as a destructive method in the past few decades due to high nitrate reduction and removal efficiency and low or no cost for the post treatment processes [70–80]. Several different monometallic and bimetallic catalysts on different supports have been used for catalytic nitrate reduction [70,72–75,81–83,236,237]. Noble metals such as Pd and Pt, transition metals such as Ni and Rh have

been used as monometallic catalysts and also used with promoter metals such as Cu, Sn and In as bimetallic catalyst [68,71,78,80,238–247]. The noble metals are highly effective for nitrate reduction due to their high H-adsorption ability and they provide the best result when used with the promoter metals. When nitrate and reductant (e.g. H_2) are present, promoter metal first initiates the reaction by reducing nitrate to nitrate and is oxidized itself [236]. Then H_2 is adsorbed on the noble metal as nascent hydrogen (H) and reduces the oxidized promoter metal back to zero valent metal which again becomes active for nitrate reduction to nitrite [236]. The formed nitrite is adsorbed to the noble metal and is further reduced to NO, N_2O as intermediates and N_2 and NH_3 as final products depending on the N:H ratio [242,245,248–250]. Bimetallic catalyst has shown better activity towards nitrate reduction compared to monometallic catalysts [68,71,78,80,238–247]. If only noble metals were used, nitrate reduction decreased as the metal was covered by the reductant hydrogen and nitrate was not adsorbed on the metal surface and also nitrate was not converted to nitrite due to the absence of promoter metal [236]. If only promoter metals are used, the nitrite formation became very high as it could not be further adsorbed and reduced due to the absence of the noble metals [236]. Previous researches have shown the use of Pd, Pt, Cu, Sn, In, Ni and Rh for catalytic nitrate reduction with high removal efficiency. However catalytic and electrocatalytic nitrate reduction suffer from the production of undesirable ammonia. The formation of NH_3 is unwanted due to several health risks [251]. Therefore the World Health Organization (WHO) has set a drinking water limit of 30 μM. The NO_3^- reduction processes via intermediate formation are as follows [252]:

$$NO_3^- + H^+ + 2e^- \xrightarrow{Pd-M} NO_2^- + OH^- \quad (2\text{-}6)$$

$$NO_3^- + \frac{5}{2}H^+ + 4e^- \xrightarrow{Pd-M} \frac{1}{2}N_2O + \frac{5}{2}OH^- \quad (2\text{-}7)$$

$$NO_3^- + 3H^+ + 5e^- \xrightarrow{Pd-M} \frac{1}{2} N_2 + 3OH^- \quad (2\text{-}8)$$

$$NO_3^- + 6H^+ + 8e^- \xrightarrow{Pd-M} NH_3 + 3OH^- \quad (2\text{-}9)$$

Electrochemical NO_3^- reduction is better than catalytic reduction in some aspects which is the no requirement of an external electron donor (e.g., H_2). However, electrochemical NO_3^- reduction also suffer from the production of high concentrations of NO_2^- and NH_3 [70,74,75,81–83], and reaction rates are typically low in weak ionic strength solutions. Solution conditions play an important role towards nitrate reduction. For example, the O_2 reduction reaction (ORR) occurs at similar cathodic potentials as NO_3^- reduction [253], and dissolved organic matter (DOM), other cations (e.g. Ca^{2+} and Mg^{2+}) may adsorb, deposit and block catalytic sites [254,255]. However, most electrochemical studies use clean, deaerated electrolyte solutions and therefore knowledge regarding the effects of solution conditions is limited.

Electrochemical NO_3^- reduction have been studied in both batch [81,82,240,252,256] and continuous flow-through reactors [257–264]. The electrochemical NO_3^- reduction in a flow-through electrode setup first used a Ni packed bed reactor [230]. However the reactor was not suitable for nitrate reduction confirmed by the author [230]. The development of porous, monolithic electrodes and composite conductive membranes has emerged as an efficient flow-through technology which use electrochemistry [54,64,226,265–274]. REMs have been applied to electrochemical oxidation of organic compounds [54,269], antifouling membranes [269,271], membrane fouling regeneration [269,272], and bacteria inactivation [226,257,270,273]. However, REMs have not been applied for electrochemical NO_3^- reduction.

Different porous and non-porous electrodes/catalysts have been extensively used for water and wastewater treatment application as they can use EAOP. The promising materials among them include boron-doped diamond electrode (BDD), substoichiometric TiO_2, doped-TiO_2, PbO_2

and doped-SnO_2 [47–50,53,55–57,62,114,124,275–279]. The leaching of Pb (toxic metal) for PbO_2 electrode and high cost associated with BDD fabrication limited their application for water treatment application [280,281]. However doped-TiO_2 and –SnO_2 does not suffer from severe problems such as toxic material leaching and high fabrication cost [280,281]. The doping of TiO_2 using reductant (e.g. H_2) has been widely used to form highly conductive, porous and monolithic Magnéli phases (Ti_nO_{2n-1}, n = 4 to 10) electrodes [64,219,227]. Among all the Magnéli phases Ti_4O_7 has been found to be the most conductive one with conductivity of 1000 S cm^{-1} [219]. Due to high conductivity, porous structure, corrosion resistance, mechanical strength and ability to use EAOP, Ti_nO_{2n-1} anodes have been widely used as REM for the electrochemical oxidation of recalcitrant organic compounds in water matrix. Doped-SnO_2 has been used as another effective anode-coating material for electrochemical oxidation of organic compounds due to high conductivity and stability [47,57,278]. A very high oxygen evolution potential (OEP) of doped-SnO_2 has been reported as 1.7 V vs Ag/AgCl which facilitated water oxidation for $OH^{\bullet}$ production before O_2 evolution [282,283]. Due to high OEP of doped-SnO_2, it can be used as an anode to utilize EAOP for electrochemical organic oxidation. Different dopants (e.g. Sb, Bi, P) have been used for SnO_2 doping among which Sb was the mostly used dopant [282,284–286]. However, the application of Sb doped SnO_2 for water treatment application was limited due to high toxicity of Sb (EPA MCL = 6 ppb) [10]. Bi-doped SnO_2 (BDTO) coated carbon nanotubes with very high OEP (1.71 V vs Ag/AgCl) has been recently used for electrochemical organics oxidation with improved reactivity, current efficiency and energy consumption [282].

3. Selective Electrochemical Detection of Ciprofloxacin with a Porous Nafion/Multi-Walled Carbon Nanotube Composite Film Electrode

3.1 Abstract

This study focuses on the development of electrochemical sensors for the detection of Ciprofloxacin (CFX) in natural waters and wastewater effluents. The sensors are prepared by depositing a layer of multi-walled carbon nanotubes (MWCNTs) dispersed in a porous Nafion film on to a boron-doped diamond (BDD) electrode substrate. The porous-Nafion-MWCNT/BDD electrode enhanced detection of CFX due to selective adsorption, which was accomplished by a combination of electrostatic attraction at $-SO_3^-$ sites in the porous Nafion film, and the formation of charge assisted hydrogen bonding between CFX and -COOH MWCNT surface functional groups. By contrast, the bare BDD electrode did not show any activity for CFX oxidation. The sensors were selective for CFX detection in the presence of other antibiotics (i.e., amoxicillin) and other non-target water constituents (i.e., Cl^-, Ca^{2+}, humic acid, sodium dodecylbenzenesulfonate, salicylic acid, 4-aminobenzoic acid, and 4-hydroxybenzoic acid). A limit of detection of 5 nM (S/N = 5.04 ± 0.26) in a 0.1 M KH_2PO_4 supporting electrolyte (pH = 4.5) was obtained using differential pulse voltammetry. The linear dynamic ranges with respect to CFX concentration were 0.005-0.05 μM and 0.05-10 μM, and the sensitivities were 41 ± 5.2 μA μM^{-1} and 2.1 ± 0.22 μA μM^{-1}, respectively. Sensor fouling was observed at high concentrations of some organic compounds, such as 1 mM 4-aminobenzoic acid and 4-hydroxybenzoic acid. However, a short cathodic treatment fully restores sensor response. The

results indicate that these sensors have application in detecting CFX in natural waters and wastewater effluents.

3.2 Introduction

Ciprofloxacin (CFX) is a second-generation fluoroquinolone, which is used as an antibiotic against both gram-positive and gram-negative aerobic pathogens [95–97,101,104,201,203], and is widely administered to humans and livestock. Since the drug is not fully metabolized, CFX has been found in surface waters that are highly impacted by agricultural runoff and domestic wastewater effluents [96,101]. Additional studies have also detected CFX in cow's milk at concentrations as high as 0.1–100 ng mL^{-1} [104]. The presence of CFX and other antibiotics in the environment is a cause for concern, due to the potential emergence of antibiotic-resistant bacteria [95,96,101,104,203]. For this reason the development of sensitive and selective sensors to monitor antibiotics in the environment (wastewater, surface water, milk, etc.) is an active area of research.

Multiple analytical methods have been used to detect CFX in different matrices including liquid chromatography—mass spectroscopy [85], high-performance liquid chromatography [84,287], spectrophotometry [89,288], spectrofluorimetry [87,88], capillary electrophoresis [86], immunoassay [104], chemiluminescence [90], and electrochemical techniques [91,95,96,101,104,203]. Among these methods, the electrochemical techniques (impedance spectroscopy, voltammetry) are the most extensively used methods due to their low energy requirement, low cost, high sensitivity, short time requirement, and ease of use.

The functionalization of different electrodes is commonly performed in order to increase sensitivity for analyte detection [92,93,101,121,198,201,206,289–291]. Carbon nanotubes (CNTs) and multi-walled carbon nanotubes (MWCNTs) have been extensively used to modify

electrodes (e.g., glassy carbon electrode (GCE)) for the detection of numerous organic, inorganic, and biological compounds [57,93,101,201,292,293]. CNTs have high conductivity, high chemical and mechanical stability, and a very high specific surface area, which has resulted in their use in different chemical and electrochemical sensors [93,201,206]. CNTs are more resistant to electrochemical oxidation compared to carbon and show long-term stability and reproducibility for sensor applications at an applied potential of 1.5 V vs. standard hydrogen electrode (SHE) [294,295].

Functionalization of CNTs with different surface groups (e.g., -OH, -COOH, $-NH_2$) has been accomplished using various different methods (e.g., electrochemical oxidation, acid treatment, plasma treatment), which can greatly affect compound adsorption [215,216,296–298]. Adsorption of organic compounds to CNTs occurs by various mechanisms, including electrostatic and hydrophobic interactions, hydrogen bonding, and electron-donor-acceptor (π -π) interactions [215,216,296–298]. Oxygenated CNTs decrease the hydrophobic adsorption of compounds, but increases the formation of hydrogen bonding due to a higher content of oxygen groups on the CNTs [215,216,296–298]. Oxygenated CNTs also increase the strength of electrostatic attraction between deprotonated acid groups (e.g., $-COO^-$) and positively charged compounds. Functionalized CNTs have been extensively used to detect different analytes including lectin and gonadotropin [299].

The presence of CFX in domestic wastewater effluent (0.09-6 µg L^{-1}), industrial wastewater effluent, and hospital wastewater effluent (0.2-2.0 µg L^{-1}) is due to the fact it is not fully removed during traditional wastewater treatment processes [300–304]. Most studies on sensor development focused on the detection of CFX in human serum, urine, and tablets [96,101,203],

but application of sensors for the detection of CFX in wastewater or natural water matrices has not been explored.

In this work, we developed a sensitive, selective, and fast method for the determination of CFX in water by modifying a boron-doped diamond (BDD) electrode with a porous, conductive Nafion/MWCNT film. Different modified electrodes were prepared and tested for their sensitivity and selectivity towards CFX detection. Here we report the experimental results of CFX detection via selective adsorption and anodic oxidation at various modified electrodes. The prepared sensors were characterized by scanning electron microscopy (SEM), transmission electron microscopy (TEM), X-ray photoelectron spectroscopy (XPS), and cyclic voltammetry (CV) with common redox couples. The optimized sensor was used to detect CFX in a secondary wastewater effluent solution and in the presence of other interfering compounds. The sensor was also tested for organic compound fouling and subsequent electrochemical regeneration. Experimental results were interpreted to gain information regarding the active site for CFX adsorption.

3.3 Experimental

3.3.1 Reagents. The MWCNTs (inside diameter: 4 nm, outer diameter: < 20 nm, length: 1-12 μm, purity: > 99 wt.%) were obtained from Cheap Tubes Inc. (Grafton, VT, USA). All chemicals were of reagent grade and obtained from either Sigma Aldrich or Fisher Scientific, and were used without additional purification. Solutions were made from Barnstead Nanopure water (18.2 MΩ-cm at 21 °C).

3.3.2 Fabrication of Porous-Nafion-MWCNT/BDD Electrode. The BDD electrode on a bead blasted Ta substrate was obtained from Advanced Diamond Technologies (Romeoville, IL). The BDD electrode was prepared by a chemical vapor deposition (CVD) process using trimethyl

borane (TMB) at concentrations of 750–12,000 ppm in a CH_4 gas stream and at a temperature between 700 and 800 ^{0}C. The BDD film was nanocrystalline, had a thickness of approximately 2 μm, and a resistivity between 0.05 and 0.1 Ω cm [143]. The BDD electrode was chosen due to its high potential window and electrochemical stability, and was considered an ideal substrate to study the effects of the composite film on CFX detection. Other electrode materials (e.g., glassy carbon) may be suitable substrates, but were not investigated in this study. An anodic pretreatment process (20 mA cm^{-2} for 20 minutes) was used to clean the BDD electrode. Although anodic treatment followed by cathodic treatment was reported as an activation method in prior BDD sensor work [305], the effect of BDD surface treatment on CFX detection was not investigated in this study. The anodic pretreatment was followed by methanol and water rinses.

Sensor preparation began by first preparing a 1 mL solution containing equal volumes of Nafion solution (5 wt%) (0.5 mL) and a 0.1 M KH_2PO_4 electrolyte (0.5 mL). Then 4 mg of MWCNT was added to the solution. The 0.1 M KH_2PO_4 electrolyte was added to enhance the dispersion of MWCNTs and to create a porous film upon drying. The MWCNTs were also dispersed by the hydrophobic interactions between MWCNTs and Nafion [293,306]. The mixture was sonicated for 30 minutes (Branson 1800), and 50 μL was drop cast onto a cleaned BDD electrode (electrode area: 1 cm^2) and dried under a steady air stream for 30 minutes. The KH_2PO_4 salt crystallized during the drying process and allowed the creation of a porous MWCNT/Nafion film. A stable coating was achieved by drop casting another 100 μL of a Nafion and 0.1 M KH_2PO_4 mixture (1:1 v/v) (without MWCNT) on the modified electrode, which was dried under air for another 1 hour. The resulting sensor is identified as porous-Nafion-MWCNT/BDD.

The dried electrode was subjected to multiple cyclic voltammetry (CV) scans (potential = 0 to 1.6 V versus standard hydrogen electrode (SHE); 200 cycles; scan rate (ν) = 100 mV s^{-1}) to remove residual salts and to obtain a consistent electrochemical response. Additional sensors identified as Nafion/BDD, Nafion-MWCNT/BDD, and porous-Nafion/BDD were prepared by similar methods and were used for CFX detection.

3.3.3 Oxidation of MWCNT. Oxidized MWCNTs were also incorporated into sensor films to determine the effect of oxygen functional groups on CFX detection. The oxidative treatments were performed on the as-received MWCNTs (0.2 g per 10 mL of solution) by heating in a 50 mL solution of H_2SO_4 and HNO_3 (H_2SO_4:HNO_3= 3:1, v/v) at 50 ^{0}C for 5 hours with sonication [307,308]. The oxidized MWCNTs were washed with DI water to remove residual acid and dried in an oven at 60 ^{o}C for 10 hours.

3.3.4 Characterization. The functional groups of the MWCNTs were characterized by X-ray photoelectron spectroscopy (XPS) (Kratos Axis-165). The sensor morphologies were investigated using variable pressure scanning electron microscopy (VPSEM) (Hitachi S-3000N, Japan) and transmission electron microscope (TEM) (JEOL JEM-3010, USA). The BET surface areas of MWCNT and oxidized MWCNT (MWCNT-O) were determined using N_2 gas adsorption at 77 K (Micromeritics ASAP-2020, USA).

3.3.5 CFX Detection Experiments. CV and differential pulse voltammetry (DPV) experiments (parameters: initial voltage = 0.2V, final voltage = 1.8V, step size = 4 mV, sample period = 1 sec, pulse time = 0.05 sec and pulse size = 50 mV) were utilized for CFX detection using a three-electrode setup. The BDD electrode, Pt wire (99.95%- metal basis) (Alfa Aesar), and Ag/AgCl/KCl electrode (Pine Research Instrumentation, Durham, NC) were used as working electrode, counter electrode, and reference electrode, respectively. Electrochemical

measurements were performed with a Gamry Reference 600 potentiostat/galvanostat (Warminster, PA) and in a 100 mL jacketed, glass reactor (Adams and Chittenden Scientific Glass, Berkeley, CA), which was maintained at 20 °C using a re-circulating water bath (Thermo Scientific). The 1 cm^2 BDD electrode was mounted into a custom-made PEEK rotating disk electrode (RDE) holder and was connected to a modulated speed rotator (Pine Research Instrumentation, Durham, NC) through a 316 stainless steel current collector contained within the electrode holder. A water-tight seal between the electrode and the holder was accomplished using a Viton® gasket. The holder provided a 0.35 cm^2 geometric surface area exposed to the solution.

The background electrolyte, unless otherwise stated, was a 0.1 M KH_2PO_4 (pH = 4.5) solution. A stock solution of 1 mM CFX was prepared in 0.1 M KH_2PO_4, and was added to the background electrolyte to achieve a given CFX concentration. Before each experiment the electrode was rotated at 800 rpm for 15 minutes to ensure a well-mixed solution. For DPV measurements, the potential was swept from 0.2 to 1.8 V/SHE. The secondary wastewater effluent sample was procured from Stickney Water Reclamation Plant (Cicero, IL, USA).

3.3.6 Capacitance Measurements. Measurements were performed to determine the double layer capacitance (C_{dl}) for selected sensors, which is a measure of the electroactive surface area. CV scans were performed for different sensors in a 0.1 M KH_2PO_4 supporting electrolyte at v between 10 and 100 mV s^{-1} and over a potential range of -0.5 to 0.5 V/SHE. This potential range was chosen because it is within the range of water stability and therefore all current is assumed to be generated from non-faradaic processes. The average current responses ($i/2$) were plotted versus v, and the slopes of the regressed data were used to calculate C_{dl} values.

3.3.7 Adsorption Experiments and CFX Analysis. A stock solution of 1 mM CFX was prepared in a 0.1 M KH_2PO_4 supporting electrolyte (pH 4.50). Equilibrium adsorption experiments were performed using 5 mL glass vials with PTFE-lined screw caps. Each vial was filled with 5 mL CFX solution (1 mM) with different MWCNT loadings (5, 10, 15, 20, 30, 50 and 100 mg), and were mechanically shaken at 200 rpm for 72 hours on a reciprocating shaker (Eberbach Corporation, Michigan, USA) at a temperature of 21°C. Solutions were filtered through 0.45 μm filters (PVDF, Fisher scientific) and analyzed by HPLC. All adsorption experiments were performed in duplicate.

The liquid phase CFX concentrations were measured using high performance liquid chromatography (HPLC, Shimadzu, USA) equipped with a Kinetex C18 column (2.6 μm, 2.1×75 mm, Phenomenex) and detected by a photo-diode array detector (Shimadzu) at a wavelength of 254 nm. The amount of CFX adsorbed to the MWCNTs was calculated by the difference between the initial and equilibrium aqueous solute concentration as follows:

$$q_e = \frac{(C_0 - C_e)V}{W} \quad (3\text{-}1)$$

where q_e is the amount of CFX adsorbed by MWCNTs (mg g^{-1}), C_0 and C_e are the initial and equilibrium liquid-phase concentrations of CFX (mg L^{-1}), respectively, V is the solution volume (L), and W is the weight of MWCNTs used in the adsorption tests (g). Control experiments were performed in the same manner described above but without the addition of MWCNTs.

Langmuir and Freundlich isotherms models were both fit to equilibrium adsorption data. The Langmuir isotherm is mainly applied to monolayer adsorption on perfectly smooth and homogeneous surfaces, and the Freundlich isotherm is widely employed for adsorption on surfaces with a non-uniform energy distribution. The Langmuir isotherm is:

$$q_e = \frac{K_L q_{max} C_e}{1 + K_L C_e} \quad (3\text{-}2)$$

where q_{max} is the maximum adsorption capacity (mg g^{-1}) and K_L is the Langmuir adsorption constant (L mg^{-1}). The Freundlich isotherm is:

$$q_e = K_F C_e^n \quad (3\text{-}3)$$

where K_F is the adsorption equilibrium constant ((mg g^{-1}) (mg $L^{-1})^{-n}$) and n is an empirical constant indicative of adsorption intensity.

3.3.8 Statistical Analysis. Linear regression was performed to determine calibration curves for the peak current response as a function of CFX concentration, and standard errors are provided as a measure of uncertainty of the slope and intercept values. The LOD for CFX detection was determined as the lowest CFX concentration that produced a signal that corresponded to S/N ratio ≥ 5. The S/N ratio was calculated by dividing the average peak current for CFX detection by the average background current (n = 4). Errors on the S/N were calculated at the 95% confidence interval, and represented the variation of the peak current, as the background current varied by < 0.25 %.

3.4 Results and Discussion

3.4.1 Physical and Chemical Characterization. The morphologies of the BDD, porous-Nafion/BDD, and porous-Nafion-MWCNT/BDD electrodes were characterized by SEM and TEM (Figure 3-1). Figure 3-1a shows a SEM image of the BDD electrode, which has a rough surface due to the bead blasted Ta substrate. The deposited BDD coating has a nanocrystalline grain size, which is not visible at this resolution. Figure 3-1b shows an image of the porous-Nafion/BDD electrode, which contains a smooth Nafion film with several cracks in the film. The crack shown in Figure 3-1b is approximately 70 μm wide. It was observed that cracks became larger during the vacuum drying process before SEM analysis, and therefore the cracks in the hydrated porous-Nafion/BDD electrode used for CFX detection were likely much smaller. By contrast, cracks were not observed in the Nafion film covering the Nafion/BDD electrode (image not shown). The mixing of Nafion with the electrolyte solution was responsible for increasing

the porosity of the Nafion film by creating structural defects caused by the precipitating salt during the drying process.

Figures 3-1c and 3-1d show SEM images of the porous-Nafion-MWCNT/BDD electrode at different magnifications. Figure 3-1c displays the general film morphology, which shows a highly porous Nafion film consisting of a range of pore sizes. The MWCNTs are dispersed within the Nafion film and within the pores and are visible as wire-like features in Figure 3-1c. The addition of MWCNTs provided a more continuous film than observed for the porous-Nafion/BDD electrode, likely due to the high strength and flexibility of the MWCNTs. Figure 3-1d shows a higher magnification of the porous-Nafion-MWCNT/BDD electrode within a single pore. The SEM image shows the wire-like MWCNTs covered with a film of Nafion, where the bright spots in the image were due to charging of the Nafion film. Figures 3-1e and 3-1f show TEM images of an unsupported porous-Nafion-MWCNT film. Figure 3-1e shows that the MWCNTs are interconnected, and Figure 3-1f shows higher magnification of a single MWCNT. The SEM and TEM images show that the porous-Nafion-MWCNT/BDD electrode has a porous, high surface area coating, with a high dispersion of interconnected MWCNTs that is anticipated to increase CFX adsorption and detection.

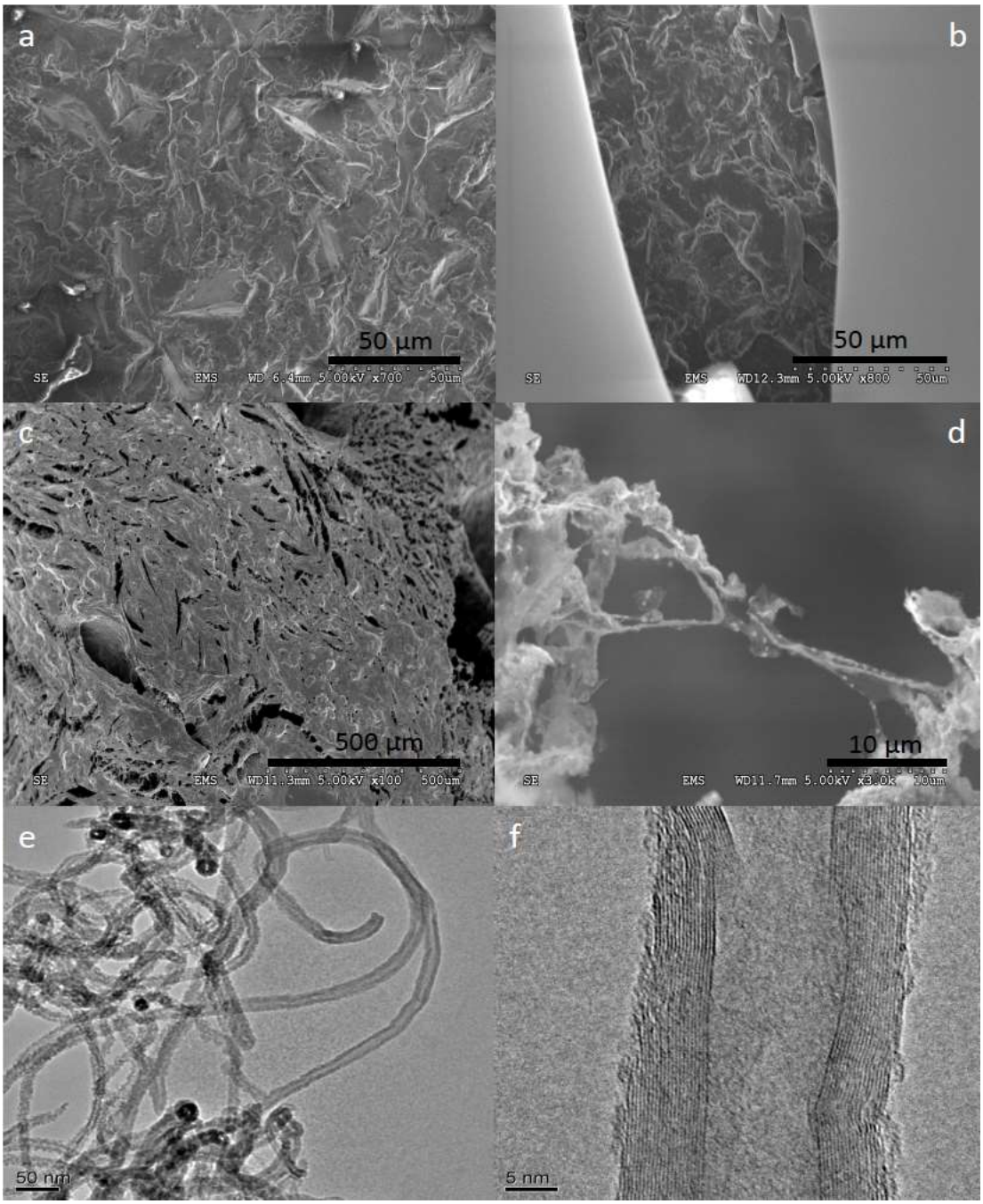

Figure 3-1. SEM images of (a) bare BDD, (b) porous-nafion/BDD and (c, d) porous-nafion-MWCNT/BDD. TEM images of (e, f) unsupported porous-nafion-MWCNT.

The MWCNT and MWCNT-O samples were analyzed by XPS in order to investigate the surface carbon-oxygen functional groups. The XPS data of the C1s region of the two different samples is shown in the Appendix A (Figures S-3-1a and S-3-1b), and results are summarized in

Table 3-1. The deconvoluted model fit to the XPS data was resolved into seven sub-bands. The [O/C] ratio increased for MWCNT-O by approximately 11-fold compared to MWCNT, indicating that the O content increased significantly after the mixed acid pretreatment. The binding energy (BE) ranges for each functional group is provided in Table 3-1. The percentage of the oxygenated functional groups (e.g. -C–OH, -C=O, -COOH) increased due to the acid treatment, which corresponded with a decrease in the percentage of C=C groups and an increase in the percentage of C-C groups. XPS results were consistent with the literature [307,309,310].

Table 3-1 - Deconvolution results of C1s XPS spectra for MWCNT and MWCNT-O (values given in atomic percent).

Sample	**Functional Groups (eV)**							
	[O/C] %	C=C (284.5)	C-C (285.3 ± 0.3)	-C-OH (286.3 ±0.25)	-C=O (287.3 ± 0.2)	-COOH (288.7 ± 0.15)	$-CO_3$ (289.8)	π-π* (291.2 ± 0.02)
MWCNT	1.29	66.8	10.6	5.55	4.14	3.36	2.39	7.14
MWCNT-O	14.24	47.6	19.0	6.70	4.88	6.45	1.94	13.4

3.4.2 Electrochemical Characterization. Cyclic voltammetry provides useful information regarding the change in surface structure of the modified electrodes. CV scans were performed in the presence of a 5 mM $Fe(CN)_6^{4-/3-}$ redox couple in a 0.1 M KH_2PO_4 background electrolyte, and in the presence of a 5 mM $Fe^{3+/2+}$ redox couple in a 0.1 M $HClO_4$ background electrolyte. The anodic peak current ($I_{p,a}$) was used to assess the effect of different surface modifications to the electrodes. Figure 3-2 shows CV scans for the different modified electrodes in the presence of the redox couples. The bare BDD electrode showed a higher anodic current response for the $Fe(CN)_6^{4-/3-}$ redox couple ($I_{p,a}$ = 1.60 mA cm^{-2}) compared to the Nafion/BDD ($I_{p,a}$ = 0.40 mA cm^{-2}), porous-Nafion/BDD electrodes ($I_{p,a}$ = 1.55 mA cm^{-2}), and Nafion-MWCNT/BDD ($I_{p,a}$ = 0.62 mA cm^{-2}), which is attributed to electrostatic repulsion of the $Fe(CN)_6^{4-/3-}$ redox couple by the Nafion $–SO_3^-$ groups and blockage of the BDD surface by the Nafion film (Figure 3-2a). The porous-Nafion-MWCNT/BDD ($I_{p,a}$ = 1.61 mA cm^{-2}) showed almost the same anodic current response as the bare BDD ($I_{p,a}$ = 1.60 mA cm^{-2}). This result is attributed to the increase in porosity of the Nafion film and surface area (due to MWCNT), which countered the electrostatic repulsion due to the presence of Nafion.

The CV scans in Figure 3-2b confirm the presence of an electrostatic effect, which show a significant increase in the $I_{p,a}$ for the $Fe^{3+/2+}$ redox couple at all the modified electrodes relative to the BDD electrode ($I_{p,a}$= 0.93 mA cm^{-2}). The Nafion/BDD electrode ($I_{p,a}$ = 7.41 mA cm^{-2}) showed an 8.0-fold enhancement in $I_{p,a}$ relative to BDD, and the Nafion-MWCNT/BDD electrode ($I_{p,a}$ = 13.3 mA cm^{-2}) showed a 1.8-fold enhancement in $I_{p,a}$ relative to the Nafion/BDD electrode. These results indicate that the Nafion film increased the current response due to the electrostatic attraction between the negatively charged $–SO_3^-$ groups of Nafion and the positively charged redox couple. The addition of MWCNTs provided further enhancement of the current

response by increasing the surface area of the electrode. The addition of porosity to the Nafion film showed a uniform decrease in the $I_{p,a}$ for the porous-Nafion/BDD ($I_{p,a}$ = 1.31 mA cm^{-2}) and porous-Nafion-MWCNT/BDD ($I_{p,a}$ = 3.00 mA cm^{-2}) electrodes relative to the Nafion/BDD and Nafion-MWCNT/BDD electrodes by a factor of 5.7 and 4.4, respectively. This decrease in $I_{p,a}$ is attributed to the increased porosity, which decreased the compactness and coverage of the Nafion film on the BDD electrode.

The C_{dl} of three modified electrodes (BDD, porous-Nafion/BDD, and porous-Nafion-MWCNT/BDD) was measured using CV at different scan rates. These three electrodes were chosen in order to assess any change in the C_{dl} due to the addition of the porous Nafion film (porous-Nafion/BDD) and MWCNTs (porous-Nafion-MWCNT/BDD). Table 3-2 contains the measured C_{dl} values of the different modified electrodes, which is a surrogate for the electroactive surface area. The C_{dl} value for the bare BDD electrode was 720 μF (2.1 mF cm^{-2}) after anodic electrochemical cleaning, which indicates that the bead blasted Ta substrate, nanocrystalline grain size, and electrochemical cleaning procedure all contributed to a significantly higher C_{dl} value compared to typical values (3-10 μF cm^{-2}) [311]. This result is consistent with past studies using nanocrystalline BDD electrodes, that showed that an anodic treatment was able to increase the C_{dl} from 14 μF cm^{-2} to as high as 3.2 mF cm^{-2} for the pristine and oxidized electrodes, respectively [311]. This result was attributed to electrochemical etching of the grain boundaries of the nanocrystalline BDD surface [311]. The small grain size of nanocrystalline BDD allows for much higher capacitance compared to microcrystalline BDD electrodes (165—234 μF cm^{-2}) [312–314].

Table 3-2 - Double layer capacitances for different modified electrodes

Type of electrode	C_{dl} (µF)
BDD	720
Porous-Nafion/BDD	431
Porous-Nafion-MWCNT/BDD	840

The C_{dl} value decreased for the porous-Nafion/BDD electrode relative to the bare BDD, due to coverage of the BDD electrode by the Nafion film. However, the porous-Nafion-MWCNT/BDD electrode showed an approximate 2-fold increase in C_{dl} compared to the porous-Nafion/BDD electrode, due to the presence of the high surface area MWCNTs. This result suggests that the 1.8-fold enhancement in peak current for the $Fe^{2+/3+}$ redox couple at the porous-Nafion-MWCNT/BDD electrode relative to the porous-Nafion/BDD electrode was related to an increase in the electroactive surface area.

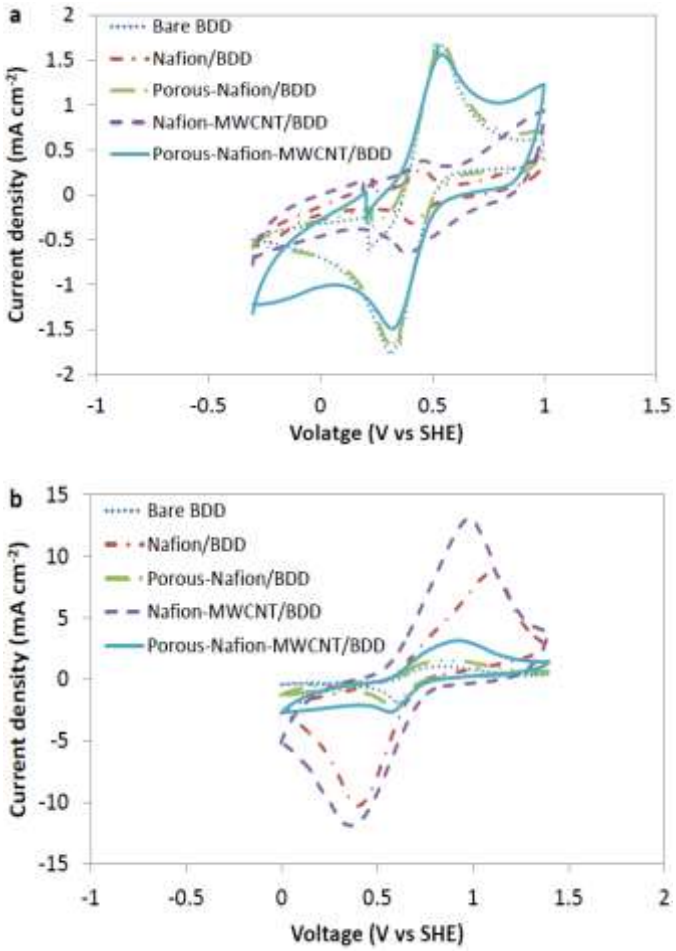

Figure 3-2. CV curves of bare BDD, Nafion/BDD, porous-Nafion/BDD, Nafion-MWCNT/BDD, and porous-Nafion-MWCNT/BDD in (a) 0.1 M KH_2PO_4 electrolyte containing 5mM $K_3Fe(CN)_6/K_4Fe(CN)_6$ and (b) 0.1M $HClO_4$ electrolyte containing 5mM $Fe(ClO_4)_2/Fe(ClO_4)_3$.

3.4.3 Electrochemical Detection of CFX. To explore the sensitivity of the fabricated sensors for CFX detection, DPV was performed in a 0.1 M KH_2PO_4 supporting electrolyte containing 50 µM of CFX with the BDD, Nafion/BDD, porous-Nafion/BDD, Nafion-MWCNT/BDD, and porous-Nafion-MWCNT/BDD electrodes. Figure 3-3 shows the DPV response for the different electrodes. A peak was not observed for the BDD electrode, whereas a broad peak ($I_{p,a}$ = 6µA, corrected for background) appeared for CFX oxidation at approximately 1.4 V/SHE for the Nafion/BDD electrode. This oxidation peak occurred at a slightly higher potential than observed

by others [315], which is likely attributed to the acidic solution pH and high electrical resistance of the Nafion film. The porous-Nafion/BDD electrode showed an approximate 2-fold increase in the current response ($I_{p,a}$ = 11 μA, corrected for background) compared to the Nafion/BDD electrode. The Nafion-MWCNT/BDD showed an approximate 2.5-fold increase in the current response ($I_{p,a}$ = 15 μA, corrected for background) compared to the Nafion/BDD electrode. The porous-Nafion-MWCNT/BDD electrode showed a significant increase in the current response ($I_{p,a}$ = 63 μA, corrected for background), which was 10.5-fold higher than the Nafion/BDD, 5.7-fold higher than the porous-Nafion/BDD and 4.2-fold higher than the Nafion-MWCNT/BDD.

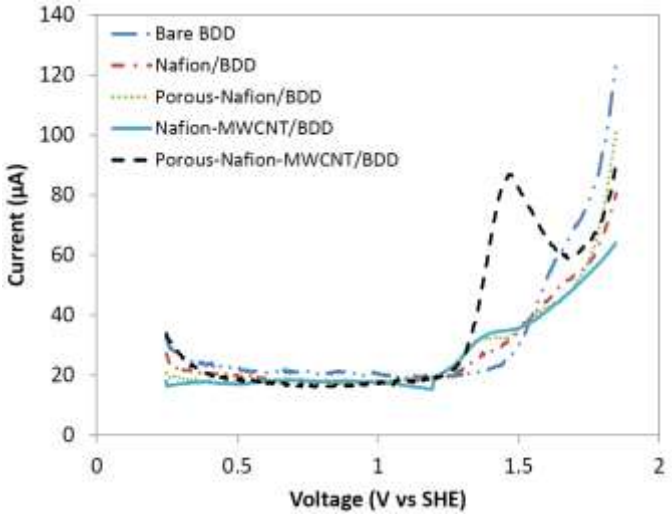

Figure 3-3. DPV curves of 50 μM CFX on BDD, Nafion/BDD, porous-Nafion/BDD, Nafion-MWCNT/BDD, and porous-Nafion-MWCNT/BDD electrodes in 0.1 M KH_2PO_4 solution (pH = 4.50).

The differences in CFX detection for the different electrodes are likely due to several factors including, electrostatics, porosity, and conductivity of the film. At the pH of the DPV experiments shown in Figure 3-3 (pH = 4.5), CFX is positively charged due to the formation of -NH_2^+ at the terminal –NH group and protonation of the -COOH group (pK_{a1} = 6.2 (carboxyl group), pK_{a2} = 8.68 (amine group)) [316,317]. The electrostatic attraction between the negatively

charged $–SO_3^-$ groups of Nafion and the positively charged $-NH_2^+$ groups of CFX resulted in CFX detection. The $I_{p,a}$ increased for the Nafion-MWCNT/BDD electrode due to the presence of the high surface areas MWCNTs. The $I_{p,a}$ increased further for the porous-Nafion/BDD electrode, due to the increase in porosity and defects in the Nafion film. The CV results with the $Fe^{3+/2+}$ redox couple showed the highest $I_{p,a}$ at the Nafion-MWCNT/BDD electrode (Figure 3-2b), which is attributed to electrostatic attraction by the $–SO_3^-$ groups of Nafion, transport of the relatively small $Fe^{3+/2+}$ redox couple through the polymer film, and the increase in the surface area of the electrode. By contrast, CFX showed the highest $I_{p,a}$ at the porous-Nafion-MWCNT/BDD electrode (Figure 3-3), because the relatively large CFX molecule is unable to diffuse through a dense Nafion film, and therefore the added porosity of the porous-Nafion/BDD electrode allows access of CFX to the conductive MWCNTs and BDD surface, while the $–SO_3^-$ groups within the pores enhance CFX adsorption compared to the nonporous electrodes.

The 5.7-fold increase in $I_{p,a}$ for CFX detection for the porous-Nafion-MWCNT/BDD electrode relative to the porous-Nafion/BDD electrode is greater than the approximate 2-fold increase in electroactive surface area (Table 3-2), which indicates that other factors are enhancing CFX detection. Specific functional groups on the MWCNT surface may enhance adsorption of CFX, which will be discussed further in section *3.4.8*.

3.4.4 Effect of pH and Scan Rate (ν) *on CFX Detection*. The effect of solution pH on the electrochemical detection of CFX for both Nafion/BDD and porous-Nafion-MWCNT/BDD was studied, and background-subtracted results are shown in Figure 3-4a. The maximum $I_{p,a}$ occurred at different pH values for the two electrodes. The porous-Nafion-MWCNT/BDD electrode had the highest $I_{p,a}$ at a pH of 4.5, and the Nafion/BDD electrode had the highest $I_{p,a}$ at a pH of 4.96. The current response for porous-Nafion-MWCNT/BDD was much more sensitive to pH than that

of Nafion/BDD (Figure 3-4a), which suggests that acidic functional groups (e.g., -COOH) on the MWCNT surface aid in selective CFX adsorption and therefore increased the sensitivity for CFX detection.

In order to gain information on the rate-controlling mechanism for CFX oxidation, the effect of ν on $I_{p,a}$ was studied and results are presented in Figure 3-4b. The $I_{p,a}$ varied linearly with ν (Figure 3-4b), according to the following equation:

$$I_{p,a}(\mu A) = 1792\nu + 96.62 \quad (3\text{-}4)$$

with $R^2 = 0.992$. These results indicate that the oxidation process of CFX at the porous-Nafion-MWCNT/BDD electrode was an adsorption-controlled process.

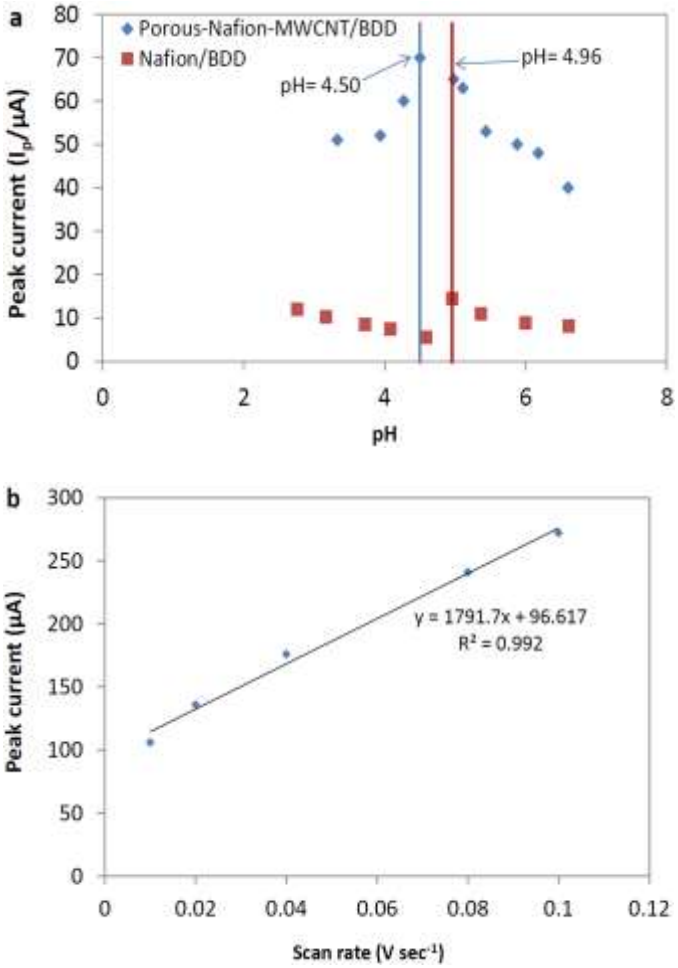

Figure 3-4. (a) Effect of pH on the peak currents of 100 µM CFX in 0.1 M KH_2PO_4. (b) Linear relationship of peak current (I_p) vs scan rate (v) in 0.1 M KH_2PO_4 with 50 µM CFX.

3.4.5 CFX Detection at Porous-Nafion-MWCNT/BDD. Under optimized solution conditions (pH = 4.50), DPV was used to test the electrochemical performance of the porous-Nafion-MWCNT/BDD electrode for CFX detection in a 0.1 M KH_2PO_4 supporting electrolyte. Figure 3-5a shows the background-corrected DPV scans for CFX detection as a function of concentration (0.05 - 10 µM). The $I_{p,a}$ varied linearly with the concentration of CFX (Figure 3-5b). The linear regression equation was determined as:

$$I_{p,a}(\mu A) = 2.07\ C_{CFX}(\mu M) + 4.91 \quad (3\text{-}5)$$

The coefficient of determination for linear regression was R^2 = 0.992 and the linear range was 0.05 to 10 μM. The limit of detection (LOD) of our sensor was defined as the lowest CFX concentration that would yield a signal/noise (S/N) ratio of ≥ 5 during DPV experiments. An LOD of 5.0 nM was found (S/N = 5.04 ± 0.26; n = 4, 95% confidence interval), which to our knowledge is the lowest LOD reported in the literature for a CFX sensor (Table 3-3), and is included in the linear range of 5.0 to 50 nM (Table S-3-1). Our very low LOD was a result of the highly porous, high surface area, conductive MWCNT/Nafion coating. The role of the MWCNTs towards CFX adsorption may also contribute to the low LOD, which can enhance CFX adsorption through several mechanisms (e.g., hydrophobic effect, electrostatic interaction, electron-donor-acceptor mechanism (π-π interaction), Lewis acid base interaction). The effects of MWCNTs towards CFX adsorption will be discussed in more detail in section *3.4.8*.

The repeatability of the sensor for CFX detection was determined by performing five DPV experiments with 15 μM of CFX using a single sensor, which gave a relative standard deviation (RSD) for repeatability of 4.3%. The reproducibility of the sensor was also studied by fabricating five different sensors and performing DPV experiments for a 15 μM CFX solution. The RSD for reproducibility was 6.35%. These results indicate that the sensor exhibits both high repeatability and reproducibility during CFX detection.

Table 3-3 - Comparison of different methods for the determination of Ciprofloxacin

Electrode	**Linear Range (µM)**	**(LOD) (µM)**	**References**
DNA biosensor	40 – 80	24	[318]
Enzymatic rotating biosensor	0.1 – 60	0.01	[319]
MWCNT-GCE	3 – 1200	0.9	[320]
Modified CPE	0.1 - 20	0.05	[321]
ds-DNA -BDD	0.5 - 60	0.44	[315]
MWCNT-GCE	40 - 1000	6	[101]
P-β-Cyclodextrin-L-arginine/CPE	0.05 - 100	0.01	[97]
$MgFe_2O_4$-MWCNT/GCE	0.1 - 1000	0.01	[203]
Porous-Nafion-MWCNT/BDD	0.005 – 0.05, 0.05-10	0.005	This work

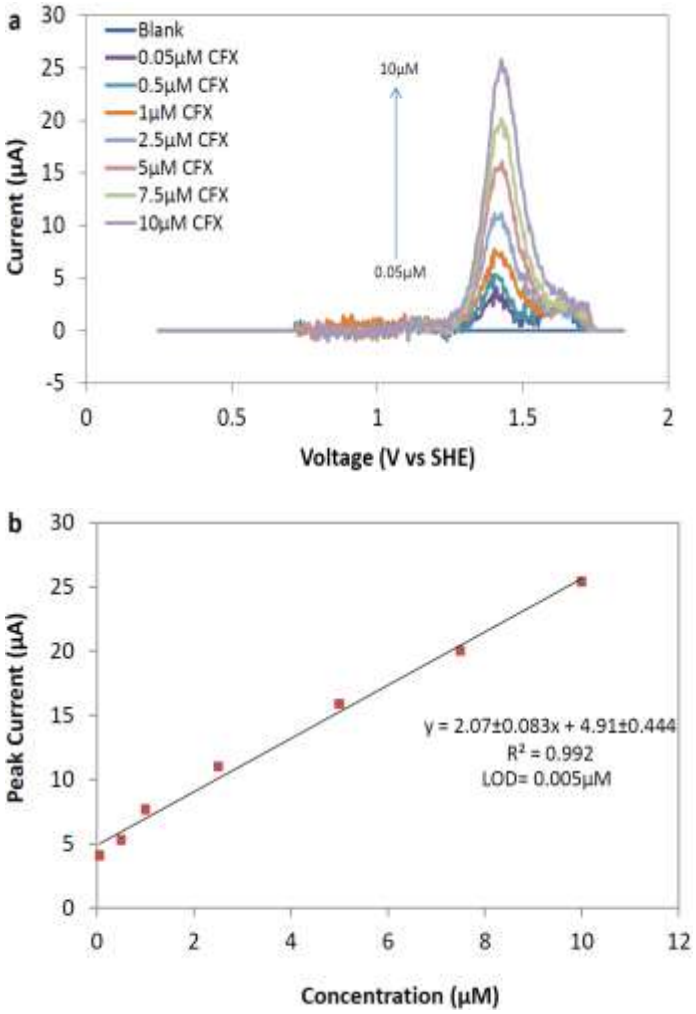

Figure 3-5. (a) DPV curves of porous-Nafion-MWCNT/BDD at different concentrations of CFX in 0.1 M KH_2PO_4 (b) The corresponding calibration graph of CFX.

3.4.6 CFX Detection in the Presence of Non-target Water Constituents. A primary objective of this work was to assess the ability of the sensor to quantify CFX in domestic wastewater effluent and drinking water sources. CFX may be present in wastewater effluent and enter receiving waters, and is a health concern especially in water recycling applications. Different ions and compounds often coexist with CFX in wastewater effluent or in natural waters. Therefore, several non-target water constituents were chosen to investigate their effect on CFX detection. These constituents include common ions (Ca^{2+} and Cl^-), surfactant (sodium dodecyl benzene sulfonate (SDBS)), humic acid, and the commonly used antibiotic amoxicillin. All of these compounds are found in wastewater effluent (WWE) except humic acid, which is found in natural waters. Results for CFX detection in the presence of 1 mM of the various non-target water constituents are summarized in Table 3-4. The LOD for CFX detection in the presence of all the non-target water constituents was not compromised (LOD = 5 nM) (Table 3-4). The inhibition for CFX detection increased (slopes (or sensitivity) decreased) in the following order: Cl^- < Amoxicillin < humic acid < SDBS < Ca^{2+}.

The sensitivity was lowest in the presence of Ca^{2+}, which is attributed to the electrostatic attraction between the positively charged Ca^{2+} and negatively charged $–SO_3^-$ groups of Nafion, and competitive adsorption of Ca^{2+} at the –COOH groups on the MWCNTs [322], which would block access of CFX to the active –COOH adsorption sites. The individual calibration curve with Ca^{2+} is shown in the Appendix A (Figure S-3-2a). The linear ranges for CFX detection remained essentially unchanged with all other non-target water constituents (see Table 3-4). These results indicate that the porous-Nafion-MWCNT/BDD sensor is useful for the detection of CFX in the presence of representative concentrations of common non-target water constituents.

3.4.7 Detection of CFX on Porous-Nafion-MWCNT/BDD in wastewater effluent (WWE). To verify the applicability of the sensor for the detection of CFX in WWE, the porous-Nafion-MWCNT/BDD electrode was used to detect CFX in a secondary WWE sample. The sample had a pH of 7.8 and a chemical oxygen demand (COD) concentration of 12.27 mg L^{-1}. The sensor was tested in the as received WWE, but a current peak was not observed (data not shown), indicating that CFX was not present in the WWE at significant concentrations. Therefore, to ascertain the feasibility of CFX detection in the WWE, various concentrations of CFX were spiked to the WWE solution. Calibration curves derived from DPV measurements (Appendix A; Figures S-3-3 to S-3-5) of different concentrations of CFX at the porous-Nafion-MWCNT/BDD electrode in the as received WWE, WWE after pH adjustment to 4.5 ($WWE_{pH=4.5}$), and the wastewater sample at pH = 4.5 and in 0.1 M KH_2PO_4 ($WWE_{pH=4.5,\ I=0.1}$) are provided in the Appendix A (Figure S-3-2b). The detection of CFX in the blank electrolyte is also included in Figure S-3-2b as a point of reference.

Data in Table 3-4 summarizes the LOD, linear ranges, sensitivities, and linear equations for the different WWE samples tested. Comparing the slopes it was observed that the sensitivity for CFX detection increased in the following order: WWE < $WWE_{pH=4.5}$ < $WWE_{pH=4.5,\ I=0.1}$ < supporting electrolyte (without WWE). It was also observed that the LOD (5 nM) remained the same for all the samples except the as received WWE. The LOD in the WWE increased to 5 µM, indicating that pH and ionic strength adjustment is necessary. The development of *in situ* monitoring sensors will require electrode isolation behind a selective membrane to achieve desired results.

Table 3-4 - Determination of CFX in the presence of different interferences. Errors on estimates represent the standard errors. Data for lower concentration linear ranges are included in the Appendix A.

Interferences	**LOD (µM)**	**Linear range (µM)**	**Sensitivity (Slope(µA µM^{-1}), R^2, Intercept)**
No interference	0.005	0.05 – 10	Slope = 2.08 ± 0.085, R^2 = 0.99 Intercept= 5.362 ± 0.484
		0.005 – 0.05	Slope = 41 ± 5.196, R^2 = 0.98 Intercept= 2.055 ± 0.153
Ca^{2+}	0.005	1- 15	Slope = 0.69 ± 0.034, R^2 = 0.99 Intercept= 5.734 ± 0.286
Chloride (1mM)	0.005	0.05 - 10	Slope = 2.38 ± 0.067, R^2 = 0.996 Intercept= 4.122 ± 0.349
SDBS (1mM)	0.005	0.05 - 15	Slope = 1.23 ± 0.027, R^2 = 0.997 Intercept= 1.741 ± 0.195
Humic acid(11mg L^{-1})	0.005	0.05 - 10	Slope = 1.69 ± 0.078, R^2 = 0.993 Intercept= 3.105 ± 0.408
Amoxicillin (1mM)	0.005	0.05 - 15	Slope = 2.19 ± 0.083, R^2 = 0.991 Intercept= 4.272 ± 0.596
Without WWE	0.005	0.05 - 1, 1 - 15	$Slope_1$ = 3.78 ± 0.59, R^2 = 0.976 $Slope_2$ = 1.68 ± 0.11, R^2 = 0.983 $Intercept_1$= 3.729±0.385, $Intercept_2$= 7.068±0.911
$WWE_{pH= 4.5}$	0.005	0.05 - 1, 1 - 15	$Slope_1$ = 1.05 ± 0.15, R^2 = 0.98 $Slope_2$ = 0.32 ± 0.007, R^2 = 0.998 $Intercept_1$= 0.991±0.099, $Intercept_2$= 1.742±0.059
$WWE_{pH= 4.5, I= 0.1}$	0.005	0.05 - 2.5, 2.5 – 15	$Slope_1$ = 2.35 ± 0.19, R^2 = 0.987 $Slope_2$ = 1.04 ± 0.07, R^2 = 0.987 $Intercept_1$= 0.668±0.259, $Intercept_2$= 3.586±0.636
WWE	5	5 - 15	Slope = 0.15 ± 0.03, R^2 = 0.912 Intercept= 0.328±0.341
Without organics	0.005	0.05 - 1, 1-15	$Slope_1$ = 3.87 ± 0.51, R^2 = 0.974 $Slope_2$ = 0.92 ± 0.03, R^2 = 0.996 $Intercept_1$= 3.254±1.073, $Intercept_2$= 8.380±0.249
1:1 CFX:HBA	0.005	0.05 - 1, 1 - 15	$Slope_1$ = 3.14 ± 0.703, R^2 = 0.952 $Slope_2$ = 0.72 ± 0.052, R^2 = 0.999 $Intercept_1$= 2.826±0.082, $Intercept_2$= 6.144±0.112
1:10 CFX:HBA	1	1 - 15	Slope = 0.65 ± 0.012, R^2 = 0.99 Intercept= 1.329±0.103
1:1 CFX:ABA	0.005	0.05 - 1, 1 - 15	$Slope_1$ = 3.42 ± 0.31, R^2 = 0.98 $Slope_2$ = 0.85 ± 0.012, R^2 = 0.990 $Intercept_1$= 4.423±0.423, $Intercept_2$= 7.328±0.105
1:10 CFX:ABA	0.05	0.05 - 1, 1 - 15	$Slope_1$ = 2.10 ± 0.064, R^2 = 0.999 $Slope_2$ = 0.78 ± 0.029, R^2 = 0.99 $Intercept_1$= 3.832±0.845, $Intercept_2$= 6.524±0.074

*ABA- 4-aminobenzoic acid & HBA- 4-hydroxybenzoic acid

3.4.8 Elucidation of Adsorption Sites for CFX Detection. Results from Figure 3-4b indicate that CFX oxidation at the porous-Nafion-MWCNT/BDD electrode was adsorption-controlled. Additionally, experimental results indicate that the addition of the MWCNTs to the BDD electrode caused a pH-dependence for CFX detection, with an optimal pH for CFX detection of 4.5 (Figure 3-4a). These results suggest that adsorption of CFX may be controlled by acidic functional groups on the MWCNT surface. XPS results showed the presence of both –COOH and –OH groups on the MWCNT sample (Figure S-3-1 and Table 3-1). The pK_a for –COOH groups has been reported between 3 and 6, and the pK_a for –OH groups has been reported at 7.1 on MWCNTs [323,324]. Thus the optimal CFX response at pH = 4.5 (Figure 3-4a) suggests that –COOH groups may be involved in CFX adsorption.

One possible mechanism for pH-dependent CFX adsorption is through a negative charge-assisted H-bond (CAHB) [325,326]. The CAHB is a covalent bond that involves the sharing of a H atom between the sorbate and sorbent, compared to typical H-bonds that are electrostatic [325,326]. The adsorption of various compounds containing –COOH groups have been shown to undergo CAHBs at CNTs [326]. The strength of the CAHB increases with decreasing ΔpK_a, which is defined as the difference in pK_a of the acidic CNT functional group and the weak acid group of the sorbate[325,326]. The pK_a of -COOH groups on CNTs are between 3 and 6 [323], and the pK_a of the -COOH group of CFX is between 5.8 and 6.2 [316,317,324,327,328]. Therefore, the CAHB should be most energetically favorable at pH values between 4.4 and 6.1, which compares well with experimental results shown in Figure 3-4a (pH = 4.5).

To further investigate the CAHB mechanism for CFX adsorption at the porous-Nafion-MWCNT/BDD electrode, competitive adsorption experiments were performed with CFX and

three model organic compounds containing –COOH groups with different pK_a values. Model compounds were 4-hydroxybenzoic acid (HBA) (pK_a = 4.1), 4-aminobenzoic acid (ABA) (pK_a = 4.9), and salicylic acid (SA) (pK_a = 2.97). The strength of the CAHB should follow the order: SA > HBA > ABA > CFX, and therefore the model organic compounds should inhibit CFX detection to varying degrees. CFX detection was assessed with the individual addition of SA, HBA, and ABA at an equimolar (1:1) concentration with respect to CFX (Appendix A; Figures S-3-6 to S-3-9). As expected, the current response for CFX in the presence of HBA was lower than in the presence of ABA (Appendix A; Figure S-3-10). However, SA experiments did not follow the expected trend, which may be attributed to steric hindrance associated with SA having the -OH and –COOH groups in the ortho position, compared to the para position for HBA. The LOD was not compromised for any of the equimolar competitive adsorption experiments (Table 3-4). A higher concentration of HBA and ABA were also tested (1:10 = CFX:organics). The sensitivity (slope) of the calibration curve for CFX with 1:10 ABA was much higher than that with 1:10 HBA (Table 3-4). CFX detection with 1:10 CFX:HBA (LOD = 1 μM) was affected much more than that with 1:10 CFX:ABA (LOD = 50 nM) (Table 3-4), indicating that HBA inhibited CFX detection to a greater extent than ABA, which was expected from the ΔpK_a values.

To investigate the effect of the -COOH group of MWCNT on CFX detection, MWCNT-O was used to prepare a sensor and tested for CFX detection. XPS data of the C1s region of the two different samples is included in the Appendix A (Figures S-3-1a and S-3-1b), and results are summarized in Table 3-1. Results indicate that the percentage of –COOH groups was 3.36% on the MWCNT sample and 6.46% on the MWCNT-O sample (Table 3-5). The [O/C] ratio

increased for MWCNT-O approximately 11-fold compared to MWCNT, indicating that the O content increased significantly after the mixed acid pretreatment (Table 3-1).

Batch adsorption experiments were performed with MWCNT and MWCNT-O to determine the effect of –COOH groups on CFX adsorption. Control experiments did not show a decrease in the concentration of CFX without MWCNTs. The data for CFX adsorption on MWCNT and MWCNT-O are shown in the Appendix A (Figure S-3-11). The adsorption capacity of CFX on MWCNT was lower than that on MWCNT-O, indicating that the higher quantity of -COOH functional groups (6.46%) on the MWCNT-O increased the adsorption of CFX relative to the MWCNT sample (-COOH = 3.36%). The acidic functional groups presumably increased the adsorption of CFX through a CAHB, as discussed previously.

The Freundlich and Langmuir models were fit to the experimental adsorption data. A summary of the fitted parameters for the two adsorption isotherm models are provided in Table 3-6. The data indicates that the Freundlich model matched the data better than the Langmuir model, likely due to a distribution of adsorption energies on the MWCNT samples. Both adsorption isotherm models indicate that MWCNT-O has a higher affinity for CFX adsorption than MWCNT. Since the MWCNT and MWCNT-O samples had a similar specific surface area (Table 3-5), these results clearly indicate that oxygenated functional groups enhanced the adsorption of CFX. These results coupled with the pH-dependence of CFX detection (Figure 3-4a) and the competitive adsorption experiments (Table 3-4), strongly suggest that the –COOH groups of MWCNTs enhances CFX adsorption and thus detection, possibly through the formation of a CAHB between the –COOH groups of CFX and MWCNTs [325,326].

Table 3-5 - The comparison of normalized slopes for CFX calibration with porous-Nafion-MWCNT/BDD and porous-Nafion- MWCNT-O/BDD. Errors on calculations represent standard errors.

Parameter	Porous-Nafion-MWCNT/BDD	Porous-Nafion-MWCNT-O/BDD
Slope ($\mu A\ \mu M^{-1}$)	1.94 ± 0.049	1.80 ± 0.13
C_{dl} (μF)	840	205
-COOH (%)	3.36	6.46
Normalized slope ($\mu A\ \mu M^{-1}$)	0.58	1.14
BET ($m^2\ g^{-1}$)	205	240

Sensors fabricated with both MWCNT and MWCNT-O were used for CFX detection and were labeled as porous-Nafion-MWCNT/BDD and porous-Nafion-MWCNT-O/BDD, respectively. The porous-Nafion-MWCNT/BDD electrode (1.93 ± 0.049 $\mu A\ \mu M^{-1}$) had almost the same sensitivity as the porous-Nafion-MWCNT-O/BDD electrode (1.80 ± 0.13 $\mu A\ \mu M^{-1}$) (Appendix A; Figure S-3-12). This result was unexpected, as it was anticipated that the porous-Nafion-MWCNT-O/BDD electrode would have higher sensitivity based on adsorption isotherm data.

The conductivity of the porous-Nafion-MWCNT-O/BDD electrode might have changed due to the formation of defects during the acid treatment [329]. Therefore, the C_{dl} values (measure of electroactive surface area) were measured for the two different electrodes. The C_{dl} values provided in Table 3-5 indicate that the porous-Nafion-MWCNT/BDD had over a 4-fold higher electroactive surface area than the porous-Nafion-MWCNT-O/BDD electrode, while only a slight increase in the BET surface area was observed for the MWCNT-O sample. In order to normalize the sensor response by the electroactive –COOH content, the slopes were divided by the corresponding –COOH content and multiplied by $C_{dl,1}/C_{dl,i}$. This model assumes a

homogeneous distribution of –COOH groups on the MWCNT surface. The $C_{dl,1}$ is the C_{dl} value of the porous-Nafion-MWCNT/BDD electrode and *i* is the electrode of interest (see Table 3-5). The normalized slopes were calculated as 0.58 and 1.14 μA μM^{-1} for the porous-Nafion-MWCNT/BDD and porous-Nafion-MWCNT-O/BDD electrodes, respectively. These results suggest that the MWCNT-O did not increase the overall sensitivity of the sensor because oxidation resulted in a decrease in the conductivity of the film, which caused many of the adsorption sites to be electrochemically inactive. However, the normalized slopes calculated above indicate that an increase in –COOH groups on MWCNTs could lead to enhanced sensitivity for CFX detection, if the groups are electroactive, indicating further research in this area is needed.

Table 3-6 - Results of adsorption isotherm models fitting to adsorption data of CFX on MWCNT and MWCNT-O

	Langmuir Model			**Freundlich Model**		
Samples	**q_{max}**	**K_L**	**R^2**	**K_F**	**n**	**R^2**
MWCNT	106.5	0.38	0.84	31.85	0.256	0.90
MWCNT-O	173.0	0.10	0.73	48.37	0.259	0.99

3.4.9 Fouling and Regeneration of the Sensor. Results in Table 3-4 show that the LOD was compromised when the porous-Nafion-MWCNT/BDD electrode was exposed to a high concentration of organic compounds. To investigate the fouling and regeneration of the sensor, a freshly prepared porous-Nafion-MWCNT/BDD electrode was first used for CFX detection in a blank electrolyte and then it was fouled with 1 mM ABA. After which, the sensor was again tested for CFX in a blank electrolyte. Two different regeneration methods were tested. The first method was cathodic treatment (-1 V/SHE for 60 sec) and the second method used a 0.01 M

NaOH rinse for 10 minutes. After these regeneration treatments the sensor was again tested for CFX detection in a blank electrolyte. As shown in Figure 3-6a, a peak (22 µA, corrected for background) appeared for CFX oxidation at 1.43 V/SHE for the 'as prepared' electrode. The sensor was then immersed in 1 mM ABA with 0.1 M KH_2PO_4 and DPV was performed to oxidize ABA. Only one peak (77 µA, corrected for background) appeared at 1.1 V/SHE, which was attributed to ABA oxidation. After which, the sensor was used for CFX detection in a blank electrolyte, but a peak for CFX was not observed. The sensor was then treated cathodically (-1V/SHE for 60 sec) in a blank electrolyte solution (0.1 M KH_2PO_4) to regenerate the sensor. The sensor was again tested for CFX detection and a peak (11 µA) appeared for CFX oxidation at 1.43 V/SHE, which was approximately 50% of that for the 'as prepared' electrode. Regeneration was attributed to the reduction of water at the electrode surface that created a local alkaline region that destroyed the CAHBs between ABA and carboxyl groups on the MWCNTs. However, the solution used during regeneration was 0.1 M KH_2PO_4 (pH buffer), which may have minimized the pH increase at the electrode surface. Therefore, another set of experiments was performed under identical conditions, except the regenerant solution was 0.1 M NaCl (Figure 3-6b). The current response before fouling was the same as after cathodic cleaning in the NaCl solution, concluding that cathodic cleaning (-1V/SHE for 60 sec) could fully regenerate the sensor in a non-buffering solution (Figure 3-6b). Another set of experiments was performed using 1 mM ABA as the foulant, and the electrode was regenerated by washing in 0.01 M NaOH solution for 10 minutes. The DPV response before fouling was exactly the same as the response after base wash, concluding full regeneration of the sensor was due to basic pH conditions (Figure 3-6c).

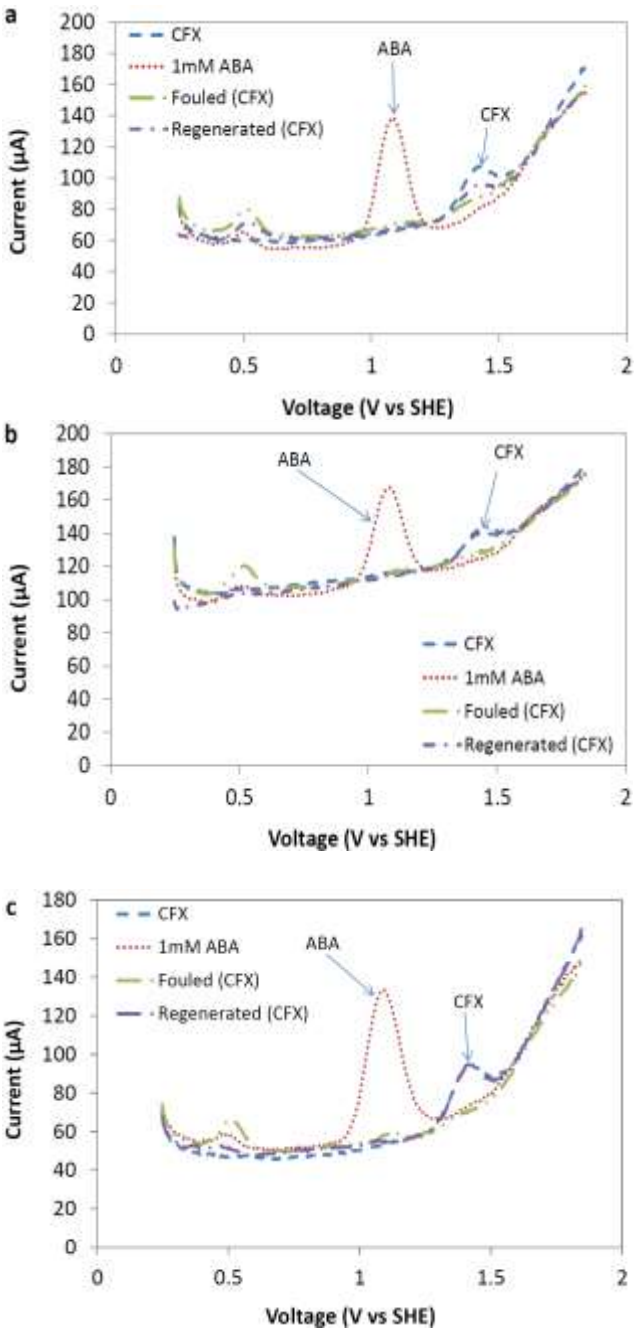

Figure 3-6. DPV curves before fouling (25 µM CFX), fouling with 1mM ABA, after fouling (25 µM CFX), and after cleaning (25 µM CFX): (a) with cathodic treatment (-1 V vs SHE for 60 sec) in 0.1 M KH_2PO_4 solution (b) with cathodic treatment (-1 V vs SHE for 60 sec) in 0.1 M NaCl solution and (c) with base wash (0.01 M NaOH).

3.5 Conclusions

In summary, a facile and novel porous-Nafion-MWCNT/BDD sensor was synthesized via a drop cast method and used to detect CFX with a LOD = 5 nM, using the DPV method. This LOD is the lowest reported in the literature for an electrochemical-based sensor. Nafion was used to enhance CFX adsorption by electrostatic attraction and a porous Nafion film was created to increase the surface area and permeability of the film to CFX. MWCNT increased the surface area as well as created -COOH adsorption sites for CFX, which increased sensor sensitivity. The sensor was able to detect CFX in the presence of different interfering non-target water constituents (e.g., Cl^-, SDBS, Ca^{2+}, humic acid, Amoxicillin, and various organic compounds), and was also able to detect CFX in a pH-adjusted wastewater effluent matrix with full sensitivity. The sensor was fouled with a high concentration of organic compounds, but was fully regenerated using cathodic treatment (-1.0 V/SHE for 60 sec in 0.1 M NaCl solution) or base wash (0.01 M NaOH).

3.6 Acknowledgements

We acknowledge University of Illinois at Chicago for funding. We acknowledge Dr. Yin Wang from University of Wisconsin-Milwaukee for performing the BET surface area measurements of MWCNT samples. We also acknowledge Alan Nicholls, Tad Daniel and Olivia Thompson (Research Resources Center, UIC) for the assistance with XPS, SEM and TEM analyses, respectively.

4. Fluorination of Boron-doped Diamond Film Electrodes for Minimization of Perchlorate Formation

4.1 Abstract

This research investigated the effects of surface fluorination on both rates of organic compound oxidation (phenol, terephthalic acid (TA)) and ClO_4^- formation at boron-doped diamond (BDD) film anodes at 22^o C. Different fluorination methods (i.e., electrochemical oxidation with perfluorooctanoic acid (PFOA), radio frequency plasma, and silanization) were used to incorporate fluorinated moieties on the BDD surface, which was confirmed by X-ray photoelectron spectroscopy (XPS). The silanization method was found to be the most effective fluorination method using a 1H, 1H, 2H, 2H-perfluorodecyltrichlorosilane precursor to form a self-assembled monolayer (SAM) on the oxygenated BDD surface. The ClO_4^- formation decreased from rates of 0.45 ± 0.03 mmol m^{-2} min^{-1} during 1 mM $NaClO_3$ oxidation and 0.28 ± 0.01 mmol m^{-2} min^{-1} during 10 mM NaCl oxidation on the BDD electrode to below detectable levels (< 0.12 μmoles m^{-2} min^{-1}) for the BDD electrode functionalized by a 1H, 1H, 2H, 2H-perfluorodecyltrichlorosilane SAM. These decreases in rates corresponded to 99.94% and 99.85% decreases in selectivity for ClO_4^- formation during the electrolysis of 10 mM NaCl and 1 mM $NaClO_3$ electrolytes, respectively. By contrast the oxidation rates of phenol were only reduced by 16.3% in the NaCl electrolyte and 61% in a nonreactive 0.1 M KH_2PO_4 electrolyte. Cyclic voltammetry with $Fe(CN)_6^{3-/4-}$ and $Fe^{3+/2+}$ redox couples indicated that the long fluorinated chains created a blocking layer on the BDD surface that inhibited charge transfer via steric

hindrance and hydrophobic effects. The surface coverage and thickness of the fluorinated films controlled the charge transfer rate, which was confirmed by estimates of film length using XPS. The aliphatic silanized electrode also showed very high stability under $OH^{\bullet}$ production. Perchlorate formation rates were below the detection limit (< 0.12 μmoles m^{-2} min^{-1}) for up to 10 consecutive $NaClO_3$ oxidation experiments.

4.2 Introduction

The electrochemical advanced oxidation process (EAOP) is emerging as an effective and versatile water and wastewater treatment technology [52,53,110,111]. Boron-doped diamond (BDD) film electrodes have been considered the best EAOP electrode due to their large potential window, high stability, resistance to fouling, and ability to generate high yields of hydroxyl radicals ($OH^{\bullet}$) via water oxidation [51,330]. BDD electrodes are efficient at oxidizing recalcitrant compounds in water through the production of $OH^{\bullet}$ and direct electron transfer (DET) reactions at the electrode surface [53,111–113,116,331,332]. The formation of $OH^{\bullet}$ is desirable because it is highly reactive with numerous organic compounds at diffusion-limited rates and does not leave a residual in treated water since it decays to form water [62].

However, the application of BDD electrodes to water and wastewater treatment is limited by the formation of ClO_4^- via the oxidation of Cl^- [188–190,333]. The formation of ClO_4^- is problematic because it has been linked to health risks, including disruption of the thyroid gland and carcinogenic potential [63,334]. The U.S. EPA has set a health advisory level for ClO_4^- at 0.15 μM for drinking water sources, and Massachusetts and California have set even lower standards of 0.02 and 0.06 μM, respectively [335,336]. Removal of Cl^- prior to electrochemical oxidation is not practical since deionization would decrease the conductivity of the solution, which increases the energy cost of electrochemical oxidation, and the Cl^- removal step would

add costs and complexities to the treatment process. Methods to limit ClO_4^- formation during EAOPs are necessary in order for them to develop into a feasible treatment technology in the water and wastewater treatment sectors.

The formation of ClO_4^- results from the step-wise oxidation of Cl^-, with ClO_x^- species as intermediates ($1 \leq x \leq 3$). The rate determining step during ClO_4^- formation is the oxidation of ClO_3^- [187,189], which was determined to be a two-step process, as shown in reactions (4-1) and (4-2) [195].

$$ClO_3^- \rightarrow ClO_3^{\bullet} + e^- \quad (4\text{-}1)$$

$$ClO_3^{\bullet} + OH^{\bullet} \rightarrow HClO_4 \quad (4\text{-}2)$$

The first step involves the formation of the chlorate radical ($ClO_3^{\bullet}$) from ClO_3^- via a DET reaction at the electrode surface, followed by the bimolecular reaction between $ClO_3^{\bullet}$ and $OH^{\bullet}$ to form $HClO_4$ [195].

The functional groups on the BDD surface have a significant effect on the rates of DET reactions [167]. Our previous work showed that the incorporation of ≡C-F and C–C_nF_{2n+1} ($1 \leq n \leq 7$) functional groups to the BDD surface via electrochemical oxidation of perfluorooctanoic acid (PFOA) was effective at lowering ClO_4^- formation by 96%, which was attributed to a combination of repulsive dipole-dipole interactions, steric hindrance, and reduced Van der Waals attraction caused by the blocking film and inhibited electron tunneling via reaction (4-1) [167]. In the same study, the fluorination of the BDD surface slightly enhanced the oxidation rates of aromatic non-ionic compounds (i.e., phenol, benzoquinone), but inhibited the rate of a model aliphatic ionic compound (i.e., oxalic acid) [167]. Several methods have been used to fluorinate BDD electrodes, including RF plasma in a gaseous CF_4 [162], F_2 [165] or XeF_2 [166] environment, electrochemical oxidation using PFOA [165,167], or silanization [337,338].

However, their application towards reducing electrode selectivity towards ClO_4^- formation while maintaining organic compound oxidation has only been investigated in our prior study [167].

To that end, this study investigates the effects of surface fluorination of BDD electrodes on rates for both ClO_4^- formation and model organic compound oxidation (i.e. phenol and terephthalic acid (TA)). Various fluorination methods were applied to BDD electrodes, including RF plasma with H_2 and CF_4, electrochemical oxidation of PFOA, and silanization with perfluorinated silanes (i.e., 1H,1H,2H,2H perfluorodecyltrichlorosilane and triethoxy(pentafluorophenyl)silane). X-ray photoelectron spectroscopy (XPS) was used to characterize the surface functional groups incorporated by these different surface modifications. Batch electrochemical oxidation experiments were performed to determine reaction rates as a function of different electrode functionalization methods. Cyclic voltammetry (CV) scans were performed with ionic redox couples (i.e., $Fe(CN)_6^{3-/4-}$ and $Fe^{3+/2+}$) to characterize the coverage of the film and effects it has on charge transfer. Stability of the surface modifications of selected modified BDD electrodes were also studied using anodic ageing tests.

4.3 Materials and Methods

4.3.1 Reagents. All chemicals were reagent-grade and obtained from Fisher Scientific and Sigma-Aldrich. Chemicals were received and were used without further modification. All solutions were prepared with Type I purity water (18.2 MΩ.cm at 21°C) from a Barnstead NANOpure system (Thermo Scientific).

4.3.2 Electrode Preparation. BDD nanocrystalline film electrodes (2 μm thick; resistivity = 0.05-0.1 Ω cm) were purchased from Advanced Diamond Technologies (Romeoville, IL). The BDD films were deposited on 2 mm thick, 1 cm^2 diameter Ta disk substrates by chemical vapor deposition (CVD), with a concentration of trimethyl borane of 750-12000 ppm in flowing CH_4

and at a temperature between 700 and 800°C. The BDD film electrodes were characterized by near-edge X-ray absorption fine structure (NEXAFS) spectroscopy, which showed they were comprised of high quality sp^3 diamond [339].

4.3.3 Electrode Fluorination Experiments. Three methods were used for fluorination of the BDD surface, including plasma fluorination, electrochemical oxidation, and silanization. Plasma fluorination of the BDD electrode was accomplished by reactive ion etching (RIE) with radio frequency (RF) plasma using a Surface Technology System 340 RIE. The BDD electrode was placed in the RIE chamber with H_2 flow of 100 standard cubic centimeters per minute (sccm) to remove oxygen termination from the BDD electrode (RF power = 100 W, time = 10 min, chamber pressure = 200 mTorr). This procedure was followed by fluorination of the BDD surface with CF_4 at 45 sccm (RF power = 50 W, time = 5 min, chamber pressure = 40 mTorr).

Fluorination via electrochemical oxidation was performed in a jacketed 100 mL single cell batch reactor at 22 °C using a recirculating water bath according to methods from a previously published study [165]. The BDD electrode was treated with H_2 RF plasma to eliminate oxygen termination followed by electrochemical oxidation in a formic acid (99%) solution containing 100 mM perfluorooctanoic acid (PFOA) and 100 mM $NaClO_4$ as a supporting electrolyte. Electrochemical experiments used a Gamry Reference 600 potentiostat/galvanostat (Warminster, PA) with a rotating disc electrode (RDE) experimental setup. Experiments were conducted using a three-electrode setup, with 0.35 cm^2 BDD as the working electrode, Pt wire (Alfa Aesar) as counter electrode, and a $Hg/Hg_2SO_4/K_2SO_4$ reference electrode. An anodic potential of 3.64 V vs standard hydrogen electrode (/SHE) was applied for 6.0 hours while rotating at 3000 rotations per minute (rpm) with a N_2 purge. The applied potential (3.64 V/SHE) was suitable for PFOA oxidation at BDD anodes, as it was reported that PFOA oxidation occurred at ≥ 3.0 V/SHE at

BDD electrodes [176]. After electrochemical oxidation the BDD surface was cleaned in ethanol and water for 5 minutes each and air-dried.

Fluorination of the BDD electrode by silanization was performed in an anaerobic glove box with a N_2 atmosphere and relative humidity of ~ 2%. First, the BDD electrode was electrochemically oxidized in 0.5 M $NaClO_4$ electrolyte with a current density of 0.1 mA cm^{-2} for 60 minutes to create a high density of –OH groups on the surface [154]. Then, the BDD electrode was immersed in a 10 vol% aliphatic (1H,1H,2H,2H perfluorodecyltrichlorosilane) or aromatic (triethoxy(pentafluorophenyl)silane) silane solution (1 mL) in 9 mL anhydrous toluene (99.8%) for 30 minutes. This method formed a self-assembled monolayer (SAM) on the BDD surface. After which, the electrode was removed from the solution, cleaned with toluene and DI water to remove non-bonded compounds, and dried under ambient conditions at room temperature.

4.3.4 Electrochemical Oxidation Experiments. All oxidation experiments were conducted at 22 ^{o}C and in a two-compartment, glass, jacketed cell, with a three-electrode RDE setup, as described previously. A Nafion N115 membrane (Ion Power, Inc., New Castle, DE) was used to separate anode and cathode compartments. The mass transfer rate of the organic compounds to the electrode surface was determined from the Levich equation [340,341]. All potentials are corrected for potential drop in solution (iR_s) and reported versus the SHE. Before each experiment, the BDD electrode was preconditioned in a 1 M $NaClO_4$ electrolyte for 20 minutes at a current density of 20 mA cm^{-2} to remove adsorbed species from the electrode surface. The RDE was rotated at 5000 rpm for all experiments except ClO_3^- oxidation, which was rotated at 3000 rpm. All experiments were performed in duplicate.

The organic compound (TA and phenol) oxidation experiments were performed in 100 mM $NaClO_4$ electrolyte with 0.1 mM TA or 1 mM phenol at a constant anodic potential of 3.25 V/SHE (current ~20 mA cm^{-2}). Phenol was selected as a model neutrally charged organic contaminant, and TA was chosen as a probe compound for $OH^{\bullet}$ formation [342]. To determine the ClO_4^- formation rates from ClO_3^-, oxidation experiments were performed in a 10 mM KH_2PO_4 solution containing 1 mM $NaClO_3$ and at a constant anodic potential of 3.76 V/SHE. Chloride oxidation (10 mM), in the presence and absence of 1 mM phenol was conducted under constant current conditions (10 mA cm^{-2}), which yielded an anodic potential between 3.5 and 3.6 V/SHE and 3.9 and 4.1 V/SHE for the oxygenated and aliphatic silanized BDD electrodes, respectively. Free chlorine (Cl_2), ClO_3^-, and ClO_4^- formation were all monitored during experiments containing NaCl.

4.3.5 Electrode Ageing Experiments. Electrode ageing experiments were conducted for PFOA-modified BDD electrodes at 22^o C. The PFOA-modified BDD electrode was aged in a 1.0 M $NaClO_4$ electrolyte to an applied charge of 100 mAh cm^{-2} (i.e., 10 mA cm^{-2} for 10 hours). The aliphatic silanized-modified BDD electrode was aged by conducting several consecutive 2 hr ClO_3^- oxidation experiments, where the total applied charge was ~ 55 mAh cm^{-2}.

The following abbreviated sample names for the electrodes will be used throughout the manuscript from this point forward: unmodified oxygen terminated electrode = BDD-O; plasma fluorinated BDD = BDDF-plasma; fluorinated BDD by PFOA oxidation = BDDF-PFOA; aliphatic silanized BDD = BDDF-aliphatic; aromatic silanized BDD = BDDF-aromatic; aged BDDF-PFOA = BDDF-PFOA-aged; and aged BDDF-aliphatic = BDDF-aliphatic-aged.

4.3.6 Electrochemical Characterization Methods. CV scans were performed with two different ionic redox couples (5mM $Fe(CN)_6^{3-/4-}$ and 5 mM $Fe^{3+/2+}$) to assess the effects of dipole-dipole

interactions between the redox couples and the surface functional groups on charge transfer at the BDD electrode surface and to investigate film surface coverage. The charge transfer of these redox couples is very sensitive to surface modifications [343–345]. CV experiments were conducted in a 100 mM $NaClO_4$ background electrolyte for $Fe(CN)_6^{3-/4-}$ and a 100 mM $HClO_4$ background electrolyte for $Fe^{3+/2+}$. The potential was swept at a scan rate of 100 mV s^{-1}.

4.3.7 Analytical Methods. Removal and formation rates were determined analytically by measuring the disappearance and formation of constituents with time. All errors reported on rate constants represent 95% confidence intervals obtained by simultaneous regression of concentration versus time profiles of duplicate experiments. Concentrations of Cl^-, ClO_3^- and ClO_4^- were determined by ion chromatography (Dionex ICS-2100; Dionex Ion Pac AS16 column; KOH eluent; 1.2 mL min^{-1} flow rate). Free available chlorine was measured by Hach method 8021 (USEPA *N*,*N*-diethyl-*p*-phenylenediamine (DPD) method) [346]. Concentrations of phenol and TA were measured using a Shimadzu UFLC XR HPLC with a Phenomenex Kinetex® 5 μm C18 column and a photodiode array detector (PDA) (Nexera X2, Shimadzu) (190nm-300nm). HPLC with a fluorescent detector (RF-20A, Shimadzu) was used for 2-hydroxyterephthalic acid (HTA) quantification (λ_{ex} = 315 nm and λ_{em} = 435 nm). For TA and HTA measurement the mobile phase was 60:40 mixture of methanol and 0.1% formic acid in DI water at a flow rate of 1.0 mL min^{-1}. For phenol measurement the mobile phase was a 70:30 mixture of methanol to DI water at a flow rate of 0.5 mL min^{-1}. For analysis, the PDA detector was set to 254 nm for phenol and TA. XPS measurements were performed with a Kratos Axis-165 at the Research Resource Center at the University of Illinois at Chicago. The peaks were assigned according to literature values [347–349].

4.3.8 Quantum Mechanical Simulations. Optimized structures for the fluorinated functional groups were determined using density functional theory (DFT) simulations, which were performed using Gaussian 16 software [350]. Simulations utilized the reactive site model, where a 10-carbon atom cluster was used to represent the BDD surface [311,351]. Unrestricted spin, all-electron calculations were calculated using the 6-31G+(d) basis set for geometry optimization and energy calculations. A scale factor of 0.9806 was used to correct for known systematic errors involving this basis set [352]. The gradient corrected Becke, three-parameter, Lee−Yang−Parr (B3LYP) functional was used for exchange and correlation. Implicit water solvation was incorporated using the SMD model [353].

4.4 Results and Discussion

4.4.1 Physical Characterization. The functionalized BDD electrodes were characterized by XPS to determine their surface termination (Figure 4-1). A prominent F 1s peak was observed at 688 eV for all electrodes after fluorination, which confirmed the presence of fluorine groups on the BDD surface (Figure 4-1). The F 1s and Si 2p peaks were observed at 688 and 102 eV, respectively, confirming effective silanization for the BDDF-aromatic and BDDF-aliphatic electrodes (Figure 4-1d and 4-1e).

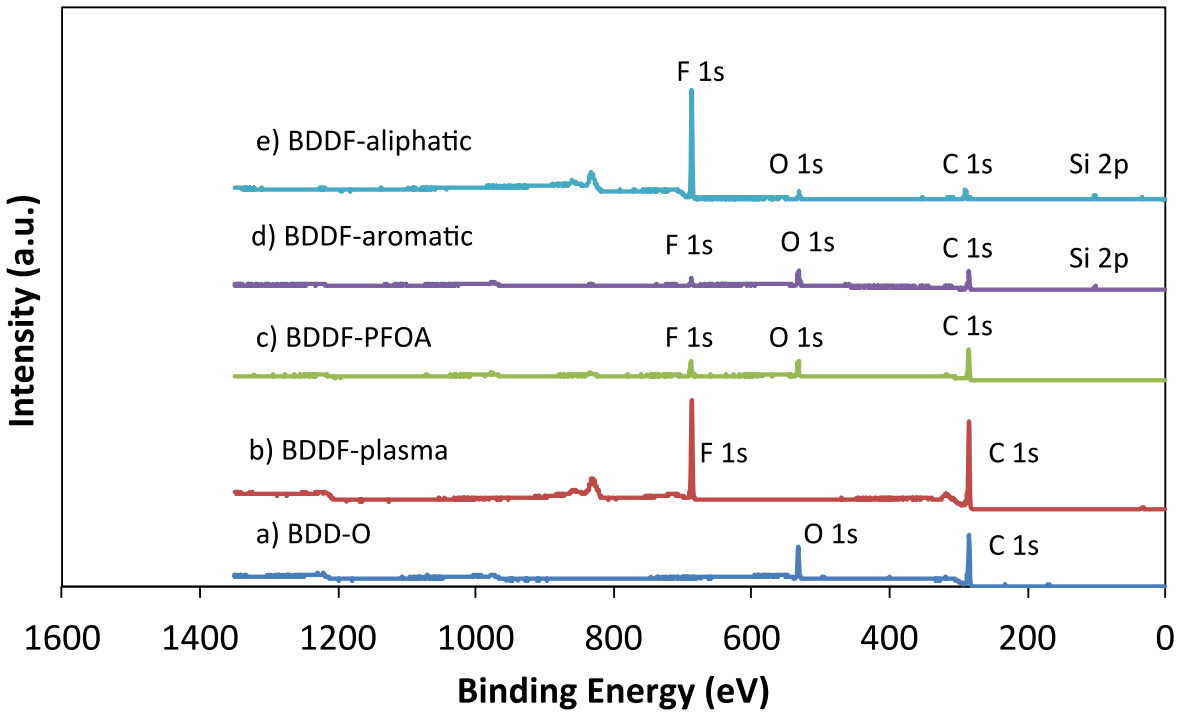

Figure 4-1. XPS spectra of a) BDD-O b) BDDF-plasma, c) BDDF-PFOA, d) BDDF-aromatic and e) BDDF-aliphatic

The deconvoluted results for the C 1s XPS spectra of the fluorinated electrodes are provided in the Appendix B (Section S-4-2 and Figure S-4-1), and the atomic concentrations of C, O, F, and Si are summarized in Table 4-1.

Table 4-1. Atomic Concentrations of C, O, F, and Si determined by XPS for different surface modifications (values given in atomic percent).

Electrode	C (%)	O (%)	F (%)	Si (%)
BDD-O	82.5	17.5	-	-
BDDF-plasma	76.3	-	23.7	-
BDDF-PFOA	76.2	15.2	8.60	-
BDDF-aromatic	66.2	25.7	6.20	1.88
BDDF-aliphatic	31.5	5.40	59.3	3.80
BDDF-PFOA-aged	75.8	15.4	8.80	-
BDDF-aliphatic-aged	32.2	6.49	57.4	3.91

Table 4-2. Deconvoluted XPS results for C 1s spectra for BDD-O, BDDF-plasma, BDDF-PFOA, BDDF-aliphatic, BDDF-aromatic, BDDF-PFOA-aged, and BDDF-aliphatic-aged electrodes (values given in atomic percent). Functional groups: C1 (284.5 eV): =C=C=; C2 (285.3±0.2 eV): ≡C-C≡; C3 (286.3±0.3 eV): ≡C-OH; C4 (287.0±0.1 eV): =C=O; C5 (287.6±0.04 eV): ≡C-F; C6 (288.5±0.2 eV): -COOH; C7 (290.5±0.3 eV): $=CF_2$; C8 (292.8±0.5 eV): $-CF_3$.

Electrode	Functional Groups (Atomic %)								
	C1	C2	C3	C4	C5	C6	C7	C8	$CF:CF_2:CF_3$
BDD-O	51.2	25.1	11.1	9.90	-	2.70	-	-	0:0:0
BDDF-plasma	37.0	54.7	-	-	4.32	-	2.81	1.17	3.7:2.4:1.0
BDDF-PFOA	94.0	-	-	1.66	-	1.29	2.16	0.85	0:2.6:1.0
BDDF-aromatic	71.5	9.34	7.34	-	9.06	2.76	-	-	9.1:0:0
BDDF-aliphatic	12.9	17.3	-	-	-	-	62.2	7.53	0:8.3:1
BDDF-PFOA-aged	94.2	-	-	1.52	-	1.03	2.33	0.92	0:2.5:1
BDDF-aliphatic-aged	13.6	17.6	-	-	-	-	61.6	7.20	0:8.6:1

The percentages of F were 0.00, 23.7, 8.60, 6.20, and 59.3 for the BDD-O, BDDF-plasma, BDDF-PFOA, BDDF-aromatic, and BDDF-aliphatic electrodes, respectively. Peak assignments

for the deconvoluted C 1s spectrum (Appendix B, Section S-4-2 and Figure S-4-1) were chosen based on literature values [40-42, 48], and the data are summarized in Table 4-2. The peaks have been assigned as follows: C1: =C=C=; C2: ≡C-C≡; C3: ≡C-OH; C4: =C=O; C5: ≡C-F; C6: -COOH; C7: $=CF_2$; C8: $-CF_3$.

The XPS results of the electrodes can provide insights into the effectiveness of the fluorination methods. BDD-O electrode contained 17.5% surficial oxygen and oxygenated functional groups consisted of ≡C-OH (11.1%), =C=O (9.90%), and -COOH (2.70%), where percentages were determined from the C 1s spectra (Figure S-4-1a and Table 4-2). The presence of these oxygenated carbon species were attributed to the oxidation of the BDD surface by air [139] and during the anodic pretreatment [151]. The BDDF-plasma electrode did not contain detectable oxygenated carbon species (Figure S-4-1b), nor a detectable O 1s peak in the survey scan (Figure 4-1 and Table 4-1), which confirmed that the H_2 RF plasma pretreatment was able to remove oxygen from the BDD-O surface. However, the BDDF-plasma electrode contained a mixture of ≡CF (4.32%), $=CF_2$ (2.81%), and $–CF_3$ (1.17%) groups (Figure S-4-1b and Table 4-2), which yielded a $CF:CF_2:CF_3$ molar ratio of 3.7:2.4:1 (Table 4-2). These results indicated that the attachment of free radicals (e.g., $CF^{\bullet}$, $CF_2^{\bullet}$, $CF_3^{\bullet}$, $F^{\bullet}$) occurred during the CF_4 plasma treatment [354]. The BDDF-PFOA electrode showed 15.2% surficial oxygen content, which may have formed during the synthesis process, (i.e., electrochemical oxidation of formic acid and water) [355]. The $CF:CF_2:CF_3$ ratio for the BDDF-PFOA electrode was 0:2.6:1 (Table 4-2). This ratio suggested a mixture of $–C_3F_7$ and $–C_4F_9$ groups were deposited on the electrode surface via PFOA oxidation (Figure S-4-1c and Table 4-2) [356,357]. The BDDF-aromatic electrode contained a high surficial content of oxygen (25.7%), which is attributed to a low attachment of triethoxy(pentafluorophenyl)silane molecules to the pre-oxidized surface. A more complete

silanization reaction would block the detection of the O content by XPS, as was the case for the BDDF-aliphatic (Table 4-1). The Si:CF ratio for the BDDF-aromatic was 1:4.8 which compared well to that of an aromatic silane molecule (Si:CF = 1:5) (Figure S-4-1e and Table S-4-1 (Section S-4-2)). The BDDF-aliphatic electrode had the highest F content (F = 59.3%) and low oxygen content (5.4%), indicating effective fluorination by the silanization method. The low oxygen content detected by XPS is due to high surface area coverage by the aliphatic silane SAM, since XPS is a surface characterization technique. The XPS data for the BDDF-aliphatic electrode provided ratios of F:Si = 15.6 and F:C = 1.88, which compared well to atomic ratios for a 1H,1H,2H,2H perfluorodecyltrichlorosilane molecule (F:Si = 17, F:C = 1.7) (Figure S-4-1d and Table S-4-1). The calculated atomic ratio for Si:CF_2:CF_3 was 0.51:8.3:1 on the BDDF-aliphatic electrode surface, which was also similar to that for a 1H,1H,2H,2H perfluorodecyltrichlorosilane molecule (1:7:1), confirming effective silanization of the electrode (Table S-4-1 and Table 4-2).

4.4.2 Electrochemical Characterization. The CV data was interpreted by considering the surface modifications as non-conductive blocking layers, which would inhibit electron transfer rates. The standard heterogeneous rate constant for electron transfer (k^o (m s^{-1})) can be expressed according to equation (4-3):

$$k^o = K\nu\kappa(x)\exp(\frac{-E_a^o}{RT}) \tag{4-3}$$

where K is the precursor equilibrium constant (cm), ν is the nuclear frequency factor (s^{-1}), E_a^o is the activation energy of the reaction at the standard reduction potential (kJ mol^{-1}), and R and T have their usual meanings. The parameter $\kappa(x)$ is the electronic transmission coefficient, which is related to the probability of electron tunneling, and is given by equation (4-4).

$$\kappa(x) = \kappa^o \exp(-\beta x) \tag{4-4}$$

where κ^o is the electronic transmission coefficient at the electrode surface and β is a distance factor for extended charge transfer [340]. Based on equation 4-4, the value of k^o is a function of the length of the blocking layer.

A summary of the CV data for the $Fe(CN)_6^{3-/4-}$ and $Fe^{3+/2+}$ redox couples for all electrodes is provided in the Appendix B (Table S-4-2 (Section S-4-3)) and that for the BDD-aliphatic electrode is shown in Figure 4-2. The CV results were similar for all the fluorinated electrodes, except BDDF-plasma. The BDDF-plasma sample showed a larger peak separation and decreased peak currents for the $Fe(CN)_6^{3-/4-}$ redox couple, and a smaller peak separation and increased peak currents for the $Fe^{2+/3+}$ redox couple compared to the BDD-O electrode (Figure S-4-2a,b and Table S-4-2). The charge dependent results of the redox couples are attributed to the electrostatic repulsion/attraction between the ionic redox couples and the net negative charge of the electronegative F atoms on the modified electrode surface (Figure S-4-2a,b) [167,358]. These results also indicated that extended charge transfer was not an important factor for the BDDF-plasma electrode, as the fluorinated functional groups (≡CF, $=CF_2$, and $-CF_3$) were only ~ 1.5-2.0 Å in length and thus would not greatly affect κ.

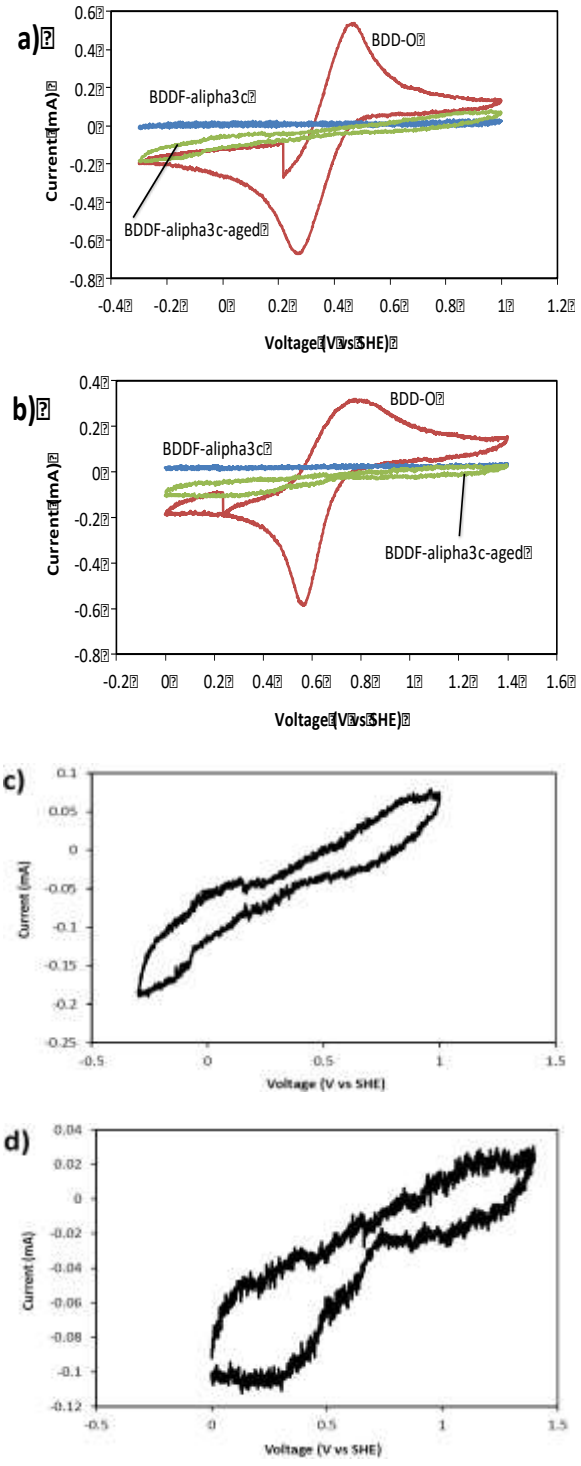

Figure 4-2. CV scans of 5 mM a) $Fe(CN)_6^{3-/4-}$ and b) $Fe^{3+/2+}$ for BDD-O, BDDF-aliphatic and BDDF-aliphatic-aged; c) BDDF-aliphatic-aged: 5mM $Fe(CN)_6^{3-/4-}$; d) BDDF-aliphatic-aged: 5 mM $Fe^{3+/2+}$ in 100mM $NaClO_4$ (for $Fe(CN)_6^{3-/4-}$) and 100mM $HClO_4$ (for $Fe^{3+/2+}$).

CV results for the BDDF-PFOA, BDDF-aliphatic, and BDDF-aromatic electrodes showed increases in peak separations for both redox couples, which was attributed to a reduction in κ due to an increased separation distance between the redox couples and the BDD surface caused by the surface modifications (Appendix B (Section S-4-3), Figure S-4-2c-f, Figure 4-2a,b, and Table S-4-2). These results indicated that the fluorinated-functional groups were capable of blocking the electrode surface.

The BDDF-aliphatic electrode showed complete blockage of both redox couples, indicating a low pinhole blocking layer was formed. The thickness of the blocking layer was estimated at approximately 1.5 nm by DFT calculations, which is an appropriate thickness to prevent electron tunneling [340]. The BDDF-PFOA and BDDF-aromatic electrodes showed significant but not complete blockage of both redox couples, which is attributed to the lack of complete surface coverage and a thinner blocking film. The BDDF-PFOA film thickness was estimated by DFT at ~ 0.62 nm, assuming a $-C_4F_9$ structure determined from XPS data; and the BDDF-aromatic film thickness was estimated by DFT at ~ 0.61 nm. The optimized structures determined by DFT are provided in the Appendix B (Figure S-4-3 (Section S-4-4)). The similar blocking film thicknesses also correlate with similar peak separations for the two electrodes with both redox couples (Appendix B (Section S-4-3), Table S-4-2), supporting the blocking film model proposed in equations 4-3 and 4-4. However, since a relatively high O content was detected on both electrodes, complete surface coverages of the blocking films were not obtained, indicating that the oxygenated surface groups on the BDD surface also influenced charge transfer and reactivity of the electrodes.

4.4.3 Perchlorate Formation Rates. The effect of the different fluorination methods on ClO_4^- formation rates was assessed by the oxidation of 1mM ClO_3^- in a 10 mM KH_2PO_4 supporting

electrolyte and at a constant anodic potential of 3.76 V/SHE (Figure 4-3). The ClO_4^- formation rate measured on the BDDF-plasma (rate = 0.45 ± 0.07 mmole m^{-2} min^{-1}) and BDDF-aromatic electrodes (rate = 0.42 ± 0.005 mmole m^{-2} min^{-1}) were not significantly different from that measured on the non-fluorinated BDD-O electrode (rate = 0.45 ± 0.03 mmole m^{-2} min^{-1}) (Figure 4-3). The BDDF-plasma electrode contained a high surficial content of F (23.7%) (Figure 4-1 and Table 4-1), but the lack of an effect on the ClO_4^- formation rate was likely due to the very short length of the fluorinated groups formed by plasma fluorination (e.g., ≡CF, $=CF_2$, and $-CF_3$), which is consistent with CV results. These $–CF_x$ groups did not block ClO_3^- from the electrode surface and therefore did not inhibit the DET reaction (equation 4-1). Furthermore, dipole-dipole interactions between ClO_3^- and the $–CF_x$ groups were not significant at the high anodic potential of the experiments (3.76 V/SHE). This result is contrary to CV scans conducted with the anionic redox couple (Figure S-4-2a). However, CV scans were conducted at low applied potentials (± 200 mV versus OCP) and with a 0.1 M supporting electrolyte, both of which would limit the effect of the electric field. The BDDF-aromatic electrode did not inhibit ClO_4^- formation due to the low surface coverage of aromatic silane groups, as determined by XPS (Figure S-4-1e and Table 4-1). The low surface coverage for BDDF-aromatic may be due to a slower hydrolysation rate of the ethoxy groups of triethoxy(pentafluorophenyl)silane compared to chloride groups of 1H,1H,2H,2H perfluorodecyltrichlorosilane, leading to ineffective silanization and thus detection of high O content by XPS [358].

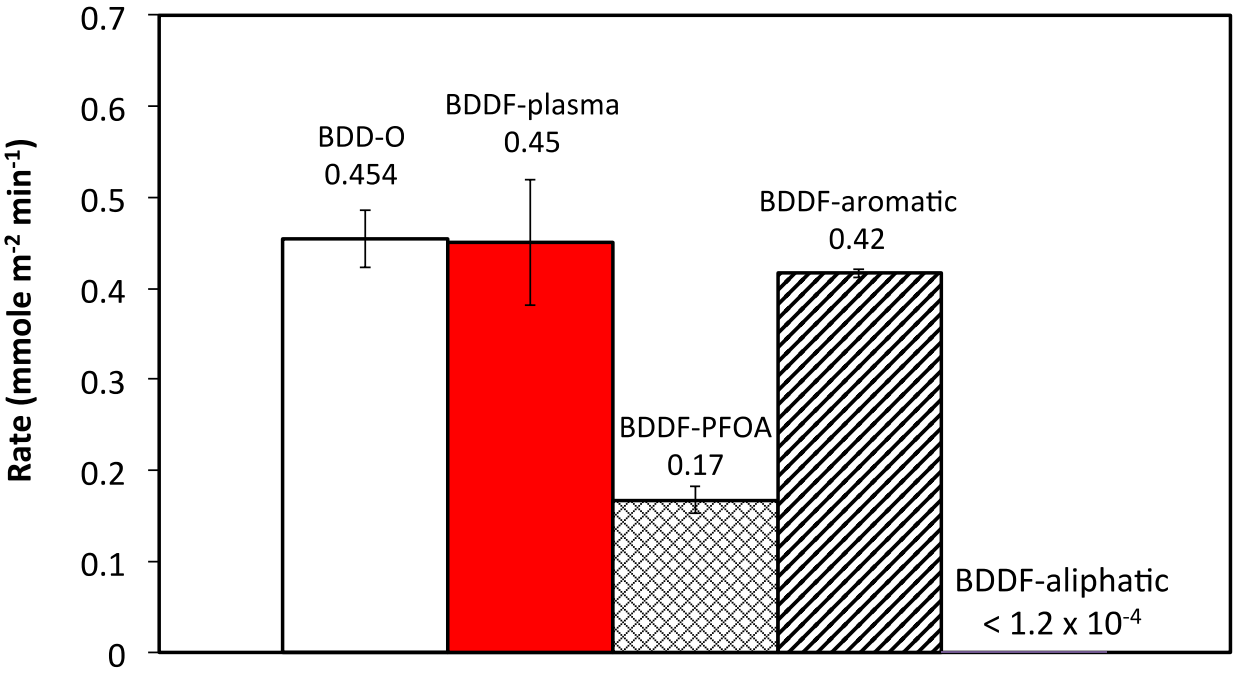

Figure 4-3. Perchlorate formation rates on BDD-O, BDDF-plasma, BDDF-PFOA, BDDF-aromatic, and BDDF-aliphatic. The data for perchlorate formation were normalized according to corresponding BDD-O as different oxygenated BDD electrodes (BDD-O) were used for each of the different modifications [$BDDF_{i\text{-}normalized} = (BDDF_{i\text{-}experimental}/BDD\text{-}O_{i\text{-}experimental})*BDD\text{-}O$, where i = aliphatic, aromatic, PFOA or plasma].

The ClO_4^- formation rates decreased for the BDDF-PFOA electrode by 63.2% (Figure 4-3) which is significantly more than the BDDF-aromatic electrode. Since the estimated film thicknesses of the two electrodes were similar, the differences in the ClO_4^- formation rates were attributed to differences in surface coverages of the fluorinated films and the presence of oxygenated functional groups on the non-fluorinated BDD surface. Previous work has shown that the ClO_4^- formation rate is highly dependent on the oxygenated functional groups present on the BDD surface [167,195]. It is proposed that the higher content of oxygen on the BDDF-aromatic electrode (O = 25.7%) compared to the BDDF-PFOA (O = 15.2%) was responsible for

the higher ClO_4^- formation rate [167]. However, the exact oxygenated functional groups that affect perchlorate formation have not been determined and require further experimental investigation.

The ClO_4^- formation rate decreased for the BDDF-aliphatic electrode by > 99.96% (Figure 4-3). The ClO_4^- concentration was less than the detection limit (10 nM (1 ppb)) at the conclusion of the 2-hr experiment for the BDDF-aliphatic electrode, which yielded a formation rate < 0.12 μmoles m^{-2} min^{-1}. The detection limit is lower than the U.S. EPA health advisory level (150 nM) and enforceable standards set by the states of Massachusetts (20 nM) and California (60 nM). The decrease in the ClO_4^- formation rate was attributed to blocking of the electrode surface by the surface fluorinated groups, which increased the distance of approach of ClO_3^- to the electrode surface and thus decreased the probability of electron tunneling via reaction 4-1. The lower ClO_4^- formation rate on the BDDF-aliphatic electrode compared to the BDDF-PFOA electrode is attributed to the higher surface coverage of fluorinated groups (Figure 4-1 and Table 4-1) and the thicker blocking film. The above results indicated that the aliphatic silanization was the most effective fluorination method for the BDD electrode.

In order to mimic more realistic treatment conditions, the ClO_4^- formation rates for BDD-O and BDDF-aliphatic electrodes were also measured during the oxidation of a 10 mM NaCl electrolyte in the presence and absence of 1 mM phenol (Figure 4-4 and Figure S-4-4 (Section S-4-5)). The ClO_4^- formation rates with the BDD-O electrode were 0.28 ± 0.01 mmoles m^{-2} min^{-1} in the absence of phenol and 0.22 ± 0.02 mmoles m^{-2} min^{-1} in the presence of 1.0 mM phenol. These results indicated that the presence of organic compounds limited ClO_4^- formation rates, which was caused by both competition for DET sites at the electrode surface and $OH^\bullet$ [196]. The BDDF-aliphatic electrode did not form detectable concentrations of ClO_4^- (< 10 nM (1 ppb)) in

any of the experiments. The Cl^- oxidation rate and ClO_3^- and ClO_4^- formation rates were calculated as 3.51 ± 0.03, 0.95 ± 0.01, and < 1.2 x 10^{-4} mmoles m^{-2} min^{-1}, respectively, in the absence of phenol. The Cl^- oxidation rate and ClO_3^- and ClO_4^- formation rates were also determined as 2.19 ± 0.02, 0.59 ± 0.01, and < 1.2 x 10^{-4} mmoles m^{-2} min^{-1}, respectively, in the presence of phenol. The Cl^- oxidation rate decreased by 71.5% in the 10 mM Cl^- solution, and ClO_3^- and ClO_4^- formation rates decreased by 87.4% and > 99.95%, respectively, as a result of silanization. Similar results were observed for the 10 mM Cl^-/1 mM phenol solutions, where the Cl^- oxidation rate decreased by 78.6% and the ClO_3^- and ClO_4^- formation rates decreased by 90.7% and > 99.94%, respectively, after silanization. Free chlorine concentration was lower after aliphatic silanization than that with BDD-O. The free chlorine concentration was also lower in the presence of phenol compared to the absence of phenol for both the BDD-O and BDDF-aliphatic electrodes.

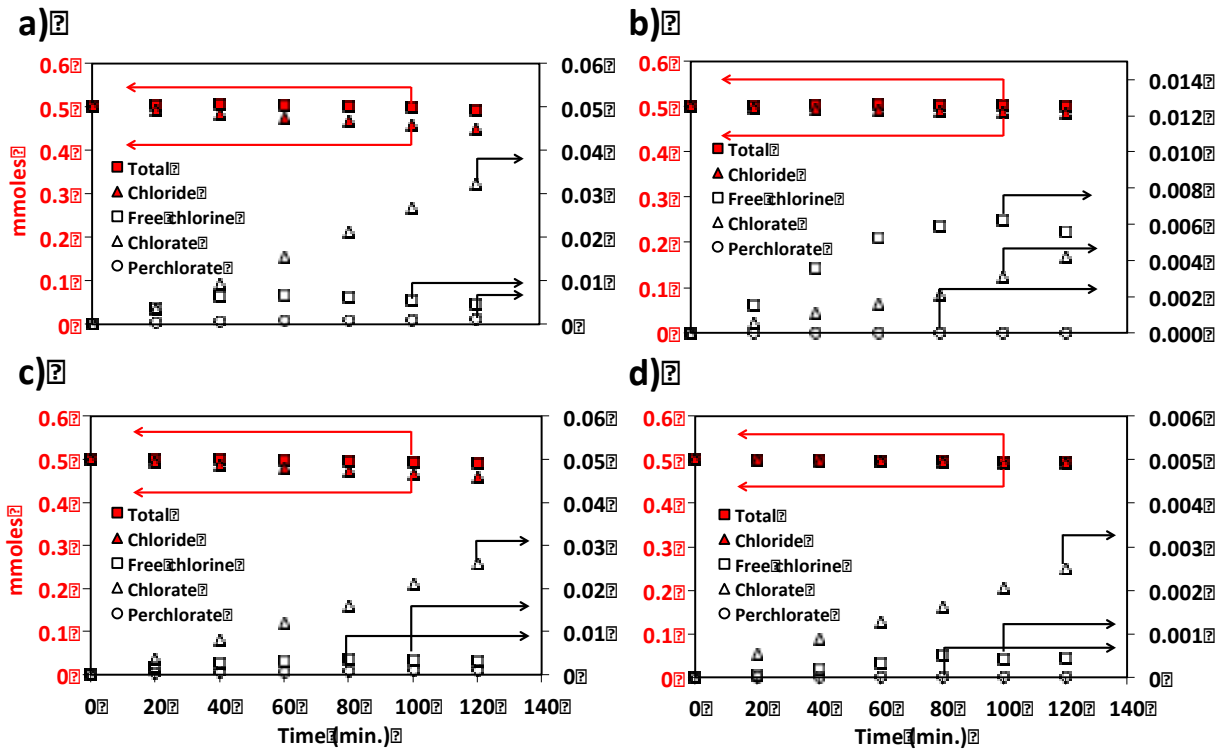

Figure 4-4. Total, free chlorine, chlorate, perchlorate and chloride mole balances for a) BDD-O without phenol, b) BDDF-aliphatic without phenol, c) BDD-O with 1 mM phenol and d) BDDF-aliphatic with 1 mM phenol. Experimental parameters: Supporting electrolyte = 10 mM NaCl; current density = 10 mA cm^{-2}; T = 22° C.

The decrease in the ClO_x^- formation rates for the BDDF-aliphatic electrode was once again attributed to the blocking of the electrode surface by the long fluorinated carbon chains, which prevented DET reactions from occurring. All Cl-species except for ClO_3^- are capable of reacting with $OH^\bullet$ with diffusion-limited rate constants (i.e., $k_{Cl^-,OH^\cdot}$ = 4.3 x 10^9, $k_{OCl^-,OH^\cdot}$ = 8.8 x 10^9, and $k_{ClO_2^-,OH^\cdot}$ = 6.6 x 10^9 M^{-1} s^{-1}), which can explain the residual reactivity of these species observed on the BDDF-aliphatic electrode. The decrease in the formation of ClO_x^- species in the presence of phenol may be due to either reactions between phenol and ClO_x^- species or competition for $OH^\bullet$ and reaction sites at the electrode surface. The Cl mole balances (total moles of Cl species detected / moles of oxidized Cl^- * 100) for the duplicate experiments were determined as 109 + 15% for BDD-O and 124 + 12% for the BDDF-aliphatic in the absence of

phenol, and 87.7 + 9.5% for BDD-O and 63 + 8.8% for BDDF-aliphatic in the presence of phenol. The results without phenol confirmed that the total moles of Cl were accounted for during the experiments (Figure 4-4a,b). However, in the presence of phenol the total moles of Cl were not accounted for (Figure 4-4c,d), indicating the possible formation of chlorinated organic compounds, which is a known problem during electrochemical oxidation [359]. However, these compounds should be mineralized at extended oxidation times [360], and warrants more study.

The average current efficiency for ClO_4^- formation from Cl^- on the BDD-O electrode was calculated as 3.57 ± 0.13% without phenol, and 2.83 ± 0.09% in the presence of 1.0 mM phenol. The current efficiency for the ClO_4^- formation from Cl^- on the BDDF-aliphatic electrode was calculated as < 0.002% based on the IC detection limit (10 nM). These results translate to a 1,415- to 1,785-fold decrease in selectivity for ClO_4^- formation on the BDDF-aliphatic electrode relative to the BDD-O electrode. These results demonstrated the extreme promise of the BDDF-aliphatic electrode for water treatment applications, where the formation of ClO_4^- is unacceptable.

4.4.4 Organic Compound Oxidation. Phenol and TA were used to show the effect of fluorination on organic compound oxidation rates as they both undergo reactions with $OH^\bullet$ [274]. Only BDDF-PFOA and BDDF-aliphatic electrodes were investigated for organic compound oxidation, since their respective fluorination methods were shown to limit ClO_4^- formation (Figure 4-3). The mass transfer rates of phenol and TA were calculated as 7.99 and 0.463 mmole m^{-2} min^{-1}, respectively (Appendix B, Section S-4-1). The experimental reaction rates for phenol (5.99 ± 0.23 mmole m^{-2} min^{-1}) and TA (0.20 ± 0.011 mmole m^{-2} min^{-1}) (Table 4-3) were lower but comparable to the calculated mass transfer rate values, indicating the bulk oxidation of phenol and TA were under mixed kinetic-mass transfer control (Appendix B, Section S-4-1).

Table 4-3. Phenol and TA Oxidation Rates for Different Fluorinated Electrodes**.** The data for organic compound oxidation are normalized according to BDD-O as different oxygenated BDD electrodes (BDD-O) were used for each of the different modifications.

Electrode	**Phenol oxidation rate (mmoles m^{-2} min^{-1})**	**TA oxidation rate (mmoles m^{-2} min^{-1})**
BDD-O	5.99 ± 0.23	0.20 ± 0.011
BDDF-PFOA	7.57 ± 0.57	0.24 ± 0.012
BDDF-PFOA-aged	7.14 ± 0.43	0.23 ± 0.024
BDDF-aliphatic	2.33 ± 0.07	0.09 ± 0.012
BDDF-aliphatic-aged	3.99 ± 0.09	0.15 ± 0.023

Phenol and TA oxidation rates with BDD-O, BDDF-PFOA, and BDDF-aliphatic electrodes showed zero order kinetics (Figure S-4-5), and removal rates are summarized in Table 4-3. The reaction rates for phenol and TA increased by 26.4 ± 4.2% and 20.0 ± 1.2%, respectively, on the BDDF-PFOA electrode relative to BDD-O, which may be due to the enhanced hydrophobic interaction (Table 4-3), which was also reported previously [167]. The rate for phenol oxidation on the BDDF-PFOA (7.57 ± 0.57 mmole m^{-2} min^{-1}) approached the mass transfer limit of 7.99 mmole m^{-2} min^{-1}.

Organic compound oxidation rates were also performed on BDDF-aliphatic electrode. The reaction rates for phenol and TA oxidation decreased by 61 ± 2.6 % and 55 ± 2.4%, respectively, on the BDDF-aliphatic electrode relative to BDD-O (Table 4-3), which was attributed to the blocking film that formed on the electrode surface by the fluorocarbon chains. The phenol oxidation rates in the presence of 10 mM Cl^- on BDDF-aliphatic decreased by only 16.3 ± 2.8%, indicating that ClO_x^- species likely enhanced phenol oxidation. However, contrary to ClO_4^- formation rates, complete inhibition of reactivity was not observed for the organic compounds, presumably due to the ability of phenol and TA to react with $OH^\bullet$ that diffused through the

fluorocarbon chains. The ratio of reaction rate to current density (mol A^{-1} min^{-1}) was calculated for phenol oxidation as 0.25 mol mA^{-1} min^{-1} on the BDD-O electrode and 0.54 mol A^{-1} min^{-1} on the BDDF-aliphatic electrode. For TA oxidation, values of 0.008 mol A^{-1} min^{-1} and 0.017 mol A^{-1} min^{-1} were determined on the BDD-O electrode and BDDF-aliphatic electrodes, respectively. These results indicated an increased apparent selectivity for TA oxidation of 2.1-fold and an increased apparent selectivity for phenol oxidation of 2.2-fold after aliphatic fluorination. By contrast, the current efficiency of ClO_4^- formation decreased from 1.36% on the BDD-O electrode to < 0.002% on the BDDF-aliphatic electrode (data from Figure 4-3), which translates to > 680-fold decrease. These results confirmed that the BDDF-aliphatic electrode effectively inhibited ClO_4^- formation while increasing the apparent selectivity towards organic compound oxidation. The similar enhancement factors for TA and phenol cited above, suggested that the decreased reaction rates were likely attributed to blocking of the electrode surface, which limited the surface area available for $OH^\bullet$ formation, hindered diffusion of $OH^\bullet$ through the film, and provided additional time for the self-decay of the $OH^\bullet$ concentration (self-decay rate constant = 5.5×10^6 M^{-1} s^{-1}). The $OH^\bullet$ also may react with the fluorinated films, which may compromise the film stability.

4.4.5 Electrode Stability. Electrode ageing experiments were only performed on BDDF-PFOA and BDDF-aliphatic electrodes. The BDDF-PFOA electrode was aged by applying a charge of 0.1Ah cm^{-2} in 1.0 M $NaClO_4$ (BDDF-PFOA-aged). The BDDF-PFOA-aged electrode was then tested for ClO_4^- formation to determine the stability of the electrode towards anodic conditions. The ClO_4^- formation rate on the BDDF-PFOA-aged electrode was similar to that measured on the BDDF-PFOA electrode (Figure S-4-6). The phenol and TA oxidation rates on the BDDF-PFOA-aged electrode were also similar to those on the BDDF-PFOA electrode (Table 4-3).

These results confirmed that the fluorination with PFOA was stable under anodic conditions. However, further ageing experiments were not performed since ClO_4^- formation on the BDDF-PFOA was already too high for environmental applications.

By contrast, ClO_4^- was not detected for the first 10 cycles of ageing for the BDDF-aliphatic electrode, and subsequent cycles yielded rates between 0.01 and 0.03 mmole m^{-2} min^{-1} (Figure 4-5). These results showed that the aliphatic silanization of BDD electrodes was highly effective at inhibiting ClO_4^- formation and was stable under anodic conditions that included DET and $OH^{\bullet}$ reactions. Our results are in line with previous reports that a (γ-aminopropyl) triethoxysilane-modified TiO_2 photocatalyst was stable and effective for the photocatalytic degradation of 2,4-DNP, which was supported by similar reactivity during 10 consecutive 2-hour oxidation experiments [361]. A representation of the aliphatic silane SAM on the BDD electrode is shown in the inset of Figure 4-5. The current efficiency for ClO_4^- formation on the BDD-O electrode was calculated as 0.84 ± 0.06%, and the current efficiency for the first 10 cycles of the BDDF-aliphatic electrode was calculated as < 0.002% based on the IC detection limit (10 nM). The average current efficiency for the BDDF-aliphatic-aged electrode increased to 0.29 ± 0.14% from cycle 11 to 16.

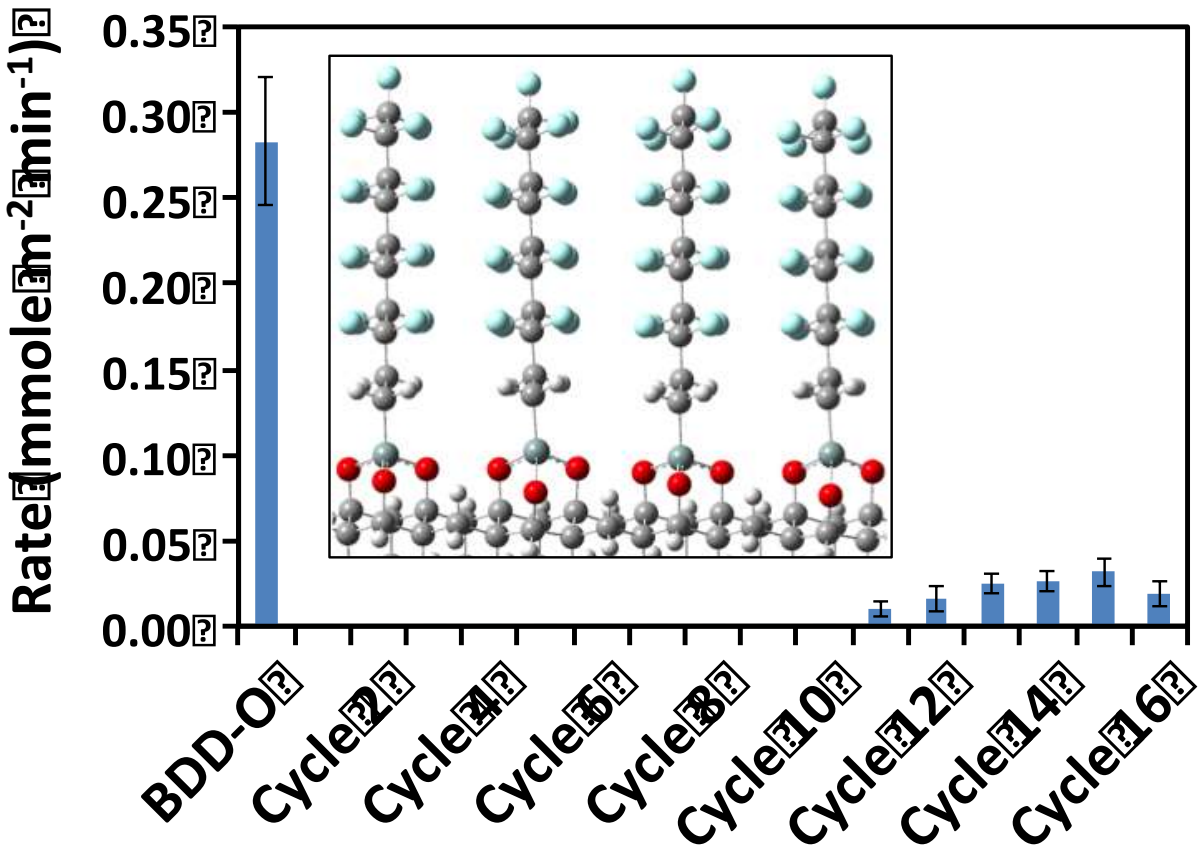

Figure 4-5. Perchlorate formation rates on BDD-O and BDDF-aliphatic (Cycle 1 – Cycle 16). Inset shows DFT calculated geometry of the BDDF-aliphatic electrode surface.

Organic compound oxidation rates were also measured on the BDDF-aliphatic-aged electrode after the completion of the 16 cycle ageing experiments. The inhibition of perchlorate formation after ageing remained high (93.6 ± 3.3%), whereas organic compound oxidation rates were only inhibited 33.4 ± 4.4% and 25 ± 3.8% for phenol and TA, respectively (Table 4-3). The ratio of reaction rate to current density (mol A^{-1} min^{-1}) was calculated for phenol oxidation as 0.54 mol A^{-1} min^{-1} on the BDDF-aliphatic electrode and 0.38 mol A^{-1} min^{-1} on the BDDF-aliphatic-aged electrode. For TA oxidation, values of 0.017 mol mA^{-1} min^{-1} on the BDDF-aliphatic electrode and 0.012 mol mA^{-1} min^{-1} on the BDDF-aliphatic-aged electrode were determined. The results indicated a decreased apparent selectivity of 1.4-fold for both phenol and

TA oxidation after ageing. However the apparent selectivity for the BDDF-aliphatic-aged electrode remained higher by 1.5-fold for both phenol and TA oxidation compared to BDD-O. By contrast, the current efficiency of ClO_4^- formation increased from < 0.002% on the BDDF-aliphatic electrode to 0.24% on the BDDF-aliphatic-aged electrode. However, the current efficiency of ClO_4^- formation remained 3.5-fold lower for BDDF-aliphatic-aged compared to BDD-O (Figure 4-5). These results confirmed that the aliphatic silanization of BDD electrodes was stable and effective at inhibiting ClO_4^- formation and maintained relatively high reactivity for organic compound oxidation under anodic conditions.

XPS analysis was also performed on the BDDF-aliphatic and BDDF-PFOA electrodes after ageing to determine the stability of the surface modifications. The XPS data showed that the atomic concentrations of C, O, F, and Si for BDDF-PFOA-aged and BDDF-aliphatic-aged were similar to those before ageing, which confirmed the relative stability of the BDDF-PFOA and BDDF-aliphatic electrodes against anodic ageing (Table 4-1, Table 4-2 and Figure S-4-1f,g). XPS data of the BDDF-aliphatic-aged electrode showed that F:Si = 14.7, F:C = 1.78, and $Si:CF_2:CF_3$ = 0.54:8.63:1, which were similar to the ratios determined for the freshly prepared BDDF-aliphatic electrode (Table S-4-1). These results confirmed a highly stable silane-functionalized BDD surface with respect to anodic polarization. However the increase in ClO_4^- formation after ageing may be due to defects that formed in the blocking film, which were not discernible by XPS analysis. The reactivity of the aliphatic silane towards DET reactions and attack by $OH^\bullet$ at the $–CH_x$ groups has not previously been investigated but warrants detailed study.

CV scans were also performed on both aged electrodes. The CV results for the BDDF-PFOA-aged electrode showed very little change relative to BDDF-PFOA in both the peak

currents and peak separations for both redox couples (Figure S-4-2c,d and Table S-4-2). CV scans for the BDDF-aliphatic-aged electrode also showed only a very small change in the peak currents and peak separations for both redox couples (Figure 4-2a-d and Table S-4-2). The CV scans on the BDDF-aliphatic-aged electrode did not show clear behavior indicative of pinhole formation, which produces an S-shaped CV curve (Figure 4-2b) [340]. Therefore, it was concluded that the size of the defect sites that formed in the BDDF-aliphatic-aged electrode were on the order of > 25 μm in size.

4.4.6 Mechanism. A schematic for a possible mechanism for the inhibition of ClO_4^- formation during the oxidation of organic compounds (e.g., phenol) on the BDDF-aliphatic electrode is shown in Figure 4-6. It is proposed that the SAM on the BDDF-aliphatic electrode can block access to ClO_x^- species ($0 \leq x \leq 3$) and organic compounds. However, the diffusion of $OH^\bullet$ through the SAM can result in the oxidation of Cl^- to ClO_3^- and the oxidation of organic compounds. The formation of ClO_3^- can occur through a $OH^\bullet$ mediated mechanism [362,363], as shown in reactions (4-5)-(4-9).

$$Cl^- + OH^\bullet \rightarrow HOCl^- \quad (4\text{-}5)$$

$$HOCl^- + OH^\bullet \rightarrow HOCl + OH^- \quad (4\text{-}6)$$

$$HOCl + OH^\bullet \rightarrow OCl^\bullet + H_2O \quad (4\text{-}7)$$

$$OCl^\bullet + OH^\bullet \rightarrow ClO_2^- + H^+ \quad (4\text{-}8)$$

$$ClO_2^- + OH^\bullet \rightarrow HClO_3 \quad (4\text{-}9)$$

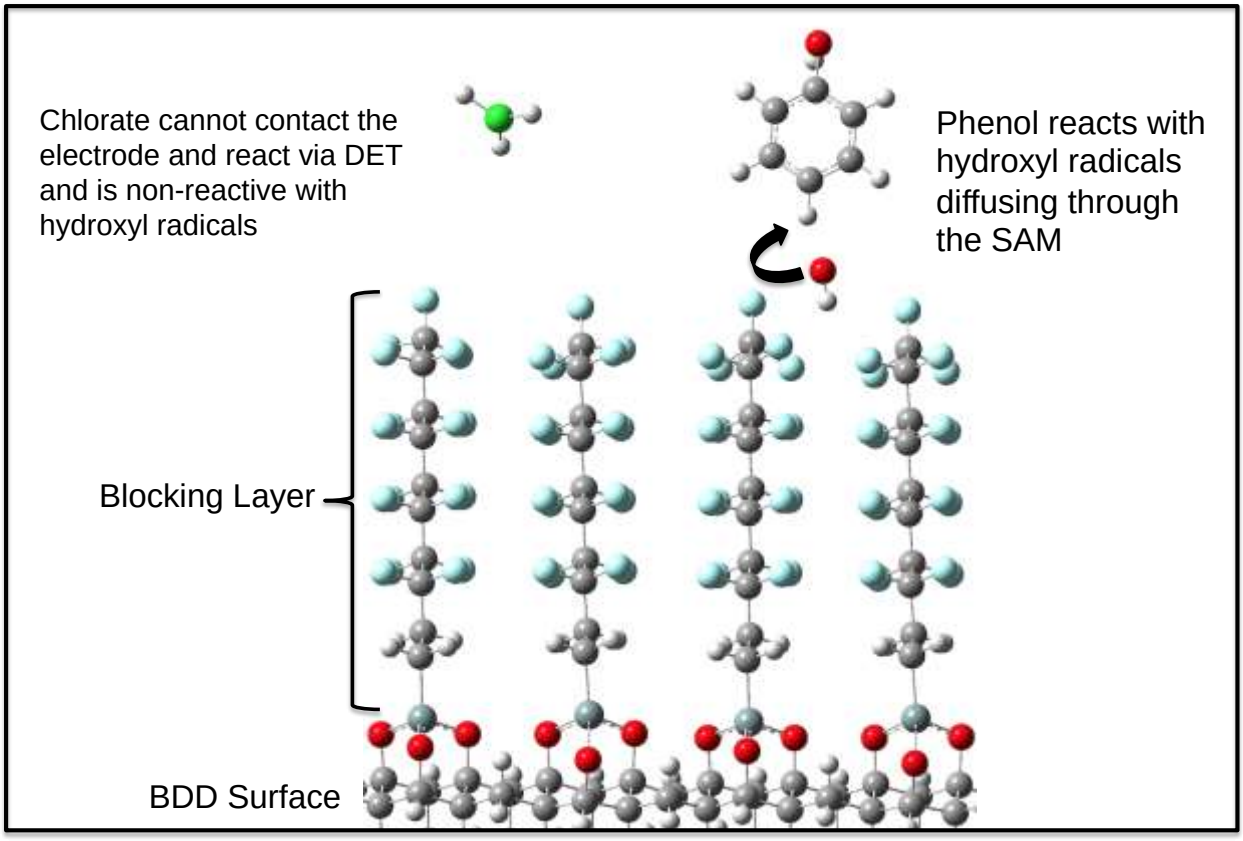

Figure 4-6. Schematic of the proposed mechanism for the inhibition of chlorate oxidation in the presence of phenol oxidation on a BDDF-aliphatic electrode. Atom key: C (grey); F (teal); O (red); H (white); Si (blue-grey); Cl (green). See online version for colors.

The oxidation of ClO_3^- to $ClO_3^{\bullet}$ cannot occur according to the DET reaction shown in reaction 4-1, since it is at a distance from the electrode surface (~ 1.5 nm) where electron tunneling is negligible. The slow degradation of the SAM was apparent during cycling tests (Figure 4-5), and it is proposed that the reactive sites are the C-H bonds of the SAM, which are susceptible to $OH^{\bullet}$ attack. Future research is needed to understand the mechanism of the SAM degradation along with developing more robust blocking films.

4.5 Conclusions

The BDD electrode surface was successfully modified by plasma (H_2 and CF_4) fluorination, electrochemical fluorination with PFOA, and aliphatic and aromatic silanization. XPS

measurements confirmed the introduction of fluorinated functional groups to the BDD electrode by all methods tested. CV scans of $Fe(CN)_6^{3-/4-}$ and $Fe^{3+/2+}$ redox couples confirmed that surface modification affected the electrochemical properties of the electrodes. For the BDDF-plasma electrode the electron transfer of the $Fe(CN)_6^{-3/-4}$ redox couple was inhibited and the $Fe^{3+/2+}$ redox couple displayed increased reversibility and increased current response, which was attributed to dipole–dipole interactions. For the BDDF-PFOA and BDDF-aliphatic electrodes, the electron transfer of both redox couples was inhibited, which was attributed to the formation of a blocking film. For the BDDF-aliphatic electrode the film was found to be pinhole free, which resulted in the complete inhibition of ClO_4^- formation during the oxidation of 10 mM NaCl and 1 mM $NaClO_3$ electrolytes. The BDDF-aliphatic electrode had 1,785 and 680-fold decreases in selectivity for ClO_4^- formation during the electrolysis of the NaCl and $NaClO_3$ electrolytes, respectively. By contrast the oxidation rates of phenol were only reduced by 16.3% in the NaCl electrolyte and 61% in the $NaClO_3$ electrolyte. The BDDF-aliphatic electrode was shown to be stable for up to 10 consecutive $NaClO_3$ oxidation experiments before the formation of low levels of ClO_4^- were observed. These results indicated that aliphatic silanization of BDD electrodes can be used to inhibit ClO_4^- formation while still allowing for significant organic compound oxidation.

5. Electrocatalytic Reduction of Nitrate using Magnéli Phase TiO_2 Reactive Electrochemical Membranes Doped with Pd-based Catalysts

5.1 Abstract

This research focused on synthesis, characterization, and application of catalytic reactive electrochemical membranes (REMs) for electrocatalytic NO_3^- reduction in a flow-through reactor. The REMs were synthesized by sintering substoichiometiric TiO_2 powders into monolithic, porous electrodes with sub-micron transport pores. The deposition of Pd-Cu and Pd-In catalysts to the REMs produced catalytic REMs (i.e., Pd-Cu/REM and Pd-In/REM) that were active for NO_3^- reduction. Electrocatalytic NO_3^- reduction was investigated as a function of electrode placement, flow rate, electrode potential, NO_3^- concentration, and under various solution conditions. Optimal performance for NO_3^- reduction was achieved with a Pd-Cu/REM with an upstream counter electrode. In this setup, NO_3^- was reduced from a 1 mM feed concentration to below the EPAs regulatory MCL (700 μM) in a single pass through the REM (residence time ~ 2 s), obtaining product selectivity of < 2% towards NO_2^-/NH_3. Nitrate reduction was not affected by dissolved oxygen and carbonate species and only slightly decreased in a surface water sample due to Ca^{2+} and Mg^{2+} scaling. A maximum current efficiency for Pd-Cu/REM of 105 ± 5.4% was observed in a 1mM $NaNO_3$ solution and it decreased to ~ 51% for a surface water sample. The energy consumption for the surface water sample was between 1.1 to 1.3 kWh mol^{-1} at 1 mM NO_3^- concentrations. Energy consumption decreased to 0.19 and 0.12 kWh mol^{-1} for 10 and 100 mM NO_3^- solutions, respectively. The high NO_3^- conversion, low NO_2^- and NH_3 formation, and low energy consumption demonstrated the extreme promise of using the Pd-Cu/REM for NO_3^- removal from natural waters.

5.2 Introduction

Nitrate is one of the most common pollutants in natural waters due to the over application of nitrogen based fertilizers and it is also present in numerous industrial wastewaters (e.g., nuclear processing, dairy, metal refining, pharmaceutical) [229–234]. The consumption of NO_3^- and NO_2^- has documented health risks [65–67,235], and therefore the US Environmental Protection Agency (EPA) has set maximum contaminant levels (MCLs) for NO_3^- and NO_2^- at 700 and 70 μM, respectively [364,365]. Several physical separation treatment methods such as electrodialysis, ion exchange, and reverse osmosis have been used for NO_3^- removal. However, the processes are nonselective and produce concentrated NO_3^- brines, which require costly post-treatment or disposal [68,69].

Catalytic and electrochemical NO_3^- reductions have been investigated as alternative destructive treatment methods [70–80]. Various catalysts and electrode materials have been investigated [70,72–75,81–83,236,237], and bi-metallic catalysts comprised of a noble metal (e.g., Pd, Pt, Rh) to facilitate adsorbed H formation and a promoter metal (e.g. Cu, Sn and In) for NO_3^- reduction generally have shown the highest reduction rates [68,71,78,80,238–247]. The main reduction products of both catalytic and electrochemical NO_3^- reduction are N_2 and NH_3, with NO_2^- and N_2O as the primary detected intermediates [242,245,248–250]. The formation of NH_3 is undesirable due to documented health risks [251], and therefore the World Health Organization (WHO) has set a drinking water limit of 30 μM. The relevant half reactions during NO_3^- reduction are as follows [252]:

$$NO_3^- + H^+ + 2e^- \xrightarrow{Pd-M} NO_2^- + OH^- \quad (5\text{-}1)$$

$$NO_3^- + \frac{5}{2}H^+ + 4e^- \xrightarrow{Pd-M} \frac{1}{2}N_2O + \frac{5}{2}OH^- \quad (5\text{-}2)$$

$$NO_3^- + 3H^+ + 5e^- \xrightarrow{Pd-M} \frac{1}{2} N_2 + 3OH^- \quad (5\text{-}3)$$

$$NO_3^- + 6H^+ + 8e^- \xrightarrow{Pd-M} NH_3 + 3OH^- \quad (5\text{-}4)$$

Electrochemical NO_3^- reduction has advantages over catalytic reduction, as it does not require the storage and delivery of an external electron donor (e.g., H_2) and thus the development of compact treatment technologies are possible. However, electrochemical NO_3^- reduction is associated with high concentrations of NO_2^- and NH_3 [70,74,75,81–83], and reaction rates are typically low in weak ionic strength solutions that typify natural waters due to electrostatic repulsion between polarized cathodes and NO_3^- [366,367]. Solution conditions may also have an adverse effect on electrochemical NO_3^- reduction. For example, the O_2 reduction reaction (ORR) occurs at similar cathodic potentials as NO_3^- reduction [253], and dissolved organic matter (DOM) may adsorb and block catalytic sites [254,255]. However, most electrochemical studies use clean, deaerated electrolyte solutions and therefore knowledge regarding the effects of solution conditions is limited.

Electrochemical NO_3^- reduction studies have been investigated in both batch [81,82,240,252,256] and continuous flow-through reactors [257–264]. The most notable study of electrochemical NO_3^- reduction in a flow-through electrode setup utilized a Ni packed bed reactor, but the authors concluded that the reactor was not appropriate for NO_3^- treatment due to low electrode conductivity caused by particle-particle contact resistance that resulted in significant potential drop in the electrode phase [230]. Recently the development of porous, monolithic electrodes and composite conductive membranes has enabled efficient flow-through electrochemistry without significant potential drops in the electrode material [54,64,226,265–274]. Porous electrodes comprised of substoichiometric TiO_2, carbon, and PbO_2 have been fabricated as reactive electrochemical membranes (REMs), where simultaneous filtration and

electrochemical conversions are possible [54,64,226,265–274]. REMs have been applied to electrochemical oxidation of organic compounds [54,269], antifouling membranes [269,271], membrane fouling regeneration [269,272], and bacteria inactivation [226,257,270,273]. However, REMs have not been applied for electrochemical NO_3^- reduction.

In this study, Pd-Cu and Pd-In catalysts are deposited on sub-stoichiometric TiO_2 REMs and the resulting electrodes are characterized and studied for NO_3^- reduction and product selectivity in a flow-through setup. Various operating conditions were investigated including flow direction, flow rate, electrode potential, NO_3^- concentration, and reactor number. Different solution conditions were tested to determine the effects that dissolved oxygen, carbonate species, and other natural water constituents had on NO_3^- reduction and product selectivity. A simple kinetic model was used to interpret the experimental data and determine rate constants for NO_3^- removal.

5.3 Materials and Methods

5.3.1 Reagents. All chemicals were reagent grade and purchased from Sigma-Aldrich and Fisher Scientific. All gases (purity of 99.999%) were obtained from Praxair. Chemicals were used as received. All reactions solutions were made using Type I water (> 18.2 MΩ.cm at 25°C) obtained from a Barnstead NANOpure system (Thermo Scientific).

5.3.2 Catalyst Loaded Magnéli Phase Powder Preparation. The TiO_2 powder was reduced to a Magnéli phase titanium suboxide (Ti_nO_{2n-1}) (n = 4, 6) at 1050 °C under flowing H_2 gas in a tube furnace (OTF-1200X, MTI) for 6 hours. Catalysts were deposited on 2.5 g of Ti_nO_{2n-1} powder using the incipient wetness method. A 2 wt% Pd with a 2:1 molar ratio of Pd to promoter metal (M = Cu or In) was prepared by dissolving the corresponding salts in an aqueous solution containing 1 mM HNO_3 (pH = 3), where the solution volume corresponded to the approximate

pore volume of the powder (150 µL g^{-1}). For Pd-Cu deposited powder (Pd-Cu/Ti_nO_{2n-1}), 0.125 g $Pd(NO_3)_2$•$2H_2O$ and 0.057 g $Cu(NO_3)_2$•$3H_2O$ were dissolved in 1 mM HNO_3 and mixed with 2.5 g of Ti_nO_{2n-1} powder. For Pd-In deposited powder (Pd-In/Ti_nO_{2n-1}), 0.125 g $Pd(NO_3)_2$•$2H_2O$ and 0.065 g $In(NO_3)_3$•H_2O were dissolved in 1 mM HNO_3 and mixed with 2.5 g of Ti_nO_{2n-1} powder. The Pd-In/Ti_nO_{2n-1} and Pd-Cu/Ti_nO_{2n-1} powders were calcined/reduced at 120 and 200 ^{0}C, respectively. The lower synthesis temperature for the Pd-In/Ti_nO_{2n-1} powder was chosen to avoid volatilization of In species as InH_3 [368,369].

5.3.3 Catalyst Loaded REM Preparation. Magnéli phase REMs were synthesized from Magnéli phase powder. First, a given amount of powder was weighed and mixed thoroughly with paraffin oil as binder (8 drops per g of powder). Then, approximately 0.6 g of the mixed powder was loaded into a stainless steel cylindrical die and pressed with a hydraulic press under a uniaxial pressure of 20.7 bar to obtain a 2.5 mm thick, 1.1 cm diameter Magnéli phase pellet. The pellet was sintered in a tube furnace under a flowing H_2 atmosphere at 1050 ^{0}C for 6 hours to remove the paraffin oil and sinter the particles. The as prepared pellet was used in control experiments and is defined as the "REM". Catalysts were deposited on the REMs using the incipient wetness method, as described above, with the same catalyst loadings. The Pd-M/REM pellets were then calcined in air and subsequently reduced in flowing H_2 at the same temperatures as the Pd-M/Ti_nO_{2n-1} powders.

5.3.4 Batch Nitrate Reduction Experiments. Nitrate reduction experiments were performed in a batch system using Pd-Cu/Ti_nO_{2n-1} and Pd-In/Ti_nO_{2n-1} powders. The batch reactor was filled with 297 mL of DI water and charged with 0.2 g of Pd-M/Ti_nO_{2n-1} powder. The solution was purged with H_2 and CO_2 at flow rates of 85 and 15 mL min^{-1}, respectively, for 10 minutes before spiking the solution with 3 mL of a 100 mM $NaNO_3$ stock solution to give a concentration of 1 mM

$NaNO_3$. The gas purging was continued for the duration of the experiment. Samples were taken at consistent time intervals, filtered, and analyzed by ion chromatography (IC).

5.3.5 Flow-through Nitrate Reduction Experiments. Electrocatalytic NO_3^- reduction was also performed with the REM, Pd-Cu/REM, and Pd-In/REM in a flow-through reactor (Appendix C, Figure S-5-1). The electrochemical cell (polyether ether ketone (PEEK)) consisted of the Pd-M/REM as the working electrode, boron-doped diamond (BDD) film electrode on Ta substrate as the counter electrode, and a 1 mm diameter Ag/AgCl/KCl (1M) reference electrode (Harvard Apparatus, MA, USA). A hole of ~ 3.8 mm was drilled in the center of the BDD/Ta counter electrode and the reference electrode was inserted through this hole to obtain a 3.3 mm gap between the working and reference electrodes. Electrochemical potentials and currents were controlled and monitored using a Gamry Reference 600 potentiostat/galvanostat (Warminster, PA). All potentials were solution potential drop corrected (iR_s) and documented versus the standard hydrogen electrode (SHE). Two flow modes were investigated, referred to as cathode-anode and anode-cathode flow modes (see Figure S-5-1). In the cathode-anode flow mode the counter electrode is placed downstream, and solution first flows through the REM cathode followed by the BDD anode. In the anode-cathode flow mode the counter electrode is placed upstream, and solution first flows through the BDD anode followed by the REM cathode. For the anode-cathode flow mode, the H_2 evolved at the REM surface would pass through the entire REM pellet and thus could be utilized for catalytic nitrate reduction. However, the O_2 evolved at the upstream anode may inhibit nitrate reduction activity and selectivity. For cathode-anode flow mode, the H_2 evolved at the outer surface of the REM would be transported towards the BDD anode via convective flow and would have minimal contact with the catalytic sites within the

inner surface of the REM. However, the REM cathode would be unaffected by the O_2 evolved at the downstream BDD anode.

Reduction experiments were conducted using either a $NaNO_3$ (1 to 100 mM) or $NaNO_2$ (1 mM) feed solution. Before the application of an electrode potential, the feed solution was purged with Ar for 15 minutes under vigorous stirring to remove dissolved oxygen or with air to saturate with dissolved oxygen. Gas purging continued for the duration of the experiment. The feed solution was pumped through the REM pellet at flow rates of 0.2 to 1.8 mL min^{-1}, which corresponded to surface area normalized permeate membrane fluxes (J) of 240 to 2160 L m^{-2} h^{-1} (LMH). A cathodic potential was applied to the REM after 10 minutes of fluid flow and the permeate was collected for anion and cation analysis. A portion of the collected sample was immediately acidified with 0.1 M HCl to pH 3.0 to convert NH_3 to NH_4^+. Cathodic potentials between -0.01 and -3.6 V/SHE were applied for all the reduction experiments. Electrocatalytic reduction experiments were also conducted on Pd-Cu/REM as a function of J at a constant potential of -2.5 V/SHE with air purging and anode-cathode flow mode. Catalytic NO_3^- and NO_2^- reduction experiments were performed with only Pd-Cu/REM in anode-cathode flow mode under H_2 purging and with J between 240 and 2160 LMH, in order to assess catalytic reduction in the absence of an applied electrode potential.

5.3.6 Membrane Characterization. The REM, Pd-Cu/REM, Pd-In/REM, and Ti_nO_{2n-1} powder without catalyst were characterized by X-ray diffraction (XRD, Siemens D-5000) with a Cu X-ray tube (40 kV and 25 mA). Scans were controlled and analyzed with DataScan software (MDI, v. 4.3.355, 2005) at a 0.01° step size and a 0.5 s dwell time.

Scanning electron microscopy (SEM) was performed using a Tescan Vega3 XMU instrument (Tescan Orsay Holding, Brno, Czech Republic) to characterize the surface morphology of the

REM, Pd-Cu/REM, and Pd-In/REM pellets at 4 to 25 kV and from 3 to 6 k magnifications. To show the presence and distribution of the different catalyst metals within the REM, elemental analysis using SEM with energy dispersive X-ray spectroscopy (EDS) was performed on the different REM surfaces. The X-rays maps were acquired using SEM with an IXRF i550 SSD Energy Dispersive X-ray detector (IXRF Systems, Texas, USA). The SEM with microprobe mapping was performed on vertical cross sections of the REMs to show the catalyst penetration depths within the REM pellets. The X-ray maps of the samples were collected using a JEOL JXA-8200 (JEOL Ltd., Tokyo, Japan) electron microprobe at the Department of Earth and Planetary Science/Institute of Meteoritics, University of New Mexico. To determine the elemental concentrations of the REM, Pd-Cu/REM and Pd-In/REM, an acid digestion method was used to extract the elements. The acid digestion used a mixture of 3 mL HF (48 %), 3 mL HNO_3 (70 %), and 5 mL HCl (37 %). Then the mixture was introduced into a 50 mL Teflon digestion tube containing a single pellet (0.5 – 0.6 g) and heated in a Digi prep MS SCP Science block heater at 95 ^{0}C for 2 hours. Prior to analysis acid extracts were diluted to 25 mL and filtered (0.45 µm) to remove any suspended solids. All the acid digestion experiments were performed in triplicate. Elemental concentrations of Pd, Cu, and In were measured in these acid extracts using a PerkinElmer Optima 5300DV Inductively Coupled Plasma-Optical Emission Spectrometer (ICP-OES) (detection limit ~ 0.5 mg L^{-1}).

The through plane electrical conductivity (σ) for the REM and Pd-M/REMs were determined using electrochemical impedance spectroscopy (EIS) with an amplitude of ±7 mV about the open circuit potential (OCP) and a frequency range of 0.5 to 100 kHz using a Gamry Reference 600 potentiostat/galvanostat (Warminster, PA). Values for σ were calculated according to the following equation:

$$\sigma = \frac{x}{AR_{REM}} \quad (5\text{-}5)$$

where, R_{REM} is the measured resistance (ohm) of the pellet, A is the pellet cross-sectional area (1 cm^2) and x is the pellet thickness (0.25 cm).

5.3.7 Analytical Methods. Concentrations of NO_3^-, NO_2^-, NH_3OH^+, and NH_4^+ were determined using IC (Dionex ICS-2100). The pH was measured using a meter and probe (PC2700, Oakton). Chemical oxygen demand (COD) was measured by Hach method 8000 (USEPA Reactor Digestion Method). Total nitrogen (N) was determined through oxidative digestion of all dissolved nitrogen species, excluding dissolved N_2, to NO_3^- followed by IC detection [370].

5.3.8 Product Selectivity, Current Efficiency, and Energy Calculations. The selectivity of NO_3^- reduction (S_i) was calculated by equation (5-6):

$$S_i(\%) = v_i \frac{C_{p,i}}{C_{f,NO_3^-} - C_{p,NO_3^-}} * 100 \quad (5\text{-}6)$$

where species i is NO_2^-, NH_3, N_2O, or N_2, and v_i is the stoichiometric coefficient of species i (e.g., moles of i per mole of NO_3^- degraded). The apparent N_2 selectivity was calculated assuming that it represented the gap in the N mass balance, as other soluble products were not detected (e.g., NH_3OH^+). Total N analysis of acidified permeate samples was performed immediately after collection, both with and without CO_2 purging, and the difference between these measurements was used as an estimate of N_2O production. This approach was deemed reasonable based on previous reports that electrochemical NO_3^- reduction results in mainly NO_2^-, NH_3, N_2, N_2O, and NH_3OH^+ [248].

Current efficiency (*CE*) was calculated using the following equation:

$$CE(\%) = \frac{JFz(C_{f,NO_3^-} - C_{p,NO_3^-})}{j} \times 100 \quad (5\text{-}7)$$

where z is the moles of electrons transferred per moles of reactant, j is the current density (A cm^{-2}), F is the Faraday constant (96485 C mol^{-1}), and C_{f,NO_3^-} and C_{p,NO_3^-} are feed and permeate concentrations (mol m^{-3}) of NO_3^-, respectively. All experiments were performed at room temperature (21 ± 1 °C). Values for z were determined based on the observed product distributions.

Energy consumption (EC) (kWh mol^{-1}) was calculated according to the following equation:

$$EC = 10^{-3} * \frac{V_{cell} I}{Q(C_{f,NO_3^-} - C_{p,NO_3^-})} \tag{5-8}$$

where, V_{cell} is cell potential (V), I is the current (A) and Q is the volumetric flow rate of the permeate (m^3 h^{-1}). In order to normalize by the concentration of contaminant, the electrical energy per order (E_{EO}) metric was also calculated. The E_{EO} is a measure of the electric energy (kWh m^{-3}) needed to reduce the NO_3^- concentration by 1 order of magnitude per unit volume of solution [371,372], and is given by the following equation.

$$E_{EO} = 10^{-3} * \frac{V_{cell} I}{Q * \log\left[\frac{C_{f,NO_3^-}}{C_{p,NO_3^-}}\right]} \tag{5-9}$$

5.4 Results and Discussion

5.4.1 Materials Characterization. The bulk elemental compositions of the REM, Pd-Cu/REM, and Pd-In/REM samples were determined by acid digestion and measurement of elemental compositions by ICP-OES. The results provided molar ratios of Pd:Cu = 2.0 ± 0.2 for Pd-Cu/REM and Pd:In = 2.2 ± 0.1 for Pd-In/REM, which were similar to the expected molar ratio of 2:1. The catalyst metals were not detected on the REM sample. The results confirmed successful catalyst deposition on REMs using the incipient wetness method. The pore radius of the REMs

was determined as 0.46 ± 0.04, 0.40 ± 0.02, and 0.44 ± 0.03 μm for the REM, Pd-Cu/REM, and Pd-In/REM, respectively. These results indicated that the pore size did not change significantly as a result of catalyst deposition (Appendix C, Figure S-5-2).

The XRD data for the Ti_nO_{2n-1} powder, REM, Pd-Cu/REM, and Pd-In/REM are shown in Figure 5-1 along with the XRD characteristic peaks for Ti_4O_7, Ti_5O_9, Ti_6O_{11}, Pd, Cu, and In. The XRD data for the Ti_nO_{2n-1} powder contained characteristic peaks representative of Ti_4O_7 (10-2), (104), (120), (2-13) and (1-20) crystal faces, with minor amounts of Ti_5O_9 (10-2) and Ti_6O_{11} ((1-21) and (101)). The Ti_nO_{2n-1} REM contained additional peaks for Ti_4O_7 (1-22), (10-4), and (200) crystal faces. The XRD data for Pd-Cu/REM and Pd-In/REM had similar patterns to the Ti_nO_{2n-1} powder, with additional characteristic peaks for Pd(111), Pd(200), Cu(111), and Cu(200) for Pd-Cu/REM and Pd(111), Pd(200), In(111), In(200), and In(002) for Pd-In/REM. Significant peaks were not detected for CuO, Cu_2O, In_2O_3, PdO, or PdO_2, which indicated that the catalyst precursors were predominately reduced to their metallic oxidation states (Figure 5-1).

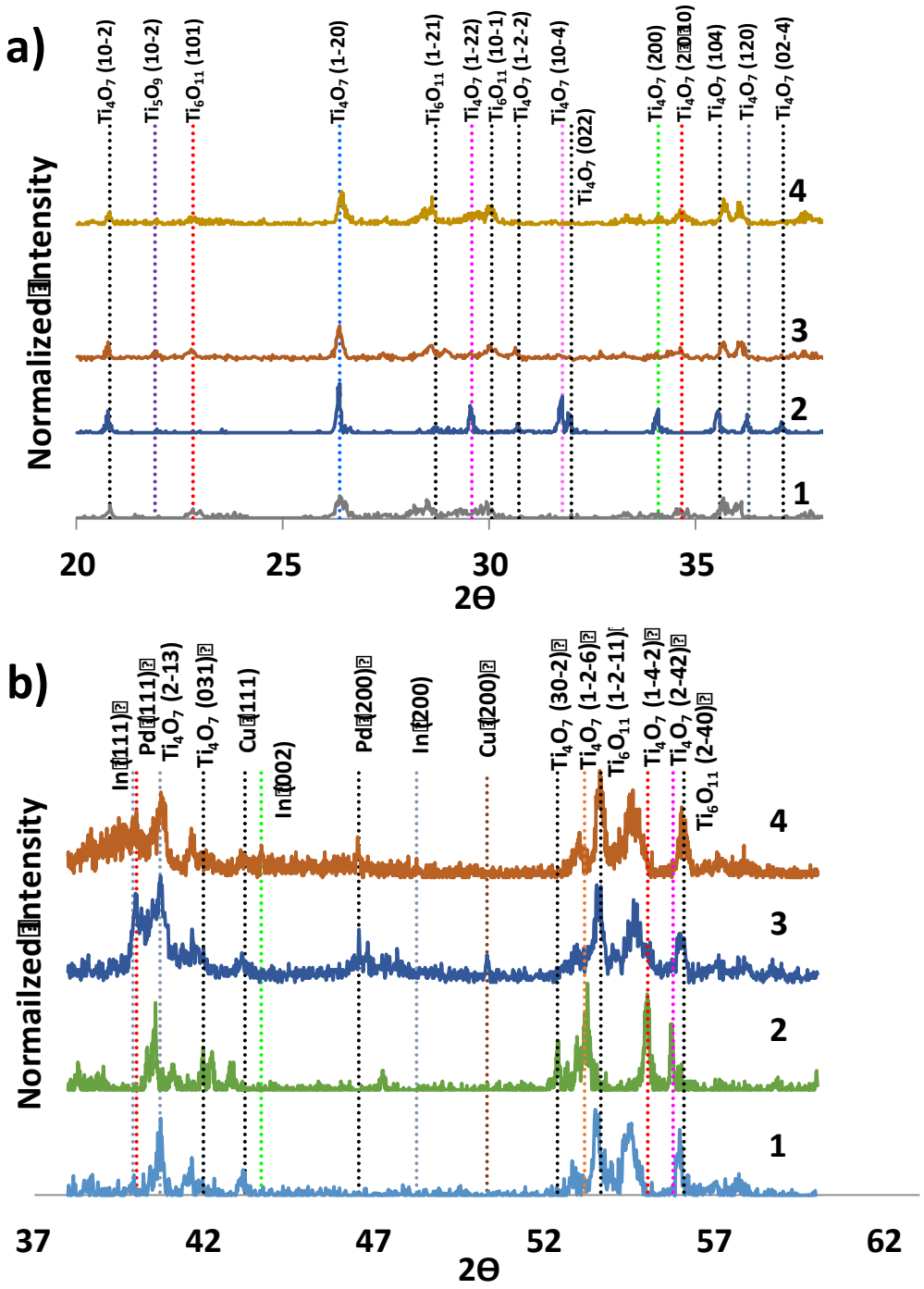

Figure 5-1. XRD data for 1) Ti_nO_{2n-1} powder, 2) REM, 3) Pd-Cu/REM and 4) Pd-In/REM. The locations of the characteristic peaks for Ti_4O_7, Ti_6O_{11}, In, Pd, and Cu are represented by the vertical dashed lines. a) 2Θ = 20-38 deg and b) 2Θ = 38-52 deg.

The through plane conductivity of the REM was measured as σ = 785 ± 15 S m^{-1} and it increased to σ = 835 ± 21 for Pd-Cu/REM and σ = 824 ± 12 S m^{-1} for Pd-In/REM. The slight increases in σ values were attributed to the deposition of the highly conductive Pd, Cu, and In metals. The measured σ values were similar to that reported previously for a high purity Ti_4O_7 ultrafiltration REM [373].

To characterize the spatial distribution of the catalysts, SEM/EDS mapping was conducted on the Pd-M/REM samples. The SEM image of the REM shows a porous structure with particle size of approximately 2 μm (Figure 5-2). The results of the Pd-M/REMs showed fairly uniform distribution of the catalyst metals on the planar surface and a high spatial correlation between Pd and M (Figure 5-3). Analyses using SEM/EDS and electron microprobe mapping were performed on vertical cross sections of the Pd-M/REM samples to determine the penetration depths of the catalysts into the REMs. The results for the Pd-Cu/REM showed that the catalyst metals penetrated to approximate depths of 420 μm for Pd and 400 μm for Cu (Figure 5-4). However, for the Pd-In/REM depths of 900 μm for Pd and 800 μm for In were observed, and more uniform distributions of the catalysts were observed with depth compared to the Pd-Cu/REM (Figure 5-4). The differences in the depths of penetration may be affected by the electroless deposition of Cu^0 onto the REM substrate (reaction (5-10)), followed by a galvanic replacement reaction that deposited Pd^0 (reaction (5-11)). By contrast, the redox potential for the deposition of In^{3+} is much more negative (reaction (5-12)) and not feasible at the measured OCP (E_{ocp} = 0.3 V/SHE) [374,375].

$$Cu^{2+} + 2e^- \rightarrow Cu^0 \qquad E^0 = 0.34 \text{ V/SHE} \qquad (5\text{-}10)$$

$$Cu^0 + Pd^{2+-} \rightarrow Cu^{2+} + Pd^0 \qquad E_{rxn} = 0.61 \text{ V/SHE} \qquad (5\text{-}11)$$

$$In^{3+} + 3e^- \rightarrow In^0 \qquad E^0 = -0.34 \text{ V/SHE} \qquad (5\text{-}12)$$

Therefore, in the case of the Pd-In system, deposition onto the REM support is likely controlled by weaker physisorption interactions and thus the metals were able to penetrate to a further depth into the pellet.

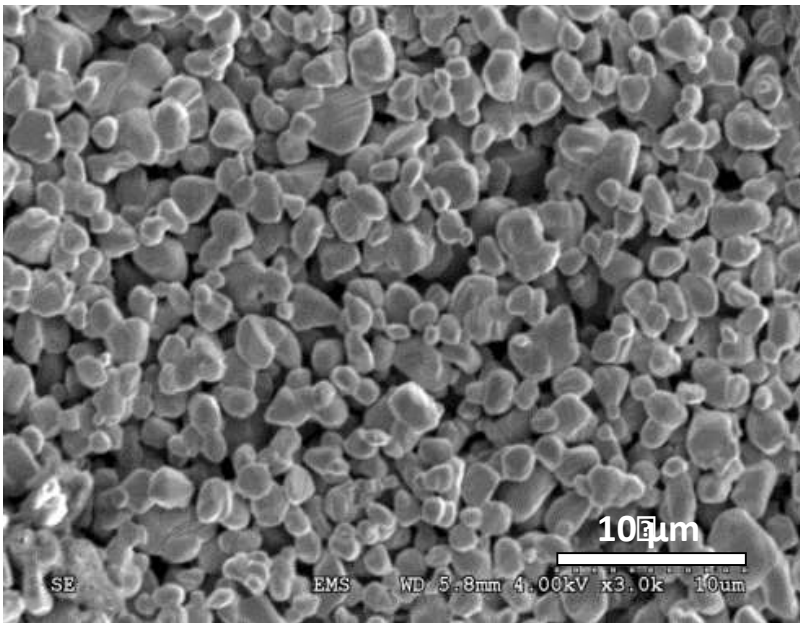

Figure 5-2. SEM image of REM surface.

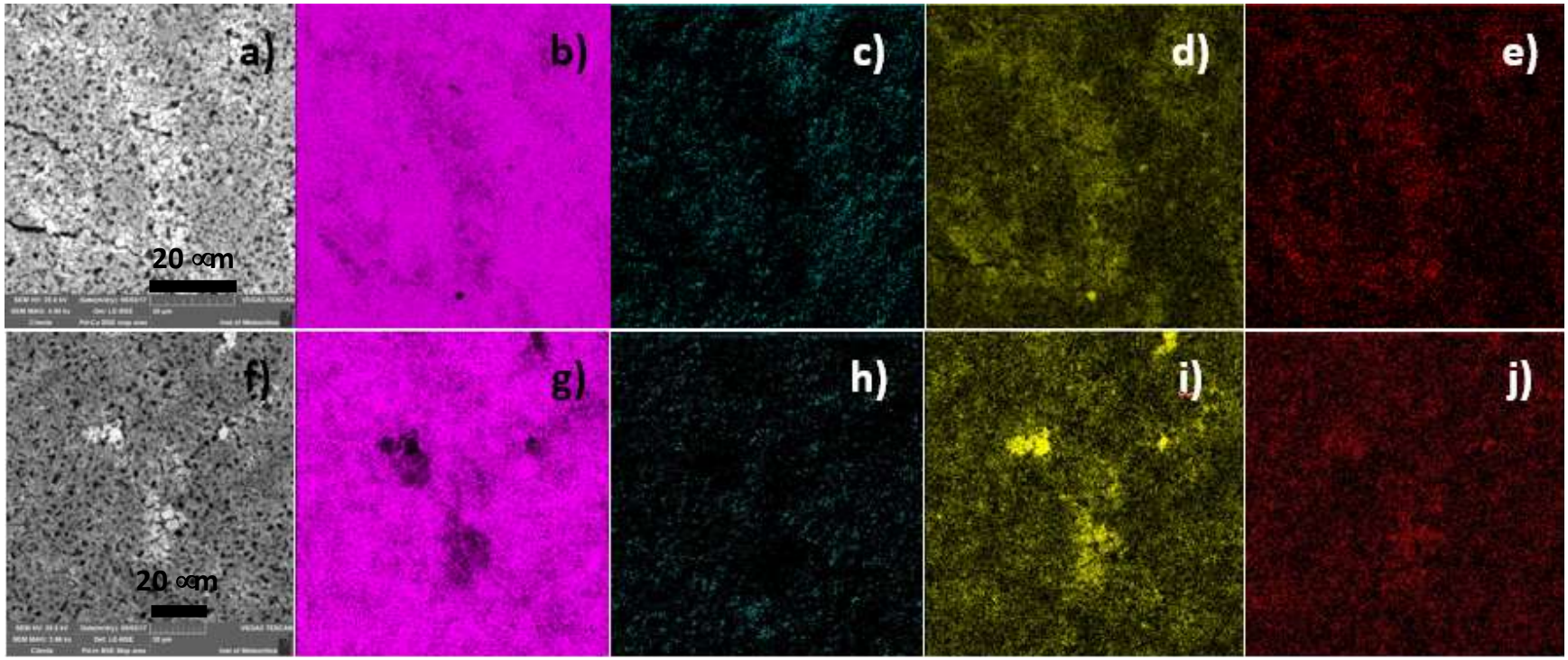

Figure 5-3. Scanning electron microscope images of the a) Pd-Cu/REM and f) Pd-In/REM surface. SEM/EDS elemental mapping of b) Ti; c) O; d) Pd; and e) Cu on the Pd-Cu/REM surface and g) Ti; h) O; i) Pd; and j) In on the Pd-In/REM surface.

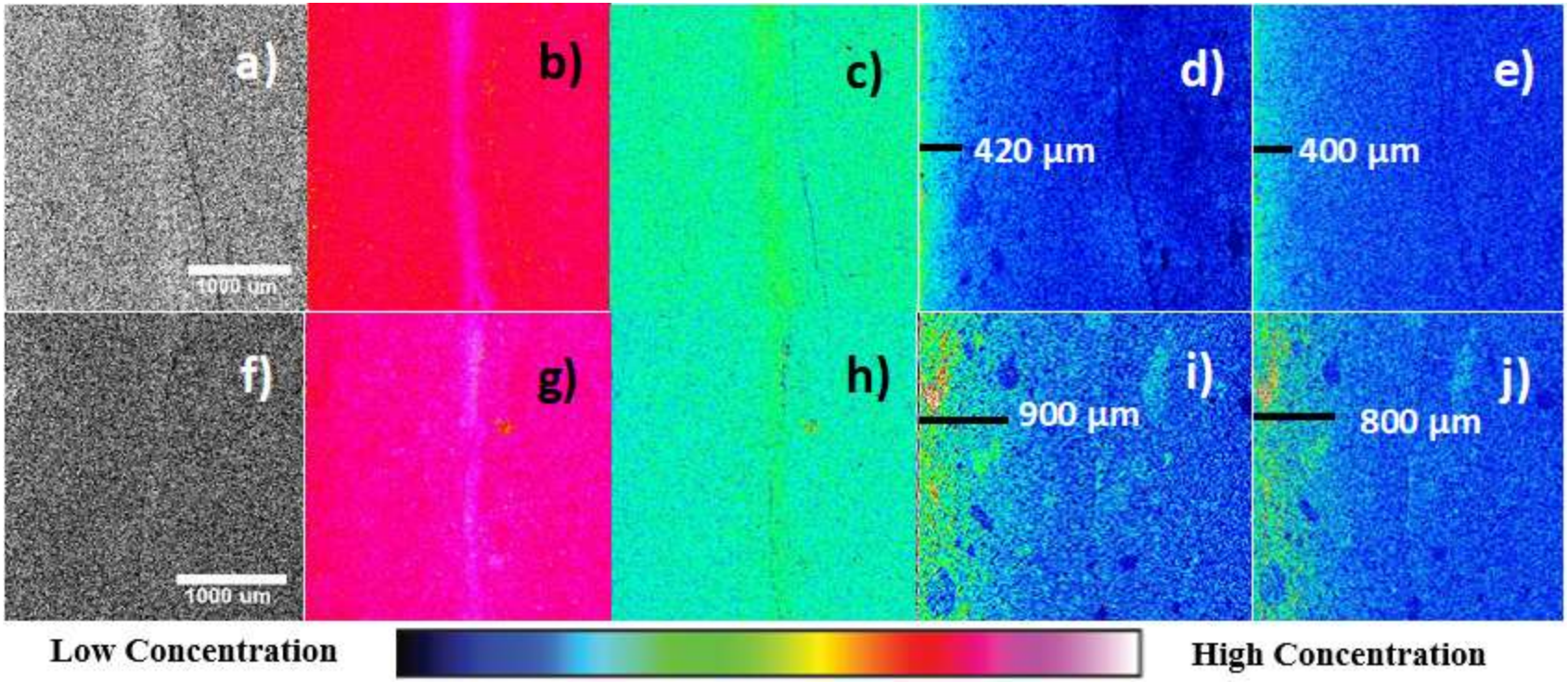

Figure 5-4. Scanning electron microscope and microprobe image of the vertical cross-section of a) Pd-Cu/REM and f) Pd-In/REM. Scanning electron microscope and microprobe mapping of the vertical cross-section: b) Ti, c) O, d) Pd, and e) Cu in Pd-Cu/REM; and g) Ti, h) O, i) Pd, and j) In in Pd-In/REM. Top surface of the pellet is the left side of the image. Solid black lines on panels d, e, i, and j are estimated penetration depths of the catalyst metals.

5.4.2 Catalytic Nitrate Reduction. Batch experiments were conducted to assess the Pd-Cu/Ti_nO_{2n-1} and Pd-In/Ti_nO_{2n-1} powders for catalytic NO_3^- reduction in the presence of H_2 as a reductant. A Pd-Cu/TiO_2 catalyst was also tested to ascertain the effect of the Magnéli phase support on NO_3^- reduction. Pseudo first-order rate constants for up to 50% conversion were fit to the NO_3^- concentration versus time profiles. Concentration profiles for NO_3^- and NO_2^- and first-order rate constant fits for NO_3^- reduction are shown in the Appendix C (Figure S-5-3). The catalyst metal normalized NO_3^- reduction kinetics were faster for Pd-Cu/Ti_nO_{2n-1} (3.6 ± 0.2 L g_{metal}^{-1} min^{-1}) than for Pd-In/Ti_nO_{2n-1} (1.4 ± 0.2 L g_{metal}^{-1} min^{-1}) and Pd-Cu/TiO_2 (0.9 ± 0.1 L g_{metal}^{-1} min^{-1}) (Figure S-5-3). The 2.7-fold increase in rate constant for the Pd-Cu/Ti_nO_{2n-1} catalyst compared to the Pd-Cu/TiO_2 catalyst was unexpected since the surface area of the Ti_nO_{2n-1} catalyst was 7.0 times less (e.g., 1.2 m^2 g^{-1} (Ti_nO_{2n-1}) versus 8.4 m^2 g^{-1} (TiO_2)). The increase in reactivity was attributed to the oxygen vacancies in the Ti_nO_{2n-1} support, which created Ti^{3+} sites that reduced Pd and Cu to their metallic states during reaction and thus increased catalytic turnover [376].

The measured rate constant for Pd-Cu/Ti_nO_{2n-1} (3.6 ± 0.2 L g_{metal}^{-1} min^{-1}) was comparable to values for Pd-Cu catalysts reported in the literature (0.1 – 5.1 L g_{metal}^{-1} min^{-1}) [237,238,241,377–379]. The measured rate constant for Pd-In/Ti_nO_{2n-1} (1.4 ± 0.2 L g_{metal}^{-1} min^{-1}) was also comparable to literature values (1.7 – 2.9 L g_{metal}^{-1} min^{-1}) [377,378]. However, due to the low specific surface area of the Ti_nO_{2n-1} powder support (1.2 m^2 g^{-1}) compared to that of typical catalyst supports (~100-200 m^2 g^{-1}), these rate constants would be much higher if compared on a surface area normalized basis. However, catalytic metal dispersion is rarely reported and therefore an accurate comparison on a surface area basis cannot be made.

The maximum NO_2^- concentrations during the batch experiments were 25 ± 4 μM for the Pd-Cu/Ti_nO_{2n-1} catalyst and 47 ± 2 μM for the Pd-In/Ti_nO_{2n-1} catalyst (Figure S-5-3b). The NO_2^- was completely removed at the end of the experiment for the Pd-Cu/Ti_nO_{2n-1} catalyst, whereas the concentration was 38 ± 6 μM for Pd-In/Ti_nO_{2n-1}. The NO_2^- concentration remained below the U.S. EPA's MCL (70 μM) for both catalysts. The final $S_{NO_2^-}$ values were calculated as 4.2 ± 0.2% for Pd-In/Ti_nO_{2n-1} and < 5.2 x 10^{-3} % for Pd-Cu/Ti_nO_{2n-1}. The final S_{NH_3} were determined as 19 ± 1% for Pd-In/Ti_nO_{2n-1} and 22 ± 2% for Pd-Cu/Ti_nO_{2n-1}. These results indicated that the catalysts exhibited high catalytic NO_3^- activity but substantial NH_3 production.

5.4.3 Electrocatalytic Nitrate Reduction. After successful performance of the powder Pd-Cu/Ti_nO_{2n-1} and Pd-In/Ti_nO_{2n-1} catalysts for NO_3^- reduction in batch mode, the REM, Pd-Cu/REM, and Pd-In/REM were tested for electrocatalytic NO_3^- reduction in flow-through mode. The REM, Pd-Cu/REM, and Pd-In/REM were operated with both cathode-anode and anode-cathode flow modes (as described previously) and under either Ar- or air-saturated conditions (Figure 5-5 and Figure S-5-1). Both REM and Pd-Cu/REM were also tested separately for NO_3^- reduction in a bicarbonate buffer and surface water sample using the anode-cathode flow mode and in air-saturated solutions. Two Pd-Cu/REMs operated in series were also tested for electrochemical NO_3^- reduction in an air-saturated bicarbonate buffer and surface water sample (Table 5-1). Results for all experiments are summarized in Table S-5-1 and experiments conducted at a cathodic potential of -2.5 V/SHE are summarized in Table 5-2.

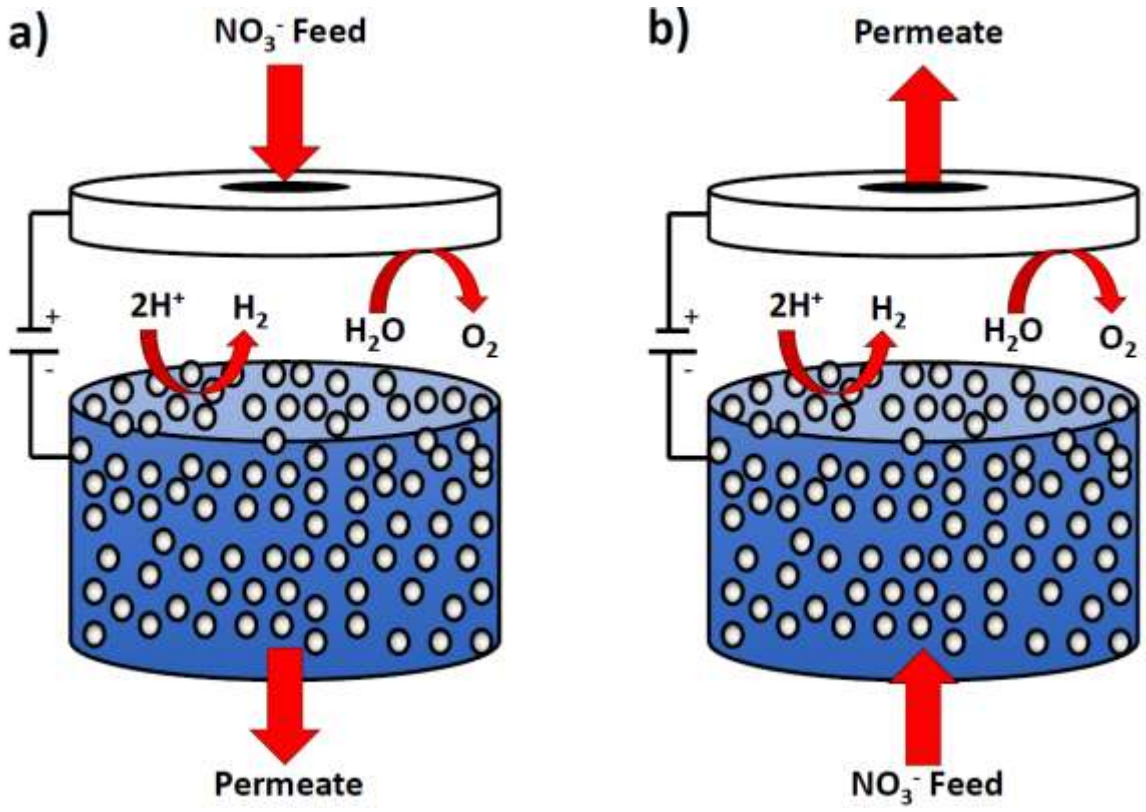

Figure 5-5. Schematic showing REM flow-through reactor with a) anode-cathode flow mode (upstream counter electrode) and b) cathode-anode flow mode (downstream counter electrode).

Table 5-1. Water quality data of the surface water sample.

	Filtered Surface Water
Sodium	0.56 mM
Potassium	0.17 mM
Calcium	0.90 mM
Magnesium	0.25 mM
Chloride	0.63 mM
Sulfate	0.015 mM
Bicarbonate	2.42 mM
Alkalinity	124 mg L^{-1} as $CaCO_3$
COD	39 mg L^{-1}
pH	8.1

5.4.3.1 Effect of Flow Direction. Flow schematics of the cathode-anode and anode-cathode flow modes are shown in Figure 5-5. All the flow mode experiments were performed under Ar purging to remove dissolved oxygen, which was expected to compete with NO_3^- for either adsorbed H or direct electron transfer reaction sites. Reduction experiments for the cathode-anode flow mode were performed at the OCP, -0.01, -0.2, -1.2, -2.5, and -3.6 V/SHE (J = 600 LMH). The same potentials were used for the anode-cathode flow mode, with the exception that a potential of -3.6 V/SHE was not used due to the formation of large quantities of H_2 bubbles at the REM surface, which blocked the electrode surface, resulting in increased pressure drop across the REM and large fluctuations in current. The NO_3^- and NO_2^- concentration versus time profiles at different potentials are summarized in Figure 5-6 for the anode-cathode flow mode and Figure 5-7 for the cathode-anode flow mode.

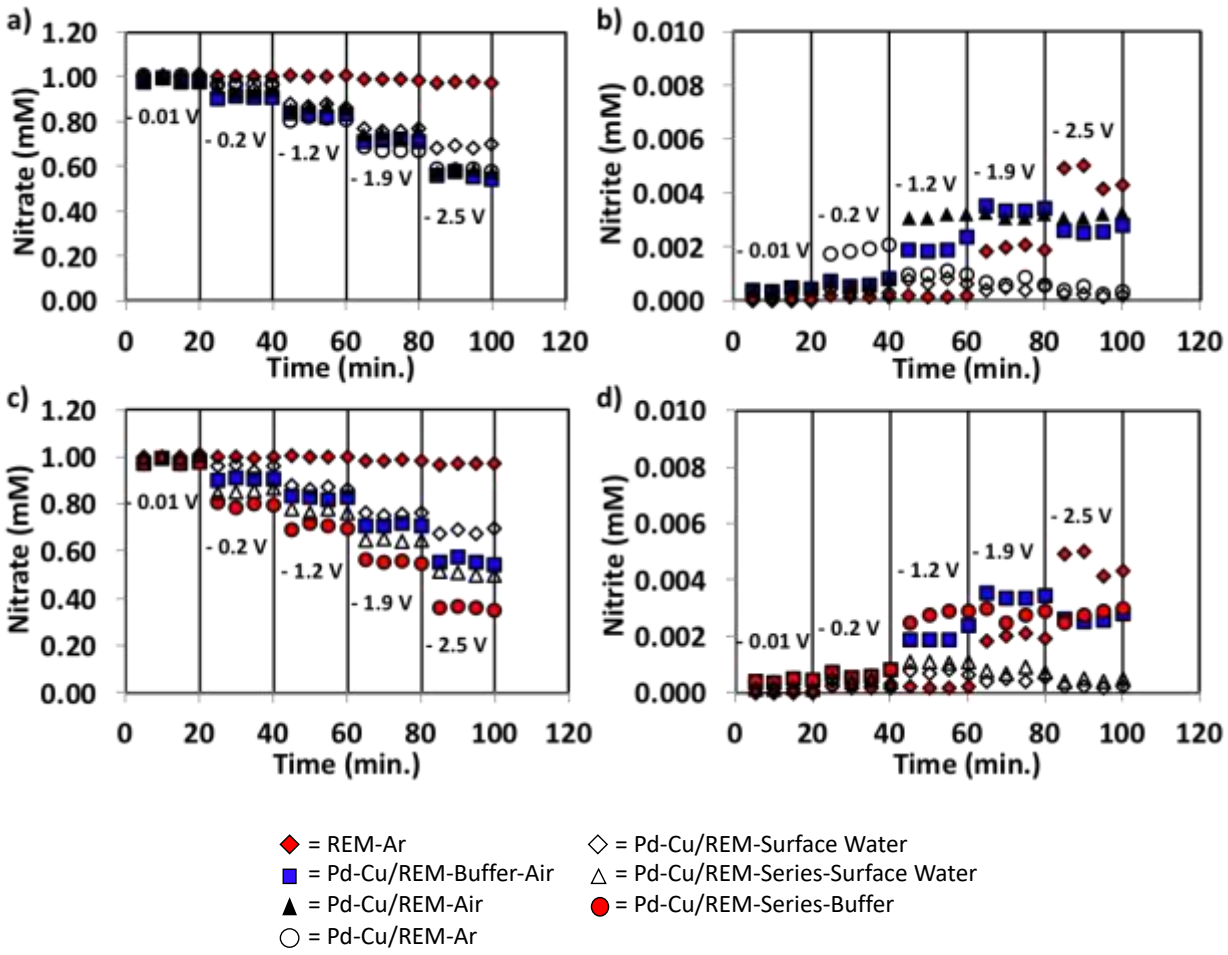

Figure 5-6. a) Nitrate and b) nitrite concentration profiles for REM and Pd-Cu/REM at different potentials in the anode-cathode flow mode under different solution conditions. c) Nitrate and d) nitrite concentration profiles for REM and two Pd-Cu/REM in series at different potentials in anode-cathode mode.

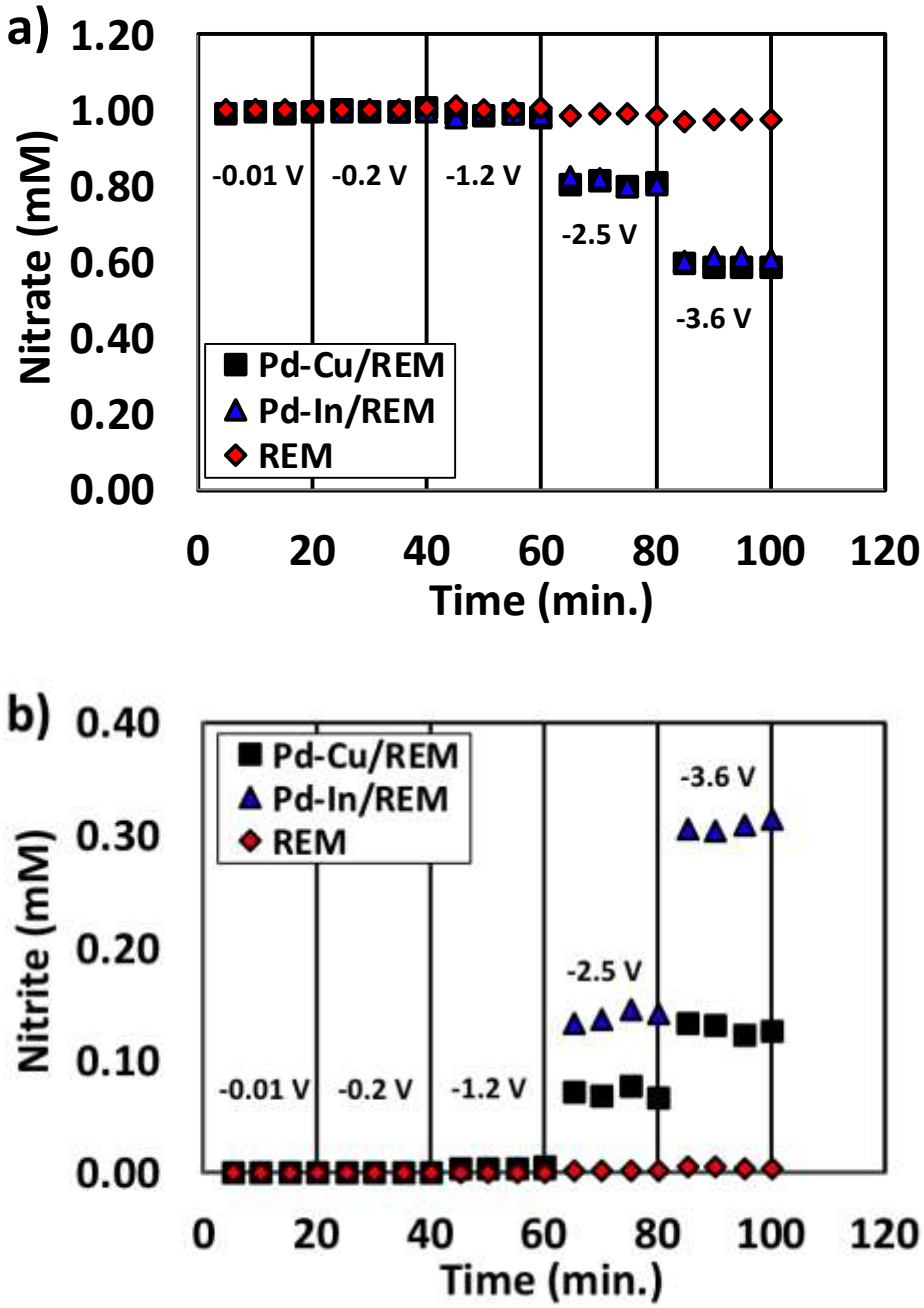

Figure 5-7. a) Nitrate and b) nitrite concentration profiles for catalyst-free REM, Pd-Cu/REM and Pd-In/REM in cathode-anode flow mode.

The extent of NO_3^- conversion for both flow modes was highest for Pd-Cu/REM, followed by Pd-In/REM and REM (Table S-5-1). Both catalysts showed significant enhancements in NO_3^- conversion compared to the REM. These results were consistent with LSV scans, which showed

increased current for Pd-M/REM compared to REM in the presence of 5 mM $NaNO_3$ (Figure S-5-4a). LSV scans also indicated that NO_3^- reduction became mass transport limited in the anode-cathode flow mode at potentials less than ~ -2.0 V/SHE (Figure S-5-4b). For both flow modes, the product selectivity was more favorable for the Pd-Cu/REM relative to the Pd-In/REM, where the later consistently had higher selectivity towards NO_2^- and NH_3. These results for electrocatalytic NO_3^- reduction are similar to catalytic batch experiments that showed that Pd-Cu was more active and selective then Pd-In.

There were also several differences in performance observed for the two flow modes. Discernable NO_3^- reduction for all REMs was observed at lower potentials for the anode-cathode flow mode (-0.2 V/SHE) compared to the cathode-anode flow mode (-1.2 V/SHE). The extent of NO_3^- conversion was greater for the anode-cathode flow mode relative to the cathode-anode flow mode at a given potential (Figures 5-6 and 5-7). For example, at a potential of -2.5 V/SHE NO_3^- conversion for the Pd-Cu/REM was approximately 20% in cathode-anode flow mode and 43% in anode-cathode flow mode (Table 5-2). The most noticeable difference between the two flow modes was related to the distribution of NO_3^- reduction products. The cathode-anode flow mode resulted in high selectivity towards both NO_2^- and NH_3, while the selectivity in the anode-cathode flow mode was primarily towards N_2 and N_2O (Table S-5-1, Table S-5-2 and Table 5-2). At a potential of -2.5 V/SHE, NO_3^- selectivity for the Pd-Cu/REM in the cathode-anode flow mode was $S_{NO_2^-}$ = 35%, S_{NH_3} = 31%, S_{N_2O} = 13%, and S_{N_2} = 23%; and the selectivity in the anode-cathode flow mode was $S_{NO_2^-}$ = 0.07%, S_{NH_3} < 2.3%, S_{N_2O} = 71%, and S_{N_2} = 29% (Table 5-2).

Table 5-2. Summary of results for nitrate reduction with a Pd-Cu/REM at a cathodic potential of -2.5 V/SHE

Reaction Conditions	**NO_3^- Conversion (%)**	**S(NO_2^-) (%)**	**S(NH_3) (%)**	**S(N_2O) (%)**	**S(N_2) (%)**	**Effluent pH**	**CE (%)**	**E_{EO} (kWh m^{-3})**	**EC (kWh mol^{-1})**
Cathode-Anode/Ar Purging	20 ± 1.02	35 ± 2.4	31 ± 2.3	12 ± 0.09	23 ± 0.91	9.8 ± 0.2	60 ± 2.4	2.6 ± 0.06	1.9 ± 0.02
Anode-Cathode/Ar Purging	43 ± 2.2	0.07 ± 0.02	< 2.3 ± 0.11	70 ± 0.38	29 ± 0.72	9.2 ± 0.1	102 ± 5.7	1.1 ± 0.23	0.90 ± 0.07
Anode-Cathode/Air Purging	42 ± 1.8	0.78 ± 0.04	< 2.3 ± 0.1	55 ± 0.29	43 ± 1.01	9.4 ± 0.2	106 ± 5.4	1.1 ± 0.12	1.06 ± 0.03
Anode-Cathode/Air Purging/Bicarbonate Buffer	44 ± 1.4	0.56 ± 0.02	< 2.2 ± 0.07	42 ± 0.36	57 ± 0.03	7.8 ± 0.4	51 ± 2.5	2.3 ± 0.34	1.3 ± 0.08
Anode-Cathode/Air Purging/Surface Water	32 ± 1.09	0.07 ± 0.01	< 3.1 ± 0.11	43 ± 0.32	56 ± 0.49	8.8 ± 0.2	51 ± 4.3	2.7 ± 0.17	1.4 ± 0.03
Anode-Cathode/Air Purging/Bicarbonate Buffer/Series	65 ± 1.3	0.40 ± 0.06	< 1.5 ± 0.04	43 ± 0.36	56 ± 0.94	8.0 ± 0.2	60 ± 4.2	3.5 ± 0.27	2.4 ± 0.06
Anode-Cathode/Air Purging/Surface Water/Series	51 ± 2.07	0.07 ± 0.14	< 1.9 ± 0.08	52 ± 0.84	47 ± 0.93	8.9 ± 0.3	35 ± 5.01	6.9 ± 0.13	3.7 ± 0.04

The higher NO_3^- conversion and lower NO_2^- formation for the anode-cathode flow mode relative to the cathode-anode flow mode were attributed to the placement of the counter electrode. These results were consistent with prior studies that concluded a downstream counter electrode (cathode-anode) resulted in lower conversion compared to an upstream counter electrode (anode-cathode) in the presence of a more favorable side reaction (i.e., H_2 evolution) [380]. Therefore, in our experiments the H_2 evolution reaction was more significant in the cathode-anode flow mode relative to the anode-cathode flow mode and inhibited NO_3^- conversion. The differences in H_2 production also affected the observed product selectivity in the two flow modes, as it is well accepted that product distributions are controlled by the local N:H concentration ratio [238,381]. A high N:H ratio was present in the anode-cathode flow mode and would favor N coupling reactions (e.g., N_2O, N_2), where the low N:H ratio was present in the cathode-anode flow mode and would favor hydrogenation reactions (e.g., NH_3) [238,381]. The NH_3 selectivities in the anode-cathode flow mode were much lower than previously reported selectivities (28 to 92%) for electrochemical NO_3^- reduction [382–389].

These experiments indicated that the Pd-Cu/REM operated in the anode-cathode flow mode was the most active for NO_3^- reduction and had the best product selectivity for N atom coupling. At a potential of -2.5 V/SHE the permeate concentrations were below the EPA MCLs of 0.7 mM for NO_3^- and 70 μM for NO_2^-, and NH_3 concentrations were always below the IC detection limit (< 10 μM), which was less than the WHO limit of 30 μM. Considering the higher activity and selectivity of the anode-cathode over the cathode-anode flow mode, we selected the anode-cathode flow mode for all additional experiments.

5.4.3.2 Effect of Solution Conditions. Prior studies indicated that solution conditions have an adverse effect on both catalytic NO_3^- reduction activity and product selectivity [68,237,240,245,247,248,385,390–392], but few studies have investigated the effects of solution conditions on electrocatalytic NO_3^- reduction. Therefore, electrocatalytic NO_3^- reduction experiments were performed under a variety of solution conditions, including air-saturated water, 10 mM $NaHCO_3$ buffer (pH = 8.2), and in a surface water sample (pH = 8.1) (see Table 5-2 and Table S-5-1). Both Pd-Cu/REM and Pd-In/REM were tested in the air saturated solution, and all other solution conditions were tested with Pd-Cu/REM. All experiments were conducted in the anode-cathode flow mode, and results are summarized in Figure 5-6, Figure S-5-5, and Table 5-2.

The results for NO_3^- conversion for both Pd-Cu/REM and Pd-In/REM in the air-saturated solution were similar to the Ar-saturated solution over the same applied cathodic potentials (Figure 5-6, Figure S-5-5, Table 5-2, and Table S-5-1), indicating that the ORR did not directly compete for NO_3^- reduction sites. LSV scans support this hypothesis, as measured currents were nearly identical for Ar-saturated and air-saturated electrolytes (Appendix C, Figure S-5-6). These results are attributed to the low ORR activity of the Ti_nO_{2n-1} support [220,393], promoter metals [394–396], and the Pd crystal faces observed by XRD (i.e., Pd(111) and Pd(200)) [381]. The lack of competition from the ORR during electrocatalytic NO_3^- reduction with the Pd-M/REMs is a significant advantage over other electrodes and catalytic systems that require deoxygenated solutions [245,377,397,398]. The product selectivities were also similar for the Pd-In/REM and Pd-Cu/REM in the air-saturated and Ar-saturated solutions (Figure S-5-5b, Figure 5-6b, and Table 5-2).

The extent of NO_3^- conversion was not significantly affected by any of the other solution conditions tested compared to the Ar-saturated solution, with the exception of the surface water sample that showed significant differences in NO_3^- conversion at a cathodic potential of -2.5 V/SHE. For example, the NO_3^- conversion in the surface water decreased by 1.4-fold compared to the 10 mM $NaHCO_3$ buffer solution of similar pH at -2.5 V/SHE (Figure 5-6a and Table 5-2). The inhibition in the NO_3^- reduction was most likely due to scaling from $CaCO_{3(s)}$ and $Mg(OH)_{2(s)}$ onto the catalyst surface, which occurred at high cathodic potentials, as the alkalinity decreased from 124 mg L^{-1} to 67 mg L^{-1}, Ca^{2+} concentration decreased from 0.88 mM to 0.66 mM, and the Mg^{2+} concentration decreased from 0.26 mM to 0.19 mM at a cathodic potential of -2.5 V/SHE. In a long-term treatment application mineral scaling can be overcome by periodic reverse polarity treatments to dissolve the scale. This approach has been demonstrated in other electrochemical studies [399].

The product selectivities during NO_3^- reduction were not greatly affected by the different solution conditions (Figure 5-6b, Table 5-2, and Table S-5-1). The NO_2^- concentrations were always significantly below the MCL and NH_3 concentrations were below the IC detection limit for all solution conditions and potentials tested. These results confirmed that Pd-Cu/REM was able to reduce NO_3^- from a 1 mM feed concentration to below the regulatory MCL in a single pass through the REM in the anode-cathode flow mode, without negative effects from dissolved oxygen and carbonate species and only minor effects from constituents found in surface water (e.g., Ca^{2+}, Mg^{2+}).

5.4.3.3 REMs in Series. Though the NO_3^- concentrations for all the experiments were lower than the MCL (0.7 mM) at the most cathodic potentials tested, two Pd-Cu/REMs in series were used to further decrease the NO_3^- concentrations. Experiments were performed in air-saturated

solutions containing 1 mM $NaNO_3$ and in the presence of either the 10 mM $NaHCO_3$ buffer or the surface water sample. Results are summarized in Figure 5-6, Table 5-2, and Table S-5-1. The results indicated that the electrochemical cells operated as approximately two first-order reactors in series, where NO_3^- conversion (*R*) followed equation (5-13):

$$R = 1 - \left(\left(\frac{C_p}{C_f}\right)_1\right)^n \quad (5\text{-}13)$$

where $\left(\frac{C_p}{C_f}\right)_1$ is the ratio of NO_3^- permeate and feed concentrations in a single reactor and *n* is the number of reactors in series. The measured NO_3^- conversion in the 10 mM $NaHCO_3$ buffer for two Pd-Cu/REMs operated in series were 20% (17%), 29% (31%), 44% (49%), and 65% (69%) at cathodic potentials of -0.2, -1.2, -1.9, and -2.5 V/SHE, respectively, where values in parentheses were those predicted by equation (5-13). In the presence of the surface water sample, the NO_3^- conversion for two reactors in series were 14% (7.5%), 23% (25%), 36% (43%), and 51% (54%) at cathodic potentials of -0.2, -1.2, -1.9, and -2.5 V/SHE, respectively, where values in parentheses were those predicted by equation (5-13) (Figure 5-6c and Table S-5-1). These results indicated that NO_3^- reduction could be approximated as a first order process. The lower NO_3^- conversion in the surface water sample again was most likely due to $CaCO_{3(s)}$ and $Mg(OH)_{2(s)}$ scaling, as the alkalinity decreased from 124 mg L^{-1} to 32 mg L^{-1}, Ca^{2+} concentration decreased from 0.88 mM to 0.49 mM, and the Mg^{2+} concentration decreased from 0.26 mM to 0.11 mM at a cathodic potential of -2.5 V/SHE. The product selectivities were similar for the one and two reactors in series operations.

5.4.4 Reactivity Characterization. Electrocatalytic and catalytic NO_3^- reduction were both tested in the Pd-Cu/REM flow-through system as a function of *J* (240 to 2160 LMH (6.7 x 10^{-5} to 5.4 x 10^{-4} m s^{-1})) and results are shown in Figure 5-8. The NO_2^- concentrations were low for both

catalytic NO_3^- reduction (0.10 to 0.13 µM) and electrocatalytic NO_3^- reduction (0.70 to 0.52 µM), and the NH_3 concentrations were always below the detection limit (< 10 µM) for both electrocatalytic and catalytic NO_3^- reduction at all fluxes at the different fluxes tested (Table S-5-3).

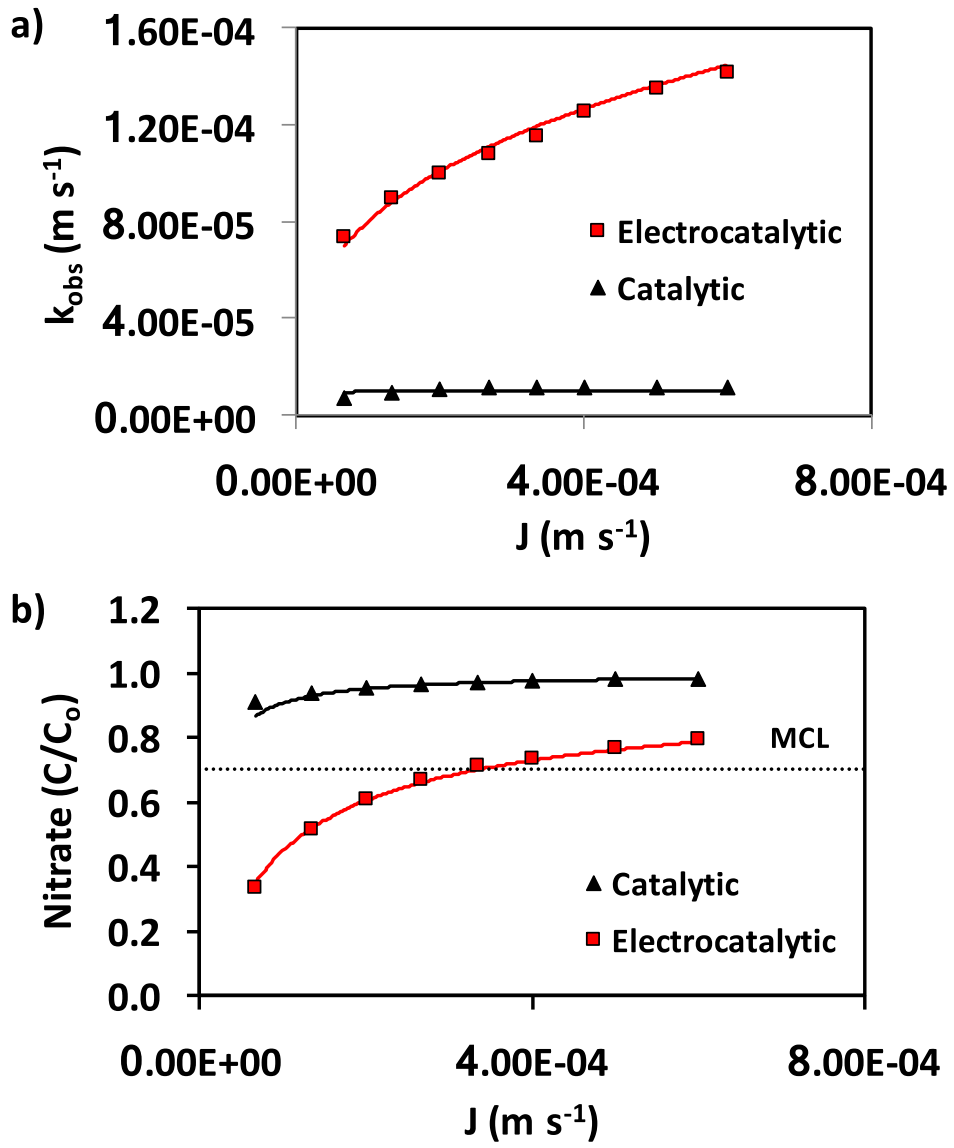

Figure 5-8. Electrocatalytic and catalytic NO_3^- reduction in the Pd-Cu/REM flow-through reactor. a) k_{obs} values versus *J*, b) NO_3^- concentration versus *J*. The solid lines are the model fits using equations 5-16 and 5-17 and the dashed horizontal line represents the MCL for NO_3^-.

Based on the analysis of the LSV data, it was determined that electrocatalytic NO_3^- removal was mass transport limited at potentials less than -2.0 V/SHE (Figure S-5-4). Therefore, at -2.5 V/SHE equation (5-14) was used to fit the electrocatlytic NO_3^- reduction data in the Pd-Cu/REM flow-through reactor.

$$\left(\frac{C_p}{C_f}\right) = \exp\left(-\frac{k_m a l}{J}\right) \tag{5-14}$$

In equation (5-14), k_m is the mass transport rate constant (m s^{-1}), a is the specific surface area (m^{-1}), and l is the reactive length of the REM (m). Values for k_m in packed bed electrochemical reactors have been shown to follow equation (5-15).

$$k_m = b\,J^{0.33} \tag{5-15}$$

where b is a proportionality constant. Since the values for a and l were unknown but constant at a given potential, equation (5-14) was rewritten as follows.

$$\left(\frac{C_p}{C_f}\right) = \exp\left(-\frac{mJ^{0.33}}{J}\right) = \exp\left(-\frac{k_{obs}}{J}\right) \tag{5-16}$$

where m is a proportionality constant that was determined to equal 0.0017 and yielded observed rate constant (k_{obs}) values between 7.0 x 10^{-5} and 1.5 x 10^{-4} m s^{-1}. The model fit of equation (5-16) to experimental data is shown in Figure 5-8.

Since the conversion of NO_3^- during catalytic experiments was small (< 10%), pseudo first-order kinetics were assumed and equation (5-16) was also used to fit the catalytic NO_3^- reduction data. However, since catalytic NO_3^- removal was much lower than the mass transport limit, k_{obs} was represented by a resistance in series model that accounts for the resistances from mass transport and reaction kinetics (equation 5-17).

$$k_{obs} = k_r / \left(1 + \frac{k_r}{k_m}\right) \tag{5-17}$$

In equation (5-17), k_r is the heterogeneous pseudo first-order reaction rate constant (m s^{-1}). Values determined for k_m from electrocatalytic experiments were used in equation (5-17) and a best fit value of k_r = 1.1 x 10^{-5} m s^{-1} was determined by fitting equation (5-17) to the experimental data (Figure 5-8). These results indicated that the k_{obs} values for catalytic NO_3^- reduction were approximately an order of magnitude less than those for electrocatalytic NO_3^- reduction, which indicated that electrocatalysis was the predominant mechanism for NO_3^- removal in all REM flow-through experiments, as the retention times (0.2 to 2.2 s) in the REM were too short to allow for significant catalytic NO_3^- reduction. Identical experiments were also performed for NO_2^- reduction, and the extent of removal with respect to *J* were similar to those for both electrocatalytic and catalytic NO_3^- reduction (Figure S-5-7), which explains why only trace NO_2^- concentrations were detected in all experiments. These results indicated the extreme promise of electrocatalyic reduction to achieve significant NO_3^- removal without significant NO_2^- production under single pass operation.

5.4.5 Technological and Environmental Implications. Sustainable water treatment technologies need to operate with minimal energy consumption. The energy requirements were calculated according to equations 5-8 and 5-9 and are reported in Table 5-2 and Table S-5-4. The E_{EO} and *EC* values showed the following order for energy efficiency: REM < Pd-In/REM < Pd-Cu/REM (Table 5-2 and Table S-5-4). The minimal *EC* and E_{EO} values for Pd-Cu/REM (EC = 0.57 kWh mol^{-1}; E_{EO} = 1.1 kWh m^{-3}) and Pd-In/REM (EC = 0.89 kWh mol^{-1}; E_{EO} = 1.7 kWh m^{-3}) were observed for the reduction of the Ar-saturated 1 mM $NaNO_3$ solutions with the anode-cathode flow mode. These values approximately doubled for the reduction of the air-saturated surface water solution with the Pd-Cu/REM (EC = 1.1 kWh mol^{-1}; E_{EO} = 2.3 kWh m^{-3}). The *EC* values were also calculated for the reduction of NO_3^- at concentrations of 1, 10 and 100 mM using the

Pd-Cu/REM in anode-cathode flow mode. EC values decreased with increasing NO_3^- concentrations, and were 0.62 ± 0.02, 0.19 ± 0.07, and 0.12 ± 0.06 kWh mol^{-1} at NO_3^- concentrations of 1, 10, and 100 mM, respectively. The calculated EC values for dilute solutions are comparable to literature values for electrochemical reduction, electrodialysis, and biological methods (0.4 to 1.2 kWh mol^{-1}) [83,400–402], and much lower than that for reverse osmosis (8.3 kWh mol^{-3}) [403]. Concentrated NO_3^- solutions showed much more favorable *EC* values, due to increased solution conductivity and a 2.3 times positive shift in the redox potential for every 10-fold increase in NO_3^- concentration, according to the Nernst equation. Therefore, coupling the REM system to technologies that separate and concentrate NO_3^- should be explored. Further improvements in electrode preparation and reactor design could lead to reduced energy consumption and more efficient utilization of the catalytic metals. For example, narrowing the inter-electrode gap will reduce solution resistance and thus lower overall cell potential, and more efficient dispersion of the catalyst metals will allow for lower loadings of precious metals.

Current efficiencies were also calculated based on the observed product distributions (Table S-5-1 and Table 5-2). The current efficiencies were calculated between 1.9 to 12% for the REM, 2.1 to 105% for the Pd-Cu/REM, and 2.3 to 71% for the Pd-In/REM. The maximum measured current efficiency for Pd-Cu/REM (105 ± 5.4%) was in the presence of air purging and 1 mM $NaNO_3$. The current efficiency was observed to decrease to between 51 and 52% in the presence of the 10 mM $NaHCO_3$ or surface water solutions (Table S-5-1 and Table 5-2). These results were attributed to the higher ionic conductivity and proton donor ability of the HCO_3^- electrolyte that gave rise to increased H_2 evolution. The range of current efficiencies observed in this study were comparable to values reported in the literature (6.2 to 90%) for different electrocatalysts [247,382,383,389,404].

Results of this study indicated that significant electrochemical NO_3^- reduction was achieved in the Pd-M/REM system with minimal NO_2^- and NH_3 production. However, the selectivity towards N_2O was significant for all the NO_3^- reduction experiments with Pd-M/REMs. The formation of N_2O has environmental implications as it acts as a greenhouse gas that destroys stratospheric ozone [405,406]. The reduction of N_2O to N_2 has been shown to occur on Pd electrocatalysts with 100% selectivity [381]. However, in our studies the residence time (< 2 s) in the REM reactor was too short for significant conversion of N_2O to N_2. For the treatment of dilute NO_3^- solutions (mM levels) the total N_2O flux is small compared to natural sources. The N_2O flux (CO_2 equivalent) was calculated as 9.6×10^5 kg yr^{-1} assuming 100% reduction of 10^6 L 1 mM NO_3^- solution per day to N_2O. This estimate was < 0.0003% of the N_2O production rate estimated by the U.S. EPA in 2015 from all U.S. sources (3.3×10^{11} kg yr^{-1}) [407]. However, more selective electrocatalysts or passing the permeate through an additional Pd catalyst bed at a lower flow rate would eliminate N_2O outgassing to the atmosphere. For the treatment of concentrated NO_3^- solutions, the produced N_2O could be recovered and used as an energy source, which would improve the energy efficiency of the treatment process. Such a strategy has been proposed for the biological treatment of nitrogen in wastewater [408,409].

5.5 Conclusions

In this study Pd-Cu/REM and Pd-In/REM were shown to be active for NO_3^- reduction. Electrocatalytic NO_3^- reduction was investigated as a function of electrode placement, flow rate, electrode potential, NO_3^- concentration, reactor number, and under various solution conditions indicative of natural waters. Optimal performance was achieved with a Pd-Cu/REM with an upstream counter electrode. This setup was able to reduce NO_3^- from a 1 mM feed concentration to below the EPAs regulatory MCL in a single pass through the REM (residence time ~ 2 s). The

concentrations of NO_2^- were always below the EPA's MCL and NH_3 concentrations were not detected. Nitrate reduction was not affected by dissolved oxygen, carbonate species, or natural organic matter, and NO_3^- reduction only slightly decreased in a surface water sample due to Ca^{2+} and Mg^{2+} mineral scaling. The maximum current efficiency of 105 ± 5.4% was achieved for the Pd-Cu/REM with an upstream counter electrode and a 1mM $NaNO_3$ solution. The current efficiency decreased to ~ 51% for a surface water sample, which was attributed to competition from H_2 production. The energy consumption for the surface water sample was between 1.1 to 1.3 kWh mol^{-1} at 1 mM NO_3^- concentrations, and decreased with increasing NO_3^- concentrations, and was 0.19 and 0.12 kWh mol^{-1} for 10 and 100 mM NO_3^- solutions, respectively.

5.6 Acknowledgements

We thank Dr. Yin Wang from the University of Wisconsin-Milwaukee for BET analysis. Funding for this work was provided by a National Science Foundation CAREER award to BPC (CBET-1453081).

6. Electrochemical Oxidation of Organic Compounds using Bismuth-doped Tin Oxide deposited Reactive Electrochemical Membranes

6.1 Abstract

In this research, bismuth-doped tin oxide (BDTO) catalyst loaded reactive electrochemical membranes (REM) were synthesized, characterized and applied to determine the performance towards organic compound oxidation in a water matrix. Porous Magnéli phase (Ti_nO_{2n-1}, n = 4 to 6) REMs were fabricated by sintering TiO_2 powder and modified with BDTO catalyst using pulsed laser deposition (PLD) and pulsed electrodeposition followed by thermal oxidation (EDT). The electrodes were characterized using scanning electron microscopy (SEM), energy dispersive spectroscopy (EDS), X-ray photoelectron spectroscopy (XPS), X-ray diffraction (XRD), inductively coupled plasma optical emission spectroscopy (ICP-OES) and linear scanning voltammetry (LSV). The SEM images showed that the average size of the deposited BDTO particles using EDT method was around 2 µm. The XPS results showed the presence of a mixture of SnO_2, SnO, and Bi_2O_3 on BDTO modified REM using EDT method. Terephthalic acid (TA) was used as hydroxyl radical probe, whereas atrazine (ATZ) and clothianidin (CDN) were chosen as potential harmful herbicide and pesticide, respectively, which may be present in surface and groundwater. DFT simulations coupled with Marcus theory provided potential dependent activation energy profiles for ATZ and CDN, which were supported by the LSV data. At all the applied potentials, BDTO deposited REM (REM/BDTO) showed higher oxidation rates compared to REM, which was attributed to enhanced production of $OH^{\bullet}$. At the highest applied potential (3.5 V/SHE), the concentrations of TA, ATZ, and CDN were all below the detection limits for REM/BDTO. Chemical oxygen demand (COD) analysis of TA and total N analysis of ATZ and CDN showed complete mineralization of the compounds at this applied

potential. The energy consumption for REM/BDTO was determined to be 2.7-times lower than that for REM for TA oxidation at 3.0 V/SHE.

6.2 Introduction

The electrochemical advanced oxidation process (EAOP) is an efficient and novel technique for electrochemical water and wastewater treatment application due to its ability for destruction and removal of recalcitrant organic compounds [52,53,111,159]. Reactive electrochemical membrane (REM) has been considered one of the best EAOP electrodes and it combines EAOP and physical separation technique into a single setup [50,54,114,274,410,411]. REMs are efficient and effective at oxidizing recalcitrant organic compounds via EAOP that involves the production of $OH^{\bullet}$ and direct electron transfer (DET) reactions [50,54,114,274,410,411]. The formation of $OH^{\bullet}$ is very effective for organic compound removal because it reacts unselectively with several organic compounds at diffusion-limited rates without any oxidant residual [62].

Several porous and non-porous EAOP electrodes have been used for water and wastewater treatment applications and the most promising materials include boron-doped diamond electrode (BDD), substoichiometric TiO_2, doped-TiO_2, PbO_2, and doped-SnO_2 [47–50,53,55–57,62,114,124,275–279]. The slow leaching of Pb for PbO_2 electrode and high cost associated with BDD fabrication limited their application for water treatment [280,281]. However doped-TiO_2 and –SnO_2 does not suffer from severe problems such as toxic metal leaching and high fabrication cost [280,281]. The doping of TiO_2 using a reductant (e.g. H_2) has been widely used to form highly conductive, porous and monolithic Magnéli phase (Ti_nO_{2n-1}, n = 4 to 10) electrodes [64,219,227]. Among all the Magnéli phases Ti_4O_7 has been found to be the most conductive one with conductivity of 1000 S cm^{-1} [219]. Due to high conductivity, porous structure, corrosion resistance, mechanical strength, and ability to produce $OH^{\bullet}$, Ti_nO_{2n-1} anodes

have been used as REMs for the electrochemical oxidation of recalcitrant organic compounds in water. Doped-SnO_2 has been used as another effective anode-coating material for electrochemical oxidation of organic compounds due to high conductivity and stability [47,57,278]. A very high oxygen evolution potential (OEP) of doped-SnO_2 has been reported as 1.7 V vs Ag/AgCl which, facilitated water oxidation for $OH^{\bullet}$ production before O_2 evolution [282,283]. Due to high OEP of doped-SnO_2, it can be used as an anode to utilize EAOP for electrochemical organic oxidation. Different dopants (e.g. Sb, Bi, P) have been used for SnO_2 doping, where Sb was the most common dopant [282,284–286]. However, the application of Sb doped SnO_2 for water treatment applications is undesirable, due to high toxicity of Sb (EPA MCL = 6 ppb) [10]. Bi-doped SnO_2 (BDTO) coated carbon nanotubes with very high OEP (1.71 V vs Ag/AgCl) have been recently used for electrochemical oxidation of organic compounds with improved reactivity, current efficiency, and energy consumption relative to bare carbon nanotubes [282]. Therefore Bi-doped SnO_2 deposited REM can be used to oxidize recalcitrant organic compounds in water matrix due to their combined attributes such as higher conductivity, higher $OH^{\bullet}$ production, improved reactivity, better current efficiency and high stability.

Porous, conductive and monolithic electrodes used in flow-through mode have been recently used for improved electrochemical organic oxidation rates. In flow-through mode the flow was convected perpendicular to the porous electrode, which increased the mass transfer rates compared to the conventional parallel flow mode. A recent work by Guo and Chaplin showed convection-enhanced rate constant with high membrane flux with plateauing observed rate constant values (k_{obs}), which approached the kinetic limit [64]. REM in combination with BDTO may be able to minimize the kinetic limitation due to the enhanced reactivity of BDTO towards organic compounds oxidation.

Atrazine (ATZ) (2-chloro-4-ethylamine-6-isopropylamino-*s*-triazine) is one of the highly used triazine based herbicide to minimize annual broadleaf growth and emergence and grass weeds in various food plants, vegetables as well as in non-agricultural areas [412–417]. ATZ is one of the most common pollutants found in ground and surface waters worldwide, due to its excessive application in agricultural areas [418–422]. ATZ is highly resistant to bacterial degradation, hydrolysis, and moderately soluble in natural waters with a half-life ($t_{1/2}$) of >200 days, which makes ATZ a persistent water contaminant [423]. EPA has set a maximum contaminant level (MCL) for ATZ at 3 ppb (14 nM) because it resulted in incomplete ossification, neurological disorder, cancer, damage of heart, liver and kidney and adverse effect on reproductive system and developing organisms [423–425]. Clothianidin (CDN) ((E)-1-(2-chloro-1,3-thiazol-5-ylmethyl)-3-methyl-2-nitroguanidine) is a nitroguanidine subgroup of nicotinoids that has been extensively used as an insecticide [426–431]. CDN is very stable under hydrolysis and can remain stable in surface water, groundwater, and soil environments with half-lives ranging from days to years (aerobic soil ($t_{1/2}$) = 148 – 1155 days, anaerobic aquatic ($t_{1/2}$) = 27 days) [432,433]. CDN has shown toxic effects such as impaired learning and homing behavior on non-target insects such as honey bees [428,429,434–437]. EPA has not set an MCL for CDN as it has not shown severe effects (e.g. carcinogenicity, genotoxicity, and developmental toxicity) on mammalian species, due to its low affinity to the nicotinic acetylcholine receptor of mammals. However recent studies have shown that CDN can cause several sub-lethal effects such as cytotoxicity, genotoxicity, and immunotoxicity [438,439]. Due to its chronic toxicity EPA has put a time-limited tolerance of 280 nM on CDN [440]. Therefore complete removal of ATZ and CDN from water matrices is highly necessary as they can pose serious health hazards to humans.

Several physical, biological, chemical, photochemical and electrochemical techniques have been used as destructive treatment methods to remove ATZ from water matrices [441–478]. However, only a single study showed photocatalytic removal of CDN from water [479]. Physical techniques mainly used different adsorbents for ATZ removal [472–477]. Physical techniques only separate ATZ from the water matrices and do not eliminate it from the environment. Biological treatment of ATZ used different types of bacteria and microorganism to degrade it [441–443]. However, application of biological treatment suffered from bacterial contamination and low removal efficiency. The photochemical techniques mainly used UV light in the presence of different materials with activated chemicals to successfully degrade ATZ [452,453,458,463–467,469–471,479]. The chemical treatment used fenton and ozonation process that required the addition of Fe(II), H_2O_2, and O_3 for the degradation of ATZ [444,446–451,454,457,472,474]. The chemical and photochemical techniques suffered from low ATZ removal rates, formation of reaction byproducts, and high cost due to the addition of chemicals. However only few electrochemical techniques have been used to oxidize ATZ in water [455,459–462,473]. All the electrochemical techniques used for ATZ oxidation in the previous studies used batch system for removal [455,459–462,473]. However the oxidation/mineralization of ATZ and CDN using catalyst loaded REM with continuous flow-through mode has not been investigated.

Most of the previous studies showed partial oxidation and mineralization of ATZ to various products [441–450,453–456,460,461,466–479]. However few studies showed complete mineralization of ATZ [480–484].

In this study, BDTO catalysts are deposited on sub-stoichiometric TiO_2 REMs followed by characterization and study for terephthalic acid (TA) oxidation with oxidation rate constant evaluation in a flow-through setup. TA oxidation was performed with different potentials as well

as with different flow rates and the rate constants were determined for both cases. A kinetic model was used to evaluate the experimental data and calculate rate constants for TA oxidation. Various catalyst deposition techniques were used to determine an optimal method. Chemical oxygen demand (COD) was performed for TA oxidation to determine the extent of mineralization in the permeate. ATZ and CDN oxidation were also tested on catalyst loaded REM because of their potential toxicity in water matrix. Total N analysis was performed on the feed and permeates to show the extent of oxidation/mineralization of ATZ and CDN at different applied potentials.

6.3 Materials and Methods

6.3.1 Reagents. All chemicals were reagent grade and purchased from Sigma-Aldrich and Fisher Scientific. All gases (purity = 99.999%) were obtained from Praxair. BDTO precursor target ($Sn_{0.91}Bi_{0.09}O_2$, 99.9%) for pulsed laser deposition (PLD) application was procured from Kurt J. Lesker (Jefferson Hills, PA). Chemicals were received and used without further modification. All experimental solutions were made using Type I water (> 18.2 MΩ.cm at 25°C) from a Barnstead NANOpure system (Thermo Scientific).

6.3.2 Catalyst Loaded REM Preparation. Magnéli phase REMs were prepared from Magnéli phase powder (Ti_nO_{2n-1}) (n = 4, 6). Initially, the Magnéli phase powder was synthesized from TiO_2 powder by reducing at 1050 °C under H_2 gas flow in a tube furnace (OTF-1200X, MTI) for 6 hours. After that, a certain amount of Magnéli phase powder was weighed and mixed with paraffin oil as binder (8 drops per g of powder). Then, approximately 0.6 g of the binder mixed powder was poured into a stainless steel (SS) die and pressed using a hydraulic press under a uniaxial pressure of 20.7 bar that gave a 2.5 mm thick, 1.1 cm diameter REM pellet. Then the

pellet was heated in the tube furnace at 1050 ^{0}C for 6 hours under H_2 flow to remove the binder and sinter the particles. The as prepared pellet was designated as the "REM".

Catalysts (BDTO) were deposited on the REMs using two different methods: pulsed laser deposition (PLD) and pulsed electrodeposition followed by thermal oxidation (EDT). PLD method used 20 laser pulses in the presence of BDTO precursor target to modify the REM with BDTO and the modified electrode was designated as "REM/BDTO/PLD20". Initially the PLD chamber was pumped down to 5×10^{-6} - 9×10^{-6} Torr using a turbo-molecular pump (Pfeiffer Vacuum, Germany) and the temperature in the chamber was maintained at 25 ^{0}C. The REM was placed 5.0 cm away from the BDTO target ($Sn_{0.91}Bi_{0.09}O_2$) during the PLD process. PLD method used a krypton fluoride excimer laser (COMPexPRO201, Coherent, CA, USA) at a wavelength of 248 nm with laser frequency, number of pulses, pulse duration, energy density, and laser energy of 10 Hz, 20, 25 ns, 3 mJ cm^{-2} and 400 mJ, respectively.

BDTO modified REM using EDT method (REM/BDTO/EDT) used pulsed electrodeposition in the presence of precursor solution followed by thermal oxidation in DI water. The precursor solution (Sn:Bi = 10:1, mol/mol) was prepared by dissolving 2.25 g of $SnCl_2$, $2H_2O$ and 0.48 g of $Bi(NO_3)_3$, $5H_2O$ in 1000 mL 1 M HCl solution. Pulsed electrodeposition was used in the presence of the precursor solution and it was pumped through the REM cathode followed by a BDD anode. The parameters for pulsed electrodeposition are as follows: current density = -100 mA cm^{-2}, pulse on (t_{on}) = 10 ms, pulse off (t_{off}) = 1000 ms, and number of pulses = 3564. After electrodeposition, the metal deposited REM was heated in DI water at 80 ^{0}C for 1 hour to oxidize the metals to metal oxides. After that, the REM/BDTO/EDT was dried in an oven at 50 ^{0}C for 3 hours.

6.3.3 Batch Organics Oxidation Experiments. Batch oxidation experiments of ATZ and CDN were performed in a two-compartment (H-cell) jacketed glass reactor using conventional three-electrode rotating disk electrode (RDE) setup (Pine Instruments, PA) according to the previously published studies [167,485]. Different temperatures (20, 30 and 40 ^{0}C) were maintained using a water bath (Thermo Scientific Neslab RTE 7). To separate the anodic and cathodic reactions a Nafion N115 membrane (Ion Power, Inc., New Castle, DE) has been used. For ATZ oxidation, 1.5 and 1.8 V/SHE were applied at the three different temperatures whereas 1.14 and 1.5 V/SHE were used for CDN oxidation. Normalized concentrations of ATZ and CDN were plotted versus time to determine the reaction rate constants (k) at different temperatures and potentials (Figure S-6-1). For example, at a constant anodic potential of 1.5 V/SHE ATZ was oxidized with time at 20, 30 and 40 ^{0}C and a first order concentration profile was fitted to determine the rate constants at different temperatures. After that ln(k) values were plotted against inverse of temperature (1/T) according to the Arrhenius equation.

6.3.4 Flow-through Organics Oxidation Experiments. Electrochemical oxidation of organic compounds (TA, ATZ and CDN) was performed with the REM, REM/BDTO/EDT, and REM/BDTO/PLD20 in a flow-through reactor. The flow-through cell was made of polyether ether ketone (PEEK) and contained the REM/BDTO as the working electrode, 316 SS as the counter electrode, and a 1 mm diameter Ag/AgCl/KCl (1M) as reference electrode (Harvard Apparatus, MA, USA). The reference electrode was placed at a distance of ~3.3 mm from the working electrode. Potentials and currents for all electrochemical experiments were applied by a Gamry Reference 600 potentiostat/galvanostat (Warminster, PA). All potentials were solution potential drop corrected (iR_s) and documented versus the standard hydrogen electrode (/SHE). Only anode-cathode flow mode was used for organics oxidation experiments. The working

electrode (REM) is placed upstream, and solution first flows through the REM anode followed by the SS cathode in the anode-cathode flow mode (Figure S-6-2).

Oxidation experiments were performed using either TA (1 mM), ATZ (10 μM), or CDN (10 μM) in 100 mM KH_2PO_4 as feed solution with anode-cathode flow mode. The oxidation experiments were studied at the OCP as well as at different anodic potentials of 2.1, 2.6, 3.0 and 3.5 V/SHE while pumping the feed solution through the REM at 0.5 mL min^{-1} to show the effect of potential. At a constant anodic potential of 3.0 V/SHE, the feed solution was pumped through the REM pellet at flow rates ranging from 0.2 to 1.0 mL min^{-1}, which gave surface area normalized membrane fluxes (J) of 240 to 1200 L m^{-2} h^{-1} (LMH) to show the effect of flow rates. With the feed flow through the REM, the anodic potential was applied and permeate was collected for anion, cation, and organic concentration analysis. As NH_3 is a possible reaction product from ATZ and CDN oxidation, samples were collected and immediately acidified with 0.1 M HCl (pH 3.0) to convert NH_3 to NH_4^+.

6.3.5 Membrane Characterization. The REM, REM/BDTO/EDT and REM/BDTO/PLD20 samples were characterized by X-ray diffraction (XRD, Siemens D-5000) with a Cu X-ray tube (40 kV and 25 mA). Scans were monitored and analyzed using DataScan software (MDI, v. 4.3.355, 2005) at a step size and dwell time of 0.01° and 0.5 s, respectively. The electrodes were also characterized using X-ray photoelectron spectroscopy (XPS) with a Kratos Axis-165 at the Research Resource Center at the University of Illinois at Chicago. The XPS spectrum was analyzed and deconvoluted using XPSPEAK 4.1 software. To investigate surface morphology before and after catalyst deposition, scanning electron microscopy (SEM) was performed using a variable pressure scanning electron microscope (VPSEM) (Hitachi S-3000N, Japan) at 3 to 4 kV and from 3 to 4 k magnifications. To show the elemental distribution and concentration of the

BDTO catalysts within the REMs, SEM coupled with energy dispersive X-ray spectroscopy (EDS) was used on the surface as well as on the X-section of different REMs. An acid digestion method using a mixture of 2 mL H_2O_2 (30 %), 4 mL HF (10 %), 8 mL HNO_3 (70 %), and 10 mL HCl (37 %) was performed to determine the metal loading of the REM/BDTO/EDT and REM/BDTO/PLD20. The pellet (0.5 – 0.6 g) was crushed into powder and the powder with the acid mixture was introduced into a 50 mL Teflon digestion tube that was heated at 200 ^{0}C for 1 hour. Elemental concentrations of Bi and Sn were measured in these acid extracts using a Thermo iCAP 7600 Inductively Coupled Plasma-Optical Emission Spectroscopy (ICP-OES) (detection limit ~ 1 - 3 ppb).

Electrochemical impedance spectroscopy (EIS) was used to measure the through plane electrical conductivity (σ) for the REM, REM/BDTO/EDT and REM/BDTO/PLD20. The EIS used an amplitude of ±7 mV about the open circuit potential (OCP) and a frequency range of 0.5 to 100 kHz with a Gamry Reference 600 potentiostat/galvanostat. The electrical conductivities were calculated according to the following equation:

$$\sigma = \frac{x}{AR} \tag{6-1}$$

where, R is the measured resistance (ohm) of the different REMs, A is the pellet cross-sectional area (1 cm^2) and x is the pellet thickness (0.25 cm).

6.3.6 Electrochemical Characterization Methods. Linear sweep voltammetry (LSV) scans were used with two different electrodes (BDD and REM/BDTO) with ATZ and CDN to show the oxidation potential of the compounds. LSV experiments were performed in either 10 µM ATZ or 10 µM CDN in a 100 mM KH_2PO_4 background electrolyte. The potential was swept from 0.2 V/SHE to 2.0 V/SHE at a scan rate of 100 mV s^{-1}. LSV scans were also performed at the scan

rates of 10, 20, 40, 60, 80 and 100 mV sec^{-1} in either 10 µM ATZ or 10 µM CDN in a 100 mM KH_2PO_4 background electrolyte to understand the rate controlling mechanism for oxidation.

6.3.7 Analytical Methods. Concentrations of NO_3^- and NH_4^+ were determined using IC (Dionex ICS-2100). Anions concentrations were measured using an anion exchange column (Dionex IonPac AS18) and cations were determined using a cation exchange column (Dionex IonPac CS16). Concentrations of TA, ATZ, and CDN were determined using a Shimadzu UFLC XR HPLC with a Phenomenex Kinetex® 5 µm C18 column and a photodiode array (PDA) detector (Nexera X2, Shimadzu) (190 nm – 300 nm). HPLC with a fluorescent detector (RF-20A, Shimadzu) was utilized to measure 2-hydroxyterephthalic acid (HTA) concentration (λ_{ex} = 315 nm and λ_{em} = 435 nm). The mobile phase was a mixture of methanol and 0.1% formic acid in DI water (60:40) at 1.0 mL min^{-1} flow rate for TA and HTA quantification. A mobile phase consisting of a mixture of methanol and DI water (55:45) was used at a flow rate of 1.0 mL/min for ATZ and CDN concentration measurements,. Chemical oxygen demand (COD) for TA oxidation was determined using Hach method 8000 (USEPA Reactor Digestion Method). Total nitrogen (N) for ATZ and CDN oxidation was determined through oxidative digestion of all dissolved nitrogen species present in the permeate, followed by IC detection of NO_3^- [370].

6.3.8 Quantum Mechanical Simulations. Density functional theory (DFT) simulations were done using Gaussian 09 software [350]. Unrestricted spin, all-electron calculations were done using the 6-31G+(d) and 6-311G+(3df, 2p) basis set for frequency optimization and energy calculations, respectively. 0.9806 and 0.989 were used as scale factors to correct the systematic errors involving frequency optimization and energy calculations, respectively [486]. The gradient corrected Becke, three-parameter, Lee−Yang−Parr (B3LYP) functional was utilized for exchange and correlation. SMD model was used for the simulation of implicit water solvation

[353].

DFT simulation was performed to interpret the experimental data, determine standard reduction potential for DET (E^0) and total reorganization energy for the oxidation reaction (λ_f), and determine the activation energy (E_a) for both ATZ and CDN oxidation using E^0 and λ_f values. The E^0 values were calculated according to the following equation:

$$E_0 = -\frac{\Delta_r G^0}{nF} - E^0_{abs}(SHE) \quad (6\text{-}2)$$

Where, $\Delta_r G^0$ is free energy for reduction, F is the Faraday constant, *n* is the number of electrons transferred, and $E^0_{abs}(SHE)$ absolute standard reduction potential reference value of SHE ($E^0_{abs}(SHE)$ = 4.28 eV) [487,488].

Gibbs free energy of activation (E_a) for DET reaction for ATZ and CDN oxidations were determined using Marcus theory according to the following equation [340]:

$$E_a = \frac{\lambda_f}{4}\left[1 - \frac{96.5(E - E^0)}{\lambda_f}\right]^2 \quad (6\text{-}3)$$

Where, E is the applied electrode potential and λ_f is the energy needed to alter the structure of reactant to that of the product, which is calculated by subtracting the free energy of the reactant from a compound with the same charge as the reactant and identical product geometry. The effect of background electrolyte on λ_f was not considered as previous researches showed negligible effects in polar solvents [340].

6.3.9 Current Efficiency and Energy Consumption Calculations. Current efficiency (*CE*) was calculated using the following equation:

$$CE(\%) = \frac{JFz(C_f - C_p)}{j} \times 100 \quad (6\text{-}4)$$

where z is the moles of electrons transferred per moles of reactant, j is the current density (A cm^{-2}), F is the Faraday constant (96485 C mol^{-1}), and C_f and C_p are feed and permeate concentrations (mol m^{-3}) of the organics, respectively. All flow-through experiments were performed at room temperature (22 ± 1 °C). Values for z were determined based on the extent of mineralization, which was measured by COD and total N analyses.

The E_{EO} metric is a measure of the electric energy (kWh m^{-3}) needed to reduce the NO_3^- concentration by 1 order of magnitude per unit volume of solution [371,489], that is normalized by contaminant concentration and is given by the following equation.

$$E_{EO} = 10^{-3} \times \frac{V_{cell} I}{Q \log\left[\frac{C_f}{C_p}\right]} \tag{6-5}$$

where, V_{cell} is the cell potential (V), I is the current (A), and Q is the volumetric flow rate of the permeate (m^3 h^{-1}).

6.4 Results and Discussion

6.4.1 Material Characterization. The pore radius of the REMs was determined by fitting the Hagen-Poiseuille equation to flux versus trans-membrane pressure data (Appendix D, Figure S-6-3). The pore radius of the REMs were determined as 0.41 ± 0.03, 0.36 ± 0.02, and 0.40 ± 0.04 µm for the REM, REM/BDTO/EDT, and REM/BDTO/PLD20, respectively. These results confirmed that the pore size did not change significantly due to catalyst deposition (Appendix D). ICP-OES was performed on acid digested samples to determine the bulk elemental compositions of the REM, REM/BDTO/EDT, and REM/BDTO/PLD20 samples. The molar ratios of Bi:Sn was determined as 6.9 ± 0.02 for REM/BDTO/EDT, which was not in line to the ratio (10:1) of Sn and Bi in the precursor solution. This may be due to the higher susceptibility of deposition of Bi than Sn under reduction current which is due to the more positive reduction

potential for Bi (0.317 V vs SHE) than that of Sn (-0.14 V vs SHE). The catalyst metals were not detected on the REM and REM/BDTO/PLD20 sample. The amount of catalyst for REM/BDTO/PLD20 was lower than the ICP-OES detection limit (1 - 3 ppb). The calculated ratio for REM/BDTO/EDT was similar to that of the deposited ratio which confirmed successful catalyst deposition on REMs using the pulsed electrodeposition (EDT) method.

The XRD was performed only on REM and REM/BDTO/EDT as the catalyst loading on the REM/BDTO/PLD20 was below the detection limit. Figure 6-1 shows the XRD data for REM and REM/BDTO/EDT along with the XRD characteristic peaks for Ti_4O_7, Ti_5O_9, Ti_6O_{11}, SnO_2, SnO, and Bi_2O_3. The XRD data for the REM showed that the REM contained mainly Ti_4O_7 crystal faces without any other phases (e.g. Ti_5O_9 and Ti_6O_{11}). However, peaks for Ti_5O_9 ((11-4), (022)) and Ti_6O_{11} ((2210), (1-2-11), (2010)) appeared along with the Ti_4O_7 peaks for REM/BDTO/EDT. The formation of more oxidized phases (Ti_5O_9 and Ti_6O_{11}) on the REM/BDTO/EDT sample was attributed to the thermal oxidation step during synthesis. The XRD data for REM/BDTO/EDT showed the presence of SnO_2(110), SnO_2(101), SnO_2(200), SnO(112), and Bi_2O_3(440) for REM/BDTO/EDT. This result confirmed that Sn was present mainly in the form of SnO_2 and SnO and Bi in the form of Bi_2O_3.

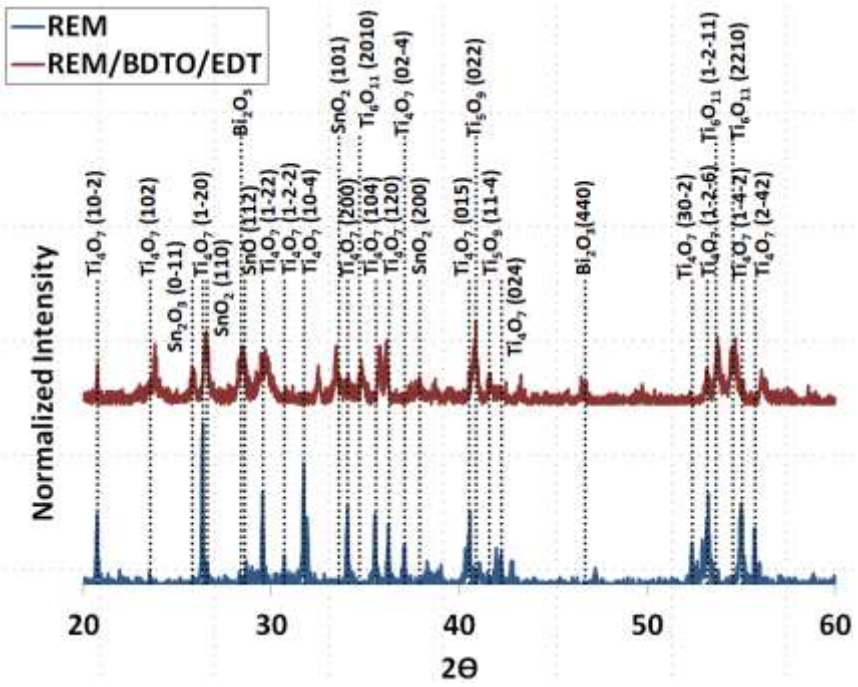

Figure 6-1. XRD data for REM and REM/BDTO/EDT with Ti_4O_7, Ti_5O_9, Ti_6O_{11}, SnO_2, SnO and Bi_2O_3 characteristic peaks.

The through plane conductivity (σ) of the REM, REM/BDTO/EDT, and REM/BDTO/PLD20 were measured as 882 ± 32, 816 ± 19 and 943 ± 28 S m^{-1}, respectively. The slight decrease in the conductivity value for REM/BDTO/EDT may be due to the formation of Ti_5O_9 and Ti_6O_{11} phases which are less conductive than Ti_4O_7 phase [219]. However the slight increase in the conductivity for REM/BDTO/PLD20 may be attributed to the deposition of highly conductive BDTO using PLD method. The measured conductivity value for REM was similar to that for a high purity Ti_4O_7 REM previously reported in the literature [64,219].

SEM/EDS was performed only on REM and REM/BDTO/EDT for the determination of particle size, morphology and elemental analysis of the catalysts deposited REMs. The SEM/EDS was used on the top surface as well as the X-section of the REM/BDTO/EDT. The SEM image of REM showed a highly porous structure of REM with the particle size of approximately 1 - 2 μm (Figure 6-2). The EDS results of REM showed the presence of only Ti

(56.53 %) and O (43.47 %) as the major elements (Figure 6-2). The SEM image of REM/BDTO/EDT also showed crystal-like structures of BDTO catalyst particles with the size range of 1 – 2 μm (Figure 6-2). The EDS of REM/BDTO/EDT showed that Sn (8.45 %) and Bi (0.83 %) were present along with Ti (44.02 %) and O (46.7 %). This result showed the similarity of determined molar ratio of Sn and Bi (Sn:Bi = 10.2:1) and the expected deposited ratio (Sn:Bi = 10:1) confirming the successful deposition of catalysts using the pulsed laser deposition method. The EDS was also performed on the vertical X-section of REM/BDTO/EDT to determine the depth dependence of the catatlyst metals. The results showed that the catalysts (atomic concentration Sn = 1.02 % and Bi = 0.09 %) present along the thickness were homogeneous and less concentrated compared to the surface (Figure 6-2).

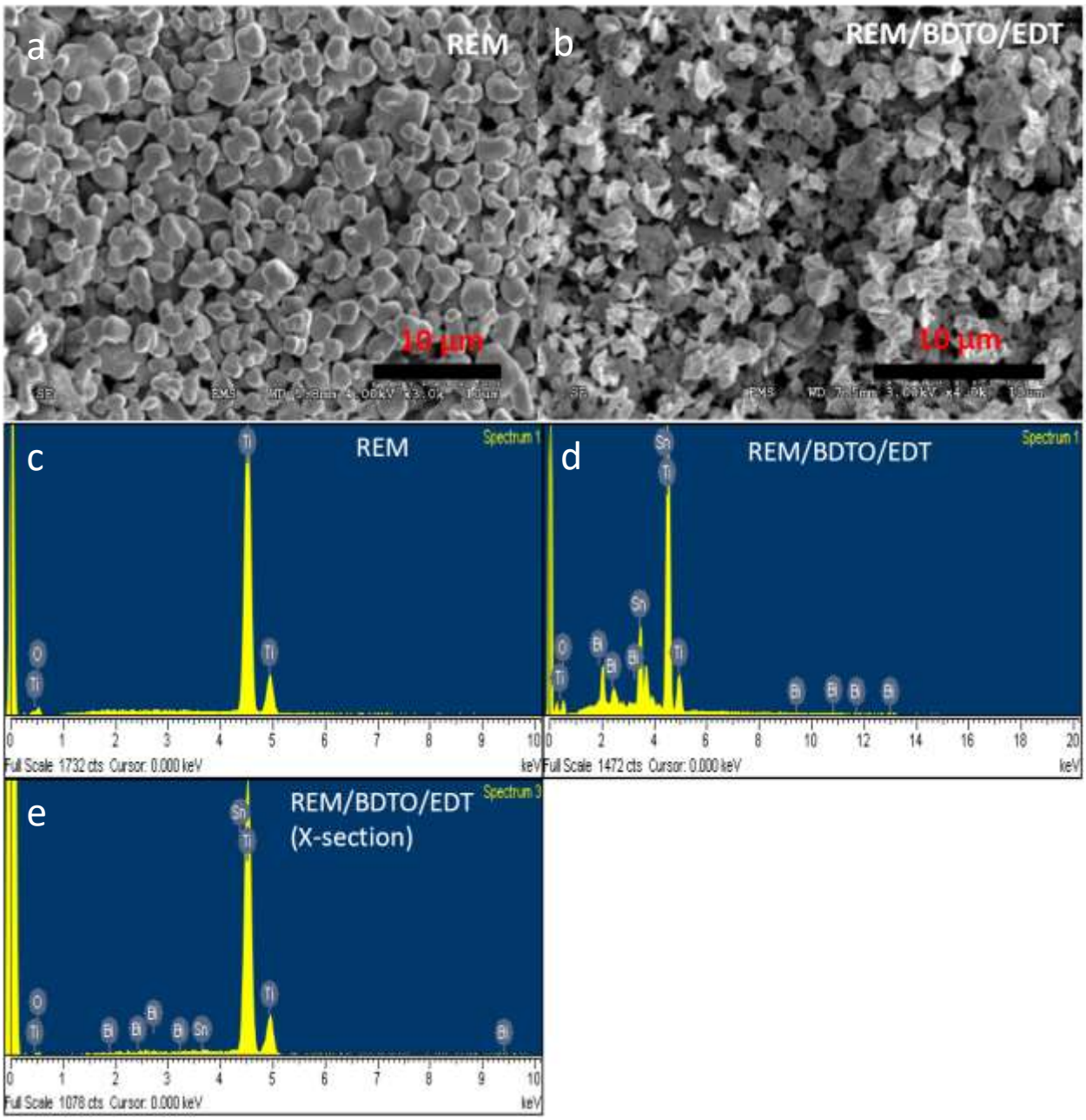

Figure 6-2. SEM images of a) REM and b) REM/BDTO/EDT. EDS of c) REM surface, d) REM/BDTO/EDT surface and e) REM/BDTO/EDT cross section.

XPS was also performed on REM, REM/BDTO/EDT, and REM/BDTO/PLD20 to determine the oxidation states of the metal components (Figure 6-3 and Table 6-1).

Table 6-1. Atomic Concentrations (atomic %) of Ti, O, Sn and Bi determined by XPS for REM, REM/BDTO/EDT and REM/BDTO/PLD20.

Electrode	Ti (%)	O (%)	Sn (%)	Bi (%)
REM	27.70	72.30	-	-
REM/BDTO/EDT	11.14	77.45	10.39	1.02
REM/BDTO/PLD20	27.03	71.80	1.06	0.11

XPS results showed the presence of Ti 2p and O 1s peak for REM, REM/BDTO/EDT and REM/BDTO/PLD20 (Table 6-1). The XPS results showed that the Sn to Bi ratio for both REM/BDTO/EDT (Sn:Bi = 10.2:1) and REM/BDTO/PLD20 (Sn:Bi = 9.6:1) was almost identical to the precursor solution (Sn:Bi = 10:1) for EDT and the precursor material for PLD (Sn:Bi in $Sn_{0.91}Bi_{0.09}O_2$ = 10:1) (Table 6-1). The XPS results also supported the EDS data which confirmed successful catalyst deposition onto REM using EDT and PLD methods. This result also confirmed that the catalyst loading was much higher for REM/BDTO/EDT compared to REM/BDTO/PLD20. The deconvoluted O 1s, Sn 3d and Bi 4f XPS spectra of REM/BDTO/EDT and only Sn 3d XPS spectra of REM/BDTO/PLD20 is provided in Appendix D (Figure S-6-4). The peak assignments for deconvoluted Sn 3d spectra of REM/BDTO/EDT was supported by the literature, which showed the presence of only SnO_2 (Sn $3d_{3/2}$ = 494.4 eV and Sn $3d_{5/2}$ = 486.0 eV) and SnO (Sn $3d_{3/2}$ = 493.7 eV and Sn $3d_{5/2}$ = 485.3 eV) [490–492]. This result was also supported by the XRD results that showed the presence of Sn in the form of SnO_2 and SnO. The deconvoluted Bi 4f spectra showed the presence of only Bi_2O_3 (Bi $4f_{5/2}$ = 163.2 eV and Bi $4f_{7/2}$ = 157.9 eV) that was also supported by the XRD data (Figure S-6-4) [493]. The Sn 3d spectra of REM/BDTO/PLD20 showed the presence of only SnO_2 (Sn $3d_{3/2}$ = 494.2 eV and Sn $3d_{5/2}$ = 486.2 eV) without any traces of SnO. However, Bi concentration was below the detection limit

of XPS. All the results confirmed successful deposition of bismuth doped tin oxide using PLD and EDT methods.

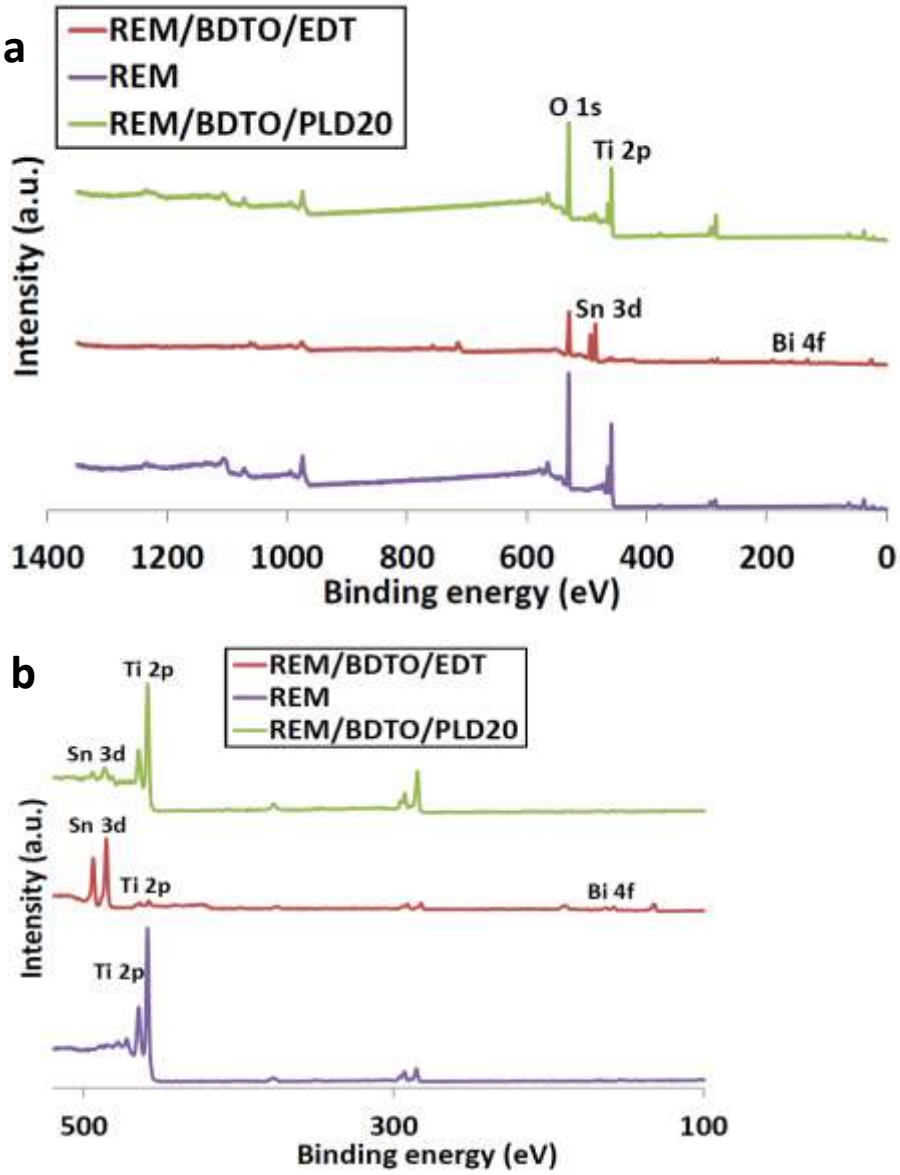

Figure 6-3. XPS of REM, REM/BDTO/EDT and REM/BDTO/PLD20 at a) 0-1350 eV and b) 100-520 eV.

6.4.2 Flow-Through REM Oxidation Experiments. To show the effect of catalyst deposition on organic compound oxidation REM, REM/BDTO/EDT, and REM/BDTO/PLD20 electrodes were tested for TA, ATZ, and CDN oxidation in flow-through mode under anodic polarizations. Reactions were conducted in an upflow configuration, where the solution passed through the anode followed by the cathode (Figure 6-4). This method of operation prevented the trapping of bubbles on the anode surface that formed as a result of O_2 evolution . All the experiments were performed under ambient conditions.

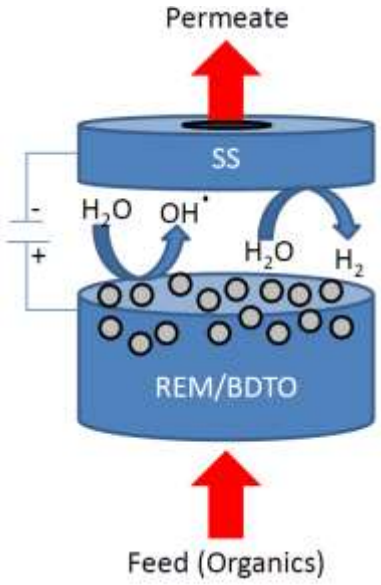

Figure 6-4. Schematic of reverse dead end flow mode.

6.4.2.1 TA Oxidation Experiments. To assess the formation of $OH^{\bullet}$ on REM, REM/BDTO/EDT, and REM/BDTO/PLD20, TA was used as hydroxyl radical probe. TA oxidation was performed at the OCP, 2.1, 2.6, 3.0, and 3.5 V/SHE and the formation of HTA was used as a qualitative measurement for $OH^{\bullet}$ production. The steady state $OH^{\bullet}$ concentration ($\left[OH^{\bullet}\right]_s$) on the electrode surface was calculated using the following equation:

$$\left[OH^{\bullet}\right]_s = \frac{k_{TA}}{k_{TA,OH^{\bullet}}} \tag{6-6}$$

Where $k_{TA,OH^{\bullet}}$ has a value of 4×10^{6} m^{3} mol^{-1} s^{-1} [494] and k_{TA} is the rate constant values for TA oxidation. The $\left[OH^{\bullet}\right]_{s}$ was determined in the range of 2.7×10^{-5} – 1.1×10^{-4}, 3.75×10^{-5} – 1.5×10^{-4} and 7.35×10^{-5} – 1.5×10^{-4} mol m^{-2} for REM, REM/BDTO/PLD20 and REM/BDTO/EDT, respectively at all the applied potentials. The concentration profile for both TA and HTA were shown in Figure 6-5. Discernible TA oxidation was not found at OCP for all the electrodes used. The TA conversion increased with increase in the anodic potential irrespective of the electrode (Table 6-2). At all the applied potentials REM/BDTO/EDT and REM/BDTO/PLD20 showed higher TA oxidation rate compared to that of REM. For example, at 3.0 V/SHE REM, REM/BDTO/EDT, and REM/BDTO/PLD20 showed TA conversions of 66.6 ± 0.17, 93.3 ± 0.87, and 95.0 ± 0.32 %, respectively (Figure 6-5 and Table 6-2). This result confirmed that BDTO catalyst showed higher activity and facilitated TA oxidation due to higher conductivity and $OH^{\bullet}$ production. At the highest applied potential of 3.5 V/SHE both REM/BDTO/EDT and REM/BDTO/PLD20 showed complete oxidation of TA (< 10 nM).

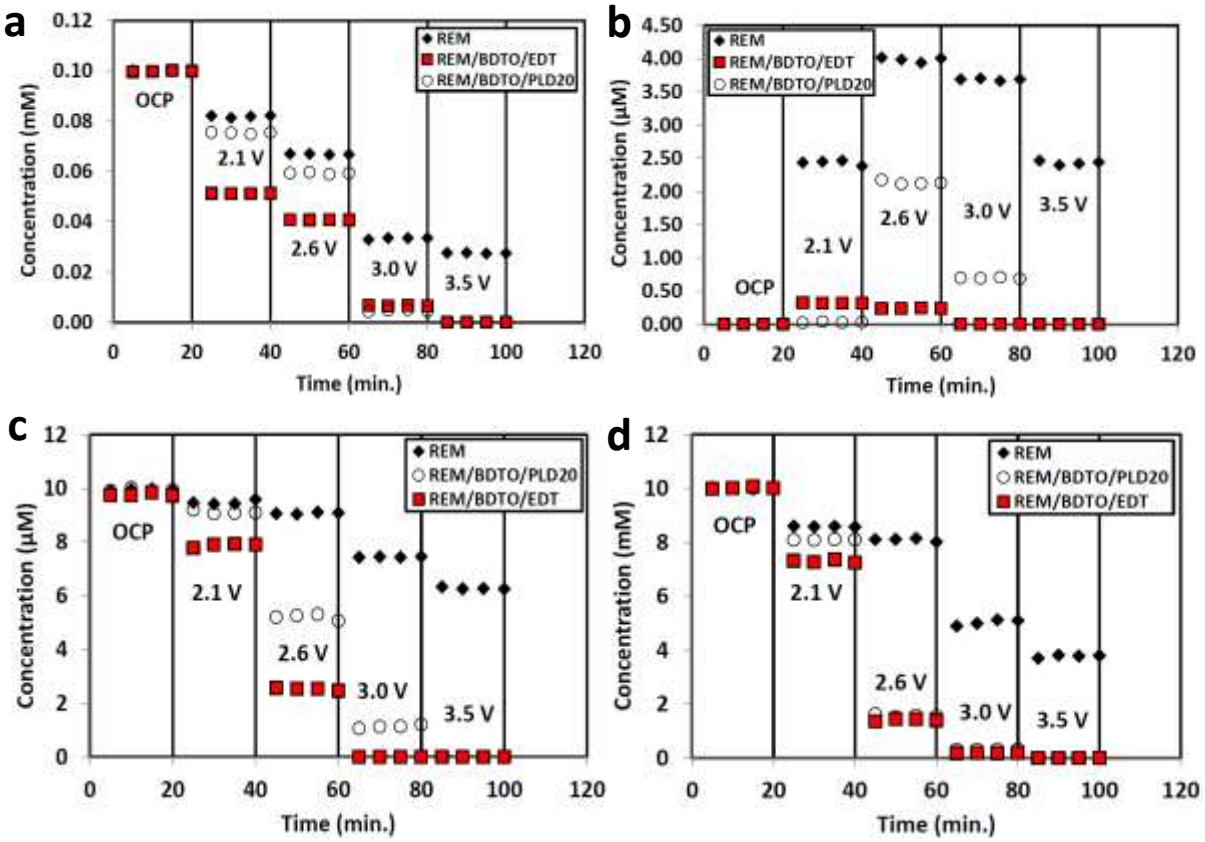

Figure 6-5. a) TA, b) HTA, c) ATZ and d) CDN concentration profiles for REM, REM/BDTO/EDT and REM/BDTO/PLD20 at different potentials in the cathode-anode flow mode.

Table 6-2. Summary of experimental data for all flow-through organics oxidation experiments.

Electrode	Voltage (V/SHE)	TA Conversion (%)	S_{HTA} (%)	COD (mg L^{-1})	Effluent pH
REM	OCP	0	0	22.7 ± 0.42	4.6 ± 0.3
	2.1	18.7 ± 0.91	13.3 ± 1.02	20.1 ± 0.63	4.6 ± 0.1
	2.6	34.3 ± 1.43	11.4 ± 1.21	17.6 ± 0.28	4.5 ± 0.3
	3.0	66.6 ± 0.17	5.63 ± 0.91	10.2 ± 0.34	4.5 ± 0.2
	3.5	72.4 ± 0.23	3.28 ± 0.74	7.89 ± 0.13	4.4 ± 0.2
REM/BDTO/EDT	OCP	0	0	22.6 ± 0.31	4.7 ± 0.1
	2.1	48.9 ± 0.26	0.63 ± 0.21	18.5 ± 0.43	4.5 ± 0.3
	2.6	59.4 ± 0.19	0.40 ± 0.34	8.46 ± 0.51	4.6 ± 0.1
	3.0	93.3 ± 0.87	<0.01	3.07 ± 0.28	4.5 ± 0.3
	3.5	>99.99	<0.01	<0.7	4.3 ± 0.2
REM/BDTO/PLD20	OCP	0	0	22.7 ± 0.28	4.6 ± 0.1
	2.1	24.7 ± 1.03	0.15 ± 0.08	19.9 ± 0.52	4.7 ± 0.2
	2.6	40.4 ± 1.85	5.12 ± 1.42	14.5 ± 1.01	4.5 ± 0.2
	3.0	95.0 ± 0.32	0.72 ± 0.17	3.13 ± 0.71	4.5 ± 0.1
	3.5	>99.99	<0.01	<0.7	4.5 ± 0.3
Electrode	Voltage (V/SHE)	ATZ Conversion (%)	NO_3^- Concentration (μM)		Effluent pH
REM	OCP	0	0		4.6 ± 0.3
	2.1	6.30 ± 1.48	2.34 ± 0.43		4.5 ± 0.3
	2.6	10.1 ± 1.21	4.12 ± 0.22		4.6 ± 0.1
	3.0	25.6 ± 0.59	9.21 ± 1.60		4.5 ± 0.1
	3.5	37.4 ± 0.32	15.1 ± 1.27		4.5 ± 0.3
REM/BDTO/EDT	OCP	0	0		4.7 ± 0.1
	2.1	18.3 ± 1.19	9.20 ± 0.21		4.5 ± 0.2
	2.6	73.8 ± 1.01	33.2 ± 1.70		4.5 ± 0.1
	3.0	>99.99	46.3 ± 2.22		4.4 ± 0.3
	3.5	>99.99	47.6 ± 1.83		4.5 ± 0.1
REM/BDTO/PLD20	OCP	0	0		4.6 ± 0.2
	2.1	10.1 ± 1.52	4.12 ± 0.12		4.5 ± 0.3
	2.6	47.5 ± 1.26	21.4 ± 1.13		4.6 ± 0.1
	3.0	88.8 ± 0.87	40.0 ± 1.61		4.5 ± 0.1
	3.5	>99.99	45.6 ± 2.18		4.4 ± 0.2
Electrode	Voltage (V/SHE)	CDN Conversion (%)	NO_3^- Concentration (μM)		Effluent pH
REM	OCP	0	0		4.6 ± 0.2
	2.1	14.2 ± 0.65	6.85 ± 0.91		4.6 ± 0.1
	2.6	18.9 ± 1.03	8.13 ± 1.01		4.6 ± 0.3
	3.0	50.1 ± 1.37	20.4 ± 1.32		4.5 ± 0.2
	3.5	62.2 ± 0.29	25.6 ± 2.78		4.4 ± 0.1
REM/BDTO/EDT	OCP	0	0		4.5 ± 0.3
	2.1	27.4 ± 0.88	11.2 ± 0.84		4.6 ± 0.3
	2.6	85.6 ± 0.84	40.5 ± 1.41		4.6 ± 0.2
	3.0	98.3 ± 0.36	46.3 ± 2.07		4.5 ± 0.1
	3.5	>99.99	47.1 ± 1.66		4.5 ± 0.2
REM/BDTO/PLD20	OCP	0	0		4.7 ± 0.1
	2.1	18.9 ± 1.52	8.23 ± 0.23		4.6 ± 0.2
	2.6	84.3 ± 1.26	39.1 ± 0.94		4.6 ± 0.2
	3.0	96.8 ± 0.87	45.0 ± 1.76		4.6 ± 0.3
	3.5	>99.99	48.2 ± 1.14		4.5 ± 0.1

The HTA formation at different applied potentials with REM, REM/BDTO/EDT, and REM/BDTO/PLD20 was shown in Figure 6-5. For all electrodes the HTA concentration first increased and then decreased with increase in anodic potential (Figure 6-5). For example, for REM/BDTO/PLD20 the HTA concentration first increased from 42 nM at 2.1 V/SHE to 2.1 µM at 2.6 V/SHE followed by a decrease to 69 nM at 3.0 V/SHE. This result indicated that the HTA formation rate initially increased with increase in the anodic potential due to an increase in $OH^{\bullet}$ production, and then at higher anodic potentials the HTA oxidation rate became higher than the HTA formation rate. The selectivity of HTA (S_{HTA}) formation result showed higher S_{HTA} for REM compared to catalyst deposited REMs. This result indicated a higher oxidation rate of both HTA and TA for REM/BDTO/EDT and REM/BDTO/PLD20 compared to REM. At the highest applied potential (3.5 V/SHE) HTA was below the detection limit (< 10 nM) for both REM/BDTO/EDT and REM/BDTO/PLD20 electrodes. The above results indicated that $OH^{\bullet}$ formation was enhanced by the deposition of BDTO to the REMs.

To obtain a better measure of the improvement of oxidation capacity of the organic compounds using BDTO catalyst deposited REMs, the permeate solutions were analyzed for COD to assess the extent of mineralization of TA (Table 6-2). The COD values showed a decrease in permeate COD concentrations with increase in potential for all three electrodes confirming higher mineralization of TA at higher potentials. At all applied potentials the REM/BDTO/EDT and REM/BDTO/PLD20 showed lower permeate COD values compared to the REM, which confirmed higher oxidation and removal rate of TA using the BDTO catalyst deposited REMs. For example the COD values decreased from 22.7 mg L^{-1} in feed to 10.2 ± 0.34, 3.07 ± 0.28, and 3.13 ± 0.71 mg L^{-1} for REM, REM/BDTO/EDT and REM/BDTO/PLD20 in the permeate at 3.0 V/SHE. At 3.5 V/SHE for both REM/BDTO/EDT and

REM/BDTO/PLD20 electrodes the COD values were below the detection limit (< 0.7 mg L^{-1}), which confirmed near complete mineralization of TA with BDTO for catalyst deposited REMs.

6.4.2.2 Organics Oxidation Experiments. After successful removal of TA using BDTO catalyst deposited REMs, ATZ and CDN were treated by electrochemical oxidation using the three different electrode materails. ATZ and CDN oxidation were performed with reverse dead end flow mode at the potential of OCP, 2.1, 2.6, 3.0, and 3.5 V/SHE. The ATZ and CDN oxidation results are summarized in Figure 6-5 and Table 6-2.

Similar to the TA oxidation, all the electrodes showed increase in the ATZ and CDN conversion with increase in the anodic potential. ATZ conversion increased by 2.9, 7.3, >3.9, and >2.7-fold for REM/BDTO/EDT and 1.6, 4.7, 3.5, and >2.7-fold for REM/BDTO/PLD20 compared to REM at 2.1, 2.6, 3.0, and 3.5 V/SHE, respectively. Both catalyst deposited REMs showed similar activity towards ATZ oxidation at the higher potentials (3.0 and 3.5 V/SHE). However at lower potentials REM/BDTO/EDT showed higher ATZ removal rate than REM/BDTO/PLD20. Concentration profile for CDN also showed similar behavior as ATZ oxidation (Figure 6-5). CDN oxidation rate also increased by 1.93, 4.53, 1.96 and >1.60-fold for REM/BDTO/EDT and 1.33, 4.46, 1.93 and >1.60-fold for REM/BDTO/PLD20 compared to REM at 2.1, 2.6, 3.0, and 3.5 V/SHE, respectively (Figure 6-5). This result again confirmed the higher activity of BDTO catalyst towards organic compound oxidation, due to higher conductivity and $OH^{\bullet}$ production rate. ATZ concentration was not detected (< 10 nM) at 3.0 and 3.5 V/SHE for REM/BDTO/EDT and at 3.5 V/SHE for REM/BDTO/PLD20, which was lower than the EPA MCL of 14 nM. For CDN oxidation, the permeate CDN concentrations were below the detection limit (< 10 nM) at 3.0 and 3.5 V/SHE for REM/BDTO/EDT and at 3.5 V/SHE for REM/BDTO/PLD20. The permeate CDN concentrations at 3.0 and 3.5 V/SHE for

REM/BDTO/EDT and at 3.5 V/SHE for REM/BDTO/PLD20 was lower than the EPA time-limited tolerance of 280 nM.

Analysis of the oxidation products of ATZ and CDN showed that NO_3^- was a major product, as indicated by the following mineralization reactions:

ATZ: $C_8H_{14}ClN_5 + 19O_2 + 6e^- \rightarrow 8CO_2 + Cl^- + 5NO_3^- + 7H_2O$ (6-7)

CDN: $C_6H_8ClN_5SO_2 + 16O_2 + 2H^+ + 8e^- \rightarrow 6CO_2 + Cl^- + 5NO_3^- + SO_2 + 5H_2O$ (6-8)

To show the extent of mineralization, IC was performed to detect NO_3^- concentration in permeates of ATZ and CDN oxidation at each potential. Theoretically complete mineralization of 10 μM of ATZ and CDN would yield 50 μM of NO_3^-. The NO_3^- concentration data are summarized in Table 6-2. The results showed an increase in NO_3^- concentration with increase in anodic potential irrespective of the electrodes. The results also showed partial removal of organics followed by partial mineralization at lower potentials. However, at the highest applied anodic potential of 3.5 V/SHE, both REM/BDTO/EDT and REM/BDTO/PLD20 showed NO_3^- concentration in the range of 45.6 ± 2.18 to 48.2 ± 1.14 μM (Table 6-2). The determined NO_3^- concentration was similar to that after total N analysis of feed and permeates which gave the NO_3^- concentration in the range of 48.0 ± 0.8 to 49.0 ± 1.61 μM. These results confirmed complete mineralization of ATZ and CDN for REM/BDTO/EDT and REM/BDTO/PLD20 at 3.5 V/SHE. The NO_3^- concentration (45.6 ± 2.18 - 48.2 ± 1.14 μM) via organics oxidation was lower than the EPA MCL of 0.7 mM. These results showed extreme promise of using BDTO catalyst deposited REMs towards organics removal from different water matrices. If NO_3^- concentration is higher than the EPA MCL then it can be reduced using bimetallic catalyst deposited REMs which has been discussed in the previous chapter.

6.4.3 Voltammetric Results. In order to determine the oxidation potential of ATZ and CDN, LSV experiments were performed with 10 µM of the compounds in 100 mM KH_2PO_4 background electrolyte on BDD and REM electrodes. LSV scans were performed on BDD to clearly identify the peaks, as the REM has a very high charging current that makes the oxidation peaks difficult to detect. The LSV scans of ATZ and CDN using the BDD electrode showed an increase in current compared to the background electrolyte at around 1.3 and 1.0 V/SHE, respectively (Figure S-6-5). The LSV scans of ATZ and CDN with the REM electrode in flow-through mode exhibited higher current compared to the background electrolyte, which confirmed the direct oxidation of ATZ and CDN (Figure S-6-5). For both BDD and REM, the current due to CDN oxidation was higher than that for ATZ oxidation, which indicated that CDN was more electroactive than ATZ.

LSV scans were also performed on ATZ and CDN with the REM electrode at different scan rates (10, 20, 40, 60, 80 and 100 mV sec^{-1}) to find the rate-controlling mechanism for oxidation. The peak currents (I_p) were plotted versus scan rate (ν) as well as with square root of scan rates (Figure S-6-6). The I_p variation with ν and √ν followed the following equations:

$$I_{p,ATZ}\ (mA) = 0.055\nu + 0.9128\ (R^2 = 0.9686) \quad (6\text{-}9)$$

$$I_{p,CDN}\ (mA) = 0.059\nu + 0.8926\ (R^2 = 0.9684) \quad (6\text{-}10)$$

$$I_{p,ATZ}\ (mA) = 0.74\sqrt{\nu} - 1.26\ (R^2 = 0.9983) \quad (6\text{-}11)$$

$$I_{p,CDN}\ (mA) = 0.81\sqrt{\nu} - 1.47\ (R^2 = 0.9985) \quad (6\text{-}12)$$

The results showed that the peak currents (I_p) for both ATZ and CDN oxidation varied more linearly with √ν (higher R^2) than that with ν (lower R^2). This result indicated that both ATZ and CDN oxidation processes were diffusion controlled [340].

6.4.4 DFT Simulation. Batch oxidation experiments were performed at 1.5 and 1.8 V/SHE for ATZ and at 1.14 and 1.5 V/SHE for CDN at temperatures of 20, 30, and 40 ^{0}C to determine the activation energy (E_a) at specific anodic potentials. The slope from this plot yielded an E_a value of 68.9 kJ mol^{-1} for ATZ at 1.5 V/SHE. Similarly, Ea values were obtained as 27.9, 68.03 and 29.16 kJ mol^{-1} for ATZ at 1.8 V/SHE, CDN at 1.14 V/SHE and CDN at 1.5 V/SHE, respectively (Figure S-6-1). DFT simulation showed the E_a profiles as a function of electrode potential for both ATZ and CDN oxidation (Figure 6-6). The results predicted the oxidation potential for ATZ and CDN at 1.32 and 0.96 V/SHE, respectively. The results were consistent with the LSV results which showed the ATZ and CDN oxidation potential at 1.28 and 1.0 V/SHE, respectively. The activation energy profile with electrode potential (DFT) showed the E_a values of 69.9 and 26.5 kJ mol^{-1} for ATZ at 1.5 and 1.8 V/SHE, respectively, and 70.6 and 26.1 kJ mol^{-1} for CDN at 1.14 and 1.5 V/SHE, respectively (Figure 6-6). These values supported the experimental results which showed E_a values of 68.9 and 27.9 kJ mol^{-1} for ATZ at 1.5 and 1.8 V/SHE, respectively, and 68.3 and 29.2 kJ mol^{-1} for CDN at 1.14 and 1.5 V/SHE, respectively. The similar results between the experimental and theoretical methods indicated that the assumptions of Marcus theory were appropriate for these two compounds. That is, their rate limiting mechanism for oxidation at the investigated potentials was attributed to an outer sphere electron transfer and that the reactants did not interact significantly will the electrode surface.

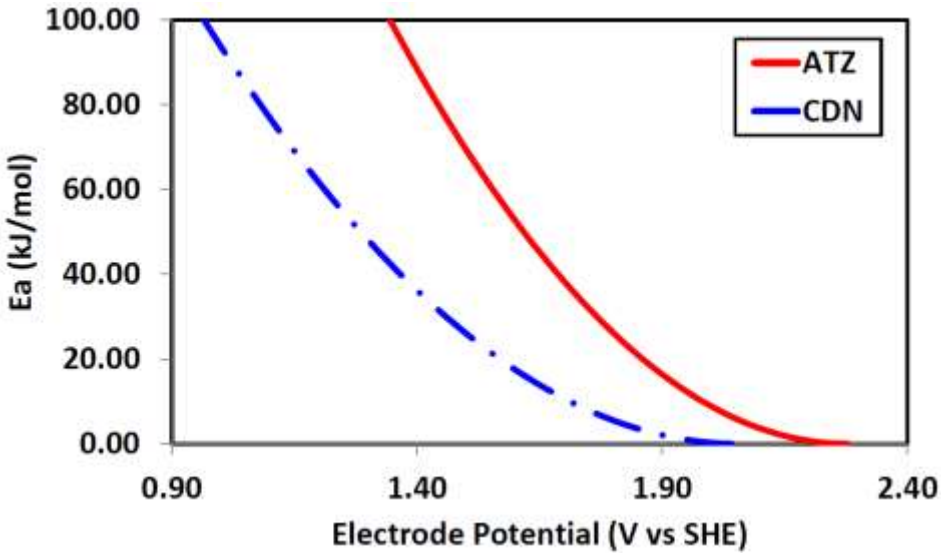

Figure 6-6. DFT determined E_a with electrode potential for ATZ and CDN.

6.4.5 Technical and Environmental Significance. Minimal energy consumption and high current efficiency are necessary for successful application of water treatment technologies. Current efficiencies were calculated using equation 6-4 depending on the number of electron transferred for complete mineralization according to equations 6-7 and 6-8. For electrochemical oxidation of all the organic compounds, the current efficiency was in the following order: REM < REM/BDTO/PLD < REM/BDTO/EDT (Table 6-3). The BDTO catalyst deposited REM showed higher current efficiency compared to REM due to improved catalytic activity towards organic oxidation via $OH^{\bullet}$ production. For example current efficiency for TA oxidation at 3.0 V/SHE was determined as 1.43 ± 0.12, 2.67 ± 0.33 and 2.06 ± 0.08 % for REM, REM/BDTO/EDT and REM/BDTO/PLD, respectively.

The energy requirements were calculated using equation 6-5 (Table 6-3). E_{EO} (kWh m^{-3}) data showed higher energy consumption for REM compared to REM/BDTO/EDT and REM/BDTO/PLD. The E_{EO} values also showed that the energy consumption for REM was 7.21

and 4.63-fold higher than REM/BDTO/EDT and REM/BDTO/PLD for CDN oxidation at 3.0 V/SHE (Table 6-3).

This study showed partial oxidation and subsequent mineralization of the organic compounds using anodic potentials with REM, REM/BDTO/EDT, and REM/BDTO/PLD. The results also showed complete mineralization of TA, ATZ, and CDN at the highest applied potentials of 3.5 V/SHE, which was confirmed by COD and total N analysis. The complete ATZ and CDN mineralization also showed no organic compound residual by producing CO_2, nitrate (50 μM), chloride, and water as major products among which nitrate has potential health risks. The produced nitrate concentration was much lower than the EPA MCL of 0.7 mM. These results confirmed extreme promise of BDTO catalyst deposited REMs for organic compound oxidation and subsequent removal from water matrices.

6.5 Acknowledgements

Funding for this work was provided by a National Science Foundation CAREER award to Brian P. Chaplin (CBET-1453081).

Table 6-3. Energy Requirement (E_{EO}, kWh m^{-3}) and Current Efficiency (CE, %) for TA, ATZ and CDN oxidation with REM, REM/BDTO/EDT and REM/BDTO/PLD20 electrodes.

Electrode	Voltage (V/SHE)	CE (%)	E_{EO} (kWh m^{-3})
	TA		
REM	OCP	-	-
	2.1	1.69 ± 0.16	3.36 ± 0.32
	2.6	1.32 ± 0.08	3.79 ± 0.08
	3.0	1.43 ± 0.12	3.01 ± 0.15
	3.5	0.97 ± 0.11	4.37 ± 0.21
REM/BDTO/EDT	OCP	-	-
	2.1	6.70 ± 0.13	0.91 ± 0.08
	2.6	3.21 ± 0.24	1.52 ± 0.14
	3.0	2.67 ± 0.33	1.11 ± 0.29
	3.5	1.60 ± 0.18	-
REM/BDTO/PLD20	OCP	-	-
	2.1	2.17 ± 0.32	2.27 ± 0.23
	2.6	1.61 ± 0.19	2.95 ± 0.05
	3.0	2.06 ± 0.08	1.10 ± 0.18
	3.5	1.32 ± 0.11	-
	ATZ		
REM	OCP	-	-
	2.1	0.09 ± 0.04	13.5 ± 1.02
	2.6	0.08 ± 0.04	18.6 ± 0.94
	3.0	0.13 ± 0.10	12.9 ± 0.57
	3.5	0.13 ± 0.09	14.2 ± 0.14
REM/BDTO/EDT	OCP	-	-
	2.1	0.37 ± 0.12	3.18 ± 0.41
	2.6	0.76 ± 0.07	1.16 ± 0.19
	3.0	0.65 ± 0.04	-
	3.5	0.39 ± 0.10	-
REM/BDTO/PLD20	OCP	-	-
	2.1	0.15 ± 0.06	8.26 ± 0.21
	2.6	0.37 ± 0.11	3.20 ± 0.13
	3.0	0.42 ± 0.03	1.82 ± 0.11
	3.5	0.33 ± 0.09	-
	CDN		
REM	OCP	-	-
	2.1	0.30 ± 0.10	5.39 ± 0.35
	2.6	0.20 ± 0.09	10.0 ± 0.91
	3.0	0.31 ± 0.11	5.97 ± 0.06
	3.5	0.27 ± 0.09	7.37 ± 0.17
REM/BDTO/EDT	OCP	-	-
	2.1	0.71 ± 0.21	2.12 ± 0.09
	2.6	1.15 ± 0.17	0.83 ± 0.03
	3.0	0.78 ± 0.16	0.83 ± 0.11
	3.5	0.50 ± 0.22	-
REM/BDTO/PLD20	OCP	-	-
	2.1	0.38 ± 0.18	4.04 ± 0.35
	2.6	0.87 ± 0.11	1.18 ± 0.27
	3.0	0.58 ± 0.20	1.29 ± 0.22
	3.5	0.42 ± 0.05	-

7. Conclusion

This dissertation presented the fabrication of electrochemical sensor for trace contaminant i.e. antibiotics detection with high selectivity and sensitivity, minimization of carcinogenic perchlorate formation, and fabrication of catalyst deposited porous conductive membranes for organic contaminant oxidation and nitrate reduction from water matrices. Chapter 3 presented fabrication of porous-Nafion-MWCNT/BDD sensor via a drop cast method and the application of the sensor for CFX detection using DPV method. Porous Nafion film and MWCNT increased CFX detection with a detection limit of 5 nM, due to the different properties such as –COOH adsorption sites, high surface area, H-bonding, adsorption ability, CAHB, porosity, and conductivity associated with MWCNT and porous nafion of the film to CFX. The sensors were able to detect CFX using differential pulse voltammetry (DPV) in the presence of other antibiotics (i.e., amoxicillin), other non-target water components and several commonly present organic compounds. The sensor was also capable of CFX detection in the presence of WWE matrix with excellent sensitivity and selectivity. High concentration of different organic compounds can foul the sensor but the fouling was easily removed using short cathodic current confirming its effectiveness for contaminant detection in diverse water matrices.

Chapter 4 presented minimization of perchlorate formation during anodic oxidation using BDD electrode with significant organic compound oxidation. To minimize perchlorate formation, fluorination of the BDD surface was performed by using RF plasma (H_2 and CF_4), electrochemical oxidation of PFOA, and aliphatic and aromatic silanization. XPS and CV characterization showed successful fluorination of BDD electrodes using the above mentioned methods. BDDF-PFOA and BDDF-aliphatic electrodes inhibited the electron transfer via DET due to the blocking layer, steric and hydrophobic effects. For the BDDF-aliphatic electrode

completely inhibited the ClO_4^- formation via 10 mM NaCl and 1 mM $NaClO_3$ oxidation. Phenol and TA oxidation rates were not significantly decreased for aliphatic silanized and PFOA modified BDD electrodes. The aliphatic silanized BDD electrode was highly stable under oxidation environment up to 10 cycles which showed no perchlorate formation. After 10^{th} cycle of chlorate oxidation experiments low concentration of perchlorate was observed. Chapter 4 concluded that BDDF-aliphatic electrodes were effective for perchlorate formation inhibition without affecting organics oxidation significantly.

Chapter 5 presented NO_3^- reduction using bimetallic catalyst such as Pd-Cu and Pd-In deposited REM. Electrocatalytic NO_3^- reduction showed optimal performance with a Pd-Cu/REM with an upstream counter electrode. The Pd-Cu/REM was able to reduce 1 mM NO_3^- feed concentration to below the EPAs regulatory MCL in a single pass through the REM. The concentrations of NO_2^- were always below the EPA's MCL and NH_3 concentrations were not detected. Nitrate reduction was not affected by dissolved oxygen, carbonate species, or natural organic matter, and NO_3^- reduction only slightly decreased in a surface water sample due to Ca^{2+} and Mg^{2+} mineral scaling. High current efficiency and low energy consumption were achieved for the Pd-Cu/REM with an upstream counter electrode which made Pd-Cu/REM highly promising for nitrate reduction in water matrices.

Chapter 6 developed bismuth-doped tin oxide (BDTO) catalyst loaded reactive electrochemical membranes (REM) for organic compounds oxidation in water matrix. Porous Magnéli phase membrane pellets (REM) were fabricated by sintering TiO_2 powder and modified with a BDTO catalyst using PLD and EDT methods. The XPS results showed the presence of a mixture of SnO_2, SnO, and Bi_2O_3 on the BDTO modified REM using the EDT method. DFT simulations provided oxidation potentials for ATZ (1.32 V/SHE) and CDN (0.96 V/SHE) and

potential dependent activation energies, which were supported by the LSV data and experimentally calculated activation energies. TA, ATZ, and CDN oxidation rates showed an increasing behavior with increase in the oxidation potential. At all the applied potentials, BDTO deposited REM (REM/BDTO) showed higher oxidation rate compared to REM confirming higher catalytic activity, conductivity and $OH^{\bullet}$ production rate of BDTO catalyst towards organic compound oxidation. At the highest applied potential, no TA, ATZ and CDN concentration were found for REM/BDTO. Chemical oxygen demand (COD) analysis of TA and total N analysis of ATZ and CDN showed complete mineralization of the compounds at the highest applied potential with low energy consumption. The results suggested that the BDTO catalyst loaded REMs were very effective in oxidizing organic compounds with low energy consumption.

The conclusions from this work opened up several future research opportunities. Chapter 3 showed that acid treatment was used on MWCNT to increase the –COOH content as the acid functional groups were responsible for charge assisted hydrogen bond formation. However, the increase in the –COOH content did not increase the sensitivity due to the defect formation on the side walls of MWCNT due to the acid treatment which made some of the sites of the MWCNTs non-conductive [329]. Therefore, future research can be performed on creating a sensor using vertically aligned multiwalled carbon nanotubes (VAMWCNTs) in a porous Nafion film. The VAMWCNT will be created on BDD using thermal CVD method and the sensor will be fabricated by depositing porous Nafion solution on to VAMWCNT/BDD. Oxidation and incorporation of –COOH groups on VAMWCNT and removal of top layer of nafion will be achieved by using oxygen plasma. The oxygen plasma will remove the top Nafion layer, expose the MWCNTs for sensor application, functionalize and incorporate –COOH groups on the edge

of the MWCNTs without creating defects to the side walls of MWCNTs. The sensor using defect free VAMWCNT with porous Nafion film may achieve excellent sensitivity and selectivity for trace contaminant detection in water matrices.

Chapter 4 showed perchlorate formation inhibition while maintaining significant organic compound oxidation using an aliphatic silanized and PFOA modified BDD. However recent research has shown cytotoxicity and genotoxicity of fluorocarbons which may limit the application of fluorinated electrode modification necessary for minimization of perchlorate formation [495–497]. Therefore inorganic oxide materials (i.e. Al_2O_3, TiO_2, ZrO_2), which are environmentally benign may be used to modify electrodes for minimization of perchlorate formation. The desired/optimum thickness of the inorganic materials will be achieved using atomic layer deposition (ALD) or PLD and the blocking layer of inorganic materials may inhibit the perchlorate formation without significantly affect organic oxidation.

Chapter 5 and 6 showed nitrate reduction and organic compound oxidation using bimetallic and metallic oxide catalysts deposited REMs, respectively. The results showed higher concentration of nitrate can be reduced with lower energy consumption and with high efficiency. Therefore nitrate brine solution from reverse osmosis systems can be treated using bimetallic catalyst deposited REMs. Water matrix containing inorganics and organic contaminants can be also treated simultaneously by using bimetallic catalyst deposited REM as cathode and metal oxide catalyst deposited REM as anode. The usage of two different catalyst deposited REMs as cathode and anode will be very effective towards successful water and wastewater treatment applications.

APPENDICES

Appendix A

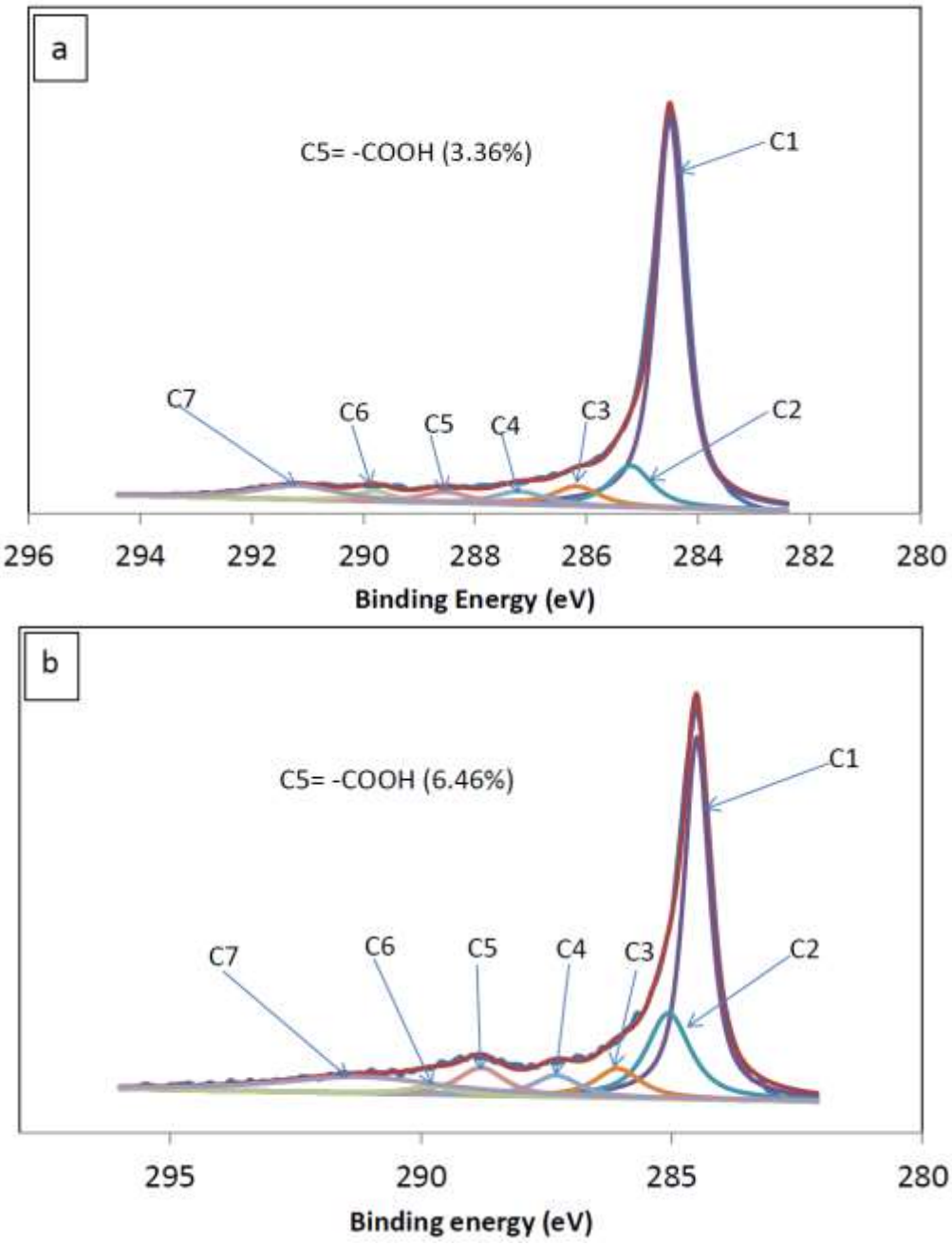

Figure S-3-1. XPS of (a) MWCNT and (b) MWCNT-O (oxidized sample).

Legend: C1: C=C; C2: C-C; C3: -C-OH; C4: -C=O; C5: -COOH; C6: -CO_3; C7: π-π*

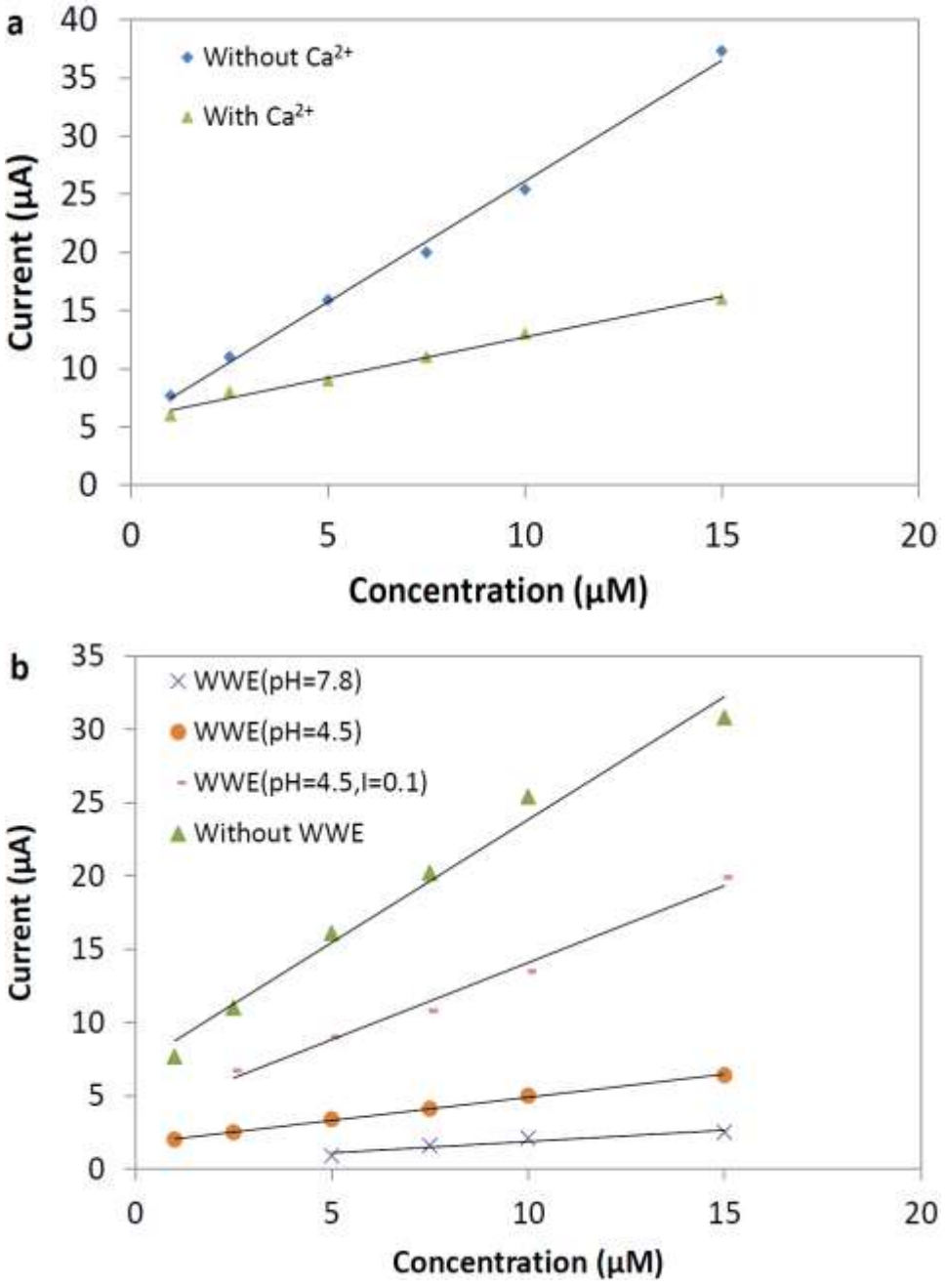

Figure S-3-2. (a) Calibration graphs at different concentration of CFX with (slope= 0.69±0.034) and without (slope= 2.08±0.085) 1mM Ca^{2+} in 0.1M KH_2PO_4 (LOD= 0.005µM, linear ranges (µM)= 0.05-1, 1-15), (b) Calibration graphs at different concentration of CFX without (y =1.6768±0.11 x + 7.0689±0.911, R^2 = 0.9831), with (y = 0.1543±0.03 x + 0.3286±0.341, R^2 = 0.9119), pH (4.5) adjusted (y = 0.3158±0.007 x + 1.7424±0.059, R^2 = 0.998 and both pH (4.5) and conductivity (0.1 M electrolyte) adjusted (y = 1.0492±0.07 x + 3.5865±0.636, R^2 = 0.9868) wastewater effluent matrix.

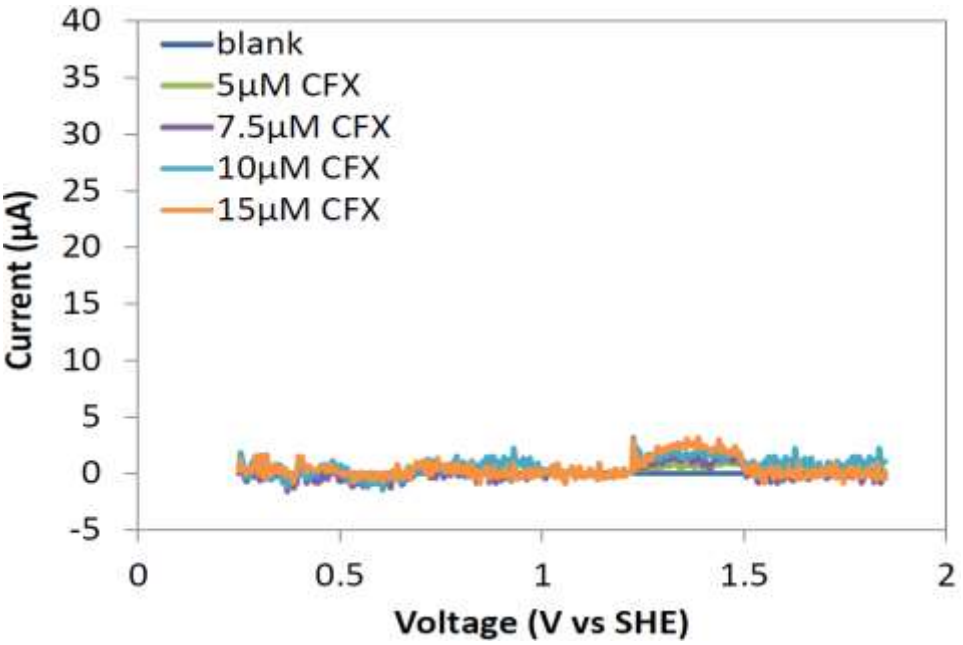

Figure S-3-3. DPV curves of porous-Nafion-MWCNT/BDD at different concentrations of CFX with WWE (pH= 7.80).

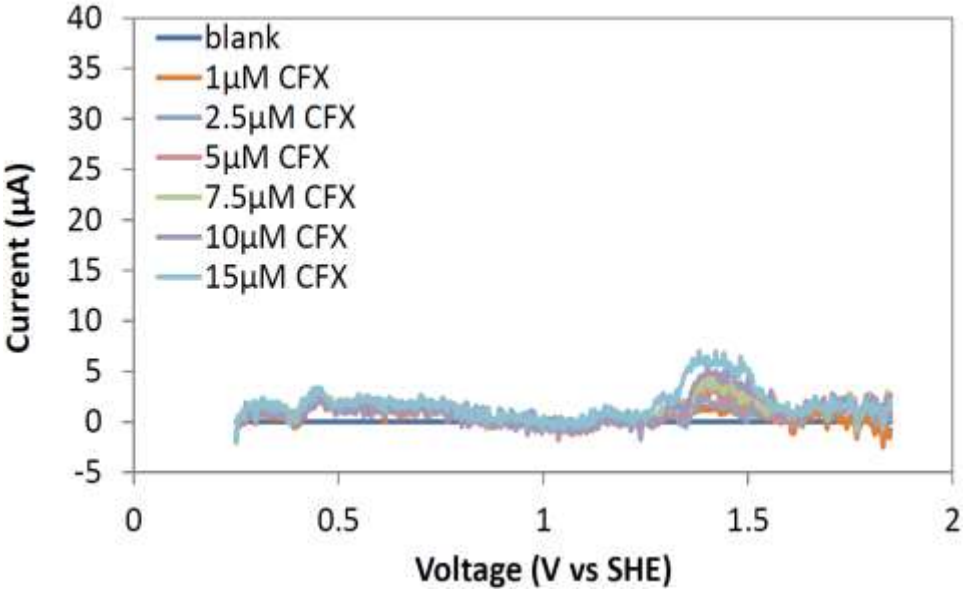

Figure S-3-4. DPV curves of porous-Nafion-MWCNT/BDD at different concentrations of CFX with WWE (pH= 4.50).

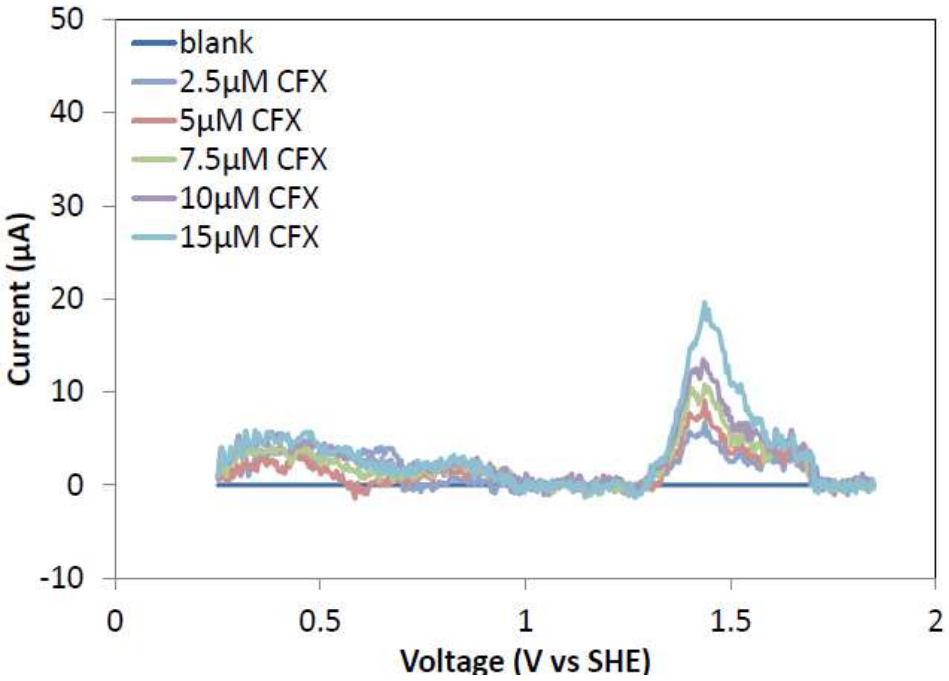

Figure S-3-5. DPV curves of porous-Nafion-MWCNT/BDD at different concentrations of CFX with WWE (pH = 4.50 & 0.1 M KH_2PO_4).

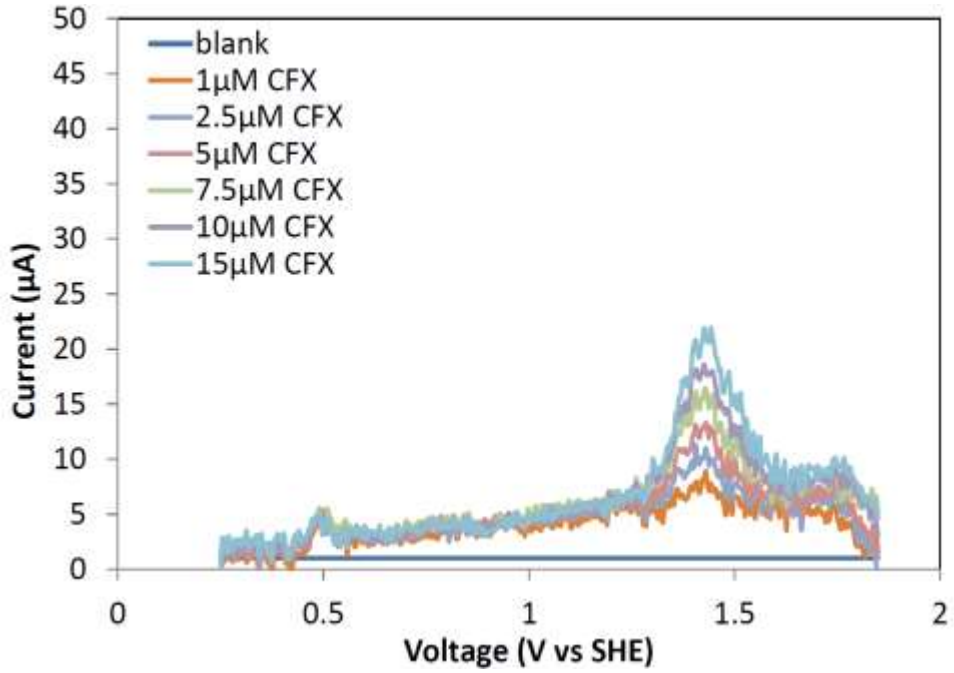

Figure S-3-6. DPV curves of porous-Nafion-MWCNT/BDD at different concentrations of CFX in 0.1 M KH_2PO_4 without organics.

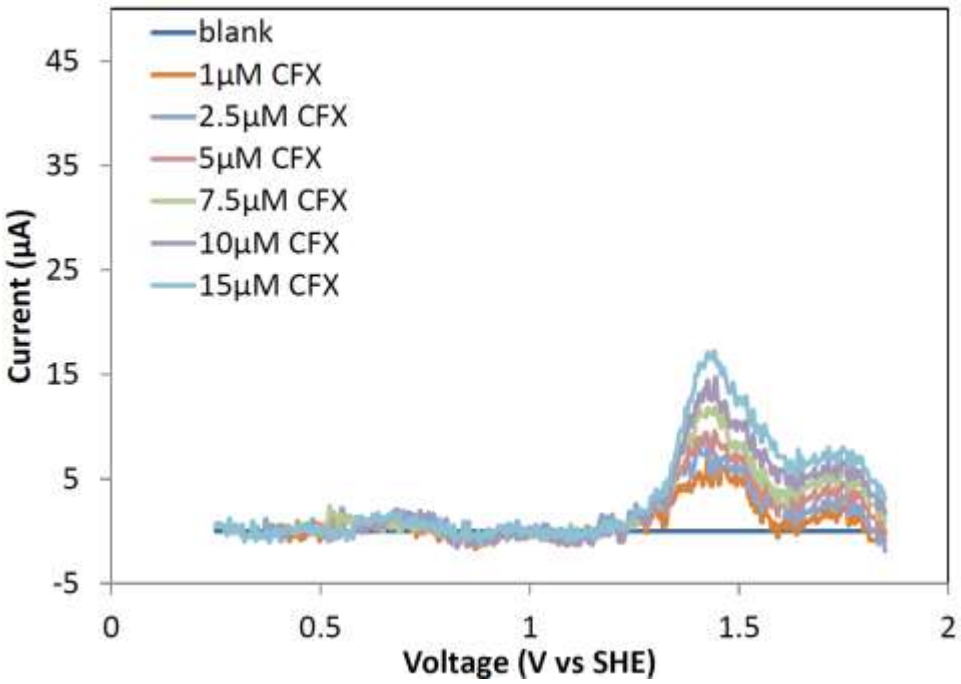

Figure S-3-7. DPV curves of porous-Nafion-MWCNT/BDD at different concentrations of CFX in 0.1 M KH_2PO_4 with 1:1 HBA.

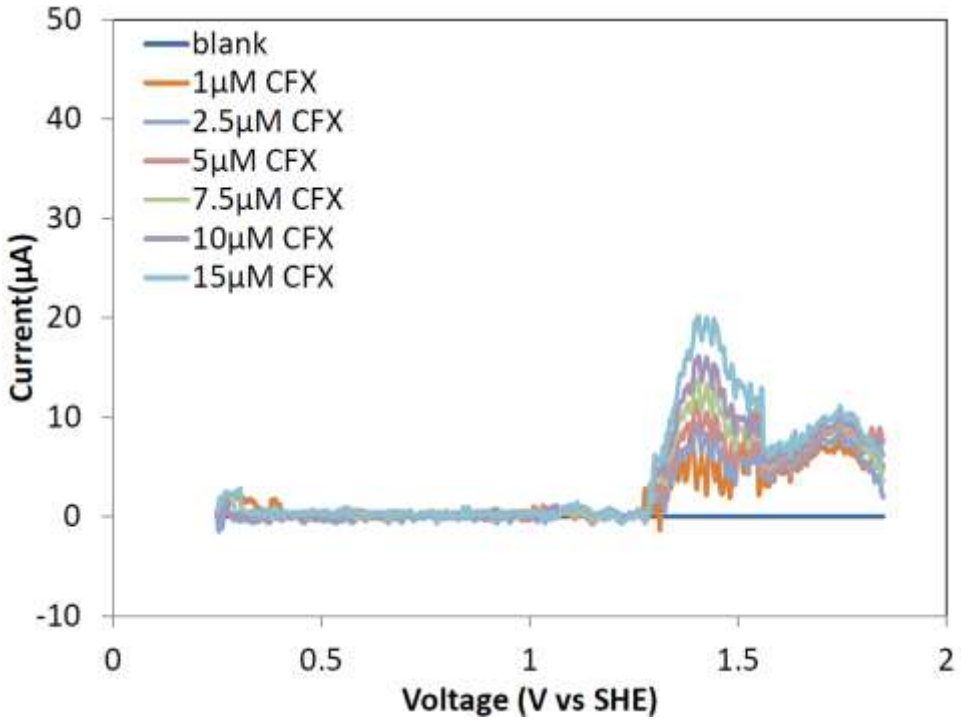

Figure S-3-8. DPV curves of porous-Nafion-MWCNT/BDD at different concentrations of CFX in 0.1 M KH_2PO_4 with 1:1 ABA.

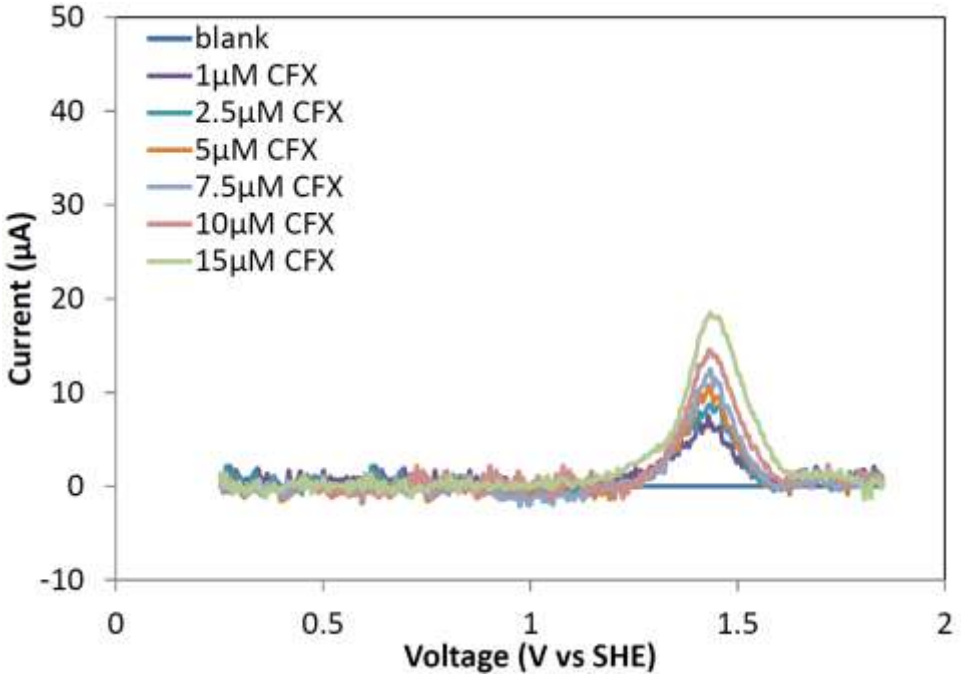

Figure S-3-9. DPV curves of porous-Nafion-MWCNT/BDD at different concentrations of CFX in 0.1 M KH_2PO_4 with 1:1 SA.

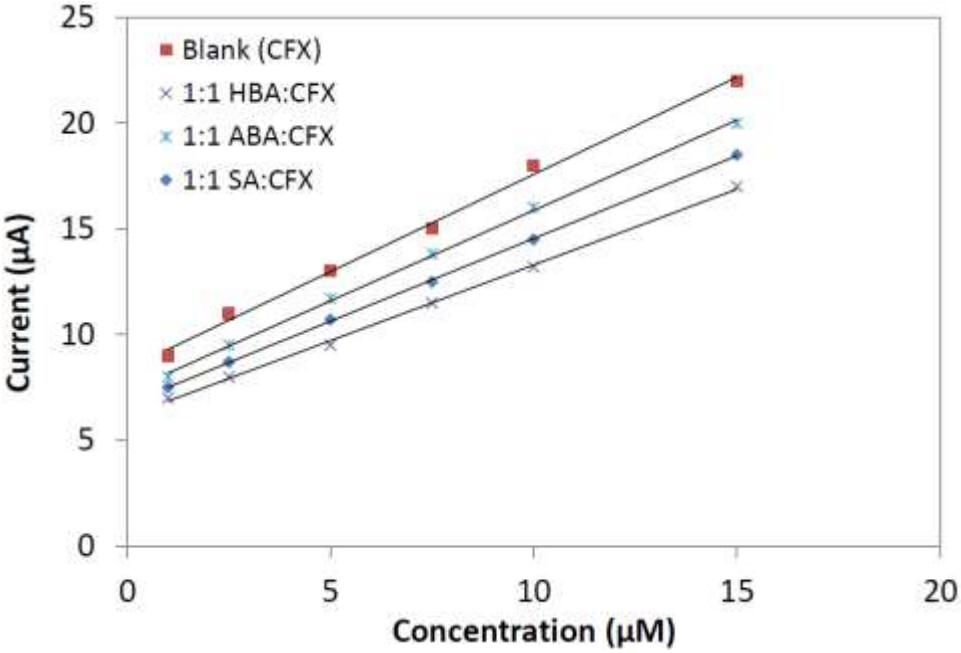

Figure S-3-10. Calibration graphs of CFX at different concentration without organics (blank/CFX only) (y = 0.920±0.03 x + 8.38±0.249, R^2 = 0.996), with equimolar ABA (y = 0.854±0.012 x + 7.328±0.105, R^2 = 0.99), equimolar HBA (y = 0.72±0.052 x + 6.144±0.112, R^2 = 0.999) and equimolar SA (y = 0.782±0.005 x + 6.723±0.046, R^2 = 0.998).

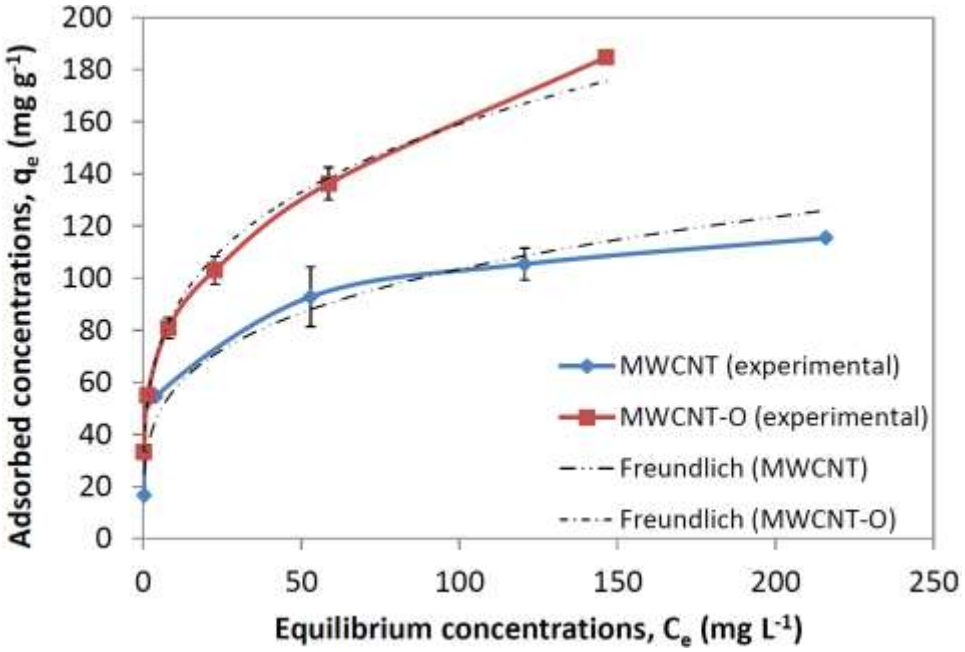

Figure S-3-11. Adsorption isotherms of ciprofloxacin on MWCNT and MWCNT-O at 20^{O} C fitted with two models (Freundlich and Langmuir model).

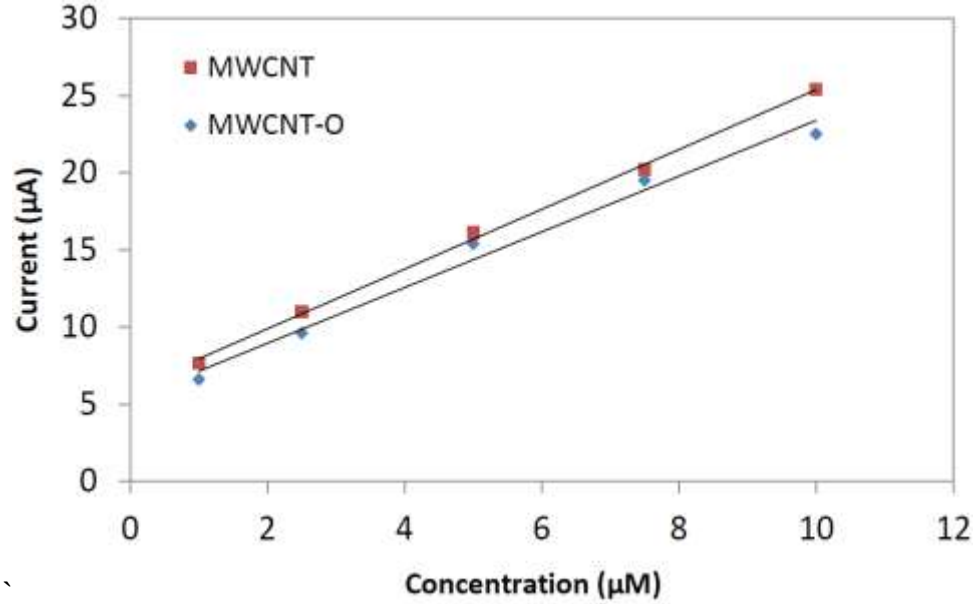

`

Figure S-3-12. Calibration graphs of CFX with porous-Nafion-MWCNT/BDD (y = 1.9379±0.049x + 5.995±0.300, R^2= 0.9981, and porous-Nafion–MWCNT-O/BDD (y=1.8036±0.13 x+5.341±0.784, R^2 = 0.9852).

Table S-3-1 - Determination of CFX in the presence of different interferences (LDRs including LODs). Errors on estimates represent the standard errors.

Interferences	**LOD (µM)**	**Linear range (µM)**	**Sensitivity (Slope(µA µM^{-1}), R^2, Intercept)**
No interference	0.005	0.005 – 0.05	Slope = 41 ± 5.196, R^2 = 0.98 Intercept= 2.055 ± 0.153
Ca^{2+}	0.005	0.005 - 1	Slope = 4.15 ± 0.849, R^2 = 0.89 Intercept= 1.9 ± 0.425
Chloride (1mM)	0.005	0.005 – 0.05	Slope = 33.84 ± 8.78, R^2 = 0.94 Intercept= 2.633 ± 0.259
SDBS (1mM)	0.005	0.005 – 0.05	Slope = 23.25 ± 7.83, R^2 = 0.907 Intercept= 0.565 ± 0.232
Humic acid(11mg L^{-1})	0.005	0.005 – 0.05	Slope = 29.63 ± 13.38, R^2 = 0.84 Intercept= 1.06 ± 0.393
Amoxicillin (1mM)	0.005	0.005 – 0.05	Slope = 24.92 ± 13.83, R^2 = 0.83 Intercept= 1.29 ± 0.407
Without WWE	0.005	0.005 – 0.05	Slope = 38.61 ± 10.53, R^2 = 0.93 Intercept= 2.19±0.311
$WWE_{pH= 4.5}$	0.005	0.005 – 0.05	Slope = 11.09 ± 4.98, R^2 = 0.84 Intercept= 0.459±0.147
$WWE_{pH= 4.5, I= 0.1}$	0.005	0.005 – 0.05	Slope = 13.42 ± 4.74, R^2 = 0.901 Intercept= 0.442±0.14
WWE	5	5 - 15	Slope = 0.15 ± 0.03, R^2 = 0.912 Intercept= 0.328±0.341
Without organics	0.005	0.005 – 0.05	Slope = 36.98 ± 16.61, R^2 = 0.83 Intercept= 2.198±0.491
1:1 CFX:HBA	0.005	0.005 – 0.05	Slope = 36.43 ± 14.73, R^2 = 0.85 Intercept= 1.198±0.482
1:10 CFX:HBA	1	1 - 15	Slope = 0.65 ± 0.012, R^2 = 0.99 Intercept= 1.329±0.103
1:1 CFX:ABA	0.005	0.005 – 0.05	Slope = 34.24± 12.34, R^2 = 0.87 Intercept= 5.198±0.861
1:10 CFX:ABA	0.05	0.05 - 1	Slope = 2.10 ± 0.064, R^2 = 0.999 Intercept= 3.832±0.845

Appendix B

S-4-1. Mass Transfer Coefficient.

The Levich equation (S-4-1) was used to calculate the mass transfer coefficient for the i^{th} species ($k_{m,i}$) [340] and was used to calculate the mass transfer rate (r_i) (equation (S-4-2)).

$$k_{m,i} = 0.62\, D_i^{2/3} \omega^{1/2} \nu^{-1/6} \quad \text{(S-4-1)}$$

$$r_i = k_{m,i} C_i \quad \text{(S-4-2)}$$

where D_i is the diffusion coefficient for the i^{th} compound, ω is the rotation speed per sec., v is the kinematic viscosity of water (1.0 x 10^{-6} m^2 s^{-1}), and C_i is the initial bulk concentration of the i^{th} species. Diffusion coefficients for phenol and terephthalic acid (TA) were 9×10^{-10} m^2 s^{-1} and 4×10^{-10} m^2 s^{-1}, respectively [498,499]. The electrode rotation rate was 523.6 s^{-1} (5000 rpm). The mass transfer rates of phenol (1mM) and TA (0.1mM) were calculated as 7.99 mmole m^{-2} min^{-1} and 0.463 mmole m^{-2} min^{-1}, respectively.

S-4-2. XPS Characterization.

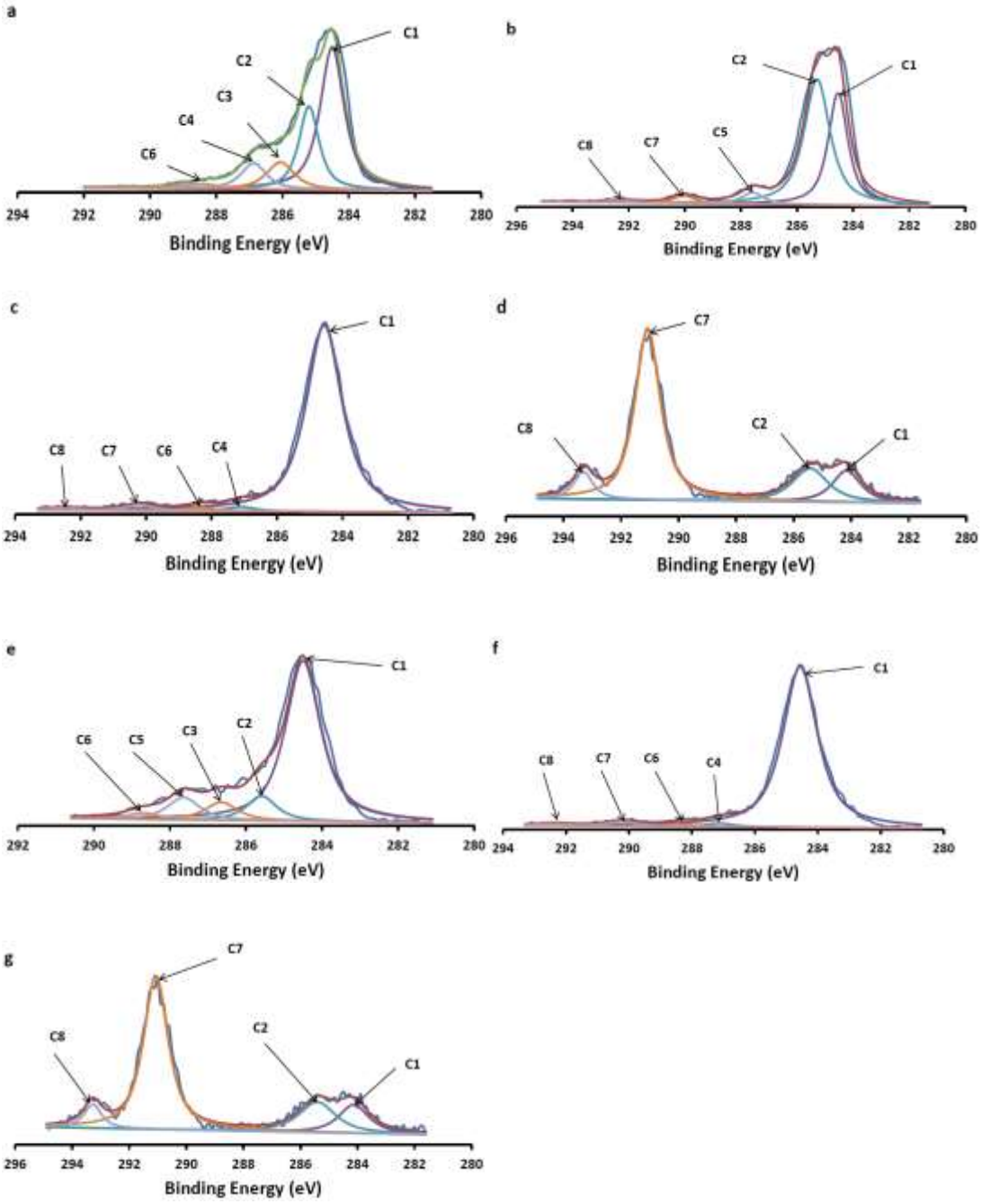

Figure S-4-1. Deconvoluted results of C 1s XPS spectra of a) BDD-O, b) BDDF-plasma, c) BDDF-PFOA, d) BDDF-aliphatic, e) BDDF-aromatic, f) BDDF-PFOA-aged and g) BDDF-aliphatic-aged. Legend: C1: =C=C=; C2: ≡C-C≡; C3: ≡C-OH; C4: =C=O; C5: ≡C-F; C6: -COOH; C7: $=CF_2$; C8: $-CF_3$

Table S-4-1. Comparison of Atomic Ratios (F:Si, F:C and Si:CF_2:CF_3) of an Aliphatic Silane molecule with BDDF-aliphatic (from XPS) and BDDF-aliphatic-aged (from XPS) and Si:CF of an Aromatic Silane molecule with BDDF-aromatic (from XPS).

Atomic Ratio →	**F:Si**	**F:C**	**Si:CF_2:CF_3**	**Si:CF**
Aliphatic Molecule	17	1.7	1:7:1	-
BDDF-aliphatic	15.6	1.88	0.51:8.3:1	-
BDDF-aliphatic-aged	14.7	1.78	0.54:8.63:1	-
Aromatic Molecule	-	-	-	1:5
BDDF-aromatic	-	-	-	1:4.8

S-4-3. Electrochemical Characterization.

The electrochemical response changed after plasma treatment of the BDD electrode. The CV scans (scan rate = 100 mV s^{-1}) in the presence of $Fe(CN)_6^{3-/4-}$ showed a decrease in peak currents for oxidation ($I_{peak,anodic,BDD-O}$= 593 µA to $I_{peak,anodic,BDDF-plasma}$= 255 µA) (Table S-4-2). The plasma treatment also increased the anodic to cathodic peak separation (ΔE_i) from ΔE_{BDD-O} = 212 mV for the BDD-O electrode to $\Delta E_{BDDF-plasma}$ = 1032 mV for the BDDF-plasma electrode (Figure S-4-2a). CV scans in the presence of $Fe^{2+/3+}$ showed an increase in current response ($I_{peak,anodic,BDD-O}$ = 350 µA and $I_{peak,anodic,BDDF-plasma}$= 390 µA) and a decrease in peak separation (ΔE_{BDD-O} = 357 mV and $\Delta E_{BDDF-plasma}$= 182 mV) for BDDF-plasma compared to BDD-O (Table S-4-2 and Figure S-4-2b).

The PFOA modified electrodes and aliphatic silanized BDD electrodes were characterized using the same redox couples. The CV scans (scan rate = 100 mV s^{-1}) in the presence of $Fe(CN)_6^{3-/4-}$ showed a decrease in peak current ($I_{peak,anodic,BDD-O}$= 521 µA and $I_{peak,anodic,BDDF-PFOA}$= 328 µA) and an increased peak separation after fluorination (ΔE_{BDD-O} = 309 mV and $\Delta E_{BDDF-PFOA}$ = 941 mV) (Table S-4-2 and Figure S-4-2c). CV scans in the presence of $Fe^{2+/3+}$ showed a decrease in peak current ($I_{peak,anodic,BDD-O}$= 507 µA and $I_{peak,anodic,BDDF-PFOA}$= 290 µA) and an increase in peak separation (ΔE_{BDD-O}= 225 mV and $\Delta E_{BDDF-PFOA}$= 1110 mV) after fluorination, as shown in Table S-4-2 and Figure S-4-2d.

The CV scans on the BDDF-aromatic electrode with the redox couples ($Fe(CN)_6^{3-/4-}$ and $Fe^{3+/2+}$) showed a similar behavior to the BDDF-PFOA electrode (Figure S-4-2e,f and Table S-4-2). The CV scans in the presence of $Fe(CN)_6^{3-/4-}$ showed a decrease in peak current ($I_{peak,anodic,BDD-O}$= 517 µA and $I_{peak,anodic,BDDF-aromatic}$= 299 µA) and an increase in peak separation ((ΔE_{BDD-O}= 217 mV and ($\Delta E_{BDDF-aromatic}$= 971 mV) after fluorination, as shown in Table S-4-2 and Figure S-

4-2e. CV scans in the presence of $Fe^{2+/3+}$ showed a decrease in the peak current ($I_{peak,anodic,BDD\text{-}O}$= 510 µA and $I_{peak,anodic,BDDF\text{-}aromatic}$= 324 µA) and an increase in peak separation ($\Delta E_{BDD\text{-}O}$= 213 mV and $\Delta E_{BDDF\text{-}aromatic}$= 997 mV) after fluorination, as shown in Table S-4-2 and Figure S-4-2f.

The CV scans were also performed on the BDDF-aliphatic electrode to show the effect of silanization on the electron transfer rates. The CV scans (scan rate = 100mV s^{-1}) in the presence of $Fe(CN)_6^{3-/4-}$ did not show any peaks associated with redox reactions (Table S-4-2 and Figure 4-2a). However, after ageing small peaks were observed (Figure S-4-2g,h)

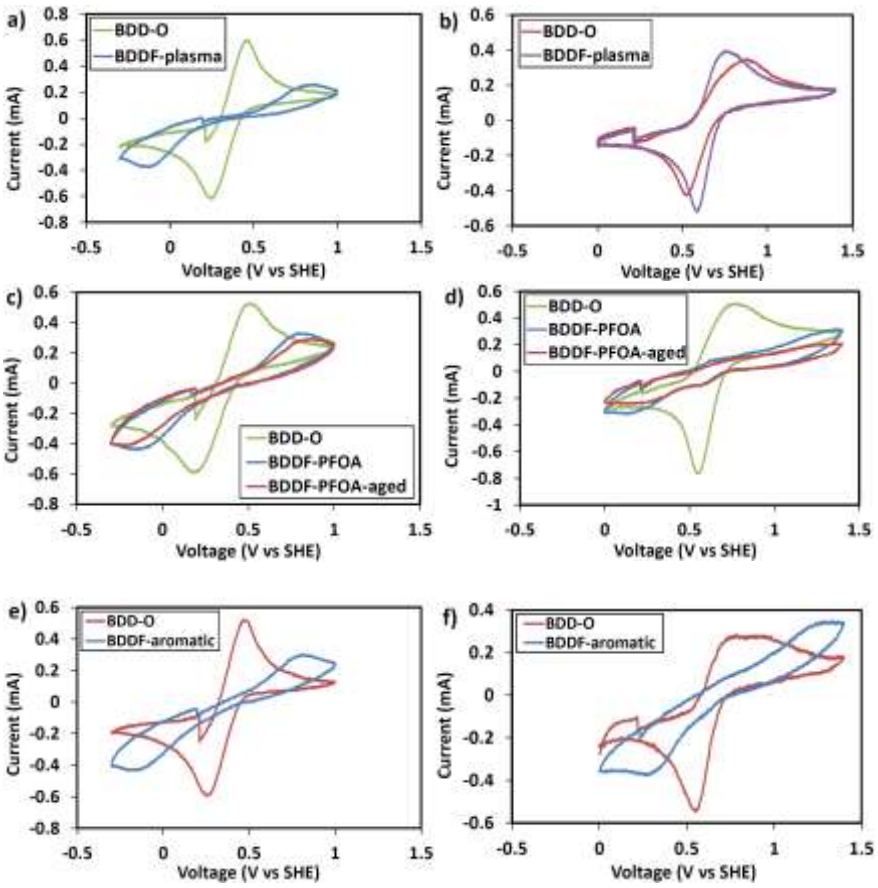

Figure S-4-2 CV scans of: a) BDD-O and BDDF-plasma: 5 mM $Fe(CN)_6^{3-/4-}$; b) BDD-O and BDDF-plasma: 5 mM $Fe^{3+/2+}$; c) BDDF-PFOA and BDDF-PFOA-aged: 5mM $Fe(CN)_6^{3-/4-}$; d) BDDF-PFOA and BDDF-PFOA-aged: 5mM $Fe^{3+/2+}$; e) BDD-O and BDDF-aromatic: 5mM $Fe(CN)_6^{3-/4-}$; f) BDD-O and BDDF-aromatic: 5mM $Fe^{3+/2+}$;

Table S-4-2. CV data of BDD-O, BDDF-plasma, BDDF-PFOA, BDDF-aliphatic, BDDF-aromatic, BDDF-aliphatic-aged and BDDF-PFOA-aged with $Fe(CN)_6^{3-/4-}$ and $Fe^{2+/3+}$ redox couple.

Electrode	$I_{peak,anodic}$ (μA) ($Fe(CN)_6^{3-/4-}$)	$I_{peak,anodic}$ (μA) ($Fe^{2+/3+}$)	ΔE (mV) ($Fe(CN)_6^{3-/4-}$)	ΔE (mV) ($Fe^{2+/3+}$)
BDD-O1*	593	350	212	357
BDDF-plasma	255	390	1032	182
BDD-O2*	521	507	309	225
BDDF-PFOA	328	290	941	1110
BDDF-PFOA-aged	291	202	1041	1052
BDD-O3*	533	316	195	223
BDDF-aliphatic	00	00	-	-
BDDF-aliphatic-aged	58	30	951	1060
BDD-O4*	517	510	217	213
BDDF-aromatic	299	324	971	997

*BDD-O1 = BDD-O before plasma, BDD-O2 = BDD-O before PFOA treatment, BDD-O3 = BDD-O before aliphatic silane treatment and BDD-O4 = BDD-O before aromatic silane treatment

S-4-4. Density Functional Theory Optimized Structures

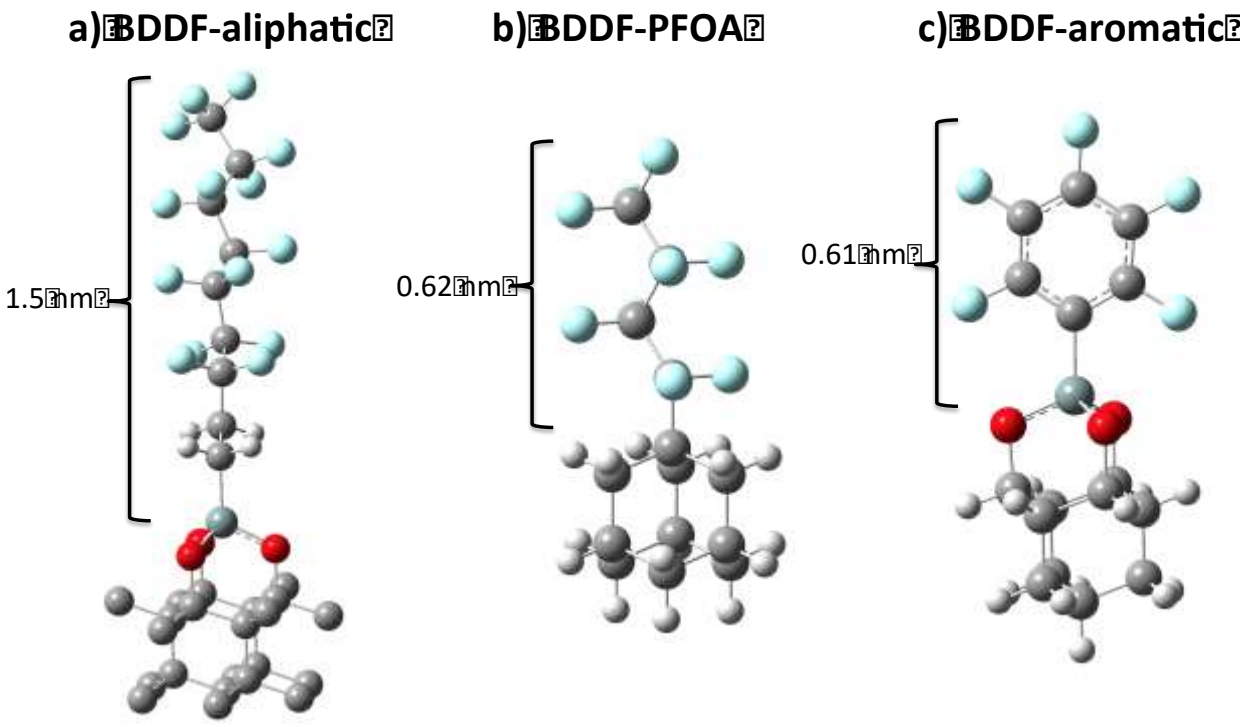

Figure S-4-3. DFT optimized structures of different fluorinated groups on a 10 carbon atom cluster that represents the BDD surface. Atom key: C (grey); F (teal); O (red); H (white); Si (blue-grey)

S-4-5. Additional Experimental Results

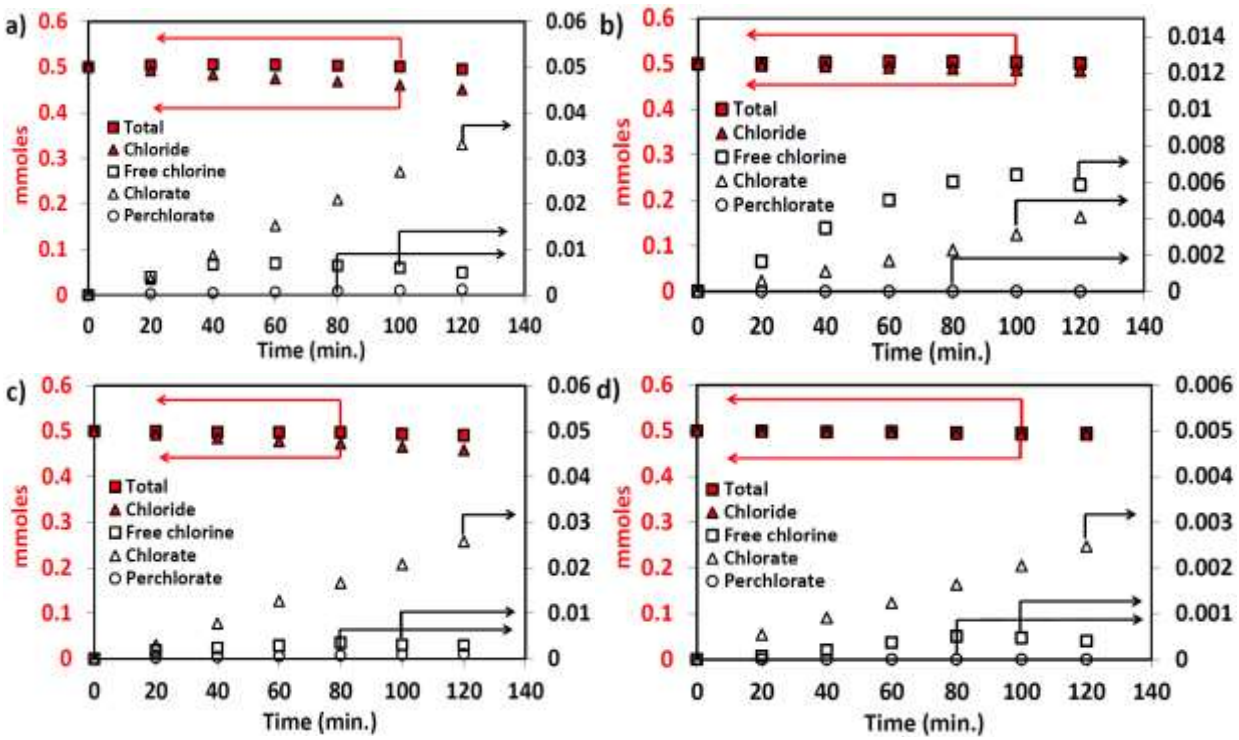

Figure S-4-4. Duplicate experiment to that shown in the main manuscript. Total, free chlorine, chlorate, perchlorate, and chlorine mole balance for a) BDD-O without phenol; b) BDDF-aliphatic without phenol; c) BDD-O with phenol; and d) BDDF-aliphatic with phenol.

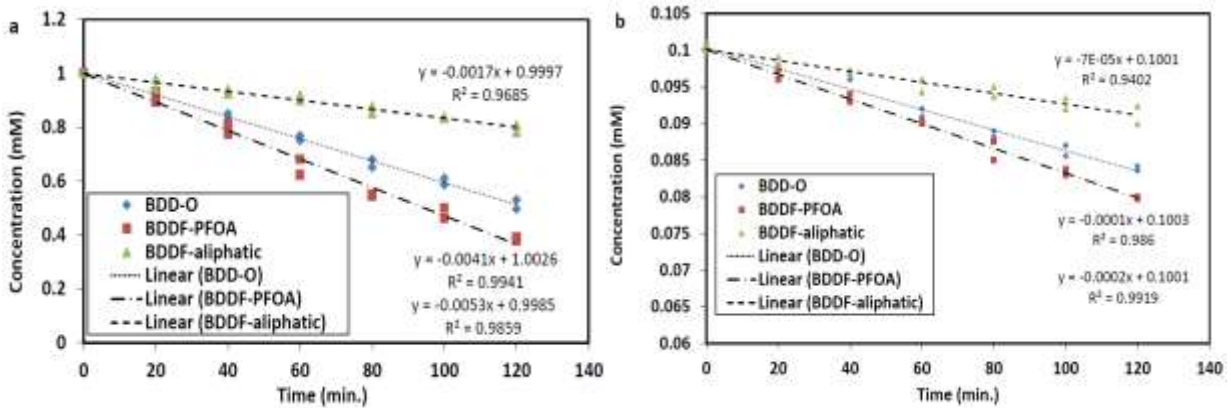

Figure S-4-5. Bulk oxidation of a) 1mM phenol and b) 0.1mM TA for BDD-O, BDDF-PFOA and BDDF-aliphatic at 22^0C.

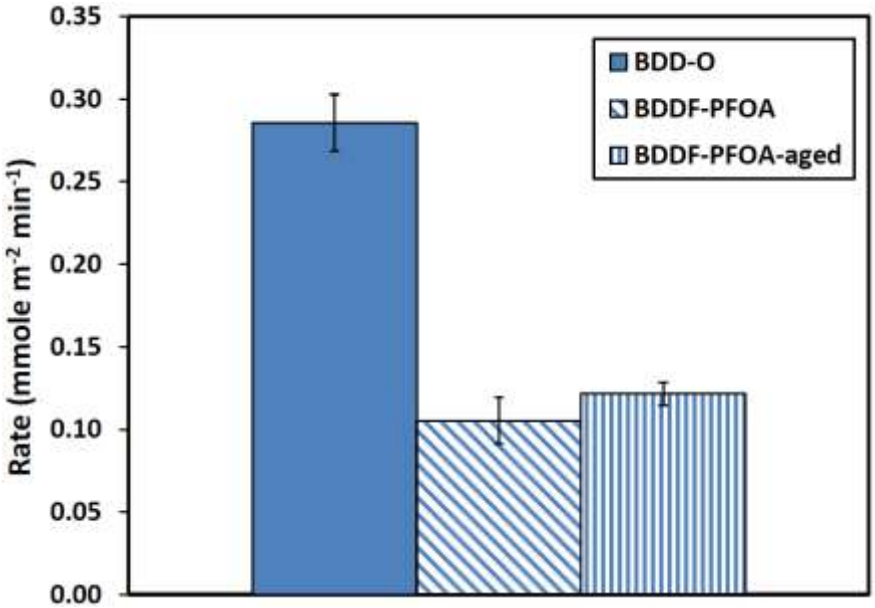

Figure S-4-6. Perchlorate formation rates for BDD-O, BDDF-PFOA & BDDF-PFOA-aged.

Appendix C

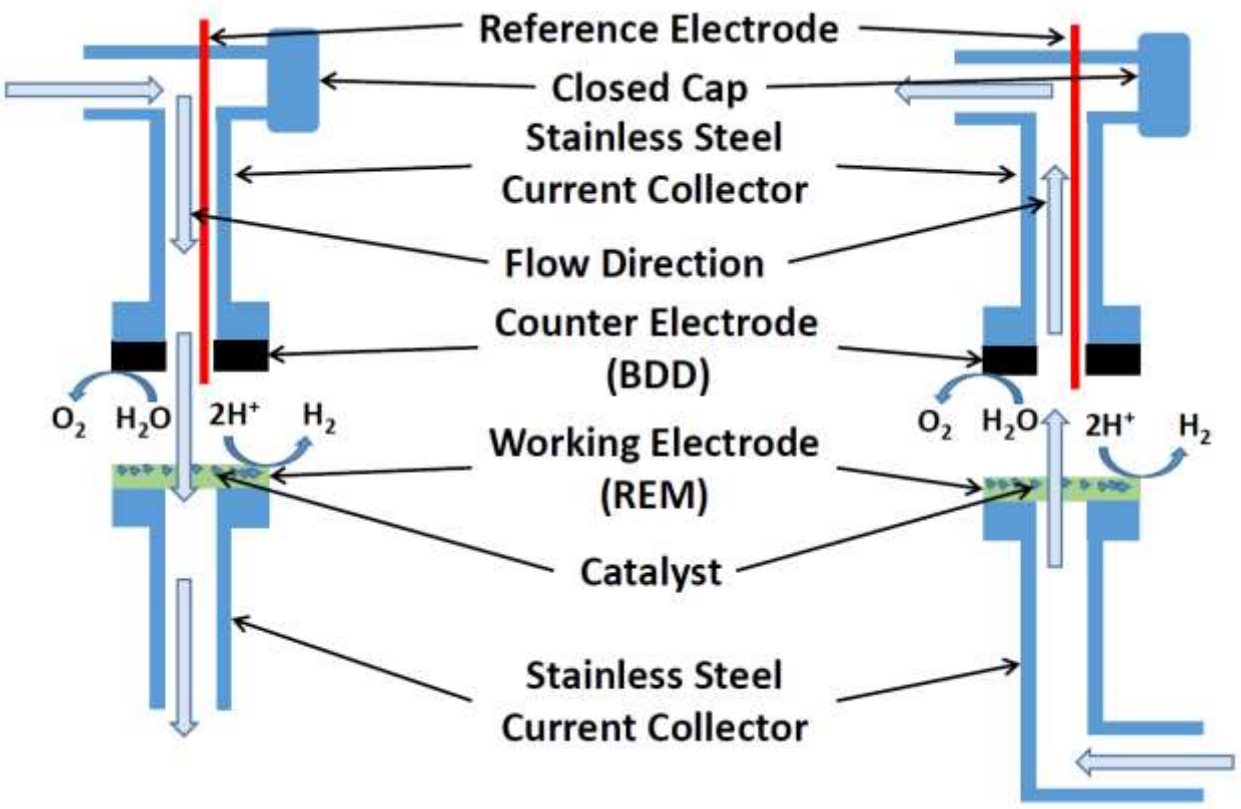

Figure S-5-1. Schematic of the experimental flow-through reactor setup: a) anode-cathode and b) cathode-anode flow mode.

Pore Size Determination

To determine the average pore size of the REM before and after catalyst deposition the flux was measured upon an increase in trans-membrane pressure (ΔP) (Figure S-5-8). The Hagen-Poiseuille equation (S-5-1) was used to determine the pore radius (r_p).

$$u = \frac{r_p^2 \Delta P \varepsilon}{8\eta \Delta x} \tag{S-5-1}$$

In equation S-5-1, u is the velocity; ε is the porosity (0.3); η is the fluid viscosity (9.78×10^{-4} Pa s (21 ^{0}C)); and Δx is the membrane thickness (2.5 mm). The pore radius was determined from equation S-1 as 0.46 ± 0.04, 0.40 ± 0.02, and 0.44 ± 0.03 µm for catalyst-free REM, Pd-Cu/REM, and Pd-In/REM, respectively. These results indicated that the pore size did not change significantly as a result of catalyst deposition.

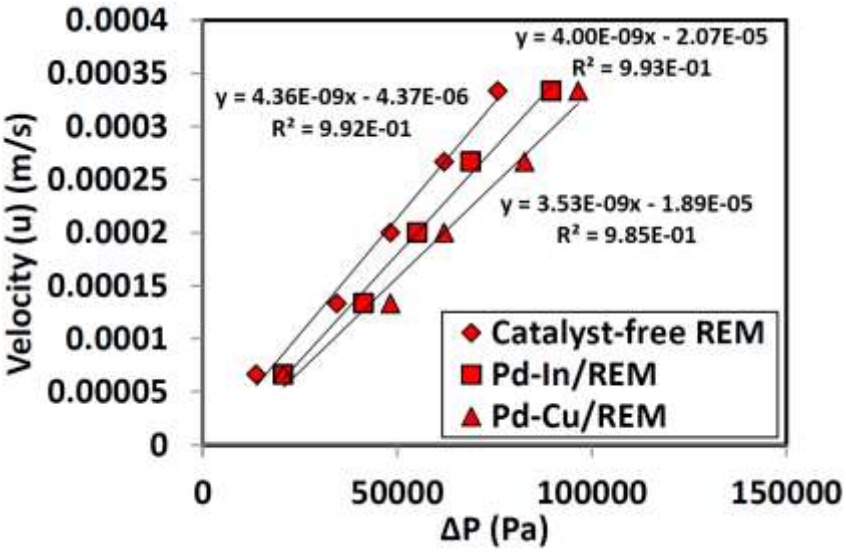

Figure S-5-2. Experimental measurements of flow velocity (u) with pressure drop (ΔP) for REM and Pd-M/REMs.

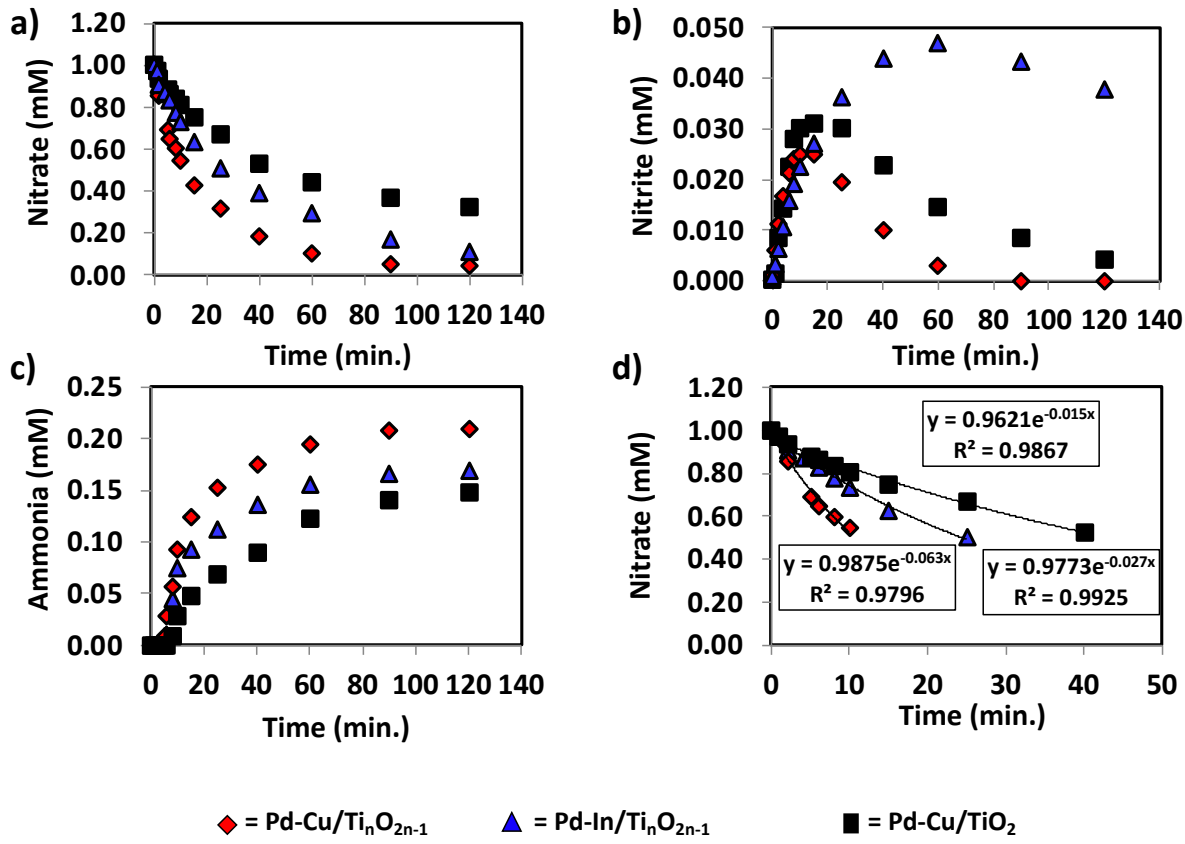

Figure S-5-3. a) Nitrate, b) nitrite, and c) ammonium concentration profiles, and d) first-order fit for initial (50%) nitrate reduction for Pd-Cu/TiO_2, Pd-Cu/Ti_nO_{2n-1}, and Pd-In/ Ti_nO_{2n-1} in batch mode.

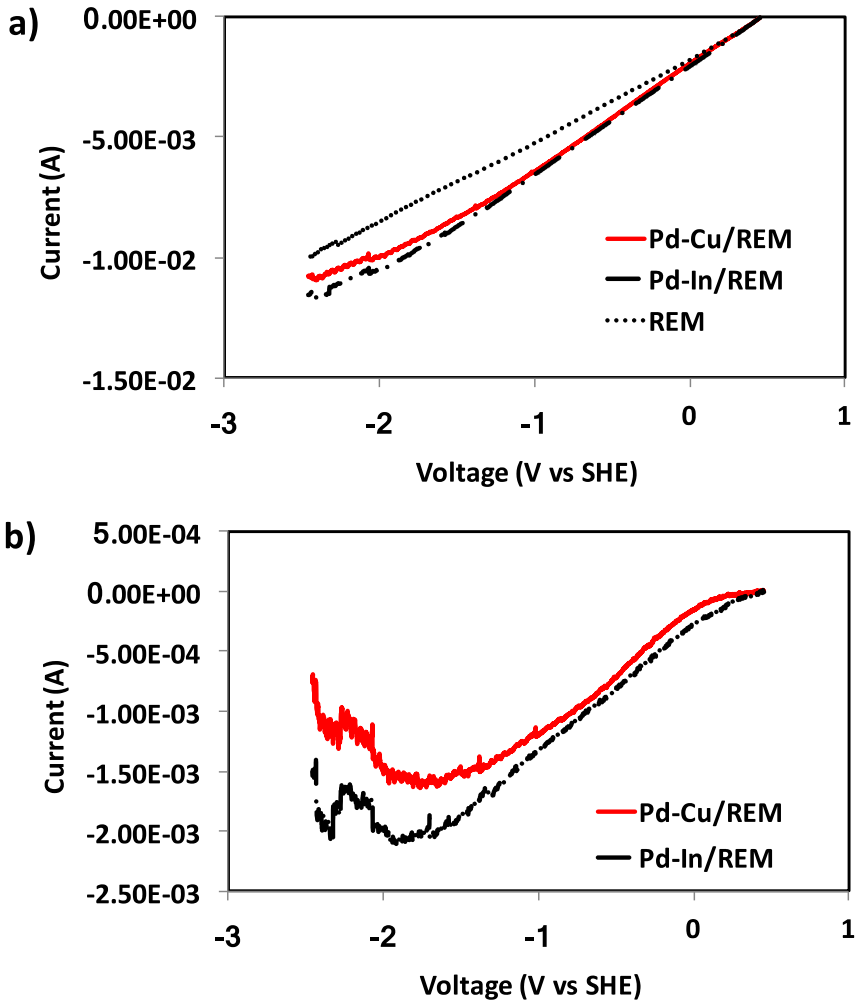

Figure S-5-4. Anode-cathode flow mode. a) LSV scans of solutions with 5 mM $NaNO_3$ in 100 mM $NaHCO_3$ for REM, Pd-Cu/REM, and Pd-In/REM. b) Background subtracted LSV scans for Pd-Cu/REM and Pd-In/REM.

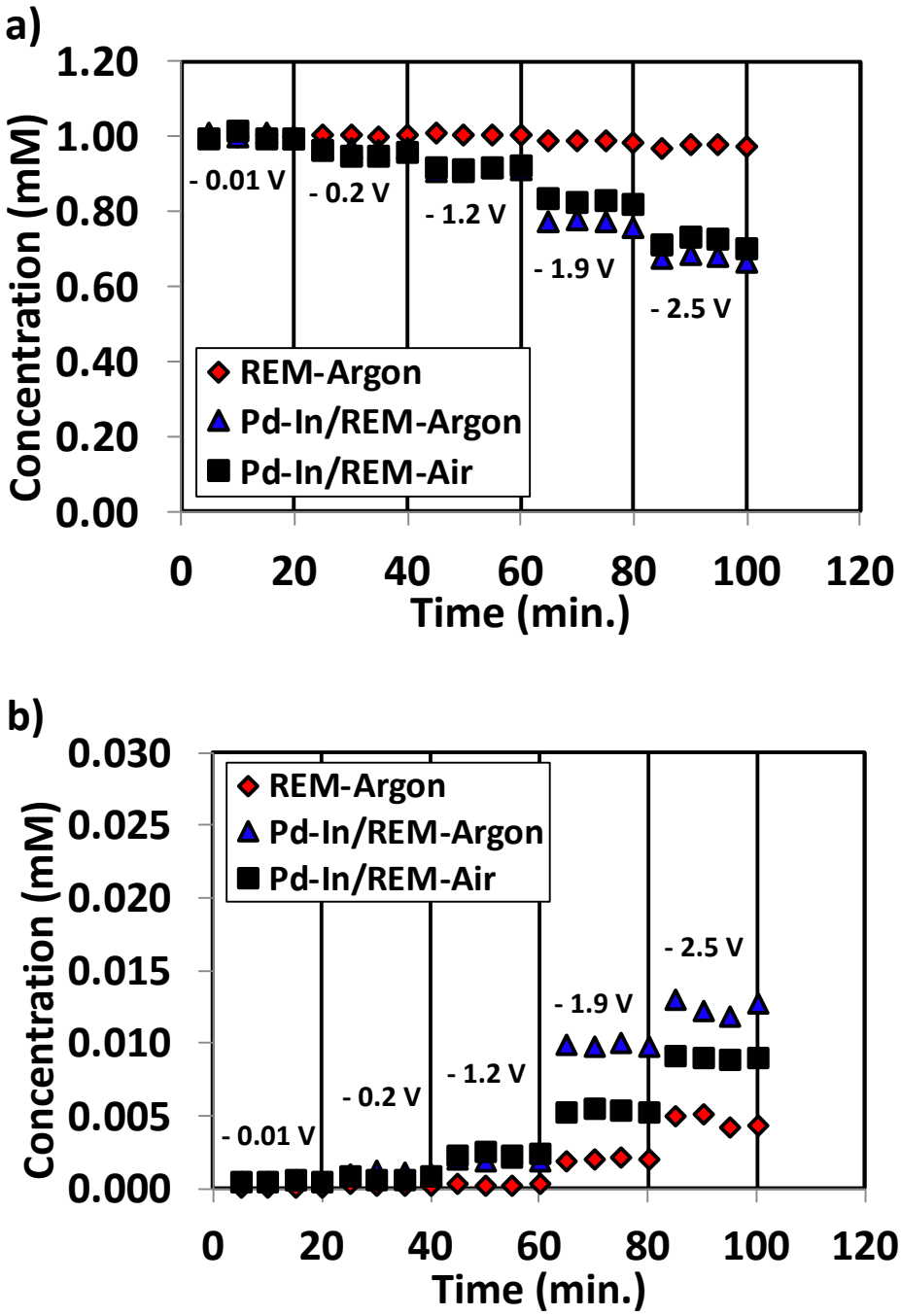

Figure S-5-5. a) Nitrate and b) nitrite concentration profiles for REM and Pd-In/REM at different applied potential in the anode-cathode mode and under different solution conditions.

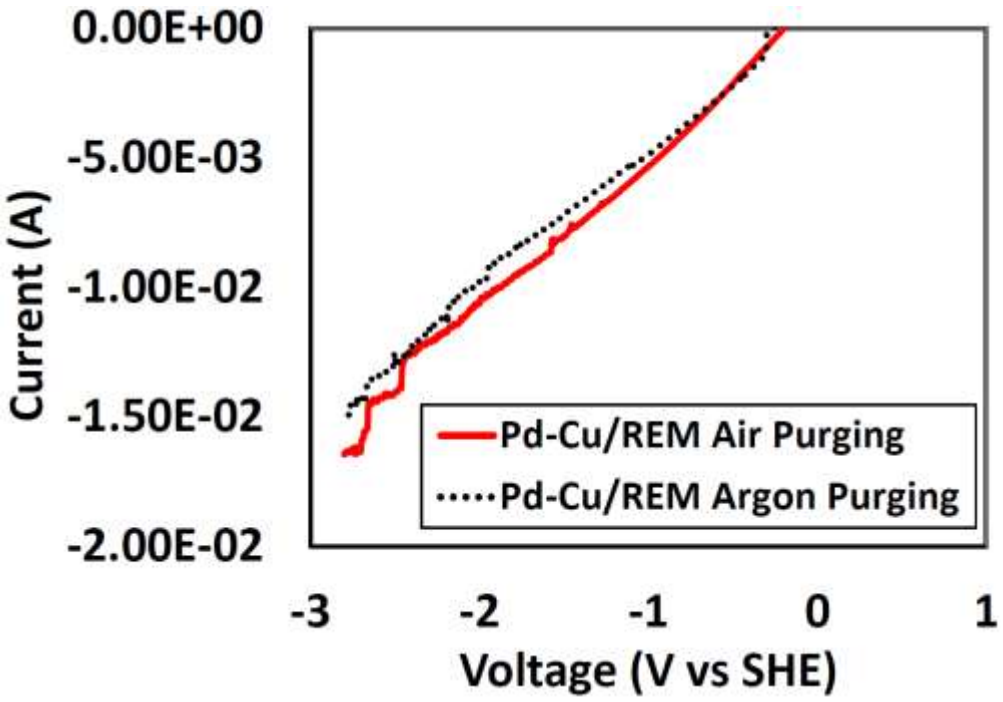

Figure S-5-6. LSV scans of 5 mM $NaNO_3$ in a 100 $NaHCO_3$ electrolyte for Pd-Cu/REM under air and argon purging.

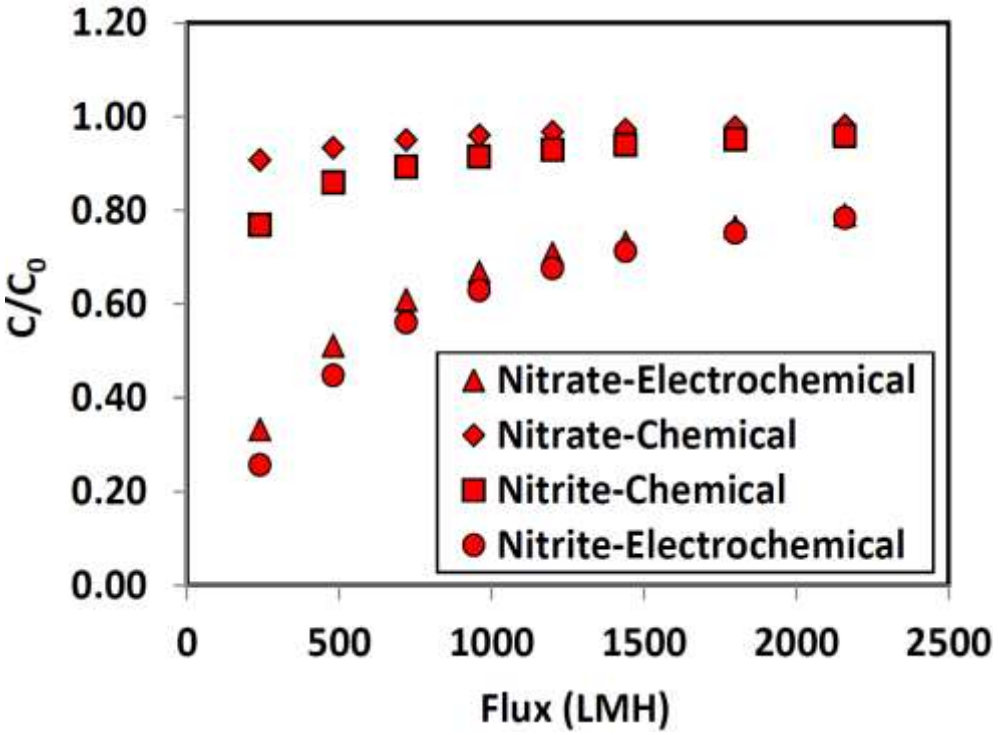

Figure S-5-7. Nitrate and nitrite concentration (C/C_0) profile with flux for chemical and electrochemical reaction methods.

Table S-5-1. Summary of experiment data for all flow-through experiments.

Electrode	Voltage (V/SHE)	NO_3^- Conversion (%)	$S(NO_2^-)$ (%)	$S(NH_3)$ (%)	$S(N_2O)$ (%)	$S(N_2)$ (%)	Effluent pH	Rate Constant ($L\ g_{metal}^{-1}\ min^{-1}$)
Cathode-Anode/Ar Purging								
REM	-0.01	0	0	0	0	0	6.3 ± 0.1	-
	-0.2	0	0	0	0	0	6.5 ± 0.2	-
	-1.2	0.48 ± 0.09	9.5 ± 1.2	<100	0	89 ± 1.09	7.0 ± 0.2	-
	-2.5	1.0 ± 0.08	14 ± 1.7	<100 ± 7.4	0	84 ± 0.81	7.9 ± 0.3	-
	-3.6	2.5 ± 0.61	16 ± 1.4	<40 ± 1.04	0	82 ± 1.10	8.4 ± 0.2	-
Pd-Cu/REM	-0.01	0	0	0	0	0	6.7 ± 0.2	0
	-0.2	0	0	0	0	0	7.3 ± 0.1	0
	-1.2	2.0 ± 0.41	21 ± 2.02	<50.0 ± 8.5	7.1 ± 0.38	69 ± 1.1	8.9 ± 0.3	$(7.7 \pm 1.1) \times 10^{-4}$
	-2.5	20 ± 1.02	35 ± 2.4	31 ± 2.3	12 ± 0.09	23 ± 0.91	9.8 ± 0.2	$(7.7 \pm 0.32) \times 10^{-3}$
	-3.6	42 ± 1.3	30 ± 2.3	26 ± 2.3	19 ± 0.16	23 ± 1.3	10 ± 0.1	$(1.6 \pm 0.09) \times 10^{-2}$
Pd-In/REM	-0.01	0	0	0	0	0	6.6 ± 0.3	0
	-0.2	0	0	0	0	0	7.1 ± 0.2	0
	-1.2	2.0 ± 0.41	22 ± 1.3	<50.0 ± 8.5	6.4 ± 0.08	70 ± 0.19	8.2 ± 0.1	$(6.7 \pm 1.1) \times 10^{-4}$
	-2.5	19 ± 1.1	73 ± 5.7	36 ± 5.9	0.55 ± 0.23	0.50 ± 0.03	9.1 ± 0.3	$(6.3 \pm 0.27) \times 10^{-3}$
	-3.6	39 ± 1.2	73 ± 7.9	38 ± 6.04	1.3 ± 0.09	0.56 ± 0.21	9.9 ± 0.2	$(1.3 \pm 0.11) \times 10^{-2}$
Anode-Cathode/Ar Purging								
REM	-0.01	0	0	0	0	0	6.2 ± 0.2	-
	-0.2	0	0	0	0	0	6.7 ± 0.3	-
	-1.2	0.37 ± 0.05	9.1 ± 0.73	<100	0	88 ± 1.6	7.5 ± 0.2	-
	-1.9	1.5 ± 0.08	14 ± 1.1	<66 ± 0.55	0	85 ± 0.95	8.1 ± 0.1	-
	-2.5	3.2 ± 0.19	16 ± 2.3	<31 ± 1.9	0	82 ± 1.1	8.6 ± 0.2	-

Table S-5-1 (cont.)

Electrode	Voltage (V/SHE)	NO_3^- Conversion (%)	$S(NO_2^-)$ (%)	$S(NH_3)$ (%)	$S(N_2O)$ (%)	$S(N_2)$ (%)	Effluent pH	Rate Constant (L g_{metal}^{-1} min^{-1})
				Anode-Cathode/Ar Purging				
Pd-Cu/REM	-0.01	0.38 ± 0.09	45.2	<100	37.5±0.07	12.5±0.04	6.3±0.2	(1.5 ± 0.48) x 10^{-4}
	-0.2	5.0 ± 0.62	1.8 ± 0.31	<20 ± 2.1	27 ± 0.17	69 ± 0.19	6.5 ± 0.1	(1.9 ± 0.23) x 10^{-3}
	-1.2	19 ± 1.5	0.47 ± 0.18	<5.3 ± 0.41	53 ± 1.01	46 ± 0.09	7.2 ± 0.1	(7.3 ± 0.16) x 10^{-3}
	-1.9	32 ± 1.4	0.19 ± 0.08	<3.1 ± 0.10	65 ± 0.91	33 ± 1.04	8.6 ± 0.3	(1.2 ± 0.11) x 10^{-2}
	-2.5	43 ± 2.2	0.07 ± 0.02	<2.3 ± 0.11	70 ± 0.38	29 ± 0.72	9.2 ± 0.1	(1.6 ± 0.07) x 10^{-2}
Pd-In/REM	-0.01	0.51 ± 0.08	0	<100	27 ± 0.31	9.1 ± 0.27	6.2 ± 0.2	(1.7 ± 0.38) x 10^{-4}
	-0.2	4.0 ± 0.34	2.5 ± 0.42	<25 ± 2.04	35 ± 0.09	67 ± 1.3	6.6 ± 0.1	(1.3 ± 0.14) x 10^{-3}
	-1.2	9.0 ± 1.08	2.2 ± 0.24	<11 ± 1.1	73 ± 0.19	24 ± 0.73	7.3 ± 0.1	(3.0 ± 0.11) x 10^{-3}
	-1.9	24 ± 2.04	4.0 ± 0.89	<4.2 ± 0.23	61 ± 0.41	34 ± 0.94	8.3 ± 0.2	(8.0 ± 0.04) x 10^{-3}
	-2.5	33 ± 2.3	3.6 ± 0.28	<3.0 ± 0.15	68 ± 0.32	28 ± 0.13	9.3 ± 0.2	(1.1 ± 0.03) x 10^{-2}
				Anode-Cathode/Air Purging				
Pd-Cu/REM	-0.01	2.6 ± 0.48	1.9 ± 0.27	<38 ± 5.2	5.0 ± 1.4	92 ± 0.83	6.1 ± 0.3	(1.0 ± 0.18) x 10^{-4}
	-0.2	7.0 ± 0.91	1.0 ± 0.08	<14 ± 1.8	20 ± 0.89	78 ± 0.17	6.6 ± 0.2	(2.7 ± 0.11) x 10^{-3}
	-1.2	13 ± 1.2	2.2 ± 0.13	<7.1 ± 0.47	21 ± 0.08	76 ± 1.4	7.0 ± 0.2	(5.3 ± 0.09) x 10^{-3}
	-1.9	25 ± 1.03	1.3 ± 0.28	<3.9 ± 0.15	46 ± 0.53	52 ± 0.93	8.7 ± 0.1	(9.9 ± 0.12) x 10^{-3}
	-2.5	42 ± 1.8	0.78 ± 0.04	<2.4 ± 0.10	55 ± 0.29	43 ± 1.01	9.4 ± 0.2	(1.6 ± 0.06) x 10^{-2}
Pd-In/REM	-0.01	0.8 ± 0.09	5.0 ± 0.29	<100	3.7 ± 0.04	91 ± 2.01	6.2 ± 0.1	(2.6 ± 0.32) x 10^{-4}
	-0.2	5.2 ± 0.27	1.5 ± 0.09	<19 ± 1.01	17 ± 0.68	81 ± 0.39	6.4 ± 0.2	(1.7 ± 0.17) x 10^{-3}
	-1.2	9.2 ± 0.18	2.6 ± 0.33	<11 ± 0.57	58 ± 1.2	39 ± 0.08	7.6 ± 0.3	(3.1 ± 0.10) x 10^{-3}
	-1.9	17 ± 1.09	2.9 ± 0.27	<5.5 ± 0.29	64 ± 0.29	32 ± 0.17	8.6 ± 0.2	(5.9 ± 0.08) x 10^{-3}
	-2.5	28 ± 1.2	3.1 ± 0.82	<3.5 ± 0.15	72 ± 1.1	24 ± 0.13	9.6 ± 0.1	(9.3 ± 0.09) x 10^{-3}

Table S-5-1 (cont.)

Electrode	Voltage (V/SHE)	NO_3^- Conversion (%)	$S(NO_2^-)$ (%)	$S(NH_3)$ (%)	$S(N_2O)$ (%)	$S(N_2)$ (%)	Effluent pH	Rate Constant ($L\ g_{metal}^{-1}\ min^{-1}$)
Anode-Cathode/Air Purging/Bicarbonate Buffer								
Pd-Cu/REM	-0.01	2.4 ± 0.15	1.5 ± 0.08	<41 ± 2.5	1.5 ± 0.95	96 ± 0.17	7.8 ± 0.4	(9.2 ± 0.28) x 10^{-4}
	-0.2	9.4 ± 0.37	0.59 ± 0.02	<10 ± 0.47	10 ± 0.18	89 ± 1.5	7.8 ± 0.4	(3.6 ± 0.13) x 10^{-3}
	-1.2	17 ± 1.04	1.1 ± 0.17	<5.9 ± 0.33	47 ± 0.51	51 ± 0.81	7.8 ± 0.4	(6.5 ± 0.05) x 10^{-3}
	-1.9	28 ± 0.98	1.2 ± 0.13	<3.4 ± 0.11	34 ± 1.07	64 ± 1.2	7.8 ± 0.4	(1.1 ± 0.17) x 10^{-2}
	-2.5	44 ± 1.4	0.56 ± 0.02	<2.2 ± 0.07	42 ± 0.36	57 ± 0.03	7.8 ± 0.4	(1.7 ± 0.15) x 10^{-2}
Anode-Cathode/Air Purging/Surface Water								
Pd-Cu/REM	-0.01	0.5 ± 0.06	2.0 ± 0.03	<100	3.7 ± 0.15	95 ± 2.01	7.0 ± 0.3	(1.9 ± 0.31) x 10^{-4}
	-0.2	3.8 ± 0.26	1.05 ± 0.12	<26 ± 1.3	26 ± 0.08	72 ± 0.63	7.9 ± 0.2	(1.4 ± 0.16) x 10^{-3}
	-1.2	13 ± 0.89	0.49 ± 0.02	<7.6 ± 0.43	44 ± 0.63	55 ± 0.05	8.4 ± 0.1	(5.1 ± 0.09) x 10^{-3}
	-1.9	24 ± 1.3	0.16 ± 0.03	<4.1 ± 0.19	46 ± 1.02	53 ± 0.21	8.6 ± 0.3	(9.4 ± 0.09) x 10^{-3}
	-2.5	32 ± 1.1	0.07 ± 0.01	<3.1 ± 0.11	43 ± 0.32	56 ± 0.49	8.8 ± 0.2	(1.2 ± 0.11) x 10^{-2}
Anode-Cathode/Air Purging/Bicarbonate Buffer/Series								
Pd-Cu/REM	-0.01	2.2 ± 0.14	1.8 ± 0.11	<45 ± 2.8	2.0 ± 0.04	96 ± 0.78	7.9 ± 0.2	(8.5 ± 0.18) x 10^{-4}
	-0.2	19 ± 0.88	0.4 ± 0.03	<5.1 ± 0.24	47 ± 0.37	51 ± 0.19	7.9 ± 0.2	(7.6 ± 0.23) x 10^{-3}
	-1.2	29 ± 1.2	0.93 ± 0.10	<3.4 ± 0.25	41 ± 1.8	57 ± 0.27	8.0 ± 0.1	(1.1 ± 0.11) x 10^{-2}
	-1.9	44 ± 1.8	0.65 ± 0.05	<2.3 ± 0.09	52 ± 0.94	47 ± 0.59	8.0 ± 0.1	(1.7 ± 0.07) x 10^{-2}
	-2.5	65 ± 1.3	0.40 ± 0.06	<1.5 ± 0.04	43 ± 0.36	56 ± 0.94	8.0 ± 0.2	(2.5 ± 0.06) x 10^{-2}
Anode-Cathode/Air Purging/Surface Water/Series								
Pd-Cu/REM	-0.01	1.2 ± 0.03	5.0 ± 0.23	<83 ± 3.06	1.2 ± 0.07	96 ± 0.03	7.2 ± 0.2	(4.6 ± 0.41) x 10^{-4}
	-0.2	14 ± 0.21	0.33 ± 0.11	<7.1 ± 0.11	42 ± 0.69	56 ± 0.29	8.0 ± 0.3	(5.4 ± 0.27) x 10^{-3}
	-1.2	23 ± 1.1	0.47 ± 0.09	<4.3 ± 0.20	43 ± 0.08	55 ± 0.74	8.5 ± 0.2	(8.9 ± 0.13) x 10^{-3}
	-1.9	35 ± 2.3	0.18 ± 0.06	<2.8 ± 0.17	58 ± 1.1	41 ± 1.7	8.8 ± 0.1	(1.3 ± 0.08) x 10^{-3}
	-2.5	51 ± 2.07	0.07 ± 0.08	<1.9 ± 0.08	53 ± 0.84	47 ± 0.93	8.9 ± 0.3	(1.9 ± 0.12) x 10^{-2}

Table S-5-2. Total N Data for REM, Pd-In/REM, and Pd-Cu/REM under different solution conditions.

Electrode	Voltage (V/SHE)	Total N (mM) (Before oxidative digestion)	Total N (mM) (After oxidative digestion)
Cathode-Anode/Ar Purging			
REM	-0.01	0.99 ± 0.001	0.99 ± 0.002
	-0.2	0.99 ± 0.001	0.99 ± 0.002
	-1.2	0.99 ± 0.006	0.99 ± 0.006
	-2.5	0.98 ± 0.003	0.98 ± 0.002
	-3.6	0.97 ± 0.004	0.97 ± 0.001
Pd-In/REM	-0.01	0.99 ± 0.001	0.99 ± 0.001
	-0.2	0.99 ± 0.003	0.99 ± 0.005
	-1.2	0.98 ± 0.009	0.99 ± 0.006
	-2.5	0.82 ± 0.011	0.99 ± 0.009
	-3.6	0.61 ± 0.008	0.99 ± 0.01
Pd-Cu/REM	-0.01	0.99 ± 0.002	0.99 ± 0.001
	-0.2	0.99 ± 0.004	0.99 ± 0.002
	-1.2	0.98 ± 0.001	0.99 ± 0.002
	-2.5	0.80 ± 0.01	0.95 ± 0.011
	-3.6	0.58 ± 0.009	0.90 ± 0.010
Anode-Cathode/Ar Purging			
REM	-0.01	0.99 ± 0.002	0.99 ± 0.001
	-0.2	0.99 ± 0.002	0.99 ± 0.002
	-1.2	0.99 ± 0.004	0.99 ± 0.003
	-1.9	0.98 ± 0.003	0.98 ± 0.002
	-2.5	0.97 ± 0.004	0.97 ± 0.003
Pd-In/REM	-0.01	0.99 ± 0.002	0.99 ± 0.001
	-0.2	0.96 ± 0.008	0.97 ± 0.007
	-1.2	0.905 ± 0.01	0.97 ± 0.009
	-1.9	0.77 ± 0.02	0.91 ± 0.01
	-2.5	0.67 ± 0.03	0.89 ± 0.02
Pd-Cu/REM	-0.01	0.99 ± 0.001	0.99 ± 0.001
	-0.2	0.95 ± 0.01	0.97 ± 0.01
	-1.2	0.81 ± 0.01	0.92 ± 0.02
	-1.9	0.68 ± 0.01	0.88 ± 0.03
	-2.5	0.57 ± 0.02	0.87 ± 0.03
Anode-Cathode/Air Purging			
Pd-In/REM	-0.01	0.99 ± 0.002	0.99 ± 0.001
	-0.2	0.94 ± 0.007	0.95 ± 0.009
	-1.2	0.91 ± 0.01	0.96 ± 0.01
	-1.9	0.83 ± 0.02	0.94 ± 0.03
	-2.5	0.72 ± 0.01	0.92 ± 0.02
Pd-Cu/REM	-0.01	0.99 ± 0.001	0.99 ± 0.001
	-0.2	0.95 ± 0.006	0.96 ± 0.003
	-1.2	0.86 ± 0.01	0.89 ± 0.009
	-1.9	0.74 ± 0.02	0.86 ± 0.01

	-2.5	0.58 ± 0.03	0.81 ± 0.01

Table S-5-2 (cont.)

Electrode	**Voltage (V/SHE)**	**Total N (mM) (Before oxidative digestion)**	**Total N (mM) (After oxidative digestion)**
Anode-Cathode/Air Purging/Buffer			
Pd-Cu/REM	-0.01	0.98 ± 0.004	0.98 ± 0.002
	-0.2	0.91 ± 0.008	0.92 ± 0.007
	-1.2	0.83 ± 0.009	0.91 ± 0.01
	-1.9	0.71 ± 0.01	0.81 ± 0.03
	-2.5	0.55 ± 0.02	0.74 ± 0.01
Anode-Cathode/Air Purging/Surface Water			
Pd-Cu/REM	-0.01	0.99 ± 0.001	0.99 ± 0.001
	-0.2	0.96 ± 0.003	0.97 ± 0.002
	-1.2	0.86 ± 0.01	0.92 ± 0.011
	-1.9	0.75 ± 0.02	0.86 ± 0.01
	-2.5	0.68 ± 0.01	0.82 ± 0.03
Anode-Cathode/Air Purging/Bicarbonate Buffer/Series			
Pd-Cu/REM	-0.01	0.97 ± 0.004	0.97 ± 0.003
	-0.2	0.82 ± 0.01	0.91 ± 0.02
	-1.2	0.71 ± 0.03	0.83 ± 0.021
	-1.9	0.56 ± 0.03	0.79 ± 0.01
	-2.5	0.36 ± 0.02	0.64 ± 0.04
Anode-Cathode/Air Purging/Surface Water/Series			
Pd-Cu/REM	-0.01	0.97 ± 0.002	0.97 ± 0.003
	-0.2	0.86 ± 0.009	0.92 ± 0.011
	-1.2	0.77 ± 0.02	0.87 ± 0.014
	-1.9	0.64 ± 0.01	0.85 ± 0.03
	-2.5	0.49 ± 0.03	0.76 ± 0.02

Table S-5-3. Nitrite Concentration and Selectivity for Both Electrocatalytic (-2.5 V/SHE) and Catalytic NO_3^- Reduction at Different Fluxes.

Electrode	Flux (LMH)	Electrocatalytic		Catalytic	
		C_{NO2} (μM)	S_{NO2} (%)	C_{NO2} (μM)	S_{NO2} (%)
Pd-Cu/REM	240	0.7 ± 0.04	0.10 ± 0.01	0.1 ± 0.02	0.11 ± 0.04
	480	1.0 ± 0.09	0.20 ± 0.01	0.7 ± 0.04	1.0 ± 0.01
	720	4.0 ± 0.12	1.0 ± 0.03	0.9 ± 0.01	1.8 ± 0.09
	960	9.0 ± 0.27	2.7 ± 0.10	1.1 ± 0.09	2.7 ± 0.11
	1200	11 ± 0.52	3.7 ± 0.08	1.6 ± 0.11	4.8 ± 0.08
	1440	10 ± 0.21	3.7 ± 0.11	0.9 ± 0.08	3.2 ± 0.12
	1800	6.0 ± 0.11	2.5 ± 0.09	0.7 ± 0.04	3.1 ± 0.09
	2160	4.0 ± 0.08	1.9 ± 0.06	0.3 ± 0.02	1.6 ± 0.10

Table S-5-4. Energy Requirements (kWh mol^{-1}), E_{EO} (kWh m^{-3}), Current Efficiency (CE, %) for REM, Pd-Cu/REM and Pd-In/REM in All Solution Conditions and for Pd-Cu/REM with 10 and 100 mM NO_3^- Under Air Purging with Anode-Cathode Flow Mode.

Electrode	Cathode Voltage (V/SHE)	EC (kWh mol^{-1})	CE (%)	E_{EO} (kWh m^{-3})
Cathode-Anode/Ar Purging				
REM	-0.01	2.8 ± 0.11	9.6 ± 0.87	6.4 ± 0.34
	-0.2	15 ± 0.09	2.5 ± 0.28	36 ± 0.26
	-1.2	29 ± 0.83	1.8 ± 0.37	67 ± 1.9
	-2.5	6.6 ± 0.05	10 ± 1.3	15 ± 0.13
	-3.6	7.8 ± 0.10	9.3 ± 1.05	18 ± 0.19
Pd-Cu/REM	-0.01	2.01 ± 0.04	15 ± 1.2	4.6 ± 0.12
	-0.2	4.8 ± 0.11	8.6 ± 0.74	11 ± 0.16
	-1.2	9.2 ± 0.06	5.7 ± 0.84	21 ± 0.09
	-2.5	1.2 ± 0.01	60 ± 2.5	2.6 ± 0.06
	-3.6	1.2 ± 0.05	72 ± 2.2	2.2 ± 0.08
Pd-In/REM	-0.01	10 ± 0.14	2.8 ± 0.26	24 ± 0.31
	-0.2	4.8 ± 0.05	8.2 ± 0.39	11 ± 0.19
	-1.2	9.4 ± 0.08	5.6 ± 0.47	22 ± 0.23
	-2.5	1.9 ± 0.02	34 ± 1.7	4.1 ± 0.14
	-3.6	1.7 ± 0.03	50 ± 2.06	3.0 ± 0.17
Anode-Cathode/Ar Purging				
REM	-0.01	1.2 ± 0.02	9.4 ± 0.69	2.9 ± 0.09
	-0.2	4.5 ± 0.07	2.6 ± 0.39	10 ± 0.29
	-1.2	13 ± 0.09	2.5 ± 0.27	31 ± 0.34
	-1.9	5.9 ± 0.14	10 ± 0.92	14 ± 0.47
	-2.5	6.0 ± 0.11	12 ± 1.3	14 ± 0.39
Pd-Cu/REM	-0.01	1.6 ± 0.08	2.07 ± 0.12	3.9 ± 0.18
	-0.2	0.69 ± 0.02	59 ± 3.8	1.6 ± 0.06
	-1.2	0.66 ± 0.09	79 ± 3.4	1.4 ± 0.27
	-1.9	0.57 ± 0.10	103 ± 5.9	1.1 ± 0.31
	-2.5	0.64 ± 0.08	102 ± 5.7	1.1 ± 0.23
Pd-In/REM	-0.01	1.9 ± 0.04	2.3 ± 0.25	4.4 ± 0.12
	-0.2	1.0 ± 0.01	40 ± 3.8	2.3 ± 0.04
	-1.2	1.5 ± 0.10	33 ± 3.2	3.3 ± 0.39
	-1.9	0.89 ± 0.09	62 ± 4.8	1.8 ± 0.35
	-2.5	0.90 ± 0.07	70 ± 4.9	1.7 ± 0.31
Anode-Cathode/Air Purging				
Pd-Cu/REM	-0.01	0.70 ± 0.02	32 ± 2.6	1.6 ± 0.09
	-0.2	0.50 ± 0.08	83 ± 4.2	1.1 ± 0.37
	-1.2	0.90 ± 0.10	64 ± 3.4	1.9 ± 0.43
	-1.9	0.75 ± 0.06	83 ± 3.9	1.5 ± 0.34
	-2.5	0.62 ± 0.02	106 ± 5.4	1.1 ± 0.12

Table S-5-4 (cont.)

Electrode	Cathode Voltage (V/SHE)	EC (kWh mol^{-1})	CE (%)	E_{EO} (kWh m^{-3})
Pd-In/REM	-0.01	1.3 ± 0.12	24 ± 1.6	2.9 ± 0.47
	-0.2	0.65 ± 0.07	64 ± 3.6	1.5 ± 0.38
	-1.2	1.6 ± 0.10	31 ± 1.8	3.6 ± 0.41
	-1.9	1.1 ± 0.06	47 ± 2.9	2.4 ± 0.33
	-2.5	1.06 ± 0.03	58 ± 3.9	2.1 ± 0.15
Pd-Cu/REM (10 mM)	-0.21	13 ± 0.18	-	318 ± 2.8
	-0.7	0.06 ± 0.01	-	1.4 ± 0.16
	-1.2	0.14 ± 0.09	-	2.9 ± 1.1
	-1.5	0.17 ± 0.04	-	3.5 ± 0.52
	-2.1	0.19 ± 0.07	-	3.5 ± 0.73
Pd-Cu/REM (100 mM)	-0.25	48 ± 0.24	-	11135 ± 978
	-0.71	0.03 ± 0.01	-	8.3 ± 0.17
	-1.15	0.07 ± 0.02	-	15 ± 0.36
	-1.53	0.12 ± 0.06	-	26 ± 0.94
Anode-Cathode/Air Purging/Buffer				
Pd-Cu/REM	-0.01	0.99 ± 0.12	27 ± 1.4	2.3 ± 0.59
	-0.2	0.97 ± 0.09	44 ± 3.6	2.1 ± 0.44
	-1.2	1.3 ± 0.11	40 ± 2.5	2.8 ± 0.48
	-1.9	1.4 ± 0.13	44 ± 4.3	2.7 ± 0.51
	-2.5	1.3 ± 0.08	51 ± 2.4	2.3 ± 0.34
Anode-Cathode/Air Purging/Surface Water				
Pd-Cu/REM	-0.01	2.6 ± 0.21	11 ± 2.7	6.0 ± 0.89
	-0.2	2.07 ± 0.13	19 ± 3.9	4.7 ± 0.61
	-1.2	1.5 ± 0.08	36 ± 4.0	3.3 ± 0.42
	-1.9	1.1 ± 0.10	53 ± 3.9	2.3 ± 0.49
	-2.5	1.3 ± 0.03	51 ± 4.3	2.7 ± 0.17
Anode-Cathode/Air Purging/Bicarbonate Buffer/Series				
Pd-Cu/REM	-0.01	2.8 ± 0.16	22 ± 2.5	6.3 ± 0.69
	-0.2	1.2 ± 0.19	64 ± 3.7	2.6 ± 0.75
	-1.2	2.3 ± 0.08	51 ± 3.2	4.6 ± 0.32
	-1.9	2.5 ± 0.09	50 ± 3.8	4.4 ± 0.39
	-2.5	2.4 ± 0.06	60 ± 4.2	3.5 ± 0.27
Anode-Cathode/Air Purging/Surface Water/Series				
Pd-Cu/REM	-0.01	4.2 ± 0.22	60 ± 3.4	3.5 ± 1.01
	-0.2	2.2 ± 0.08	15 ± 2.3	9.6 ± 0.36
	-1.2	4.2 ± 0.18	36 ± 3.1	4.6 ± 0.73
	-1.9	3.6 ± 0.12	29 ± 2.6	8.6 ± 0.47
	-2.5	3.6 ± 0.04	35 ± 5.0	6.9 ± 0.13

Appendix D

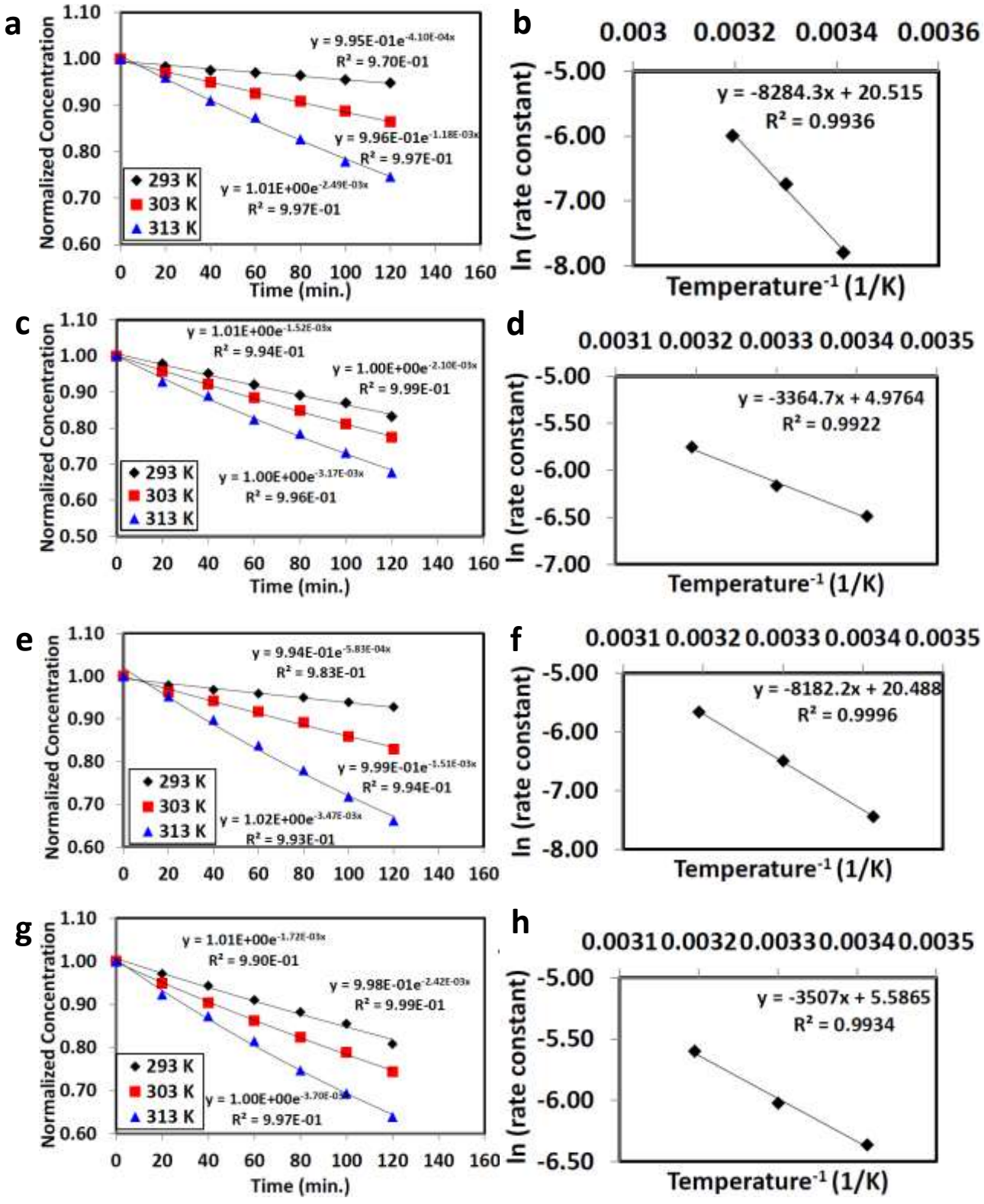

Figure S-6-1. Concentration profiles for oxidation of a) ATZ at 1.5 V/SHE, c) ATZ at 1.8 V/SHE, e) CDN at 1.14 V/SHE and g) CDN at 1.5 V/SHE at 20, 30 and 40 ^{0}C. Arrhenius plot for oxidation of b) ATZ at 1.5 V/SHE, d) ATZ at 1.8 V/SHE, f) CDN at 1.14 V/SHE and h) CDN at 1.5 V/SHE.

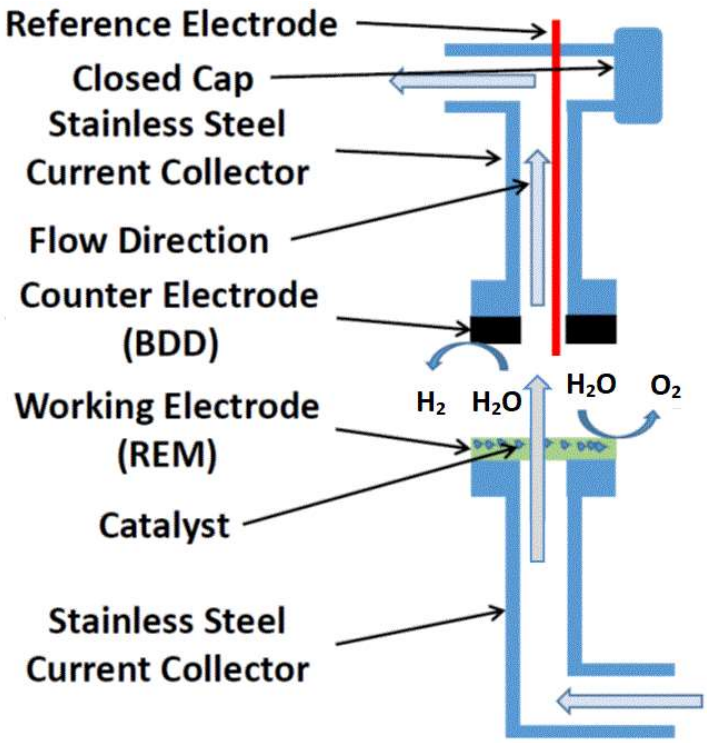

Figure S-6-2. Schematic of the flow-through reactor setup: anode-cathode flow mode.

Pore Size Determination

Average pore size/pore radius (r_p) using the Hagen-Poiseuille equation (S-6-1) by varying flow rate and trans-membrane pressure (ΔP) (Figure S-6-2).

$$u = \frac{r_p^2 \Delta P \varepsilon}{8\eta \Delta x} \qquad \text{(S-6-1)}$$

In equation S-1, u is the linear velocity; ε is the porosity (0.3); η is the fluid viscosity (9.78×10^{-4} Pa s (21 ^{0}C)); and Δx is the membrane thickness (2.5 mm). The pore radius was determined as 0.41 ± 0.03, 0.36 ± 0.02, and 0.40 ± 0.04 µm for REM, REM/BDTO/EDT, and REM/BDTO/PLD20, respectively.

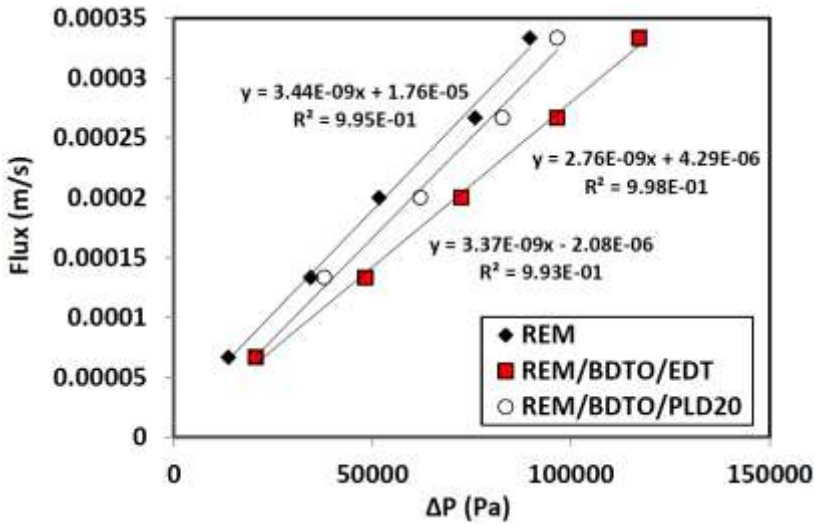

Figure S-6-3. Flow velocity (u) with pressure drop (ΔP) for REM, REM/BDTO/EDT and REM/BDTO/PLD20.

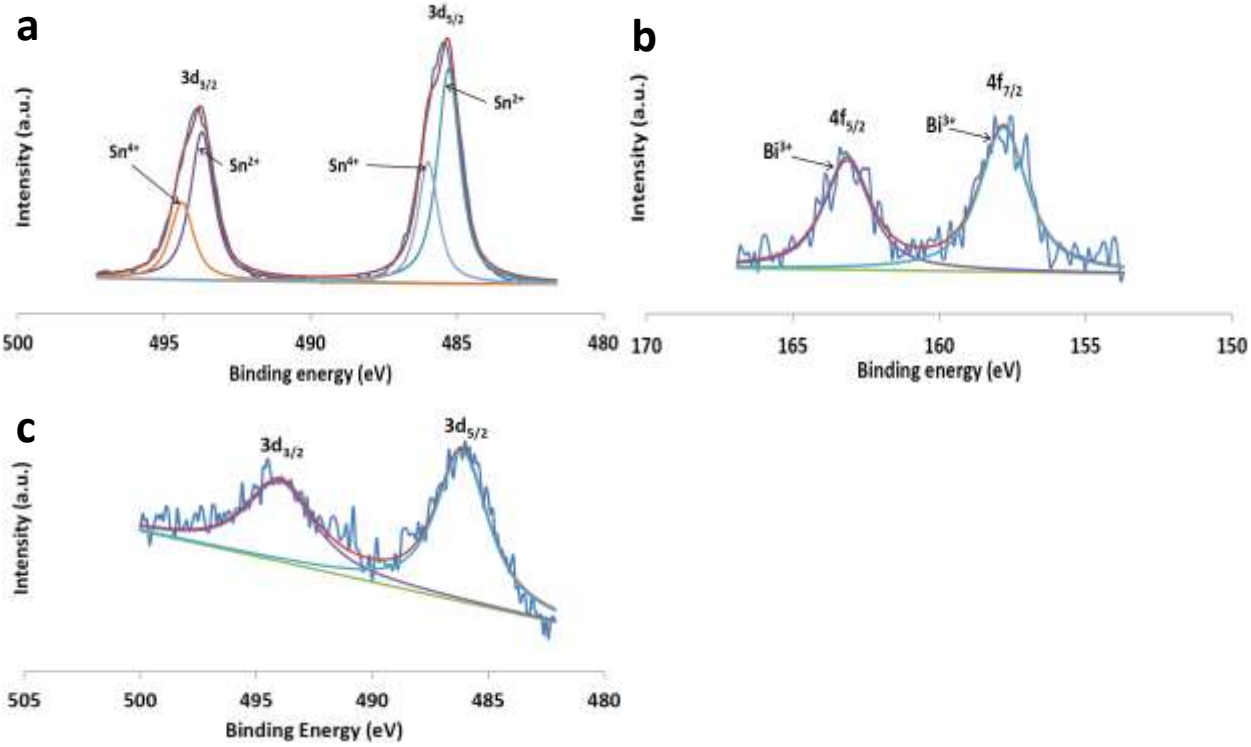

Figure S-6-4. Deconvoluted XPS of a) Sn 3d and b) Bi 4f spectra of REM/BDTO/EDT and c) Sn 3d spectra of REM/BDTO/PLD20.

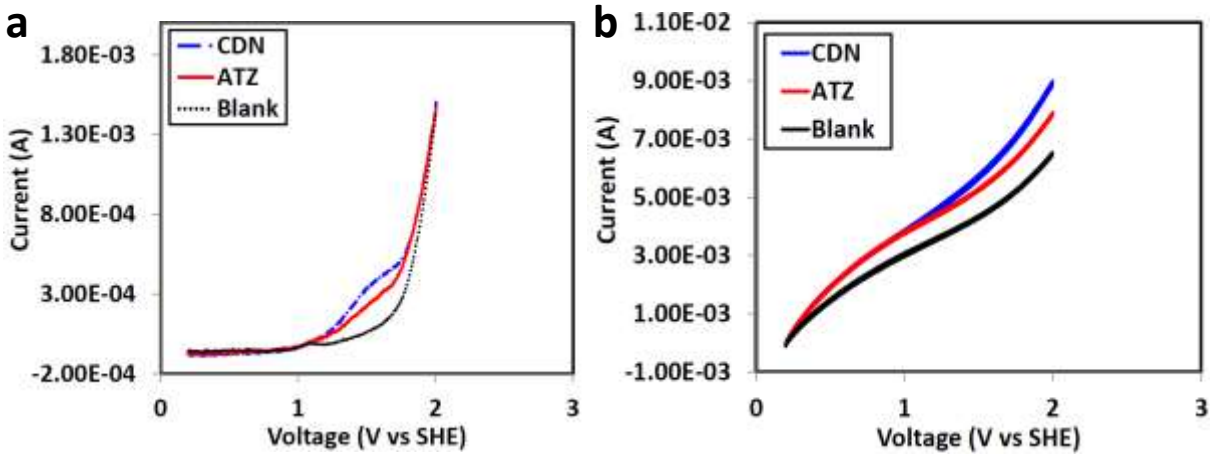

Figure S-6-5. LSV of background electrolyte (100 mM KH_2PO_4), 10 µM of ATZ and CDN in 100 mM KH_2PO_4 for a) BDD and b) REM/BDTO.

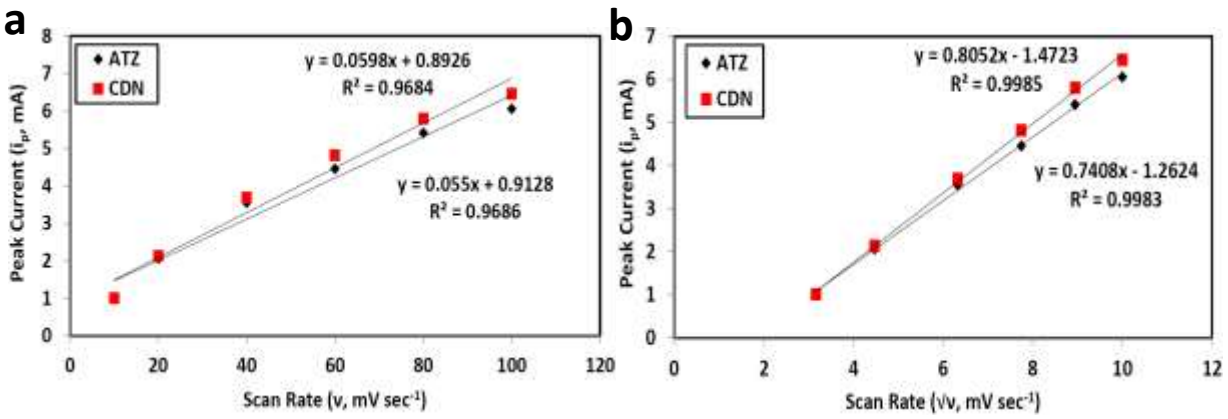

Figure S-6-6. Peak current (i_p, mA) with a) scan rate (ν) and b) square root of scan rate ($\sqrt{\nu}$) for ATZ and CDN oxidation with REM/BDTO (scan rates = 10, 20, 40, 60, 80 and 100 mV sec^{-1}).

Appendix E

ACS Publications
Most Trusted. Most Cited. Most Read.

Title: Selective Electrochemical Detection of Ciprofloxacin with a Porous Nafion/Multiwalled Carbon Nanotube Composite Film Electrode

Logged in as:
Pralay Gayen
LOGOUT

Author: Pralay Gayen, Brian P. Chaplin
Publication: Applied Materials
Publisher: American Chemical Society
Date: Jan 1, 2016

PERMISSION/LICENSE IS GRANTED FOR YOUR ORDER AT NO CHARGE

This type of permission/license, instead of the standard Terms & Conditions, is sent to you because no fee is being charged for your order. Please note the following:

- Permission is granted for your request in both print and electronic formats, and translations.
- If figures and/or tables were requested, they may be adapted or used in part.
- Please print this page for your records and send a copy of it to your publisher/graduate school.
- Appropriate credit for the requested material should be given as follows: "Reprinted (adapted) with permission from (COMPLETE REFERENCE CITATION). Copyright (YEAR) American Chemical Society." Insert appropriate information in place of the capitalized words.
- One-time permission is granted only for the use specified in your request. No additional uses are granted (such as derivative works or other editions). For any other uses, please submit a new request.

BACK CLOSE WINDOW

Title: Fluorination of Boron-Doped Diamond Film Electrodes for Minimization of Perchlorate Formation

Author: Pralay Gayen, Brian P. Chaplin

Publication: Applied Materials

Publisher: American Chemical Society

Date: Aug 1, 2017

PERMISSION/LICENSE IS GRANTED FOR YOUR ORDER AT NO CHARGE

This type of permission/license, instead of the standard Terms & Conditions, is sent to you because no fee is being charged for your order. Please note the following:

- Permission is granted for your request in both print and electronic formats, and translations.
- If figures and/or tables were requested, they may be adapted or used in part.
- Please print this page for your records and send a copy of it to your publisher/graduate school.
- Appropriate credit for the requested material should be given as follows: "Reprinted (adapted) with permission from (COMPLETE REFERENCE CITATION). Copyright (YEAR) American Chemical Society." Insert appropriate information in place of the capitalized words.
- One-time permission is granted only for the use specified in your request. No additional uses are granted (such as derivative works or other editions). For any other uses, please submit a new request.

References

[1] H. Perlman, Water Science for Schools: Where is Earth' s water located ?, Usgs. (1996) 98–99. http://ga.water.usgs.gov/edu/earthwherewater.html.

[2] I. a. Shiklomanov, World Water Rssources- A new Appraisal and Assessment for the 21st century, Report. (1998) 40. doi:10.4314/wsa.v30i4.5101.

[3] D.B. Byles, Water supply and health, Nature. 154 (1944) 660–662. doi:10.1038/154660a0.

[4] United States Geological Survey (USGS), Summary of the Water Cycle, (2016) 1–10. http://water.usgs.gov/edu/watercyclesummary.html.

[5] C.J. Vörösmarty, Global Water Resources: Vulnerability from Climate Change and Population Growth, Science (80-.). 289 (2000) 284–288. doi:10.1126/science.289.5477.284.

[6] A. Pruss, D. Kay, L. Fewtrell, J. Bartram, Estimating the Burden of Disease from Water, Sanitation, Hygene at a Global Level., Environ. Health Perspect. 110 (2002) 537. doi:10.1289/ehp.02110537.

[7] P.R. Hunter, D. Zmirou-Navier, P. Hartemann, Estimating the impact on health of poor reliability of drinking water interventions in developing countries, Sci. Total Environ. 407 (2009) 2621–2624. doi:10.1016/j.scitotenv.2009.01.018.

[8] N.J. Ashbolt, Microbial contamination of drinking water and disease outcomes in developing regions, Toxicology. 198 (2004) 229–238. doi:10.1016/j.tox.2004.01.030.

[9] L. Järup, Hazards of heavy metal contamination, Br. Med. Bull. 68 (2003) 167–182. doi:10.1093/bmb/ldg032.

[10] USEPA, National primary drinking water regulations, 1 (2009) 7. https://www.epa.gov/ground-water-and-drinking-water/national-primary-drinking-water-

regulations.

[11] ANNEX 1 DATA SHEETS FOR SURFACE WATER QUALITY STANDARDS, (n.d.).

[12] R. Remarks, E. Comments, This Annex provides a summary of the information provided by each Member State on the establishment of groundwater threshold values in accordance with Article 3 and Annex I and II of the Groundwater Directive 2006/118/EC (GWD). These Member State Annexes , (2006) 1–76.

[13] J.C. Crittenden, R.R. Trussell, D.W. Hand, K. j. Howe, G. Tchobanoglous, J.H. Borchardt, MWH ' s Water Treatment Principles and Design, (2012).

[14] V. Homem, L. Santos, Degradation and removal methods of antibiotics from aqueous matrices - A review, J. Environ. Manage. 92 (2011) 2304–2347. doi:10.1016/j.jenvman.2011.05.023.

[15] G. Dermont, M. Bergeron, G. Mercier, M. Richer-Laflèche, Soil washing for metal removal: A review of physical/chemical technologies and field applications, J. Hazard. Mater. 152 (2008) 1–31. doi:10.1016/j.jhazmat.2007.10.043.

[16] T.O. Leiknes, The effect of coupling coagulation and flocculation with membrane filtration in water treatment: A review, J. Environ. Sci. 21 (2009) 8–12. doi:10.1016/S1001-0742(09)60003-6.

[17] A.W. Zularisam, A.F. Ismail, R. Salim, Behaviours of natural organic matter in membrane filtration for surface water treatment - a review, Desalination. 194 (2006) 211–231. doi:10.1016/j.desal.2005.10.030.

[18] L.M. Camacho, L. Dumée, J. Zhang, J. de Li, M. Duke, J. Gomez, S. Gray, Advances in membrane distillation for water desalination and purification applications, Water (Switzerland). 5 (2013) 94–196. doi:10.3390/w5010094.

[19] M.A. Shannon, P.W. Bohn, M. Elimelech, J.G. Georgiadis, B.J. Marĩas, A.M. Mayes, Science and technology for water purification in the coming decades, Nature. 452 (2008) 301–310. doi:10.1038/nature06599.

[20] T. Xu, Ion exchange membranes: State of their development and perspective, J. Memb. Sci. 263 (2005) 1–29. doi:10.1016/j.memsci.2005.05.002.

[21] L.F. Greenlee, D.F. Lawler, B.D. Freeman, B. Marrot, P. Moulin, Reverse osmosis desalination: Water sources, technology, and today's challenges, Water Res. 43 (2009) 2317–2348. doi:10.1016/j.watres.2009.03.010.

[22] T.H.E. Scientific, B. Of, No Title, n.d.

[23] P. Company, Desalination. 32 (1980) 137-148 ® Elsevier Scientific, 32 (1980) 137–148.

[24] L. Ao, W. Liu, L. Zhao, X. Wang, Membrane fouling in ultrafiltration of natural water after pretreatment to different extents, J. Environ. Sci. (China). 43 (2016) 234–243. doi:10.1016/j.jes.2015.09.008.

[25] W. Gao, H. Liang, J. Ma, M. Han, Z. lin Chen, Z. shuang Han, G. bai Li, Membrane fouling control in ultrafiltration technology for drinking water production: A review, Desalination. 272 (2011) 1–8. doi:10.1016/j.desal.2011.01.051.

[26] A.K. Verma, R.R. Dash, P. Bhunia, A review on chemical coagulation/flocculation technologies for removal of colour from textile wastewaters, J. Environ. Manage. 93 (2012) 154–168. doi:10.1016/j.jenvman.2011.09.012.

[27] V. Golob, A. Vinder, M. Simonič, Efficiency of the coagulation/flocculation method for the treatment of dyebath effluents, Dye. Pigment. 67 (2005) 93–97. doi:10.1016/j.dyepig.2004.11.003.

[28] K. Suehara, Y. Kawamoto, E. Fujii, J. Kohda, Y. Nakano, T. Yano, Biological treatment

of wastewater discharged from biodiesel fuel production plant with alkali-catalyzed transesterification, J. Biosci. Bioeng. 100 (2005) 437–442. doi:10.1263/jbb.100.437.

[29] R. Rosal, A. Rodríguez, J.A. Perdigón-Melón, A. Petre, E. García-Calvo, M.J. Gómez, A. Agüera, A.R. Fernández-Alba, Occurrence of emerging pollutants in urban wastewater and their removal through biological treatment followed by ozonation, Water Res. 44 (2010) 578–588. doi:10.1016/j.watres.2009.07.004.

[30] C. Fux, M. Boehler, P. Huber, I. Brunner, H. Siegrist, Biological treatment of ammonium-rich wastewater by partial nitritation and subsequent anaerobic ammonium oxidation (anammox) in a pilot plant, J. Biotechnol. 99 (2002) 295–306. doi:10.1016/S0168-1656(02)00220-1.

[31] P.E. Wyse, United States Patent (19) 45) Date of Patent :, (1987).

[32] B.D. Tripathi, S.C. Shukla, Biological treatment of wastewater by selected aquatic plants., Environ. Pollut. 69 (1991) 69–78. doi:Doi 10.1016/0269-7491(91)90164-R.

[33] J. van Rijn, The potential for integrated biological treatment systems in recirculating fish culture—A review, Aquaculture. 139 (1996) 181–201. doi:10.1016/0044-8486(95)01151-X.

[34] D. Pant, A. Adholeya, Biological approaches for treatment of distillery wastewater: A review, Bioresour. Technol. 98 (2007) 2321–2334. doi:10.1016/j.biortech.2006.09.027.

[35] I. Oller, S. Malato, J.A. Sánchez-Pérez, Combination of Advanced Oxidation Processes and biological treatments for wastewater decontamination-A review, Sci. Total Environ. 409 (2011) 4141–4166. doi:10.1016/j.scitotenv.2010.08.061.

[36] Y. Wei, R.T. Van Houten, A.R. Borger, D.H. Eikelboom, Y. Fan, Minimization of excess sludge production for biological wastewater treatment, Water Res. 37 (2003) 4453–4467.

doi:10.1016/S0043-1354(03)00441-X.

[37] G. Ruppert, R. Bauer, G. Heisler, The photo-Fenton reaction - an effective photochemical wastewater treatment process, J. Photochem. Photobiol. A Chem. 73 (1993) 75–78. doi:10.1016/1010-6030(93)80035-8.

[38] G. Ruppert, R. Bauer, G. Heisler, UV-O3, UV-H2O2, UV-TiO2 and the photo-Fenton reaction - Comparison of advanced oxidation processes for wastewater treatment, Chemosphere. 28 (1994) 1447–1454. doi:10.1016/0045-6535(94)90239-9.

[39] O. Legrini, E. Oliveros, A.M. Braun, Photochemical Processes for Water Treatment, Chem. Rev. 93 (1993) 671–698. doi:10.1021/cr00018a003.

[40] T. Robinson, G. McMullan, R. Marchant, P. Nigam, Remediation of dyes in textile effluent: A critical review on current treatment technologies with a proposed alternative, Bioresour. Technol. 77 (2001) 247–255. doi:10.1016/S0960-8524(00)00080-8.

[41] O. Lefebvre, R. Moletta, Treatment of organic pollution in industrial saline wastewater: A literature review, Water Res. 40 (2006) 3671–3682. doi:10.1016/j.watres.2006.08.027.

[42] T.A. Kurniawan, G.Y.S. Chan, W.H. Lo, S. Babel, Physico-chemical treatment techniques for wastewater laden with heavy metals, Chem. Eng. J. 118 (2006) 83–98. doi:10.1016/j.cej.2006.01.015.

[43] S. Raghu, C. Ahmed Basha, Chemical or electrochemical techniques, followed by ion exchange, for recycle of textile dye wastewater, J. Hazard. Mater. 149 (2007) 324–330. doi:10.1016/j.jhazmat.2007.03.087.

[44] V.K. Gupta, I. Ali, T.A. Saleh, A. Nayak, S. Agarwal, Chemical treatment technologies for waste-water recycling—an overview, RSC Adv. 2 (2012) 6380. doi:10.1039/c2ra20340e.

[45] A. Babuponnusami, K. Muthukumar, Journal of Environmental Chemical Engineering A review on Fenton and improvements to the Fenton process for wastewater treatment, J. Environ. Chem. Eng. 2 (2014) 557–572. doi:10.1016/j.jece.2013.10.011.

[46] P. V Nidheesh, R. Gandhimathi, Trends in electro-Fenton process for water and wastewater treatment : An overview, DES. 299 (2012) 1–15. doi:10.1016/j.desal.2012.05.011.

[47] C. Borrás, C. Berzoy, J. Mostany, B.R. Scharifker, Oxidation of p-methoxyphenol on SnO2-Sb2O5 electrodes: Effects of electrode potential and concentration on the mineralization efficiency, J. Appl. Electrochem. 36 (2006) 433–439. doi:10.1007/s10800-005-9088-5.

[48] C. Borras, T. Laredo, B.R. Scharifker, Competitive electrochemical oxidation of p-chlorophenol and p-nitrophenol on Bi-doped PbO2, Electrochim. Acta. 48 (2003) 2775–2780. doi:10.1016/S0013-4686(03)00411-0.

[49] Y. Liu, H. Liu, Y. Li, Comparative study of the electrocatalytic oxidation and mechanism of nitrophenols at Bi-doped lead dioxide anodes, Appl. Catal. B Environ. 84 (2008) 297–302. doi:10.1016/j.apcatb.2008.04.011.

[50] D. Bejan, E. Guinea, N.J. Bunce, On the nature of the hydroxyl radicals produced at boron-doped diamond and Ebonex®anodes, Electrochim. Acta. 69 (2012) 275–281. doi:10.1016/j.electacta.2012.02.097.

[51] A. Kraft, Doped Diamond: A Compact Review on a New, Versatile Electrode Material - Open Access Library, Int. J. Electrochem. Sci. 2 (2007) 355–385. doi:10.1021/jo026183k.

[52] K.E. Carter, J. Farrell, Oxidative destruction of perfluorooctane sulfonate using boron-doped diamond film electrodes, Environ. Sci. Technol. 42 (2008) 6111–6115.

doi:10.1021/es703273s.

[53] J.-F. Zhi, H.-B. Wang, T. Nakashima, T.N. Rao, A. Fujishima, Electrochemical Incineration of Organic Pollutants on Boron-Doped Diamond Electrode. Evidence for Direct Electrochemical Oxidation Pathway, J. Phys. Chem. B. 107 (2003) 13389–13395. doi:10.1021/jp030279g.

[54] A.M. Zaky, B.P. Chaplin, Porous substoichiometric TiO2 anodes as reactive electrochemical membranes for water treatment, Environ. Sci. Technol. 47 (2013) 6554–6563. doi:10.1021/es401287e.

[55] J.M. Kesselman, O. Weres, N.S. Lewis, M.R. Hoffmann, Electrochemical Production of Hydroxyl Radical at Polycrystalline Nb-Doped TiO_2 Electrodes and Estimation of the Partitioning between Hydroxyl Radical and Direct Hole Oxidation Pathways, J. Phys. Chem. B. 101 (1997) 2637–2643. doi:10.1021/jp962669r.

[56] G. Zhao, Y.Y. Zhang, Y. Lei, B. Lv, J. Gao, Y.Y. Zhang, D. Li, Fabrication and electrochemical treatment application of a novel lead dioxide anode with superhydrophobic surfaces, high oxygen evolution potential, and oxidation capability., Environ. Sci. Technol. 44 (2010) 1754–9. doi:10.1021/es902336d.

[57] Q. Zhuo, S. Deng, B. Yang, J. Huang, G. Yu, Efficient electrochemical oxidation of perfluorooctanoate using a Ti/SnO2-Sb-Bi anode, Environ. Sci. Technol. 45 (2011) 2973–2979. doi:10.1021/es1024542.

[58] I. Tröster, M. Fryda, D. Herrmann, L. Schäfer, W. Hänni, A. Perret, M. Blaschke, A. Kraft, M. Stadelmann, Electrochemical advanced oxidation process for water treatment using DiaChem® electrodes, Diam. Relat. Mater. 11 (2002) 640–645. doi:10.1016/S0925-9635(01)00706-3.

[59] A. Kraft, M. Stadelmann, M. Blaschke, Anodic oxidation with doped diamond electrodes: A new advanced oxidation process, J. Hazard. Mater. 103 (2003) 247–261. doi:10.1016/j.jhazmat.2003.07.006.

[60] O. Ganzenko, D. Huguenot, E.D. van Hullebusch, G. Esposito, M.A. Oturan, Electrochemical advanced oxidation and biological processes for wastewater treatment: A review of the combined approaches, Environ. Sci. Pollut. Res. 21 (2014) 8493–8524. doi:10.1007/s11356-014-2770-6.

[61] C.A. Martínez-Huitle, E. Brillas, Decontamination of wastewaters containing synthetic organic dyes by electrochemical methods: A general review, Appl. Catal. B Environ. 87 (2009) 105–145. doi:10.1016/j.apcatb.2008.09.017.

[62] A. Kapałka, G. Fóti, C. Comninellis, The importance of electrode material in environmental electrochemistry. Formation and reactivity of free hydroxyl radicals on boron-doped diamond electrodes, Electrochim. Acta. 54 (2009) 2018–2023. doi:10.1016/j.electacta.2008.06.045.

[63] EPA, Interim Drinking Water Health Advisory For Perchlorate, (2008) 49. http://www.epa.gov/waterscience/.

[64] L. Guo, Y. Jing, B.P. Chaplin, Development and Characterization of Ultrafiltration TiO2Magnéli Phase Reactive Electrochemical Membranes, Environ. Sci. Technol. 50 (2016) 1428–1436. doi:10.1021/acs.est.5b04366.

[65] A.M. Fan, V.E. Steinberg, Health implications of nitrate and nitrite in drinking water: an update on methemoglobinemia occurrence and reproductive and developmental toxicity., Regul. Toxicol. Pharmacol. 23 (1996) 35–43. doi:10.1006/rtph.1996.0006.

[66] V. Mody, S.D. Ray, The National Institute of Environmental Health Sciences, Encycl.

Toxicol. 108 (2014) 456–457. doi:10.1016/B978-0-12-386454-3.00341-9.

[67] N. Gupta, Nitrate pollution of groundwater and associated human health disorders . Indian J Environ Hlth, Environ. Heal. 3 (2015) 28–39.

[68] A. Kapoor, T. Viraraghavan, Nitrate Removal From Drinking Water—Review, J. Environ. Eng. 123 (1997) 371–380. doi:10.1061/(ASCE)0733-9372(1997)123:4(371).

[69] A. Bhatnagar, M. Sillanpää, A review of emerging adsorbents for nitrate removal from water, Chem. Eng. J. 168 (2011) 493–504. doi:10.1016/j.cej.2011.01.103.

[70] G. P??rez, R. Ib????ez, A.M. Urtiaga, I. Ortiz, Kinetic study of the simultaneous electrochemical removal of aqueous nitrogen compounds using BDD electrodes, Chem. Eng. J. 197 (2012) 475–482. doi:10.1016/j.cej.2012.05.062.

[71] K. Wada, T. Hirata, S. Hosokawa, S. Iwamoto, M. Inoue, Effect of supports on Pd-Cu bimetallic catalysts for nitrate and nitrite reduction in water, Catal. Today. 185 (2012) 81–87. doi:10.1016/j.cattod.2011.07.021.

[72] M. Li, C. Feng, Z. Zhang, S. Yang, N. Sugiura, Treatment of nitrate contaminated water using an electrochemical method, Bioresour. Technol. 101 (2010) 6553–6557. doi:10.1016/j.biortech.2010.03.076.

[73] M. Li, C. Feng, Z. Zhang, X. Lei, R. Chen, Y. Yang, N. Sugiura, Simultaneous reduction of nitrate and oxidation of by-products using electrochemical method, J. Hazard. Mater. 171 (2009) 724–730. doi:10.1016/j.jhazmat.2009.06.066.

[74] D. Reyter, D. Bélanger, L. Roué, Study of the electroreduction of nitrate on copper in alkaline solution, Electrochim. Acta. 53 (2008) 5977–5984. doi:10.1016/j.electacta.2008.03.048.

[75] L. Szpyrkowicz, S. Daniele, M. Radaelli, S. Specchia, Removal of NO3-from water by

electrochemical reduction in different reactor configurations, Appl. Catal. B Environ. 66 (2006) 40–50. doi:10.1016/j.apcatb.2006.02.020.

[76] O.M. Ilinich, E.N. Gribov, P.A. Simonov, Water denitrification over catalytic membranes: Hydrogen spillover and catalytic activity of macroporous membranes loaded with Pd and Cu, Catal. Today. 82 (2003) 49–56. doi:10.1016/S0920-5861(03)00201-3.

[77] M. Vospernik, A. Pintar, G. Berčič, J. Levec, Experimental verification of ceramic membrane potentials for supporting three-phase catalytic reactions, J. Memb. Sci. 223 (2003) 157–169. doi:10.1016/S0376-7388(03)00320-X.

[78] G. Strukul, R. Gavagnin, F. Pinna, E. Modaferri, S. Perathoner, G. Centi, M. Marella, M. Tomaselli, Use of palladium based catalysts in the hydrogenation of nitrates in drinking water: from powders to membranes, Catal. Today. 55 (2000) 139–149. doi:10.1016/S0920-5861(99)00233-3.

[79] K. Daub, G. Emig, M.J. Chollier, M. Callant, R. Dittmeyer, Studies on the use of catalytic membranes for reduction of nitrate in drinking water, Chem. Eng. Sci. 54 (1999) 1577–1582. doi:10.1016/S0009-2509(99)00049-4.

[80] K. Lüdtke, K.-V. Peinemann, V. Kasche, R.-D. Behling, Nitrate removal of drinking water by means of catalytically active membranes, J. Memb. Sci. 151 (1998) 3–11. doi:10.1016/S0376-7388(98)00227-0.

[81] M. Li, C. Feng, Z. Zhang, Z. Shen, N. Sugiura, Electrochemical reduction of nitrate using various anodes and a Cu/Zn cathode, Electrochem. Commun. 11 (2009) 1853–1856. doi:10.1016/j.elecom.2009.08.001.

[82] M. Li, C. Feng, Z. Zhang, N. Sugiura, Efficient electrochemical reduction of nitrate to nitrogen using Ti/IrO2-Pt anode and different cathodes, Electrochim. Acta. 54 (2009)

4600–4606. doi:10.1016/j.electacta.2009.03.064.

[83] B. Talhi, F. Monette, A. Azzouz, Effective and selective nitrate electroreduction into nitrogen through synergistic parameter interactions, Electrochim. Acta. 58 (2011) 276–284. doi:10.1016/j.electacta.2011.09.044.

[84] G. Carlucci, Analysis of fluoroquinolones in biological fluids by high-performance liquid chromatography., J. Chromatogr. A. 812 (1998) 343–367. doi:10.1016/S0021-9673(98)00274-X.

[85] H.Y. Ji, D.W. Jeong, Y.H. Kim, H.H. Kim, D.R. Sohn, H.S. Lee, Hydrophilic interaction liquid chromatography-tandem mass spectrometry for the determination of levofloxacin in human plasma, J. Pharm. Biomed. Anal. 41 (2006) 622–627. doi:10.1016/j.jpba.2005.12.013.

[86] R.H.O. Montes, M.C. Marra, M.M. Rodrigues, E.M. Richter, R.A.A. Muñoz, Fast Determination of Ciprofloxacin by Batch Injection Analysis with Amperometric Detection and Capillary Electrophoresis with Capacitively Coupled Contactless Conductivity Detection, Electroanalysis. 26 (2014) 432–438. doi:10.1002/elan.201300474.

[87] A. Navalón, O. Ballesteros, R. Blanc, J.L. Vílchez, Determination of ciprofloxacin in human urine and serum samples by solid-phase spectrofluorimetry, Talanta. 52 (2000) 845–852. doi:10.1016/S0039-9140(00)00437-9.

[88] C. Tong, G. Xiang, Sensitive determination of norfloxacin by the fluorescence probe of terbium (III)- sodium dodecylbenzene sulfonate and its luminescence mechanism, J. Fluoresc. 16 (2006) 831–837. doi:10.1007/s10895-006-0107-7.

[89] M.I. Pascual-Reguera, G. Pérez Parras, A. Molina Díaz, A single spectroscopic flow-through sensing device for determination of ciprofloxacin, J. Pharm. Biomed. Anal. 35

(2004) 689–695. doi:10.1016/j.jpba.2004.03.002.

[90] H.W. Sun, L.Q. Li, X.Y. Chen, Flow-injection enhanced chemiluminescence method for determination of ciprofloxacin in pharmaceutical preparations and biological fluids, Anal. Bioanal. Chem. 384 (2006) 1314–1319. doi:10.1007/s00216-005-0277-1.

[91] A. Radi, M.A. El Ries, S. Kandil, Electrochemical study of the interaction of levofloxacin with DNA, Anal. Chim. Acta. 495 (2003) 61–67. doi:10.1016/j.aca.2003.08.018.

[92] B. Kim, D. Lim, H.J. Jin, H.Y. Lee, S. Namgung, Y. Ko, S.B. Park, S. Hong, Family-selective detection of antibiotics using antibody-functionalized carbon nanotube sensors, Sensors Actuators, B Chem. 166–167 (2012) 193–199. doi:10.1016/j.snb.2012.02.039.

[93] W. Wen, D.M. Zhao, X.H. Zhang, H.Y. Xiong, S.F. Wang, W. Chen, Y. Di Zhao, One-step fabrication of poly(o-aminophenol)/multi-walled carbon nanotubes composite film modified electrode and its application for levofloxacin determination in pharmaceuticals, Sensors Actuators, B Chem. 174 (2012) 202–209. doi:10.1016/j.snb.2012.08.010.

[94] K. Abnous, N.M. Danesh, M. Alibolandi, M. Ramezani, S.M. Taghdisi, A.S. Emrani, A novel electrochemical aptasensor for ultrasensitive detection of fluoroquinolones based on single-stranded DNA-binding protein, Toxicol. Appl. Pharmacol. 280 (2014) 100–106. doi:10.1016/j.snb.2016.08.100.

[95] N. Diab, I. Abu-Shqair, R. Salim, M. Al-Subu, The behavior of ciprofloxacin at a dna modified glassy carbon electrodes, Int. J. Electrochem. Sci. 9 (2014) 1771–1783.

[96] X. Zhang, Y. Wei, Y. Ding, Electrocatalytic oxidation and voltammetric determination of ciprofloxacin employing poly(alizarin red)/graphene composite film in the presence of ascorbic acid, uric acid and dopamine, Anal. Chim. Acta. 835 (2014) 29–36. doi:10.1016/j.aca.2014.05.020.

[97] F. Zhang, S. Gu, Y. Ding, Z. Zhang, L. Li, A novel sensor based on electropolymerization of β-cyclodextrin and l-arginine on carbon paste electrode for determination of fluoroquinolones, Anal. Chim. Acta. 770 (2013) 53–61. doi:10.1016/j.aca.2013.01.052.

[98] R.N. Goyal, A.R.S. Rana, H. Chasta, Electrochemical sensor for the sensitive determination of norfloxacin in human urine and pharmaceuticals, Bioelectrochemistry. 83 (2012) 46–51. doi:10.1016/j.bioelechem.2011.08.006.

[99] A.E. Radi, T. Wahdan, Z. Anwar, H. Mostafa, Electrochemical determination of gatifloxacin, moxifloxacin and sparfloxacin fluoroquinolonic antibiotics on glassy carbon electrode in pharmaceutical formulations, Drug Test. Anal. 2 (2010) 397–400. doi:10.1002/dta.143.

[100] A.E. Radi, T. Wahdan, Z. Anwar, H. Mostafa, Electrochemical and Spectroscopic Studies on the Interaction of Gatifloxacin, Moxifloxacin and Sparfloxacin with DNA and Their Analytical Applications, Electroanalysis. 22 (2010) 2665–2671. doi:10.1002/elan.201000285.

[101] L. Fotouhi, M. Alahyari, Electrochemical behavior and analytical application of ciprofloxacin using a multi-walled nanotube composite film-glassy carbon electrode, Colloids Surfaces B Biointerfaces. 81 (2010) 110–114. doi:10.1016/j.colsurfb.2010.06.030.

[102] N. Seedher, P. Agarwal, Complexation of fluoroquinolone antibiotics with human serum albumin: A fluorescence quenching study, J. Lumin. 130 (2010) 1841–1848. doi:10.1016/j.jlumin.2010.04.020.

[103] B. Uslu, B.D. Topal, S.A. Ozkan, Electroanalytical investigation and determination of pefloxacin in pharmaceuticals and serum at boron-doped diamond and glassy carbon

electrodes, Talanta. 74 (2008) 1191–1200. doi:10.1016/j.talanta.2007.08.023.

[104] G. Tsekenis, G.Z. Garifallou, F. Davis, P.A. Millner, D.G. Pinacho, F. Sanchez-Baeza, M.P. Marco, T.D. Gibson, S.P.J. Higson, Detection of fluoroquinolone antibiotics in milk via a labeless immunoassay based upon an alternating current impedance protocol, Anal. Chem. 80 (2008) 9233–9239. doi:10.1021/ac8014752.

[105] Y.M. Liu, Y.X. Jia, W. Tian, Determination of quinolone antibiotics in urine by capillary electrophoresis with chemiluminescence detection, J. Sep. Sci. 31 (2008) 3765–3771. doi:10.1002/jssc.200800373.

[106] J. Tuerk, M. Reinders, D. Dreyer, T.K. Kiffmeyer, K.G. Schmidt, H.M. Kuss, Analysis of antibiotics in urine and wipe samples from environmental and biological monitoring - Comparison of HPLC with UV-, single MS- and tandem MS-detection, J. Chromatogr. B Anal. Technol. Biomed. Life Sci. 831 (2006) 72–80. doi:10.1016/j.jchromb.2005.11.030.

[107] M.I.R.M. Santoro, N.M. Kassab, A.K. Singh, E.R.M. Kedor-Hackmam, Quantitative determination of gatifloxacin, levofloxacin, lomefloxacin and pefloxacin fluoroquinolonic antibiotics in pharmaceutical preparations by high-performance liquid chromatography, J. Pharm. Biomed. Anal. 40 (2006) 179–184. doi:10.1016/j.jpba.2005.06.018.

[108] L.A. Shervington, M. Abba, B. Hussain, J. Donnelly, The simultaneous separation and determination of five quinolone antibotics using isocratic reversed-phase HPLC: Application to stability studies on an ofloxacin tablet formulation, J. Pharm. Biomed. Anal. 39 (2005) 769–775. doi:10.1016/j.jpba.2005.04.039.

[109] A. Muñoz de la Peña, A. Espinosa Mansilla, D. González Gómez, A.C. Olivieri, H.C. Goicoechea, Interference-free analysis using three-way fluorescence data and the parallel factor model. Determination of fluoroquinolone antibiotics in human serum, Anal. Chem.

75 (2003) 2640–2646. doi:10.1021/ac026360h.

[110] M.J. Pacheco, V. Santos, L. Ciríaco, A. Lopes, Electrochemical degradation of aromatic amines on BDD electrodes, J. Hazard. Mater. 186 (2011) 1033–1041. doi:10.1016/j.jhazmat.2010.11.108.

[111] B.P. Chaplin, G. Schrader, J. Farrell, Electrochemical destruction of N-nitrosodimethylamine in reverse osmosis concentrates using Boron-doped diamond film electrodes., Environ. Sci. Technol. 44 (2010) 4264–4269. doi:Doi 10.1021/Es903872p.

[112] B.D. Film, B.P. Chaplin, G. Schrader, Electrochemical Oxidation of, Environ. Sci. Technol. 43 (2009) 8302–8307. doi:10.1002/anie.196802901.

[113] X. Zhu, M. Tong, S. Shi, H. Zhao, J. Ni, Essential explanation of the strong mineralization performance of boron-doped diamond electrodes, Environ. Sci. Technol. 42 (2008) 4914–4920. doi:10.1021/es800298p.

[114] D. Bejan, J.D. Malcolm, L. Morrison, N.J. Bunce, Mechanistic investigation of the conductive ceramic Ebonex® as an anode material, Electrochim. Acta. 54 (2009) 5548–5556. doi:10.1016/j.electacta.2009.04.057.

[115] T.A. Enache, A.M. Oliveira-Brett, Phenol and para-substituted phenols electrochemical oxidation pathways, J. Electroanal. Chem. 655 (2011) 9–16. doi:10.1016/j.jelechem.2011.02.022.

[116] X. Chen, F. Gao, G. Chen, Comparison of Ti/BDD and Ti/SnO2-Sb2O5electrodes for pollutant oxidation, J. Appl. Electrochem. 35 (2005) 185–191. doi:10.1007/s10800-004-6068-0.

[117] M. Panizza, G. Cerisola, Influence of anode material on the electrochemical oxidation of 2-naphthol: Part 1. Cyclic voltammetry and potential step experiments, Electrochim. Acta.

48 (2003) 3491–3497. doi:10.1016/S0013-4686(03)00468-7.

[118] L. Gherardini, P.A. Michaud, M. Panizza, C. Comninellis, N. Vatistas, Electrochemical Oxidation of 4-Chlorophenol for Wastewater Treatment: Definition of Normalized Current Efficiency (φ), J. Electrochem. Soc. 148 (2001) D78. doi:10.1149/1.1368105.

[119] M. Panizza, G. Cerisola, Application of diamond electrodes to electrochemical processes, 51 (2005) 191–199. doi:10.1016/j.electacta.2005.04.023.

[120] M. Nesladek, Conventional n-type doping in diamond : state of the art and recent progress, (2005). doi:10.1088/0268-1242/20/2/R01.

[121] J.H.T. Luong, B. Male, J.D. Glennon, Boron-doped diamond electrode : synthesis , characterization , functionalization and analytical applications, (2009) 1965–1979. doi:10.1039/b910206j.

[122] M.C. Granger, M. Witek, J. Xu, J. Wang, M. Hupert, A. Hanks, M.D. Koppang, J.E. Butler, G. Lucazeau, M. Mermoux, J.W. Strojek, G.M. Swain, Standard Electrochemical Behavior of Thin-Film Electrodes, 72 (2000) 3793–3804. doi:10.1021/ac0000675.

[123] W. Chen, D. Qi, X. Gao, A. Thye, S. Wee, Progress in Surface Science Surface transfer doping of semiconductors, Prog. Surf. Sci. 84 (2009) 279–321. doi:10.1016/j.progsurf.2009.06.002.

[124] P.A. Michaud, M. Panizza, L. Ouattara, T. Diaco, G. Foti, C. Comninellis, Electrochemical oxidation of water on synthetic boron-doped diamond thin film anodes, J. Appl. Electrochem. 33 (2003) 151–154. doi:10.1023/A:1024084924058.

[125] A.F. Azevedo, N.A. Braga, F.A. Souza, J.T. Matsushima, M.R. Baldan, N.G. Ferreira, The effect of surface treatment on oxidation of oxalic acid at nanocrystalline diamond films, Diam. Relat. Mater. 19 (2010) 462–465. doi:10.1016/j.diamond.2010.01.006.

[126] S. Wang, V.M. Swope, J.E. Butler, T. Feygelson, G.M. Swain, The structural and electrochemical properties of boron-doped nanocrystalline diamond thin-film electrodes grown from Ar-rich and H2-rich source gases, Diam. Relat. Mater. 18 (2009) 669–677. doi:10.1016/j.diamond.2008.11.033.

[127] Y. Show, M.A. Witek, P. Sonthalia, G.M. Swain, Characterization and electrochemical responsiveness of boron-doped nanocrystalline diamond thin-film electrodes, Chem. Mater. 15 (2003) 879–888. doi:10.1021/cm020927t.

[128] F.B. Liu, J.D. Wang, B. Liu, X.M. Li, D.R. Chen, Effect of electronic structures on electrochemical behaviors of surface-terminated boron-doped diamond film electrodes, Diam. Relat. Mater. 16 (2007) 454–460. doi:10.1016/j.diamond.2006.08.016.

[129] N. Simon, H. Girard, D. Ballutaud, S. Ghodbane, A. Deneuville, M. Herlem, A. Etcheberry, Effect of H and O termination on the charge transfer of moderately boron doped diamond electrodes, Diam. Relat. Mater. 14 (2005) 1179–1182. doi:10.1016/j.diamond.2004.12.013.

[130] A.M. Polcaro, P.C. Ricci, S. Palmas, F. Ferrara, A. Anedda, Characterization of boron doped diamond electrodes during oxidation processes: Relationship between electrochemical activity and ageing time, Thin Solid Films. 515 (2006) 2073–2078. doi:10.1016/j.tsf.2006.06.033.

[131] J. Niedziółka-Jönsson, S. Boland, D. Leech, R. Boukherroub, S. Szunerits, Preparation and reactivity of carboxylic acid-terminated boron-doped diamond electrodes, Electrochim. Acta. 55 (2010) 959–964. doi:10.1016/j.electacta.2009.09.058.

[132] X.F. Wang, M. Hasegawa, K. Tsugawa, A.R. Ruslinda, H. Kawarada, Controllable oxidization of boron doped nanodiamond covered with different solution via UV/ozone

treatment, Diam. Relat. Mater. 24 (2012) 146–152. doi:10.1016/j.diamond.2011.12.033.

[133] K. Natsui, T. Yamamoto, T. Watanabe, Y. Kamihara, Y. Einaga, Modulation of critical current density in polycrystalline boron-doped diamond by surface modification, Phys. Status Solidi. 250 (2013) 1943–1949. doi:10.1002/pssb.201349058.

[134] R. Hoffmann, H. Obloh, N. Tokuda, N. Yang, C.E. Nebel, Fractional surface termination of diamond by electrochemical oxidation, Langmuir. 28 (2012) 47–50. doi:10.1021/la2039366.

[135] B. Huang, C. Wu, W. Ke, Surface analysis of boron-doped polycrystalline diamond films deposited by a microwave plasma chemical vapor deposition system, Mater. Chem. Phys. 59 (1999) 143–148. doi:0.1016/S0254-0584(99)00036-X.

[136] A. Denisenko, A. Romanyuk, C. Pietzka, J. Scharpf, E. Kohn, Surface damages in diamond by Ar/O2 plasma and their effect on the electrical and electrochemical characteristics of boron-doped layers, J. Appl. Phys. 108 (2010). doi:10.1063/1.3489986.

[137] N. Simon, D. Ballutaud, M. Herlem, A. Etcheberry, Influence of hydrogen plasma treatment on electrochemical behavior of moderately and highly boron doped diamond electrodes, Diam. Relat. Mater. 13 (2004) 1050–1053. doi:10.1016/j.diamond.2003.11.035.

[138] F. Okino, Y. Kawaguchi, H. Touhara, K. Momota, M. Nishitani-Gamo, T. Ando, A. Sasaki, M. Yoshimoto, O. Odawara, Preparation of boron-doped semiconducting diamond films using BF3and the electrochemical behavior of the semiconducting diamond electrodes, J. Fluor. Chem. 125 (2004) 1715–1722. doi:10.1016/j.jfluchem.2004.09.009.

[139] G.R. Salazar-Banda, L.S. Andrade, P.A.P. Nascente, P.S. Pizani, R.C. Rocha-Filho, L.A. Avaca, On the changing electrochemical behaviour of boron-doped diamond surfaces with

time after cathodic pre-treatments, Electrochim. Acta. 51 (2006) 4612–4619. doi:10.1016/j.electacta.2005.12.039.

[140] M.C. Granger, The Influence of Surface Interactions on the Reversibility of Ferri/Ferrocyanide at Boron-Doped Diamond Thin-Film Electrodes, J. Electrochem. Soc. 146 (1999) 4551. doi:10.1149/1.1392673.

[141] A.F. Azevedo, M.R. Baldan, N.G. Ferreira, Doping level influence on chemical surface of diamond electrodes, J. Phys. Chem. Solids. 74 (2013) 599–604. doi:10.1016/j.jpcs.2012.12.013.

[142] H. Notsu, I. Yagi, T. Tatsuma, D.A. Tryk, A. Fujishima, Surface carbonyl groups on oxidized diamond electrodes, J. Electroanal. Chem. 492 (2000) 31–37. doi:10.1016/S0022-0728(00)00254-0.

[143] B.P. Chaplin, I. Wyle, H. Zeng, J.A. Carlisle, J. Farrell, Characterization of the performance and failure mechanisms of boron-doped ultrananocrystalline diamond electrodes, J. Appl. Electrochem. 41 (2011) 1329–1340. doi:10.1007/s10800-011-0351-7.

[144] G.M. Swain, R. Ramesham, The Electrochemical Activity of Boron-Doped polycrystalline Diamond Thin Film Electrodes, Anal. Chem. 65 (1993) 345–351. doi:10.1021/ac00052a007.

[145] K. Kobashi, K. Nishimura, K. Miyata, K. Kumagai, A. Nakaue, (110)-Oriented Diamond Films Synthesized By Microwave Chemical-Vapor Deposition, J. Mater. Res. 5 (1990) 2469–2482.

[146] M. Bernard, C. Baron, A. Deneuville, About the origin of the low wave number structures of the Raman spectra of heavily boron doped diamond films, Diam. Relat. Mater. 13 (2004) 896–899. doi:10.1016/j.diamond.2003.11.082.

[147] P.W. May, W.J. Ludlow, M. Hannaway, P.J. Heard, J.A. Smith, K.N. Rosser, Raman and conductivity studies of boron-doped microcrystalline diamond, facetted nanocrystalline diamond and cauliflower diamond films, Diam. Relat. Mater. 17 (2008) 105–117. doi:10.1016/j.diamond.2007.11.005.

[148] P. Bou, J.C. Boettner, L. Vandenbulcke, Kinetic Calculations in Plasmas Used for Diamond Deposition, Jpn. J. Appl. Phys. 31 (1992) 1505–1513. doi:10.1143/JJAP.31.1505.

[149] N. Simon, H. Girard, M. Manesse, D. Ballutaud, A. Etcheberry, Electrochemical preconditioning of moderately boron doped diamond electrodes: Effect of annealing, Diam. Relat. Mater. 17 (2008) 1371–1375. doi:10.1016/j.diamond.2008.03.003.

[150] S.C. B. Oliveira, A.M. Oliveira-Brett, Voltammetric and electrochemical impedance spectroscopy characterization of a cathodic and anodic pre-treated boron doped diamond electrode, Electrochim. Acta. 55 (2010) 4599–4605. doi:10.1016/j.electacta.2010.03.016.

[151] H. Girard, N. Simon, D. Ballutaud, M. Herlem, A. Etcheberry, Effect of anodic and cathodic treatments on the charge transfer of boron doped diamond electrodes, Diam. Relat. Mater. 16 (2007) 316–325. doi:10.1016/j.diamond.2006.06.009.

[152] S. Ferro, M. Dal Colle, A. De Battisti, Chemical surface characterization of electrochemically and thermally oxidized boron-doped diamond film electrodes, Carbon N. Y. 43 (2005) 1191–1203. doi:10.1016/j.carbon.2004.12.012.

[153] H.A. Girard, N. Simon, D. Ballutaud, A. Etcheberry, Correlation between flat-band potential position and oxygenated termination nature on boron-doped diamond electrodes, Comptes Rendus Chim. 11 (2008) 1010–1015. doi:10.1016/j.crci.2008.01.014.

[154] M. Wang, N. Simon, C. Decorse-Pascanut, M. Bouttemy, A. Etcheberry, M. Li, R.

Boukherroub, S. Szunerits, Comparison of the chemical composition of boron-doped diamond surfaces upon different oxidation processes, Electrochim. Acta. 54 (2009) 5818–5824. doi:10.1016/j.electacta.2009.05.037.

[155] N. Simon, G. Charrier, A. Etcheberry, Electrochimica Acta Electroless oxidation of diamond surfaces in ceric and ferricyanide solutions : An easy way to produce " C – O " functional groups, Electrochim. Acta. 55 (2010) 5753–5759. doi:10.1016/j.electacta.2010.05.013.

[156] G. Charrier, S. Lévy, J. Vigneron, A. Etcheberry, N. Simon, Diamond & Related Materials Electroless oxidation of boron-doped diamond surfaces : comparison between four, Diam. Relat. Mater. 20 (2011) 944–950. doi:10.1016/j.diamond.2011.05.003.

[157] S. Torrengo, R. Canteri, R. Dell'Anna, L. Minati, A. Pasquarelli, G. Speranza, XPS and ToF-SIMS investigation of nanocrystalline diamond oxidized surfaces, Appl. Surf. Sci. 276 (2013) 101–111. doi:10.1016/j.apsusc.2013.03.041.

[158] R. Boukherroub, X. Wallart, S. Szunerits, B. Marcus, P. Bouvier, M. Mermoux, Photochemical oxidation of hydrogenated boron-doped diamond surfaces, Electrochem. Commun. 7 (2005) 937–940. doi:10.1016/j.elecom.2005.05.010.

[159] B.P. Chaplin, Critical review of electrochemical advanced oxidation processes for water treatment applications, Environ. Sci. Process. Impacts. 16 (2014) 1182–1203. doi:10.1039/C3EM00679D.

[160] L. Ostrovskaya, V. Perevertailo, V. Ralchenko, A. Dementjev, O. Loginova, Wettability and surface energy of oxidized and hydrogen plasma-treated diamond films, Diam. Relat. Mater. 11 (2002) 845–850. doi:10.1016/S0925-9635(01)00636-7.

[161] Y. Kaibara, K. Sugata, M. Tachiki, H. Umezawa, H. Kawarada, Control wettability of the

hydrogen-terminated diamond surface and the oxidized diamond surface using an atomic force microscope, Diam. Relat. Mater. 12 (2003) 560–564. doi:10.1016/S0925-9635(02)00373-4.

[162] S. Ferro, A. De Battisti, Physicochemical Properties of Fluorinated Diamond Electrodes, J. Phys. Chem. B. 107 (2003) 7567–7573. doi:10.1021/jp0274280.

[163] A. Denisenko, A. Romanyuk, C. Pietzka, J. Scharpf, E. Kohn, Surface structure and surface barrier characteristics of boron-doped diamond in electrolytes after CF4 plasma treatment in RF-barrel reactor, Diam. Relat. Mater. 19 (2010) 423–427. doi:10.1016/j.diamond.2009.12.016.

[164] A. Denisenko, A. Romanyuk, C. Pietzka, J. Scharpf, E. Kohn, Electronic surface barrier properties of fluorine-terminated boron-doped diamond in electrolytes, Surf. Sci. 605 (2011) 632–637. doi:10.1016/j.susc.2011.01.001.

[165] B. Guan, J. Zhi, X. Zhang, T. Murakami, A. Fujishima, Electrochemical route for fluorinated modification of boron-doped diamond surface with perfluorooctanoic acid, Electrochem. Commun. 9 (2007) 2817–2821. doi:10.1016/j.elecom.2007.10.003.

[166] J.F. Morar, F.J. Himpsel, G. Hollinger, J.L. Jordon, G. Hughes, F.R. McFeely, C 1s excitation studies of diamond (111). II. Unoccupied surface states, Phys. Rev. B. 33 (1986) 1346–1349. doi:10.1103/PhysRevB.33.1346.

[167] W. Jawando, P. Gayen, B.P. Chaplin, The effects of surface oxidation and fluorination of boron-doped diamond anodes on perchlorate formation and organic compound oxidation, Electrochim. Acta. 174 (2015) 1067–1078. doi:10.1016/j.electacta.2015.06.034.

[168] T. Kondo, H. Ito, K. Kusakabe, K. Ohkawa, Y. Einaga, A. Fujishima, T. Kawai, Plasma etching treatment for surface modification of boron-doped diamond electrodes,

Electrochim. Acta. 52 (2007) 3841–3848. doi:10.1016/j.electacta.2006.11.001.

[169] L.A. Hutton, J.G. Iacobini, E. Bitziou, R.B. Channon, M.E. Newton, J. V. Macpherson, Examination of the factors affecting the electrochemical performance of oxygen-terminated polycrystalline boron-doped diamond electrodes, Anal. Chem. 85 (2013) 7230–7240. doi:10.1021/ac401042t.

[170] M.A. Rodrigo, P.A. Michaud, I. Duo, M. Panizza, G. Cerisola, C. Comninellis, Oxidation of 4-Chlorophenol at Boron-Doped Diamond Electrode for Wastewater Treatment, J. Electrochem. Soc. 148 (2001) D60. doi:10.1149/1.1362545.

[171] P. Cañizares, F. Martínez, M. Díaz, J. García-Gómez, M.A. Rodrigo, Electrochemical Oxidation of Aqueous Phenol Wastes Using Active and Nonactive Electrodes, J. Electrochem. Soc. 149 (2002) D118. doi:10.1149/1.1490359.

[172] M. a Rodrigo, Electrochemical oxidation of several chlorophenols on diamond electrodes, J. Appl. Electrochem. 33 (2003) 917–927.

[173] X. He, Z. Chai, F. Li, C. Zhang, D. Li, J. Li, J. Hu, Advanced treatment of biologically pretreated coking wastewater by electrochemical oxidation using Ti/RuO2-IrO2electrodes, J. Chem. Technol. Biotechnol. 88 (2013) 1568–1575. doi:10.1002/jctb.4006.

[174] J.M. Aquino, R.C. Rocha-Filho, M.A. Rodrigo, C. Sáez, P. Cañizares, Electrochemical degradation of the Reactive Red 141 dye using a boron-doped diamond anode, Water. Air. Soil Pollut. 224 (2013). doi:10.1007/s11270-012-1397-9.

[175] C. Flox, C. Arias, E. Brillas, A. Savall, K. Groenen-Serrano, Electrochemical incineration of cresols: A comparative study between PbO2and boron-doped diamond anodes, Chemosphere. 74 (2009) 1340–1347. doi:10.1016/j.chemosphere.2008.11.050.

[176] Q. Zhuo, S. Deng, B. Yang, J. Huang, B. Wang, T. Zhang, G. Yu, Degradation of

perfluorinated compounds on a boron-doped diamond electrode, Electrochim. Acta. 77 (2012) 17–22. doi:10.1016/j.electacta.2012.04.145.

[177] T. Ochiai, Y. Iizuka, K. Nakata, T. Murakami, D.A. Tryk, A. Fujishima, Y. Koide, Y. Morito, Efficient electrochemical decomposition of perfluorocarboxylic acids by the use of a boron-doped diamond electrode, Diam. Relat. Mater. 20 (2011) 64–67. doi:10.1016/j.diamond.2010.12.008.

[178] Z. Liao, J. Farrell, Electrochemical oxidation of perfluorobutane sulfonate using boron-doped diamond film electrodes, J. Appl. Electrochem. 39 (2009) 1993–1999. doi:10.1007/s10800-009-9909-z.

[179] O. Scialdone, A. Galia, S. Randazzo, Electrochemical treatment of aqueous solutions containing one or many organic pollutants at boron doped diamond anodes. Theoretical modeling and experimental data, Chem. Eng. J. 183 (2012) 124–134. doi:10.1016/j.cej.2011.12.042.

[180] S. Garcia-Segura, E. Brillas, Mineralization of the recalcitrant oxalic and oxamic acids by electrochemical advanced oxidation processes using a boron-doped diamond anode, Water Res. 45 (2011) 2975–2984. doi:10.1016/j.watres.2011.03.017.

[181] O. Scialdone, S. Randazzo, A. Galia, G. Silvestri, Electrochemical oxidation of organics in water: Role of operative parameters in the absence and in the presence of NaCl, Water Res. 43 (2009) 2260–2272. doi:10.1016/j.watres.2009.02.014.

[182] E. Weiss, K. Groenen-Serrano, A. Savall, C. Comninellis, A kinetic study of the electrochemical oxidation of maleic acid on boron doped diamond, J. Appl. Electrochem. 37 (2006) 41–47. doi:10.1007/s10800-006-9212-1.

[183] T.A. Ivandini, T.N. Rao, A. Fujishima, Y. Einaga, Electrochemical oxidation of oxalic

acid at highly boron-doped diamond electrodes, Anal. Chem. 78 (2006) 3467–3471. doi:10.1021/ac052029x.

[184] and M.A.R. P. Cañizares,J. García-Gómez,J. Lobato, and, Electrochemical Oxidation of Aqueous Carboxylic Acid Wastes Using Diamond Thin-Film Electrodes, Ind. Eng. Chem. Res. 42 (2003) 956–962.

[185] D. Gandini, E. Mahé, P.A. Michaud, W. Haenni, A. Perret, C. Comninellis, Oxidation of carboxylic acids at boron-doped diamond electrodes for wastewater treatment, J. Appl. Electrochem. 30 (2000) 1345–1350. doi:10.1023/A:1026526729357.

[186] C.A. Martínez-Huitle, S. Ferro, A. De Battisti, Electrochemical incineration of oxalic acid: Role of electrode material, Electrochim. Acta. 49 (2004) 4027–4034. doi:10.1016/j.electacta.2004.01.083.

[187] Y.J. Jung, K.W. Baek, B.S. Oh, J.W. Kang, An investigation of the formation of chlorate and perchlorate during electrolysis using Pt/Ti electrodes: The effects of pH and reactive oxygen species and the results of kinetic studies, Water Res. 44 (2010) 5345–5355. doi:10.1016/j.watres.2010.06.029.

[188] A.M. Polcaro, A. Vacca, M. Mascia, F. Ferrara, Product and by-product formation in electrolysis of dilute chloride solutions, J. Appl. Electrochem. 38 (2008) 979–984. doi:10.1007/s10800-008-9509-3.

[189] M.E.H. Bergmann, J. Rollin, Product and by-product formation in laboratory studies on disinfection electrolysis of water using boron-doped diamond anodes, Catal. Today. 124 (2007) 198–203. doi:10.1016/j.cattod.2007.03.038.

[190] M.E.H. Bergmann, J. Rollin, T. Iourtchouk, The occurrence of perchlorate during drinking water electrolysis using BDD anodes, Electrochim. Acta. 54 (2009) 2102–2107.

doi:10.1016/j.electacta.2008.09.040.

[191] D. Report, T h e O c c u r r e n c e a n d S o u r c e s o f P e r c h l o r a t e i n M a s s a c h u s e t t s, (2006).

[192] P. Contamination, P. Act, A. Report, T.O. The, L. State, W. Resources, C. Board, S. Water, R. Control, S.W. Board, R. Water, Q. Control, R.W. Boards, S. Water, B. State, W. Board, P. Regulation, P. Registration, E. Committee, P. Management, A. Committee, No Title, (2007).

[193] T. Zewdie, C.M. Smith, M. Hutcheson, C.R. West, Basis of the massachusetts reference dose and drinking water standard for perchlorate, Environ. Health Perspect. 118 (2010) 42–48. doi:10.1289/ehp.0900635.

[194] United States Environmental Protection Agency, Drinking Water Contaminants, Am. Child. Environ. (2015) 21–23. doi:10.1093/bmb/ldg027.

[195] O. Azizi, D. Hubler, G. Schrader, J. Farrell, B.P. Chaplin, Mechanism of perchlorate formation on boron-doped diamond film anodes, Environ. Sci. Technol. 45 (2011) 10582–10590. doi:10.1021/es202534w.

[196] A. Donaghue, B.P. Chaplin, Effect of select organic compounds on perchlorate formation at boron-doped diamond film anodes, Environ. Sci. Technol. 47 (2013) 12391–12399. doi:10.1021/es4031672.

[197] V. Cesarino, I. Cesarino, F.C. Moraes, S.A.S. Machado, L.H. Mascaro, Carbon nanotubes modified with SnO2 rods for levofloxacin detection, J. Braz. Chem. Soc. 25 (2014) 502–508. doi:10.5935/0103-5053.20140017.

[198] F. Wang, L. Zhu, J. Zhang, Electrochemical sensor for levofloxacin based on molecularly imprinted polypyrrole-graphene-gold nanoparticles modified electrode, Sensors Actuators,

B Chem. 192 (2014) 642–647. doi:10.1016/j.snb.2013.11.037.

[199] N. Sattarahmady, H. Heli, R. Dehdari Vais, A flower-like nickel oxide nanostructure: Synthesis and application for choline sensing, Talanta. 119 (2014) 207–213. doi:10.1016/j.talanta.2013.11.002.

[200] K. Zhang, L. Lu, Y. Wen, J. Xu, X. Duan, L. Zhang, D. Hu, T. Nie, Facile synthesis of the necklace-like graphene oxide-multi-walled carbon nanotube nanohybrid and its application in electrochemical sensing of Azithromycin, Anal. Chim. Acta. 787 (2013) 50–56. doi:10.1016/j.aca.2013.05.037.

[201] L. Fotouhi, Z. Atoofi, M.M. Heravi, Interaction of ciprofloxacin with DNA studied by spectroscopy and voltammetry at MWCNT/DNA modified glassy carbon electrode, Talanta. 103 (2013) 194–200. doi:10.1016/j.talanta.2012.10.032.

[202] F. Faridbod, T. Poursaberi, P. Norouzi, M.R. Ganjali, Ciprofloxacin nano-composite carbon paste and PVC membrane potentiometric sensors, Int. J. Electrochem. Sci. 7 (2012) 3693–3705.

[203] A.A. Ensafi, A.R. Allafchain, R. Mohammadzadeh, Characterization of MgFe2O4 Nanoparticles as a Novel Electrochemical Sensor: Application for the Voltammetric Determination of Ciprofloxacin, Anal. Sci. 28 (2012) 705–710. doi:10.1039/c1jm11909e.

[204] H. Wan, F. Zhao, W. Wu, B. Zeng, Direct electron transfer and voltammetric determination of roxithromycin at a single-wall carbon nanotube coated glassy carbon electrode, Colloids Surfaces B Biointerfaces. 82 (2011) 427–431. doi:10.1016/j.colsurfb.2010.09.014.

[205] S.A. Kumar, S.-F. Wang, C.-T. Yeh, H.-C. Lu, J.-C. Yang, Y.-T. Chang, Direct electron transfer of cytochrome C and its electrocatalytic properties on multiwalled carbon

nanotubes/ciprofloxacin films, J. Solid State Electrochem. 14 (2010) 2129–2135. doi:10.1007/s10008-010-1048-2.

[206] K.J. Huang, X. Liu, W.Z. Xie, H.X. Yuan, Electrochemical behavior and voltammetric determination of norfloxacin at glassy carbon electrode modified with multi walled carbon nanotubes/Nafion, Colloids Surfaces B Biointerfaces. 64 (2008) 269–274. doi:10.1016/j.colsurfb.2008.02.003.

[207] S. Bose, R.A. Khare, P. Moldenaers, Assessing the strengths and weaknesses of various types of pre-treatments of carbon nanotubes on the properties of polymer/carbon nanotubes composites: A critical review, Polymer (Guildf). 51 (2010) 975–993. doi:10.1016/j.polymer.2010.01.044.

[208] P.C. Ma, N.A. Siddiqui, G. Marom, J.K. Kim, Dispersion and functionalization of carbon nanotubes for polymer-based nanocomposites: A review, Compos. Part A Appl. Sci. Manuf. 41 (2010) 1345–1367. doi:10.1016/j.compositesa.2010.07.003.

[209] K. Balasubramanian, M. Burghard, Chemically functionalized carbon nanotubes, Small. 1 (2005) 180–192. doi:10.1002/smll.200400118.

[210] J. Wang, Carbon-nanotube based electrochemical biosensors: A review, Electroanalysis. 17 (2005) 7–14. doi:10.1002/elan.200403113.

[211] W. Bauhofer, J.Z. Kovacs, A review and analysis of electrical percolation in carbon nanotube polymer composites, Compos. Sci. Technol. 69 (2009) 1486–1498. doi:10.1016/j.compscitech.2008.06.018.

[212] T. Saito, K. Matsushige, K. Tanaka, Chemical treatment and modification of multi-walled carbon nanotubes, Phys. B Condens. Matter. 323 (2002) 280–283. doi:10.1016/S0921-4526(02)00999-7.

[213] H.-Z. Geng, K.K. Kim, K.P. So, Y.S. Lee, Y. Chang, Y.H. Lee, Effect of Acid Treatment on Carbon Nanotube-Based Flexible Transparent Conducting Films, J. Am. Chem. Soc. 129 (2007) 7758–7759. doi:10.1021/ja0722224.

[214] M. Trépanier, A. Tavasoli, A.K. Dalai, N. Abatzoglou, Fischer-Tropsch synthesis over carbon nanotubes supported cobalt catalysts in a fixed bed reactor: Influence of acid treatment, Fuel Process. Technol. 90 (2009) 367–374. doi:10.1016/j.fuproc.2008.10.012.

[215] H.H. Cho, B.A. Smith, J.D. Wnuk, D.H. Fairbrother, W.P. Ball, Influence of Surface Oxides on the Adsorption of Naphthalene onto Multiwalled Carbon Nanotubes, Environ. Sci. & Technol. 42 (2008) 2899–2905. http://pubs3.acs.org/acs/journals/doilookup?in_doi=10.1021/es702363e.

[216] G.C. Chen, X.Q. Shan, Y.S. Wang, Z.G. Pei, X.E. Shen, B. Wen, G. Owens, Effects of copper, lead, and cadmium on the sorption and desorption of atrazine onto and from carbon nanotubes., Environ. Sci. Technol. 42 (2008) 8297–8302. http://www.ncbi.nlm.nih.gov/pubmed/19068809.

[217] Y. Zhao, F. Yuan, X. Quan, H. Yu, S. Chen, H. Zhao, Z. Liu, N. Hilal, An electrochemical sensor for selective determination of sulfamethoxazole in surface water using a molecularly imprinted polymer modified BDD electrode, Anal. Methods. 7 (2015) 2693–2698. doi:10.1039/C4AY03055A.

[218] H.J. Lee, M.K. Hong, S.D. Han, S.H. Cho, S.H. Moon, J. Shim, S.H. Moon, J.H. Choi, J. Cho, S.H. Moon, a. W. Zularisam, a. F. Ismail, R. Salim, Q. Zhang, C.D. Vecitis, A.M. Zaky, B.P. Chaplin, G. YaP, J.I. Yang, J.U.N. Wang, J. Jia, J.I. Yang, J.U.N. Wang, F.C.C. Walsh, R.G.A. Wills, L.M. Vracar, S.L. Gojkovic, N.R. Elezovic, V.R. Radmilovic, M.M. Jaksic, N. V. Krstajic, N.G. Tsierkezos, U. Ritter, M. Toyoda, T. Yano,

B. Tryba, S. Mozia, T. Tsumura, M. Inagaki, C. Terashima, T.N. Rao, B. V. Sarada, D. a. Tryk, A. Fujishima, J.R. Smith, F.C.C. Walsh, T.S. Singh, B.. Madhava Rao, H. Mohan, J.P. Mittal, M.H. Schnoor, C.D. Vecitis, H. Ren, Q. Wang, X. Zhang, R. Kang, S. Shi, W. Cong, W.H. Reinmuth, P. Paunović, O. Popovski, E. Fidančevska, B. Ranguelov, D. Stoevska Gogovska, A.T. Dimitrov, S. Hadži Jordanov, R.S. Nicholson, I. Shain, D. Mishra, Z. Liao, J. Farrell, N. Material, B. Marselli, J. Garcia-Gomez, P.-A. Michaud, M.A. Rodrigo, C. Comninellis, G. Louit, S. Foley, J. Cabillic, H. Coffigny, F. Taran, A. Valleix, J.P. Renault, S. Pin, X. Li, A.L. Zhu, W. Qu, H. Wang, R. Hui, L. Zhang, J. Zhang, S. Levine, a. L. Smith, D. Kundu, R. Black, E.J. Berg, L.F. Nazar, P. Krishnan, S.G. Advani, A.K. Prasad, M. Komatsu, T.N. Rao, A. Fujishima, J.M. Knaup, J. Marx, T. Frauenheim, K.M. Kim, G.H. Kim, S.J. Song, J.Y. Seok, M.H. Lee, J.H. Yoon, C.S. Hwang, D. Kearney, D. Bejan, N.J. Bunce, A. Kapałka, G. Fóti, C. Comninellis, R. Jurczakowski, C. Hitz, a. Lasia, Y. Jing, G. Lun, B.P. Chaplin, K.I. Ishibashi, A. Fujishima, T. Watanabe, K. Hashimoto, J. Iniesta, K.J. Howe, M.M. Clark, S.R. Heil, M. Holz, T.M. Kastner, H. Weing&#xfffd;rtner, H. Weingartner, P.C.S. Hayfield, T. Hayashi, I. Sakurada, K. Honda, S. Motohashi, K. Uchikura, J. GOCHSTEIN, P. Giesting, S. Guggenheim, A.F. Koster Van Groos, A. Busch, P. Geng, J. Su, C. Miles, C. Comninellis, G. Chen, S. Garcia-Segura, E. Brillas, S. Ferro, C. a. Martínez-Huitle, a. Battisti, a. Elmidaoui, F. Elhannouni, M. a. Menkouchi Sahli, L. Chay, H. Elabbassi, M. Hafsi, D. Largeteau, A. V. Dudchenko, J. Rolf, K. Russell, W. Duan, D. Jassby, A. Donaghue, B.P. Chaplin, C. de Lannoy, D. Jassby, D.D. Davis, M.R. Wiesner, L. Cited, G. Chen, E.A. a. E. Betterton, R.G.G.R. Arnold, W.P. Ela, T. Charbouillot, M. Brigante, G. Mailhot, P.R. Maddigapu, C. Minero, D. Vione, B.P. Chaplin, G. BUXTON, C. GREENSTOCK, W.

HELMAN, A. ROSS, G.J. Brug, a. L.G. van den Eeden, M. Sluyters-Rehbach, J.H. Sluyters, J. Bi, C. Peng, H. Xu, A.-S. Ahmed, D. Bejan, E. Guinea, N.J. Bunce, A.J. Bard, L.R. Faulkner, N. Aouina, H. Cachet, C. Debiemme-Chouvy, T.T.M. Tran, Self-diffusion of the perchlorate ion in aqueous electrolyte solutions measured by 35Cl NMR spin?echo experiments, 2014. doi:10.1016/j.electacta.2010.05.041.

[219] F.C. Walsh, R.G.A. Wills, The continuing development of Magnéli phase titanium sub-oxides and Ebonex®electrodes, Electrochim. Acta. 55 (2010) 6342–6351. doi:10.1016/j.electacta.2010.05.011.

[220] X. Li, A.L. Zhu, W. Qu, H. Wang, R. Hui, L. Zhang, J. Zhang, Magneli phase Ti4O7 electrode for oxygen reduction reaction and its implication for zinc-air rechargeable batteries, Electrochim. Acta. 55 (2010) 5891–5898. doi:10.1016/j.electacta.2010.05.041.

[221] D. Kundu, R. Black, E.J. Berg, L.F. Nazar, A highly active nanostructured metallic oxide cathode for aprotic Li–O_2 batteries, Energy Environ. Sci. 8 (2015) 1292–1298. doi:10.1039/C4EE02587C.

[222] J.R. Smith, F.C. Walsh, Reviews in applied electrochemistry. Number 50 - Electrodes based on Magneli phase titanium oxides: the properties and applications of Ebonex (R) materials, J. Appl. Electrochem. 28 (1998) 1021–1033. doi:10.1023/A:1003469427858.

[223] G. Chen, S.R. Bare, T.E. Mallouk, Development of Supported Bifunctional Electrocatalysts for Unitized Regenerative Fuel Cells, J. Electrochem. Soc. 149 (2002) A1092. doi:10.1149/1.1491237.

[224] C.C. Waraksa, G. Chen, D.D. Macdonald, T.E. Mallouk, EIS Studies of Porous Oxygen Electrodes with Discrete Particles, J. Electrochem. Soc. 150 (2003) E429. doi:10.1149/1.1594730.

[225] B.P. Chaplin, Critical review of electrochemical advanced oxidation processes for water treatment applications, Environ. Sci. Process. Impacts. 16 (2014) 1182. doi:10.1039/c3em00679d.

[226] L. Guo, K. Ding, K. Rockne, M. Duran, B.P. Chaplin, Bacteria inactivation at a sub-stoichiometric titanium dioxide reactive electrochemical membrane, J. Hazard. Mater. 319 (2016) 137–146. doi:10.1016/j.jhazmat.2016.05.051.

[227] S. Nayak, B.P. Chaplin, Fabrication and characterization of porous, conductive, monolithic Ti4O7electrodes, Electrochim. Acta. 263 (2018) 299–310. doi:10.1016/j.electacta.2018.01.034.

[228] A. Torkkeli, Droplet microfluidics on a planar surface, VTT Publ. 62 (2003) 3–194. doi:10.1002/aic.

[229] J.D. Genders, D. Hartsough, D.T. Hobbs, Electrochemical reduction of nitrates and nitrites in alkaline nuclear waste solutions, J. Appl. Electrochem. 26 (1996) 1–9. doi:10.1007/BF00248182.

[230] J.O. Bockris, J. Kim, Electrochemical treatment of low-level nuclear wastes, J. Appl. Electrochem. 27 (1997) 623–634. doi:10.1023/A:1018419316870.

[231] Y. Fernández-Nava, E. Marañón, J. Soons, L. Castrillón, Denitrification of high nitrate concentration wastewater using alternative carbon sources, J. Hazard. Mater. 173 (2010) 682–688. doi:10.1016/j.jhazmat.2009.08.140.

[232] W.T. Mook, M.H. Chakrabarti, M.K. Aroua, G.M.A. Khan, B.S. Ali, M.S. Islam, M.A. Abu Hassan, Removal of total ammonia nitrogen (TAN), nitrate and total organic carbon (TOC) from aquaculture wastewater using electrochemical technology: A review, Desalination. 285 (2012) 1–13. doi:10.1016/j.desal.2011.09.029.

[233] N. Abdel-Raouf, A.A. Al-Homaidan, I.B.M. Ibraheem, Microalgae and wastewater treatment, Saudi J. Biol. Sci. 19 (2012) 257–275. doi:10.1016/j.sjbs.2012.04.005.

[234] A. Daverey, S.H. Su, Y.T. Huang, S.S. Chen, S. Sung, J.G. Lin, Partial nitrification and anammox process: A method for high strength optoelectronic industrial wastewater treatment, Water Res. 47 (2013) 2929–2937. doi:10.1016/j.watres.2013.01.028.

[235] nitrate.pdf, (n.d.).

[236] J. Martínez, A. Ortiz, I. Ortiz, State-of-the-art and perspectives of the catalytic and electrocatalytic reduction of aqueous nitrates, Appl. Catal. B Environ. 207 (2017) 42–59. doi:10.1016/j.apcatb.2017.02.016.

[237] B.P. Chaplin, M. Reinhard, W.F. Schneider, C. Schüth, J.R. Shapley, T.J. Strathmann, C.J. Werth, Critical review of Pd-based catalytic treatment of priority contaminants in water, Environ. Sci. Technol. 46 (2012) 3655–3670. doi:10.1021/es204087q.

[238] A. Pintar, J. Batista, J. Levec, T. Kajiuchi, Kinetics of the catalytic liquid-phase hydrogenation of aqueous nitrate solutions, Appl. Catal. B Environ. 11 (1996) 81–98. doi:10.1016/S0926-3373(96)00036-7.

[239] F. Deganello, L.F. Liotta, A. Macaluso, A.M. Venezia, G. Deganello, Catalytic reduction of nitrates and nitrites in water solution on pumice-supported Pd-Cu catalysts, Appl. Catal. B Environ. 24 (2000) 265–273. doi:10.1016/S0926-3373(99)00109-5.

[240] H. Bergmann, K. Bouzek, M. Paidar, a Sadiâlkova, Electrochemical reduction of nitrate in weakly alkaline solutions, J. Appl. Electrochem. 31 (2001) 1185–1193. doi:10.1023/A:1012755222981.

[241] R. Gavagnin, L. Biasetto, F. Pinna, G. Strukul, Nitrate removal in drinking waters: The effect of tin oxides in the catalytic hydrogenation of nitrate by Pd/SnO2 catalysts, Appl.

Catal. B Environ. 38 (2002) 91–99. doi:10.1016/S0926-3373(02)00032-2.

[242] Y. Yoshinaga, T. Akita, I. Mikami, T. Okuhara, Hydrogenation of Nitrate in Water to Nitrogen over Pd–Cu Supported on Active Carbon, J. Catal. 207 (2002) 37–45. doi:10.1006/jcat.2002.3529.

[243] A. Garron, K. Lázár, F. Epron, Effect of the support on tin distribution in Pd-Sn/Al2O 3 and Pd-Sn/SiO2 catalysts for application in water denitration, Appl. Catal. B Environ. 59 (2005) 57–69. doi:10.1016/j.apcatb.2005.01.002.

[244] V.K. Tzitzios, V. Georgakilas, Catalytic reduction of N2O over Ag-Pd/Al2O3 bimetallic catalysts., Ag–Pd/Al2O3 Chemosph. Bimetallic. 59 (2005) 887–91. doi:10.1016/j.chemosphere.2004.11.021.

[245] B.P. Chaplin, J.R. Shapley, C.J. Werth, The selectivity and sustainability of a Pd-In/γ-Al2O 3 catalyst in a packed-bed reactor: The effect of solution composition, Catal. Letters. 130 (2009) 56–62. doi:10.1007/s10562-009-9883-4.

[246] H. Lan, X. Liu, H. Liu, R. Liu, C. Hu, J. Qu, Efficient Nitrate Reduction in a Fluidized Electrochemical Reactor Promoted by Pd-Sn/AC Particles, Catal. Letters. 146 (2016) 91–99. doi:10.1007/s10562-015-1615-3.

[247] Z. Zhang, Y. Xu, W. Shi, W. Wang, R. Zhang, X. Bao, B. Zhang, L. Li, F. Cui, Electrochemical-catalytic reduction of nitrate over Pd-Cu/??Al2O3 catalyst in cathode chamber: Enhanced removal efficiency and N2 selectivity, Chem. Eng. J. 290 (2016) 201–208. doi:10.1016/j.cej.2016.01.063.

[248] M. Paidar, I. Roušar, K. Bouzek, Electrochemical removal of nitrate ions in waste solutions after regeneration of ion exchange columns, J. Appl. Electrochem. 29 (1999) 611–617. doi:10.1023/A:1026423218899.

[249] K. Vorlop, Kinetic Investigation of the Catalytic Nitrate Reduction : Construction of the Test Reactor System, (1999) 199–202.

[250] R. Zhang, D. Shuai, K.A. Guy, J.R. Shapley, T.J. Strathmann, C.J. Werth, Elucidation of Nitrate Reduction Mechanisms on a Pd-In Bimetallic Catalyst using Isotope Labeled Nitrogen Species, ChemCatChem. 5 (2013) 313–321. doi:10.1002/cctc.201200457.

[251] W.I.S. Ammonia, Ammonia Ammonia, (n.d.).

[252] B. Ambrosioni, A. Barthelemy, D. Bejan, N.J. Bunce, Electrochemical reduction of aqueous nitrate ion at tin cathodes, Can. J. Chem. 92 (2014) 228–233. doi:10.1139/cjc-2013-0406.

[253] N. Plumeré, Interferences from oxygen reduction reactions in bioelectroanalytical measurements: The case study of nitrate and nitrite biosensors, Anal. Bioanal. Chem. 405 (2013) 3731–3738. doi:10.1007/s00216-013-6827-z.

[254] N. Fallahpour, X. Mao, L. Rajic, S. Yuan, A.N. Alshawabkeh, Electrochemical dechlorination of trichloroethylene in the presence of natural organic matter, metal ions and nitrates in a simulated karst media, J. Environ. Chem. Eng. 5 (2017) 240–245. doi:10.1016/j.jece.2016.11.046.

[255] L. Rajic, N. Fallahpour, R. Nazari, A.N. Alshawabkeh, Influence of humic substances on electrochemical degradation of trichloroethylene in limestone aquifers, Electrochim. Acta. 181 (2015) 123–129. doi:10.1016/j.electacta.2015.03.121.

[256] R. Tenne, K. Patel, K. Hashimoto, A. Fujishima, Efficient electrochemical reduction of nitrate to ammonia using conductive diamond film electrodes, J. Electroanal. Chem. 347 (1993) 409–415. doi:10.1016/0022-0728(93)80105-Q.

[257] D. Wan, Y. Liu, Y. Wang, H. Wang, S. Xiao, Simultaneous bio-autotrophic reduction of

perchlorate and nitrate in a sulfur packed bed reactor: Kinetics and bacterial community structure, Water Res. 108 (2017) 280–292. doi:10.1016/j.watres.2016.11.003.

[258] Y. García-Martínez, J. Chirinos, C. Bengoa, F. Stüber, J. Font, A. Fortuny, A. Fabregat, Nitrate removal in an innovative up-flow stirred packed-bed bioreactor, Chem. Eng. Process. Process Intensif. 121 (2017) 57–64. doi:10.1016/j.cep.2017.08.001.

[259] H.K. Kim, J.Y. Jeong, H.N. Cho, J.Y. Park, Kinetics of nitrate reduction with the packed bed iron bipolar electrode, Sep. Purif. Technol. 152 (2015) 140–147. doi:10.1016/j.seppur.2015.08.010.

[260] R.L. Smith, S.P. Buckwalter, D.A. Repert, D.N. Miller, Small-scale, hydrogen-oxidizing-denitrifying bioreactor for treatment of nitrate-contaminated drinking water, Water Res. 39 (2005) 2014–2023. doi:10.1016/j.watres.2005.03.024.

[261] J.Y. Jeong, H.K. Kim, J.H. Kim, J.Y. Park, Electrochemical removal of nitrate using ZVI packed bed bipolar electrolytic cell, Chemosphere. 89 (2012) 172–178. doi:10.1016/j.chemosphere.2012.05.104.

[262] A.E. Palomares, C. Franch, A. Corma, Nitrates removal from polluted aquifers using (Sn or Cu)/Pd catalysts in a continuous reactor, Catal. Today. 149 (2010) 348–351. doi:10.1016/j.cattod.2009.05.013.

[263] A. Pintar, J. Batista, Catalytic stepwise nitrate hydrogenation in batch-recycle fixed-bed reactors, J. Hazard. Mater. 149 (2007) 387–398. doi:10.1016/j.jhazmat.2007.04.004.

[264] M. Duca, M.T.M. Koper, Powering denitrification: the perspectives of electrocatalytic nitrate reduction, Energy Environ. Sci. (2012) 9726–9742. doi:10.1039/c2ee23062c.

[265] J. Wen, X. Tan, Y. Hu, Q. Guo, X. Hong, Filtration and Electrochemical Disinfection Performance of PAN/PANI/AgNWs-CC Composite Nanofiber Membrane, Environ. Sci.

Technol. 51 (2017) 6395–6403. doi:10.1021/acs.est.6b06290.

[266] C. Cuevas, D. Kim, K.P. Katuri, P. Saikaly, S.P. Nunes, Electrochemically active polymeric hollow fibers based on poly(ether-b-amide)/carbon nanotubes, J. Memb. Sci. 545 (2018) 323–328. doi:10.1016/j.memsci.2017.09.052.

[267] Z. Liu, M. Zhu, L. Zhao, C. Deng, J. Ma, Z. Wang, H. Liu, H. Wang, Aqueous tetracycline degradation by coal-based carbon electrocatalytic filtration membrane: Effect of nano antimony-doped tin dioxide coating, Chem. Eng. J. 314 (2017) 59–68. doi:10.1016/j.cej.2016.12.093.

[268] P. Tao, Y. Xu, Y. Zhou, Coal-Based Carbon Membrane Coupled with Electrochemical Oxidation Process for the Enhanced Microalgae Removal from Simulated Ballast Water, (2017) 1–8.

[269] Y. Jing, L. Guo, B.P. Chaplin, Electrochemical impedance spectroscopy study of membrane fouling and electrochemical regeneration at a sub-stoichiometric TiO2 reactive electrochemical membrane, J. Memb. Sci. 510 (2016) 510–523. doi:10.1016/j.memsci.2016.03.029.

[270] L. Hua, L. Guo, M. Thakkar, D. Wei, M. Agbakpe, L. Kuang, M. Magpile, B.P. Chaplin, Y. Tao, D. Shuai, X. Zhang, S. Mitra, W. Zhang, Effects of anodic oxidation of a substoichiometric titanium dioxide reactive electrochemical membrane on algal cell destabilization and lipid extraction, Bioresour. Technol. 203 (2016) 112–117. doi:10.1016/j.biortech.2015.12.041.

[271] Y. Yang, J. Li, H. Wang, X. Song, T. Wang, B. He, X. Liang, H.H. Ngo, An electrocatalytic membrane reactor with self-cleaning function for industrial wastewater treatment, Angew. Chemie - Int. Ed. 50 (2011) 2148–2150. doi:10.1002/anie.201005941.

[272] X. Sun, J. Wu, Z. Chen, X. Su, B.J. Hinds, Fouling characteristics and electrochemical recovery of carbon nanotube membranes, Adv. Funct. Mater. 23 (2013) 1500–1506. doi:10.1002/adfm.201201265.

[273] C.D. Vecitis, M.H. Schnoor, M.S. Rahaman, J.D. Schiffman, M. Elimelech, Electrochemical multiwalled carbon nanotube filter for viral and bacterial removal and inactivation, Environ. Sci. Technol. 45 (2011) 3672–3679. doi:10.1021/es2000062.

[274] A.M. Zaky, B.P. Chaplin, Mechanism of p-substituted phenol oxidation at a Ti4O 7 reactive electrochemical membrane, Environ. Sci. Technol. 48 (2014) 5857–5867. doi:10.1021/es5010472.

[275] J. Iniesta, Electrochemical oxidation of phenol at boron-doped diamond electrode, Electrochim. Acta. 46 (2001) 3573–3578. doi:10.1016/S0013-4686(01)00630-2.

[276] C. Borra, Electrooxidation of aqueous p -methoxyphenol on lead oxide electrodes, (2004) 583–589.

[277] C. Borrás, T. Laredo, J. Mostany, B.R. Scharifker, Study of the oxidation of solutions of p-chlorophenol and p-nitrophenol on Bi-doped PbO2 electrodes by UV-Vis and FTIR in situ spectroscopy, Electrochim. Acta. 49 (2004) 641–648. doi:10.1016/j.electacta.2003.09.019.

[278] B. Adams, M. Tian, A. Chen, Design and electrochemical study of SnO2-based mixed oxide electrodes, Electrochim. Acta. 54 (2009) 1491–1498. doi:10.1016/j.electacta.2008.09.034.

[279] P. Cañizares, J. Lobato, R. Paz, M.A. Rodrigo, C. Sáez, Electrochemical oxidation of phenolic wastes with boron-doped diamond anodes, Water Res. 39 (2005) 2687–2703. doi:10.1016/j.watres.2005.04.042.

[280] I. Sirés, C.T.J. Low, C. Ponce-de-León, F.C. Walsh, The characterisation of PbO2-coated electrodes prepared from aqueous methanesulfonic acid under controlled deposition conditions, Electrochim. Acta. 55 (2010) 2163–2172. doi:10.1016/j.electacta.2009.11.051.

[281] P. Cañizares, R. Paz, C. Sáez, M.A. Rodrigo, Costs of the electrochemical oxidation of wastewaters: A comparison with ozonation and Fenton oxidation processes, J. Environ. Manage. 90 (2009) 410–420. doi:10.1016/j.jenvman.2007.10.010.

[282] H. Liu, A. Vajpayee, C.D. Vecitis, Bismuth-doped tin oxide-coated carbon nanotube network: Improved anode stability and efficiency for flow-through organic electrooxidation, ACS Appl. Mater. Interfaces. 5 (2013) 10054–10066. doi:10.1021/am402621v.

[283] M. Panizza, G. Cerisola, Direct And Mediated Anodic Oxidation of Organic Pollutants, Chem. Rev. 109 (2009) 6541–6569. doi:10.1021/cr9001319.

[284] Y.-S. Hsu, S.K. Ghandhi, The Effect of Phosphorus Doping on Tin Oxide Films Made by the Oxidation of Phosphine and Tetramethyltin, J. Electrochem. Soc. 127 (1980) 1596. doi:10.1149/1.2129959.

[285] R. Kötz, S. Stucki, B. Carcer, Electrochemical waste water treatment using high overvoltage anodes. Part I: Physical and electrochemical properties of SnO2 anodes, J. Appl. Electrochem. 21 (1991) 14–20. doi:10.1007/BF01103823.

[286] S. Stucki, R. Kötz, B. Carcer, W. Suter, Electrochemical waste water treatment using high overvoltage anodes Part II: Anode performance and applications, J. Appl. Electrochem. 21 (1991) 99–104. doi:10.1007/BF01464288.

[287] U. Neckel, C. Joukhadar, M. Frossard, W. Jäger, M. Müller, B.X. Mayer, Simultaneous determination of levofloxacin and ciprofloxacin in microdialysates and plasma by high-

performance liquid chromatography, Anal. Chim. Acta. 463 (2002) 199–206. doi:10.1016/S0003-2670(02)00429-4.

[288] S. Mostafa, M. El-Sadek, E.A. Alla, Spectrophotometric determination of ciprofloxacin, enrofloxacin and pefloxacin through charge transfer complex formation, J. Pharm. Biomed. Anal. 27 (2002) 133–142. doi:10.1016/S0731-7085(01)00524-6.

[289] E.A. McGaw, G.M. Swain, A comparison of boron-doped diamond thin-film and Hg-coated glassy carbon electrodes for anodic stripping voltammetric determination of heavy metal ions in aqueous media, Anal. Chim. Acta. 575 (2006) 180–189. doi:10.1016/j.aca.2006.05.094.

[290] R.F. Brocenschi, R.C. Rocha-Filho, L. Li, G.M. Swain, Comparative electrochemical response of estrone at glassy-carbon, nitrogen-containing tetrahedral amorphous carbon and boron-doped diamond thin-film electrodes, J. Electroanal. Chem. 712 (2014) 207–214. doi:10.1016/j.jelechem.2013.11.014.

[291] G.M. Swain, The Susceptibility to Surface Corrosion in Acidic Fluoride Media: A Comparison of Diamond, HOPG, and Glassy Carbon Electrodes, J. Electrochem. Soc. 141 (1994) 3382. doi:10.1149/1.2059343.

[292] G. Liu, Y. Lin, Y. Tu, Z. Ren, Ultrasensitive voltammetric detection of trace heavy metal ions using carbon nanotube nanoelectrode array, Analyst. 130 (2005) 1098. doi:10.1039/b419447k.

[293] J. Wang, M. Musameh, Y. Lin, Solubilization of carbon nanotubes by Nafion toward the preparation of amperometric biosensors, J. Am. Chem. Soc. 125 (2003) 2408–2409. doi:10.1021/ja028951v.

[294] Y. Shao, G. Yin, Y. Gao, P. Shi, Durability Study of Pt/C and Pt/CNTs Catalysts under

Simulated PEM Fuel Cell Conditions, J. Electrochem. Soc. 153 (2006) A1093. doi:10.1149/1.2191147.

[295] M.M. Rahman, A. Khan, A.M. Asiri, Chemical sensor development based on poly(o-anisidine)silverized-MWCNT nanocomposites deposited on glassy carbon electrodes for environmental remediation, RSC Adv. 5 (2015) 71370–71378. doi:10.1039/c5ra10793h.

[296] G. Gao, C.D. Vecitis, Electrochemical carbon nanotube filter oxidative performance as a function of surface chemistry, Environ. Sci. Technol. 45 (2011) 9726–9734. doi:10.1021/es202271z.

[297] F. Su, C. Lu, S. Hu, Adsorption of benzene, toluene, ethylbenzene and p-xylene by NaOCl-oxidized carbon nanotubes, Colloids Surfaces A Physicochem. Eng. Asp. 353 (2010) 83–91. doi:10.1016/j.colsurfa.2009.10.025.

[298] X.M. Yan, B.Y. Shi, J.J. Lu, C.H. Feng, D.S. Wang, H.X. Tang, Adsorption and desorption of atrazine on carbon nanotubes, J. Colloid Interface Sci. 321 (2008) 30–38. doi:10.1016/j.jcis.2008.01.047.

[299] S. Teixeira, R.S. Conlan, O.J. Guy, M.G.F. Sales, Novel single-wall carbon nanotube screen-printed electrode as an immunosensor for human chorionic gonadotropin, Electrochim. Acta. 136 (2014) 323–329. doi:10.1016/j.electacta.2014.05.105.

[300] X.S. Miao, F. Bishay, M. Chen, C.D. Metcalfe, Occurrence of antimicrobials in the final effluents of wastewater treatment plants in Canada, Environ. Sci. Technol. 38 (2004) 3533–3541. doi:10.1021/es030653q.

[301] K.D. Brown, J. Kulis, B. Thomson, T.H. Chapman, D.B. Mawhinney, Occurrence of antibiotics in hospital, residential, and dairy effluent, municipal wastewater, and the Rio Grande in New Mexico, Sci. Total Environ. 366 (2006) 772–783.

doi:10.1016/j.scitotenv.2005.10.007.

[302] K.G. Karthikeyan, M.T. Meyer, Occurrence of antibiotics in wastewater treatment facilities in Wisconsin, USA, Sci. Total Environ. 361 (2006) 196–207. doi:10.1016/j.scitotenv.2005.06.030.

[303] A.L. Batt, I.B. Bruce, D.S. Aga, Evaluating the vulnerability of surface waters to antibiotic contamination from varying wastewater treatment plant discharges, Environ. Pollut. 142 (2006) 295–302. doi:10.1016/j.envpol.2005.10.010.

[304] C.M. Manaia, A. Novo, B. Coelho, O.C. Nunes, Ciprofloxacin resistance in domestic wastewater treatment plants, Water. Air. Soil Pollut. 208 (2010) 335–343. doi:10.1007/s11270-009-0171-0.

[305] R.F. Brocenschi, R.C. Rocha-Filho, B. Duran, G.M. Swain, The analysis of estrogenic compounds by flow injection analysis with amperometric detection using a boron-doped diamond electrode, Talanta. 126 (2014) 12–19. doi:10.1016/j.talanta.2014.02.047.

[306] J.H. Lee, U. Paik, J.Y. Choi, K.K. Kim, S.M. Yoon, J. Lee, B.K. Kim, J.M. Kim, M.H. Park, C.W. Yang, K.H. An, Y.H. Lee, Dispersion stability of single-walled carbon nanotubes using nafion in bisolvent, J. Phys. Chem. C. 111 (2007) 2477–2483. doi:10.1021/jp0670485.

[307] H. Gong, S.T. Kim, J.D. Lee, S. Yim, Simple quantification of surface carboxylic acids on chemically oxidized multi-walled carbon nanotubes, Appl. Surf. Sci. 266 (2013) 219–224. doi:10.1016/j.apsusc.2012.11.152.

[308] S. Musso, S. Porro, M. Vinante, L. Vanzetti, R. Ploeger, M. Giorcelli, B. Possetti, F. Trotta, C. Pederzolli, A. Tagliaferro, Modification of MWNTs obtained by thermal-CVD, Diam. Relat. Mater. 16 (2007) 1183–1187. doi:10.1016/j.diamond.2006.11.087.

[309] V. Datsyuk, M. Kalyva, K. Papagelis, J. Parthenios, D. Tasis, A. Siokou, I. Kallitsis, C. Galiotis, Chemical oxidation of multiwalled carbon nanotubes, Carbon N. Y. 46 (2008) 833–840. doi:10.1016/j.carbon.2008.02.012.

[310] Y.C. Chiang, W.H. Lin, Y.C. Chang, The influence of treatment duration on multi-walled carbon nanotubes functionalized by H2SO4/HNO3 oxidation, Appl. Surf. Sci. 257 (2011) 2401–2410. doi:10.1016/j.apsusc.2010.09.110.

[311] B.P. Chaplin, D.K. Hubler, J. Farrell, Understanding anodic wear at boron doped diamond film electrodes, Electrochim. Acta. 89 (2013) 122–131. doi:10.1016/j.electacta.2012.10.166.

[312] T. Ohashi, J. Zhang, Y. Takasu, W. Sugimoto, Steam activation of boron doped diamond electrodes, Electrochim. Acta. 56 (2011) 5599–5604. doi:10.1016/j.electacta.2011.04.005.

[313] T. Ohashi, W. Sugimoto, Y. Takasu, Catalytic roughening of surface layers of BDD for various applications, Electrochim. Acta. 54 (2009) 5223–5229. doi:10.1016/j.electacta.2009.04.021.

[314] T. Watanabe, T.K. Shimizu, Y. Tateyama, Y. Kim, M. Kawai, Y. Einaga, Giant electric double-layer capacitance of heavily boron-doped diamond electrode, Diam. Relat. Mater. 19 (2010) 772–777. doi:10.1016/j.diamond.2010.02.022.

[315] G.S. Garbellini, R.C. Rocha-Filho, O. Fatibello-Filho, Voltammetric determination of ciprofloxacin in urine samples and its interaction with dsDNA on a cathodically pretreated boron-doped diamond electrode, Anal. Methods. 7 (2015) 3411–3418. doi:10.1039/C5AY00625B.

[316] J. Luis Vázquez, M. Berlanga, S. Merino, Ò. Domènech, M. Viñas, M. Teresa Montero, J. Hernández-Borrell, Determination by Fluorimetric Titration of the Ionization Constants of

Ciprofloxacin in Solution and in the Presence of Liposomes¶, Photochem. Photobiol. 73 (2001) 14. doi:10.1562/0031-8655(2001)073<0014:DBFTOT>2.0.CO;2.

[317] E. Escribano, A.C. Calpena, T.M. Garrigues, J. Freixas, J. Domenech, J. Moreno, Structure-absorption relationships of a series of 6-fluoroquinolones, Antimicrob. Agents Chemother. 41 (1997) 1996–2000.

[318] H. Nawaz, S. Rauf, K. Akhtar, A.M. Khalid, Electrochemical DNA biosensor for the study of ciprofloxacin-DNA interaction, Anal. Biochem. 354 (2006) 28–34. doi:10.1016/j.ab.2006.04.004.

[319] A.A.J. Torriero, E. Salinas, J. Raba, J.J. Silber, Sensitive determination of ciprofloxacin and norfloxacin in biological fluids using an enzymatic rotating biosensor, Biosens. Bioelectron. 22 (2006) 109–115. doi:10.1016/j.bios.2005.12.004.

[320] A.A.E. Nsafi, M.T. Aei, T.K. Hayamian, F.H. Asanpour, Simultaneous Voltammetric Determination of Enrofloxacin and Ciprofloxacin in Urine and Plasma Using Multiwall Carbon Nanotubes Modified Glassy Carbon Electrode by Least-Squares Support Vector Machines, 26 (2010).

[321] H. Yi, C. Li, Voltammetric determination of ciprofloxacin based on the enhancement effect of cetyltrimethylammonium bromide (CTAB) at carbon paste electrode, Russ. J. Electrochem. 43 (2007) 1377–1381. doi:10.1134/S1023193507120075.

[322] Y. Kawai, K. Matsubayashi, H. Hakusui, Interaction of quinolones with metal cations in aqueous solution, Chem. Pharm. Bull. 44 (1996) 1425–1430. doi:10.1248/cpb.37.3229.

[323] N. Bt, A. Mansor, J. Tessonnier, M.G. Kutty, R. Schlögl, S.B.A. Hamid, Chemically Modified Carbon Nanotubes (CNTs) with Oxygen and Sulfur Containing Functional Groups for Adsorption of Mercury, 20 (2011) 66–70.

[324] G.D. Vuković, A.D. Marinković, M. Čolić, M.D. Ristić, R. Aleksić, A.A. Perić-Grujić, P.S. Uskoković, Removal of cadmium from aqueous solutions by oxidized and ethylenediamine-functionalized multi-walled carbon nanotubes, Chem. Eng. J. 157 (2010) 238–248. doi:10.1016/j.cej.2009.11.026.

[325] X. Li, J.J. Pignatello, Y. Wang, B. Xing, New insight into adsorption mechanism of ionizable compounds on carbon nanotubes, Environ. Sci. Technol. 47 (2013) 8334–8341. doi:10.1021/es4011042.

[326] X. Li, B. Gámiz, Y. Wang, J.J. Pignatello, B. Xing, Competitive sorption used to probe strong hydrogen bonding sites for weak organic acids on carbon nanotubes, Environ. Sci. Technol. 49 (2015) 1409–1417. doi:10.1021/es504019u.

[327] E. David, B. Campus, Intemational Journal of Pharmaceutics, Int. J. Pharm. 143 (1996) 101–106. doi:10.1016/0378-5173(95)04332-2.

[328] A.R. Mohamed, S.M. Sapuan, M. Shahjahan, A. Khalina, Characterization of pineapple leaf fibers from selected Malaysian cultivars, J. Food, Agric. Environ. 7 (2009) 235–240. doi:10.1016/j.trac.2007.09.004.

[329] Z. Wang, Z. Wu, G. Di Benedetto, J.L. Zunino, S. Mitra, Microwave synthesis of highly oxidized and defective carbon nanotubes for enhancing the performance of supercapacitors, Carbon N. Y. 91 (2015) 103–113. doi:10.1016/j.carbon.2015.04.045.

[330] J.H.T. Luong, K.B. Male, J.D. Glennon, Boron-doped diamond electrode: synthesis, characterization, functionalization and analytical applications, Analyst. 134 (2009) 1965. doi:10.1039/b910206j.

[331] A. Kapałka, G. Fóti, C. Comninellis, Investigation of the Anodic Oxidation of Acetic Acid on Boron-Doped Diamond Electrodes, J. Electrochem. Soc. 155 (2008) E27.

doi:10.1149/1.2823459.

[332] M. Panizza, G. Cerisola, Influence of anode material on the electrochemical oxidation of 2-naphthol: Part 2. Bulk electrolysis experiments, Electrochim. Acta. 49 (2004) 3221–3226. doi:10.1016/j.electacta.2004.02.036.

[333] Unconfirmed 168431, (n.d.).

[334] EPA, Fact Sheet: Final Regulatory Determination for Perchlorate, (2011) 1–2. doi:10.1016/j.talanta.2009.04.002.

[335] V.P. Detection, Drinking-Water Sources in California, (2004).

[336] C. Massachusetts, R. Limit, F.R. Limit, C. Effects, Current Regulatory Limit : Perchlorate, 0 (2018) 2–3.

[337] S. Szunerits, R. Boukherroub, Different strategies for functionalization of diamond surfaces, J. Solid State Electrochem. 12 (2008) 1205–1218. doi:10.1007/s10008-007-0473-3.

[338] M. Schade, S. Franzka, A. Schröter, F. Cappuccio, M. Gajda, V. Peinecke, A. Heinzel, N. Hartmann, Chemical functionalization of carbon/polymer bipolar plate materials via oxygen plasma activation and subsequent silanization, Surf. Coatings Technol. 240 (2014) 255–260. doi:10.1016/j.surfcoat.2013.12.037.

[339] H. Zeng, A.R. Konicek, N. Moldovan, F. Mangolini, T. Jacobs, I. Wylie, P.U. Arumugam, S. Siddiqui, R.W. Carpick, J.A. Carlisle, Boron-doped ultrananocrystalline diamond synthesized with an H-rich/Ar-lean gas system, Carbon N. Y. 84 (2015) 103–117. doi:10.1016/j.carbon.2014.11.057.

[340] A.J. Bard, L.R. Faulkner, Fundamentals and Fundamentals and Applications, 2015. doi:10.1016/B978-0-08-098353-0.00003-8.

[341] P. Cañizares, J. García-Gómez, I. Fernández de Marcos, M.A. Rodrigo, J. Lobato, Measurement of Mass-Transfer Coefficients by an Electrochemical Technique, J. Chem. Educ. 83 (2006) 1204. doi:10.1021/ed083p1204.

[342] Y. Jing, B.P. Chaplin, Mechanistic Study of the Validity of Using Hydroxyl Radical Probes To Characterize Electrochemical Advanced Oxidation Processes, Environ. Sci. Technol. 51 (2017) 2355–2365. doi:10.1021/acs.est.6b05513.

[343] R. Seidel, S. Thürmer, J. Moens, P. Geerlings, J. Blumberger, B. Winter, Valence photoemission spectra of aqueous Fe2+/3+ and [Fe(CN)6]4-/3- and their interpretation by DFT calculations, J. Phys. Chem. B. 115 (2011) 11671–11677. doi:10.1021/jp203997p.

[344] E. Mahé, D. Devilliers, C. Comninellis, Electrochemical reactivity at graphitic micro-domains on polycrystalline boron doped diamond thin-films electrodes, Electrochim. Acta. 50 (2005) 2263–2277. doi:10.1016/j.electacta.2004.10.060.

[345] P. Chen, R.L. McCreery, Control of Electron Transfer Kinetics at Glassy Carbon Electrodes by Specific Surface Modification, Anal. Chem. 68 (1996) 3958–3965. doi:10.1021/ac960492r.

[346] D. Gang, T.E. Clevenger, S.K. Banerji, Relationship of chlorine decay and THMs formation to NOM size, J. Hazard. Mater. 96 (2003) 1–12. doi:10.1016/S0304-3894(02)00164-4.

[347] S. Agraharam, D.W. Hess, P. a. Kohl, S. a. Bidstrup Allen, Plasma chemistry in fluorocarbon film deposition from pentafluoroethane/argon mixtures, J. Vac. Sci. Technol. A Vacuum, Surfaces, Film. 17 (1999) 3265. doi:10.1116/1.582053.

[348] P. Mérel, M. Tabbal, M. Chaker, S. Moisa, J. Margot, Direct evaluation of the sp3 content in diamond-like-carbon films by XPS, Appl. Surf. Sci. 136 (1998) 105–110.

doi:10.1016/S0169-4332(98)00319-5.

[349] P. Gayen, B.P. Chaplin, Selective Electrochemical Detection of Ciprofloxacin with a Porous Nafion/Multiwalled Carbon Nanotube Composite Film Electrode, ACS Appl. Mater. Interfaces. 8 (2016) 1615–1626. doi:10.1021/acsami.5b07337.

[350] D. Revision, M.J. Frisch, G.W. Trucks, H.B. Schlegel, G.E. Scuseria, A. Robb, J.R. Cheeseman, G. Scalmani, V. Barone, B. Mennucci, G.A. Petersson, M. Caricato, X. Li, H.P. Hratchian, A.F. Izmaylov, J. Bloino, G. Zheng, M. Hada, M. Ehara, K. Toyota, R. Fukuda, J. Hasegawa, M. Ishida, Y. Honda, O. Kitao, H. Nakai, T. Vreven, J.A. Montgomery, J.E. Peralta, M. Bearpark, J.J. Heyd, E. Brothers, K.N. Kudin, V.N. Staroverov, J. Normand, K. Raghavachari, A. Rendell, J.C. Burant, S.S. Iyengar, M. Cossi, N. Rega, J.M. Millam, M. Klene, J.E. Knox, J.B. Cross, V. Bakken, J. Jaramillo, R. Gomperts, R.E. Stratmann, O. Yazyev, A.J. Austin, R. Cammi, J.W. Ochterski, R.L. Martin, K. Morokuma, V.G. Zakrzewski, G.A. Voth, J.J. Dannenberg, S. Dapprich, A.D. Daniels, Ö. Farkas, J.B. Foresman, J. Cioslowski, D.J. Fox, W. Ct, Gaussian 09, Revision, (2015) 1–20.

[351] D. Mishra, Z. Liao, J. Farrell, Understanding Reductive Dechlorination of Trichloroethene on Boron-Doped Diamond Film Electrodes, Environ. Sci. Technol. 42 (2008) 9344–9349. doi:10.1021/es801815z.

[352] C.W. Bauschlicher, H. Partridge, A modification of the Gaussian-2 approach using density functional theory, J. Chem. Phys. 103 (1995) 1788–1791. doi:10.1063/1.469752.

[353] A. V. Marenich, C.J. Cramer, D.G. Truhlar, Unviersal solvation modle based on solute electron density and a contiuum model of the solvent defind by the bulk dielectric constant and atomic surface tensions, J. Phys. Chem. B. 113 (2009) 6378–6396.

doi:10.1021/jp810292n.

[354] M.J. Schabel, T.W. Peterson, a. J. Muscat, Macromolecule formation in low density CF[sub 4] plasmas: The influence of H[sub 2], J. Appl. Phys. 93 (2003) 1389. doi:10.1063/1.1535747.

[355] B. Marselli, J. Garcia-Gomez, P.-A. Michaud, M.A. Rodrigo, C. Comninellis, Electrogeneration of Hydroxyl Radicals on Boron-Doped Diamond Electrodes, J. Electrochem. Soc. 150 (2003) D79. doi:10.1149/1.1553790.

[356] J. Niu, H. Lin, J. Xu, H. Wu, Y. Li, Electrochemical mineralization of perfluorocarboxylic acids (PFCAs) by Ce-doped modified porous nanocrystalline PbO2film electrode, Environ. Sci. Technol. 46 (2012) 10191–10198. doi:10.1021/es302148z.

[357] J. Niu, H. Lin, C. Gong, X. Sun, Theoretical and experimental insights into the electrochemical mineralization mechanism of perfluorooctanoic acid, Environ. Sci. Technol. 47 (2013) 14341–14349. doi:10.1021/es402987t.

[358] A. Ueda, D. Kato, N. Sekioka, T. Kamata, R. Kurita, H. Uetsuka, Y. Hattori, S. Hirono, S. Umemura, O. Niwa, Fabrication of electrochemically stable fluorinated nano-carbon film compared with other fluorinated carbon materials, Carbon N. Y. 47 (2009) 1943–1952. doi:10.1016/j.carbon.2009.03.041.

[359] H. Li, J. Ni, Electrogeneration of disinfection byproducts at a boron-doped diamond anode with resorcinol as a model substance, Electrochim. Acta. 69 (2012) 268–274. doi:10.1016/j.electacta.2012.02.098.

[360] O. Scialdone, A. Galia, G. Filardo, Electrochemical incineration of 1,2-dichloroethane: Effect of the electrode material, Electrochim. Acta. 53 (2008) 7220–7225. doi:10.1016/j.electacta.2008.05.004.

[361] F. Shiraishi, M. Ueno, R. Chand, Y. Shibata, H.N. Luitel, Effect of silanization of titanium dioxide on photocatalytic decomposition of 2,4-dinitropheonol under irradiation with artificial UV light and sunlight, J. Chem. Technol. Biotechnol. 89 (2014) 81–87. doi:10.1002/jctb.4100.

[362] D.K. Hubler, J.C. Baygents, B.P. Chaplin, J. Farrell, Understanding Chlorite and Chlorate Formation Associated with Hypochlorite Generation at Boron Doped Diamond Film Anodes, J. Electrochem. Soc. 161 (2014) E182–E189. doi:10.1149/2.1001412jes.

[363] J.S. Beckman, T.W. Beckman, J. Chen, P.A. Marshall, B.A. Freeman, Apparent hydroxyl radical production by peroxynitrite: implications for endothelial injury from nitric oxide and superoxide., Proc. Natl. Acad. Sci. 87 (1990) 1620–1624. doi:10.1073/pnas.87.4.1620.

[364] 20001RYK.PDF, (n.d.).

[365] U.S. Environmental Protection Agency, 2000 National Water Quality Inventory Report to Congress, (2002). https://www.epa.gov/sites/production/files/2015-09/documents/2000_national_water_quality_inventory_report_to_congress.pdf.

[366] I. Katsounaros, G. Kyriacou, Influence of nitrate concentration on its electrochemical reduction on tin cathode: Identification of reaction intermediates, Electrochim. Acta. 53 (2008) 5477–5484. doi:10.1016/j.electacta.2008.03.018.

[367] I. Katsounaros, G. Kyriacou, Influence of the concentration and the nature of the supporting electrolyte on the electrochemical reduction of nitrate on tin cathode, Electrochim. Acta. 52 (2007) 6412–6420. doi:10.1016/j.electacta.2007.04.050.

[368] Y. Liao, A. Li, Indium Hydride Generation Atomic Absorption Spectrometry with, 8 (1993) 6–9.

[369] Some Observations on the Determination of lndium by Atomic Absorption Spectrophotometry Using the Volatile Covalent Hydride Technique, 389 (1988) 387–389.

[370] C. Patton, J. Kryskalla, U.S. Geological Survey National Water Quality Laboratory: Evaluation of alkaline persulfate digestion as an alternative to kjeldahl digestion for determination of total and dissolved nitrogen and phosphorous in water, Director. (2003) 33 pp. http://www.science.gov/topicpages/a/alkaline+persulfate+digestion.html.

[371] J. Radjenovic, D.L. Sedlak, Challenges and Opportunities for Electrochemical Processes as Next-Generation Technologies for the Treatment of Contaminated Water, Environ. Sci. Technol. 49 (2015) 11292–11302. doi:10.1021/acs.est.5b02414.

[372] J.R. Bolton, K.G. Bircher, W. Tumas, C. a. Tolman, Figures-of-merit for the technical development and application of advanced oxidation technologies for both electric- and solar-driven systems (IUPAC Technical Report), Pure Appl. Chem. 73 (2001) 627–637. doi:10.1351/pac200173040627.

[373] L. Guo, Y. Jing, B.P. Chaplin, Development and Characterization of Ultrafiltration TiO2 Magn??li Phase Reactive Electrochemical Membranes, Environ. Sci. Technol. 50 (2016) 1428–1436. doi:10.1021/acs.est.5b04366.

[374] N. Fritz, H.-C. Koo, Z. Wilson, E. Uzunlar, Z. Wen, X. Yeow, S.A. Bidstrup Allen, P.A. Kohl, Electroless Deposition of Copper on Organic and Inorganic Substrates Using a Sn⁄Ag Catalyst, J. Electrochem. Soc. 159 (2012) D386. doi:10.1149/2.099206jes.

[375] P.C. Hidber, W. Helbig, E. Kim, G.M. Whitesides, Microcontact Printing of Palladium Colloids: Micron-Scale Patterning by Electroless Deposition of Copper, Langmuir. 12 (1996) 1375–1380. doi:10.1021/la9507500.

[376] M.S. Kim, D.W. Lee, S.H. Chung, J.T. Kim, I.H. Cho, K.Y. Lee, Pd-Cu bimetallic

catalysts supported on TiO2-CeO2 mixed oxides for aqueous nitrate reduction by hydrogen, J. Mol. Catal. A Chem. 392 (2014) 308–314. doi:10.1016/j.molcata.2014.05.034.

[377] B.P. Chaplin, J.R. Shapley, Regeneration of Sulfur-Fouled Bimetallic Pd-Based Catalysts, (2007) 5491–5497.

[378] L. Lemaignen, C. Tong, V. Begon, R. Burch, D. Chadwick, Catalytic denitrification of water with palladium-based catalysts supported on activated carbons, Catal. Today. 75 (2002) 43–48. doi:10.1016/S0920-5861(02)00042-1.

[379] B.P. Chaplin, E. Roundy, K.A. Guy, J.R. Shapley, C.I. Werth, Effects of natural water ions and humic acid on catalytic nitrate reduction kinetics using an alumina supported Pd-Cu catalyst, Environ. Sci. Technol. 40 (2006) 3075–3081. doi:10.1021/es0525298.

[380] M. Kramer, Porous Electrodes, 131 (1984) 1283. doi:10.1149/1.2115807.

[381] A.C.A. De Vooys, R.A. Van Santen, J.A.R. Van Veen, Electrocatalytic reduction of NO y on palladiumrcopper 3 electrodes, J. Mol. Catal. A Chem. 154 (2000) 203–215. doi:10.1016/S1381-1169(99)00375-1.

[382] O. González Pérez, J.M. Bisang, Removal of nitrate using an activated rotating cylinder electrode, Electrochim. Acta. 194 (2016) 448–453. doi:10.1016/j.electacta.2016.02.114.

[383] S. Yang, Electrochemical Reduction of Nitrate on Different Cu-Zn Oxide Composite Cathodes, Int. J. Electrochem. Sci. 12 (2017) 4370–4383. doi:10.20964/2017.05.80.

[384] L. Su, K. Li, H. Zhang, M. Fan, D. Ying, T. Sun, Y. Wang, J. Jia, Electrochemical nitrate reduction by using a novel Co3O4/Ti cathode, Water Res. 120 (2017) 1–11. doi:10.1016/j.watres.2017.04.069.

[385] L. Rajic, D. Berroa, S. Gregor, S. Elbakri, M. MacNeil, A.N. Alshawabkeh,

Electrochemically-induced reduction of nitrate in aqueous solution, Int. J. Electrochem. Sci. 12 (2017) 5998–6009. doi:10.20964/2017.07.38.

[386] L. Mattarozzi, S. Cattarin, N. Comisso, R. Gerbasi, P. Guerriero, M. Musiani, E. Verlato, Electrodeposition of compact and porous Cu-Pd alloy layers and their application to nitrate reduction in alkali, Electrochim. Acta. 230 (2017) 365–372. doi:10.1016/j.electacta.2017.02.012.

[387] E. Pérez-Gallent, M.C. Figueiredo, I. Katsounaros, M.T.M. Koper, Electrocatalytic reduction of Nitrate on Copper single crystals in acidic and alkaline solutions., Electrochim. Acta. 227 (2017) 77–84. doi:10.1016/j.electacta.2016.12.147.

[388] W. Li, C. Xiao, Y. Zhao, Q. Zhao, R. Fan, J. Xue, Electrochemical Reduction of High-Concentrated Nitrate Using Ti/TiO2 Nanotube Array Anode and Fe Cathode in Dual-Chamber Cell, Catal. Letters. 146 (2016) 2585–2595. doi:10.1007/s10562-016-1894-3.

[389] P. Kuang, C. Feng, M. Li, N. Chen, Q. Hu, G. Wang, R. Li, Improvement on Electrochemical Reduction of Nitrate in Synthetic Groundwater by Reducing Anode Surface Area, J. Electrochem. Soc. 164 (2017) E103–E112. doi:10.1149/2.0831706jes.

[390] Y. Wang, J. Qu, H. Liu, Effect of liquid property on adsorption and catalytic reduction of nitrate over hydrotalcite-supported Pd-Cu catalyst, J. Mol. Catal. A Chem. 272 (2007) 31–37. doi:10.1016/j.molcata.2007.02.028.

[391] K.A. Guy, H. Xu, J.C. Yang, C.J. Werth, J.R. Shapley, K.A. Guy, H. Xu, J.C. Yang, C.J. Werth, J.R. Shapley, Catalytic Nitrate and Nitrite Reduction with Pd # Cu / PVP Colloids in Water : Composition , Structure , and Reactivity Correlations Catalytic Nitrate and Nitrite Reduction with Pd - Cu / PVP Colloids in Water : Composition , Structure , and Reactivity Co, (2009) 8177–8185.

[392] T. Yuranova, C. Franch, A.E. Palomares, E. Garcia-Bordejé, L. Kiwi-Minsker, Structured fibrous carbon-based catalysts for continuous nitrate removal from natural water, Appl. Catal. B Environ. 123–124 (2012) 221–228. doi:10.1016/j.apcatb.2012.04.007.

[393] C. Yao, F. Li, X. Li, D. Xia, Fiber-like nanostructured Ti4O7 used as durable fuel cell catalyst support in oxygen reduction catalysis, J. Mater. Chem. 22 (2012) 16560. doi:10.1039/c2jm32866f.

[394] K. Ben Liew, W.R.W. Daud, M. Ghasemi, J.X. Leong, S. Su Lim, M. Ismail, Non-Pt catalyst as oxygen reduction reaction in microbial fuel cells: A review, Int. J. Hydrogen Energy. 39 (2014) 4870–4883. doi:10.1016/j.ijhydene.2014.01.062.

[395] A. Morozan, B. Jousselme, S. Palacin, Low-platinum and platinum-free catalysts for the oxygen reduction reaction at fuel cell cathodes, Energy Environ. Sci. 4 (2011) 1238. doi:10.1039/c0ee00601g.

[396] B. Wang, Recent development of non-platinum catalysts for oxygen reduction reaction, J. Power Sources. 152 (2005) 1–15. doi:10.1016/j.jpowsour.2005.05.098.

[397] M. Nobial, O. Devos, O.R. Mattos, B. Tribollet, The nitrate reduction process: A way for increasing interfacial pH, J. Electroanal. Chem. 600 (2007) 87–94. doi:10.1016/j.jelechem.2006.03.003.

[398] G.E. Dima, A.C.A. De Vooys, M.T.M. Koper, Electrocatalytic reduction of nitrate at low concentration on coinage and transition-metal electrodes in acid solutions, J. Electroanal. Chem. 554–555 (2003) 15–23. doi:10.1016/S0022-0728(02)01443-2.

[399] W. Duan, A. Dudchenko, E. Mende, C. Flyer, X. Zhu, D. Jassby, Electrochemical mineral scale prevention and removal on electrically conducting carbon nanotube-polyamide reverse osmosis membranes., Environ. Sci. Process. Impacts. 16 (2014) 1300–8.

doi:10.1039/c3em00635b.

[400] J.M. Ortiz, E. Expósito, F. Gallud, V. García-García, V. Montiel, V.A. Aldaz, Desalination of underground brackish waters using an electrodialysis system powered directly by photovoltaic energy, Sol. Energy Mater. Sol. Cells. 92 (2008) 1677–1688. doi:10.1016/j.solmat.2008.07.020.

[401] E.J. McAdam, S.J. Judd, Immersed membrane bioreactors for nitrate removal from drinking water: Cost and feasibility, Desalination. 231 (2008) 52–60. doi:10.1016/j.desal.2007.11.038.

[402] N. Pous, S. Puig, M. Dolors Balaguer, J. Colprim, Cathode potential and anode electron donor evaluation for a suitable treatment of nitrate-contaminated groundwater in bioelectrochemical systems, Chem. Eng. J. 263 (2015) 151–159. doi:10.1016/j.cej.2014.11.002.

[403] R. Epsztein, O. Nir, O. Lahav, M. Green, Selective nitrate removal from groundwater using a hybrid nanofiltration–reverse osmosis filtration scheme, Chem. Eng. J. 279 (2015) 372–378. doi:10.1016/j.cej.2015.05.010.

[404] R. Abdallah, F. Geneste, T. Labasque, H. Djelal, F. Fourcade, A. Amrane, S. Taha, D. Floner, Selective and quantitative nitrate electroreduction to ammonium using a porous copper electrode in an electrochemical flow cell, J. Electroanal. Chem. 727 (2014) 148–153. doi:10.1016/j.jelechem.2014.06.016.

[405] A.R. Ravishankara, J.S. Daniel, R.W. Portmann, Nitrous Oxide (N2O): The Dominant Ozone-Depleting Substance Emitted in the 21st Century, Science (80-.). 326 (2009) 123–125. doi:10.1126/science.1176985.

[406] E.M.W. SMEETS, L.F. BOUWMAN, E. STEHFEST, D.P. van VUUREN, A.

POSTHUMA, Contribution of N_2O to the greenhouse gas balance of first-generation biofuels, Glob. Chang. Biol. 15 (2009) 780–780. doi:10.1111/j.1365-2486.2009.01872.x.

[407] M. Desai, R.P. Harvey, Inventory of U.S. Greenhouse Gas Emissions and Sinks: 1990-2015, Fed. Regist. 82 (2017) 10767. doi:EPA 430-R-13-001.

[408] Y.D. Scherson, G.F. Wells, S.-G. Woo, J. Lee, J. Park, B.J. Cantwell, C.S. Criddle, Nitrogen removal with energy recovery through N_2O decomposition, Energy Environ. Sci. 6 (2013) 241–248. doi:10.1039/C2EE22487A.

[409] Y.D. Scherson, S.G. Woo, C.S. Criddle, Production of nitrous oxide from anaerobic digester centrate and its use as a co-oxidant of biogas to enhance energy recovery, Environ. Sci. Technol. 48 (2014) 5612–5619. doi:10.1021/es501009j.

[410] D. Bejan, L.M. Rabson, N.J. Bunce, Electrochemical Deodorization and Disinfection of Hog Manure, Can. J. Chem. Eng. 85 (2008) 929–935. doi:10.1002/cjce.5450850615.

[411] G. Chen, E.A. Betterton, R.G. Arnold, W.P. Ela, Electrolytic reduction of trichloroethylene and chloroform at a Pt- or Pd-coated ceramic cathode, J. Appl. Electrochem. 33 (2003) 161–169. doi:10.1023/A:1024076419515.

[412] E.R. Bennett, M.T. Moore, C.M. Cooper, S. Smith, Method for the simultaneous extraction and analysis of two current use pesticides, atrazine and lambda-cyhalothrin, in sediment and aquatic plants, Bull. Environ. Contam. Toxicol. 64 (2000) 825–833. doi:10.1007/s001280000077.

[413] L. Heydel, M. Benoit, M. Schiavon, Reducing atrazine leaching by integrating reduced herbicide use with mechanical weeding in corn (Zea mays), Eur. J. Agron. 11 (1999) 217–225. doi:10.1016/S1161-0301(99)00033-7.

[414] P. Pesticide, R. Testing, ATRAZINE : ITS USE IN CORN PRODUCTION AND ITS

LOSS TO STREAM WATERS IN SOUTHERN ONTARIO , 1975--1977 Atrazine was first introduced into Ontario Agriculture around 1960 and , since that time , it has been widely accepted as an important tool in controlling, 12 (1979).

[415] D.C. Muir, B.E. Baker, Detection of triazine herbicides and their degradation products in tile-drain water from fields under intensive corn (maize) production, J. Agric. Food Chem. 24 (1976) 122–125. doi:10.1021/jf60203a020.

[416] I.P. Management, No Title, n.d.

[417] M.M. Williams II, C.M. Boerboom, T.L. Rabaey, Significance of Atrazine in Sweet Corn Weed Management Systems Significance of Atrazine in Sweet Corn Weed, Source Weed Technol. 24 (2010) 139–142. doi:10.1614/WT-D-09-00074.1.

[418] N.D. Jablonowski, A. Schäffer, P. Burauel, Still present after all these years: Persistence plus potential toxicity raise questions about the use of atrazine, Environ. Sci. Pollut. Res. 18 (2011) 328–331. doi:10.1007/s11356-010-0431-y.

[419] M.J. Cerejeira, P. Viana, S. Batista, T. Pereira, E. Silva, M.J. Valério, A. Silva, M. Ferreira, A.M. Silva-Fernandes, Pesticides in Portuguese surface and ground waters, Water Res. 37 (2003) 1055–1063. doi:10.1016/S0043-1354(01)00462-6.

[420] P.J. Squillace, E.M. Thurman, E.T. Furlong, Groundwater As a Nonpoint-Source of Atrazine and Deethylatrazine in a River During Base-Flow Conditions, Water Resour. Res. 29 (1993) 1719–1729.

[421] R.J. Bushway, B. Perkins, S.A. Savage, S.J. Lekousi, B.S. Ferguson, Determination of atrazine residues in water and soil by enzyme immunoassay, Bull. Environ. Contam. Toxicol. 40 (1988) 647–654. doi:10.1007/BF01697509.

[422] M. Graymore, F. Stagnitti, G. Allinson, Impacts of atrazine in aquatic ecosystems,

Environ. Int. 26 (2001) 483–495. doi:10.1016/S0160-4120(01)00031-9.

[423] U.S. Department of Health and Human Services, ToxGuide for Atrazine, (2003).

[424] USEPA, Decision Documents for Atrazine, Decis. Doc. Atrazine. (2006) 1–285. https://archive.epa.gov/pesticides/reregistration/web/pdf/atrazine_combined_docs.pdf.

[425] U.S. Environmental Protection Agency: National Center for Environmental Assessment, Atrazine ; CASRN 1912-24-9, (1993) 1–14.

[426] N. Simon-Delso, V. Amaral-Rogers, L.P. Belzunces, J.M. Bonmatin, M. Chagnon, C. Downs, L. Furlan, D.W. Gibbons, C. Giorio, V. Girolami, D. Goulson, D.P. Kreutzweiser, C.H. Krupke, M. Liess, E. Long, M. Mcfield, P. Mineau, E.A. Mitchell, C.A. Morrissey, D.A. Noome, L. Pisa, J. Settele, J.D. Stark, A. Tapparo, H. Van Dyck, J. Van Praagh, J.P. Van Der Sluijs, P.R. Whitehorn, M. Wiemers, Systemic insecticides (Neonicotinoids and fipronil): Trends, uses, mode of action and metabolites, Environ. Sci. Pollut. Res. 22 (2015) 5–34. doi:10.1007/s11356-014-3470-y.

[427] M.L. Hladik, D.W. Kolpin, K.M. Kuivila, Widespread occurrence of neonicotinoid insecticides in streams in a high corn and soybean producing region, USA, Environ. Pollut. 193 (2014) 189–196. doi:10.1016/j.envpol.2014.06.033.

[428] M. Rundlöf, G.K.S. Andersson, R. Bommarco, I. Fries, V. Hederström, L. Herbertsson, O. Jonsson, B.K. Klatt, T.R. Pedersen, J. Yourstone, H.G. Smith, Seed coating with a neonicotinoid insecticide negatively affects wild bees, Nature. 521 (2015) 77–80. doi:10.1038/nature14420.

[429] A. Fairbrother, J. Purdy, T. Anderson, R. Fell, Risks of neonicotinoid insecticides to honeybees, Environ. Toxicol. Chem. 33 (2014) 719–731. doi:10.1002/etc.2527.

[430] M. Chauzat, J. Faucon, Pesticide residues in beeswax samples collected from honey bee

colonies (*Apis mellifera* L .) in France, Pest Manag. Sci. 1106 (2007) 1100–1106. doi:10.1002/ps.

[431] A.R. Main, J. V. Headley, K.M. Peru, N.L. Michel, A.J. Cessna, C.A. Morrissey, Widespread use and frequent detection of neonicotinoid insecticides in wetlands of Canada's prairie pothole region, PLoS One. 9 (2014). doi:10.1371/journal.pone.0092821.

[432] K.L. Klarich, N.C. Pflug, E.M. DeWald, M.L. Hladik, D.W. Kolpin, D.M. Cwiertny, G.H. LeFevre, Occurrence of neonicotinoid insecticides in finished drinking water and fate during drinking water treatment, Environ. Sci. Technol. Lett. 4 (2017) 168–173. doi:10.1021/acs.estlett.7b00081.

[433] USEPA, EFED Risk Assessment for the Seed Treatment of Clothianidin 600FS on Corn and Canola (PC Code 044309; DP Barcode: D278110), (2003).

[434] V. Mommaerts, S. Reynders, J. Boulet, L. Besard, G. Sterk, G. Smagghe, Risk assessment for side-effects of neonicotinoids against bumblebees with and without impairing foraging behavior, Ecotoxicology. 19 (2010) 207–215. doi:10.1007/s10646-009-0406-2.

[435] C.H. Krupke, G.J. Hunt, B.D. Eitzer, G. Andino, K. Given, Multiple routes of pesticide exposure for honey bees living near agricultural fields, PLoS One. 7 (2012). doi:10.1371/journal.pone.0029268.

[436] T. Blacquière, G. Smagghe, C.A.M. Van Gestel, V. Mommaerts, Neonicotinoids in bees: A review on concentrations, side-effects and risk assessment, Ecotoxicology. 21 (2012) 973–992. doi:10.1007/s10646-012-0863-x.

[437] G. Di Prisco, V. Cavaliere, D. Annoscia, P. Varricchio, E. Caprio, F. Nazzi, G. Gargiulo, F. Pennacchio, Neonicotinoid clothianidin adversely affects insect immunity and promotes replication of a viral pathogen in honey bees, Proc. Natl. Acad. Sci. 110 (2013) 18466–

18471. doi:10.1073/pnas.1314923110.

[438] D. Gibbons, C. Morrissey, P. Mineau, A review of the direct and indirect effects of neonicotinoids and fipronil on vertebrate wildlife, Environ. Sci. Pollut. Res. 22 (2015) 103–118. doi:10.1007/s11356-014-3180-5.

[439] G. Di Prisco, M. Iannaccone, F. Ianniello, R. Ferrara, E. Caprio, F. Pennacchio, R. Capparelli, The neonicotinoid insecticide Clothianidin adversely affects immune signaling in a human cell line, Sci. Rep. 7 (2017) 1–8. doi:10.1038/s41598-017-13171-z.

[440] H.C. Spalding, J.A. Enck, Federal Register /, Fed. Regist. 75 (2011) 17–23. doi:10.1007/s10750-004-4538-3.

[441] E. Topp, A comparison of three atrazine-degrading bacteria for soil bioremediation, Biol. Fertil. Soils. 33 (2001) 529–534. doi:10.1007/s003740100371.

[442] M. Radosevich, S.J. Traina, O.H. Tuovinen, Degradation of binary and ternary mixtures of s-triazines by a soil bacterial isolate, J. Environ. Sci. Heal. Part B. 30 (1995) 457–471. doi:10.1080/03601239509372947.

[443] Q. LI, Y. LI, X. ZHU, B. CAI, Isolation and characterization of atrazine-degrading Arthrobacter sp. AD26 and use of this strain in bioremediation of contaminated soil, J. Environ. Sci. 20 (2008) 1226–1230. doi:10.1016/S1001-0742(08)62213-5.

[444] X. Fan, J. Restivo, J.J.M. Órfão, M.F.R. Pereira, A.A. Lapkin, The role of multiwalled carbon nanotubes (MWCNTs) in the catalytic ozonation of atrazine, Chem. Eng. J. 241 (2014) 66–76. doi:10.1016/j.cej.2013.12.023.

[445] G.R.P. Malpass, D.W. Miwa, S.A.S. Machado, P. Olivi, A.J. Motheo, Oxidation of the pesticide atrazine at DSA®electrodes, J. Hazard. Mater. 137 (2006) 565–572. doi:10.1016/j.jhazmat.2006.02.045.

[446] P. Vanraes, G. Willems, A. Nikiforov, P. Surmont, F. Lynen, J. Vandamme, J. Van Durme, Y.P. Verheust, S.W.H. Van Hulle, A. Dumoulin, C. Leys, Removal of atrazine in water by combination of activated carbon and dielectric barrier discharge, J. Hazard. Mater. 299 (2015) 647–655. doi:10.1016/j.jhazmat.2015.07.075.

[447] E. Through, I.B.M.J. Galluzzo, a Trazine R Emoval, Environ. Prot. 3 (1999) 163–169.

[448] R. Broséus, S. Vincent, K. Aboulfadl, A. Daneshvar, S. Sauvé, B. Barbeau, M. Prévost, Ozone oxidation of pharmaceuticals, endocrine disruptors and pesticides during drinking water treatment, Water Res. 43 (2009) 4707–4717. doi:10.1016/j.watres.2009.07.031.

[449] E.C. Wert, F.L. Rosario-Ortiz, S.A. Snyder, Effect of ozone exposure on the oxidation of trace organic contaminants in wastewater, Water Res. 43 (2009) 1005–1014. doi:10.1016/j.watres.2008.11.050.

[450] V. Camel, A. Bermond, The use of ozone and associated oxidation processes in drinking water treatment, Water Res. 32 (1998) 3208–3222. doi:10.1016/S0043-1354(98)00130-4.

[451] C.A. Guzman-Perez, J. Soltan, J. Robertson, Kinetics of catalytic ozonation of atrazine in the presence of activated carbon, Sep. Purif. Technol. 79 (2011) 8–14. doi:10.1016/j.seppur.2011.02.035.

[452] J.A. Khan, X. He, N.S. Shah, H.M. Khan, E. Hapeshi, D. Fatta-Kassinos, D.D. Dionysiou, Kinetic and mechanism investigation on the photochemical degradation of atrazine with activated H2O2, S2O82-and HSO5-, Chem. Eng. J. 252 (2014) 393–403. doi:10.1016/j.cej.2014.04.104.

[453] X. Kong, J. Jiang, J. Ma, Y. Yang, W. Liu, Y. Liu, Degradation of atrazine by UV/chlorine: Efficiency, influencing factors, and products, Water Res. 90 (2016) 15–23. doi:10.1016/j.watres.2015.11.068.

[454] K.H. Chan, W. Chu, Modeling the reaction kinetics of Fenton's process on the removal of atrazine, Chemosphere. 51 (2003) 305–311. doi:10.1016/S0045-6535(02)00812-3.

[455] E. Brillas, I. Sire, M.A. Oturan, I. Sirés, M.A. Oturan, Electro-Fenton Process and Related Electrochemical Technologies Based on Fenton 's Reaction Chemistry, Chem. Rev. 109 (2009) 6570–6631. doi:10.1021/cr900136g.

[456] L. Yu, X. Yang, Y. Ye, D. Wang, Efficient removal of atrazine in water with a Fe_3O_4 /MWCNTs nanocomposite as a heterogeneous Fenton-like catalyst, RSC Adv. 5 (2015) 46059–46066. doi:10.1039/C5RA04249F.

[457] W. Chu, K.H. Chan, C.Y. Kwan, K.Y. Choi, Degradation of atrazine by modified stepwise-Fenton's processes, Chemosphere. 67 (2007) 755–761. doi:10.1016/j.chemosphere.2006.10.039.

[458] B.R. Garza-Campos, J.L. Guzmán-Mar, L.H. Reyes, E. Brillas, A. Hernández-Ramírez, E.J. Ruiz-Ruiz, Coupling of solar photoelectro-Fenton with a BDD anode and solar heterogeneous photocatalysis for the mineralization of the herbicide atrazine, Chemosphere. 97 (2014) 26–33. doi:10.1016/j.chemosphere.2013.10.044.

[459] K. Pratap, A.T. Lemley, Fenton Electrochemical Treatment of Aqueous Atrazine and Metolachlor, J. Agric. Food Chem. 46 (1998) 3285–3291. doi:10.1021/jf9710342.

[460] F. Zaviska, P. Drogui, J.F. Blais, G. Mercier, P. Lafrance, Experimental design methodology applied to electrochemical oxidation of the herbicide atrazine using Ti/IrO2 and Ti/SnO2 circular anode electrodes, J. Hazard. Mater. 185 (2011) 1499–1507. doi:10.1016/j.jhazmat.2010.10.075.

[461] J. Radjenovic, A. Bagastyo, R.A. Rozendal, Y. Mu, J. Keller, K. Rabaey, Electrochemical oxidation of trace organic contaminants in reverse osmosis concentrate using RuO2/IrO2-

coated titanium anodes, Water Res. 45 (2011) 1579–1586. doi:10.1016/j.watres.2010.11.035.

[462] N. Borràs, R. Oliver, C. Arias, E. Brillas, Degradation of Atrazine by Electrochemical Advanced Oxidation Processes Using a Boron-Doped Diamond Anode, J. Phys. Chem. A. 114 (2010) 6613–6621. doi:10.1021/jp1035647.

[463] J. De Laat, H. Gallard, S. Ancelin, B. Legube, Comparative study of the oxidation of atrazine and acetone by H2O2/UV, Fe(III)/UV, Fe(III)/H2O2/UV and Fe(II) or Fe(III)/H2O2, Chemosphere. 39 (1999) 2693–2706. doi:10.1016/S0045-6535(99)00204-0.

[464] J.A. Khan, X. He, H.M. Khan, N.S. Shah, D.D. Dionysiou, Oxidative degradation of atrazine in aqueous solution by UV/H2O2/Fe2+, UV/S2O82-/Fe2+ and UV/HSO5-/Fe2+ processes: A comparative study, Chem. Eng. J. 218 (2013) 376–383. doi:10.1016/j.cej.2012.12.055.

[465] I. Grčić, M. Mužic, D. Vujević, N. Koprivanac, Evaluation of atrazine degradation in UV/FeZSM-5/H2O2system using factorial experimental design, Chem. Eng. J. 150 (2009) 476–484. doi:10.1016/j.cej.2009.01.037.

[466] Y. Du, Y. Su, L. Lei, X. Zhang, Role of oxygen in the degradation of atrazine by UV/Fe(III) process, J. Photochem. Photobiol. A Chem. 208 (2010) 7–12. doi:10.1016/j.jphotochem.2009.07.026.

[467] T.A. McMurray, P.S.M. Dunlop, J.A. Byrne, The photocatalytic degradation of atrazine on nanoparticulate TiO2films, J. Photochem. Photobiol. A Chem. 182 (2006) 43–51. doi:10.1016/j.jphotochem.2006.01.010.

[468] C.L. Bianchi, C. Pirola, V. Ragaini, E. Selli, Mechanism and efficiency of atrazine degradation under combined oxidation processes, Appl. Catal. B Environ. 64 (2006) 131–

138. doi:10.1016/j.apcatb.2005.11.009.

[469] C. Chen, S. Yang, Y. Guo, C. Sun, C. Gu, B. Xu, Photolytic destruction of endocrine disruptor atrazine in aqueous solution under UV irradiation: Products and pathways, J. Hazard. Mater. 172 (2009) 675–684. doi:10.1016/j.jhazmat.2009.07.050.

[470] O. Sacco, V. Vaiano, C. Han, D. Sannino, D.D. Dionysiou, Photocatalytic removal of atrazine using N-doped TiO2supported on phosphors, Appl. Catal. B Environ. 164 (2015) 462–474. doi:10.1016/j.apcatb.2014.09.062.

[471] J. Andersen, M. Pelaez, L. Guay, Z. Zhang, K. O'Shea, D.D. Dionysiou, NF-TiO2 photocatalysis of amitrole and atrazine with addition of oxidants under simulated solar light: Emerging synergies, degradation intermediates, and reusable attributes, J. Hazard. Mater. 260 (2013) 569–575. doi:10.1016/j.jhazmat.2013.05.056.

[472] C.S. Castro, M.C. Guerreiro, M. Gonçalves, L.C.A. Oliveira, A.S. Anastácio, Activated carbon/iron oxide composites for the removal of atrazine from aqueous medium, J. Hazard. Mater. 164 (2009) 609–614. doi:10.1016/j.jhazmat.2008.08.066.

[473] N.W. Brown, E.P.L. Roberts, A. Chasiotis, T. Cherdron, N. Sanghrajka, Atrazine removal using adsorption and electrochemical regeneration, Water Res. 38 (2004) 3067–3074. doi:10.1016/j.watres.2004.04.043.

[474] Y. Zhang, Y. Li, X. Zheng, Removal of atrazine by nanoscale zero valent iron supported on organobentonite, Sci. Total Environ. 409 (2011) 625–630. doi:10.1016/j.scitotenv.2010.10.015.

[475] D. Zadaka, S. Nir, A. Radian, Y.G. Mishael, Atrazine removal from water by polycation-clay composites: Effect of dissolved organic matter and comparison to activated carbon, Water Res. 43 (2009) 677–683. doi:10.1016/j.watres.2008.10.050.

[476] I. Pulko, M. Kolar, P. Krajnc, Atrazine removal by covalent bonding to piperazine functionalized PolyHIPEs, Sci. Total Environ. 386 (2007) 114–123. doi:10.1016/j.scitotenv.2007.06.032.

[477] S. Siripattanakul, W. Wirojanagud, J.M. McEvoy, F.X.M. Casey, E. Khan, Atrazine remediation in agricultural infiltrate by bioaugmented polyvinyl alcohol immobilized and free Agrobacterium radiobacter J14a, Water Sci. Technol. 58 (2008) 2155–2163. doi:10.2166/wst.2008.810.

[478] K.H. Chan, W. Chu, Atrazine removal by catalytic oxidation processes with or without UV irradiation: Part II: An analysis of the reaction mechanisms using LC/ESI-tandem mass spectrometry, Appl. Catal. B Environ. 58 (2005) 165–174. doi:10.1016/j.apcatb.2004.12.005.

[479] R. Žabar, T. Komel, J. Fabjan, M.B. Kralj, P. Trebše, Photocatalytic degradation with immobilised TiO2 of three selected neonicotinoid insecticides: Imidacloprid, thiamethoxam and clothianidin, Chemosphere. 89 (2012) 293–301. doi:10.1016/j.chemosphere.2012.04.039.

[480] N. Oturan, E. Brillas, M.A. Oturan, Unprecedented total mineralization of atrazine and cyanuric acid by anodic oxidation and electro-Fenton with a boron-doped diamond anode, (2012) 165–170. doi:10.1007/s10311-011-0337-z.

[481] D.F. Ollis, N. Serpone, Photocatalyzed 1 .--, (1991). doi:10.1021/es00021a001.

[482] C. Analitica, U. Torino, M.L. Tosato, I. Superiore, Photocatalytic Degradation, (1990) 1559–1565. doi:10.1021/es00080a016.

[483] B. Balci, N. Oturan, R. Cherrier, M.A. Oturan, Degradation of atrazine in aqueous medium by electrocatalytically generated hydroxyl radicals . A kinetic and mechanistic

study, Water Res. 43 (2009) 1924–1934. doi:10.1016/j.watres.2009.01.021.

[484] G. Stucki, C.H.I.W. Yu, T. Baumgartner, J.F. Gonzalez-valero, ~) P e r g a m o n MICROBIAL A T R A Z I N E M I N E R A L I S A T I O N U N D E R, (1995).

[485] P. Gayen, B.P. Chaplin, Fluorination of Boron-Doped Diamond Film Electrodes for Minimization of Perchlorate Formation, ACS Appl. Mater. Interfaces. 9 (2017) 27638–27648. doi:10.1021/acsami.7b06028.

[486] C.W. Bauschlicher, H. Partridge, A modification of teh Gaussian-2 approach using density functional theory, J. Chem. Phys. 105 (1995) 1788. http://scitation.aip.org/content/aip/journal/jcp/103/5/10.1063/1.469752.

[487] M.D. Tissandier, K.A. Cowen, W.Y. Feng, E. Gundlach, M.H. Cohen, A.D. Earhart, J. V. Coe, T.R. Tuttle, The proton's absolute aqueous enthalpy and Gibbs free energy of solvation from cluster-ion solvation data, J. Phys. Chem. A. 102 (1998) 7787–7794. doi:10.1021/jp982638r.

[488] C.P. Kelly, C.J. Cramer, D.G. Truhlar, Aqueous solvation free energies of ions and ion-water clusters based on an accurate value for the absolute aqueous solvation free energy of the proton, J. Phys. Chem. B. 110 (2006) 16066–16081. doi:10.1021/jp063552y.

[489] J.R. Bolton, K.G. Bircher, W. Tumas, C.A. Tolman, Figures-of-merit for the technical development and application of advanced oxidation technologies for both electric- and solar-driven systems (IUPAC Technical Report), Pure Appl. Chem. 73 (2001) 627–637. doi:10.1351/pac200173040627.

[490] D. Shuttleworth, Preparation of metal-polymer dispersions by plasma techniques. An ESCA investigation, J. Phys. Chem. 84 (1980) 1629–1634. doi:10.1021/j100449a038.

[491] R. Shiratsuchi, K. Hongo, G. Nogami, Reduction of C02 on Fluorine-Doped Sn02 Thin-

Film Electrodes C02, J. Electrochem. Soc. 139 (1992) 2544–2549.

[492] L.K.D. and L.C. P K BISWAS, A DE, Surface characterization of sol – gel derived indium tin oxide films on glass, Bull. Mater. Sci. 29 (2006) 323–330. doi:10.1007/BF02706504.

[493] J. Bao, S. Guo, J. Gao, T. Hu, L. Yang, C. Liu, J. Peng, C. Jiang, Synthesis of Ag_2CO_3/Bi_2WO_6 heterojunctions with enhanced photocatalytic activity and cycling stability, RSC Adv. 5 (2015) 97195–97204. doi:10.1039/C5RA18938A.

[494] B. V Buxton, C.L. Greenstock, W.P. Helman, A.B. Ross, Critical review of rate constants for reactions of hydrated electrons, hydrogen atoms, and hydroxyl radicals in aqueous solution, J. Phys. Chem. Ref. Data. 17 (1988) 513.

[495] A. Florentin, T. Deblonde, N. Diguio, A. Hautemaniere, P. Hartemann, Impacts of two perfluorinated compounds (PFOS and PFOA) on human hepatoma cells: Cytotoxicity but no genotoxicity?, Int. J. Hyg. Environ. Health. 214 (2011) 493–499. doi:10.1016/j.ijheh.2011.05.010.

[496] G.B. Post, J.B. Louis, K.R. Cooper, B.J. Boros-Russo, R.L. Lippincott, Occurrence and potential significance of PFOA detected in New Jersy drinking water, Env. Sci Technol. 43 (2009) 4547–4554. doi:10.1021/es902326f.

[497] K.T. Eriksen, O. Raaschou-Nielsen, M. Sørensen, M. Roursgaard, S. Loft, P. Møller, Genotoxic potential of the perfluorinated chemicals PFOA, PFOS, PFBS, PFNA and PFHxA in human HepG2 cells, Mutat. Res. - Genet. Toxicol. Environ. Mutagen. 700 (2010) 39–43. doi:10.1016/j.mrgentox.2010.04.024.

[498] W. Loh, C.A. Tonegutti, P.L.O. Volpe, Diffusion coefficients of aqueous phenols determined by the Taylor dispersion technique. Evidence for solute adsorption on the

walls of Teflon tubing, J. Chem. Soc. Faraday Trans. 89 (1993) 113–118. doi:10.1039/FT9938900113.

[499] I. Steinborn-Rogulska, G. Rokicki, Solid-state polycondensation (SSP) as a method to obtain high molecular weight polymers: Part II. Synthesis of polylactide and polyglycolide via SSP, Polimery/Polymers. 58 (2013) 85–92. doi:10.14314/polimery.2013.085.

CV/VITA

Pralay Gayen
1451 E. 55th Street, 622N
Chicago, IL 60615
(312) 731-5969
pgayen2@uic.edu

EDUCATION
University of Illinois at Chicago (UIC), Chicago, IL
Ph.D. in Chemical Engineering, 2013 - Present
Ph.D. Thesis: "Surface Modification of Electrode Surfaces for Water Treatment and Sensing Applications"
Thesis Advisor: Brian P. Chaplin, Ph.D.

Indian Institute of Technology Bombay, Mumbai, India
M.Tech. in Chemical Engineering, 2011 - 2013
M.Tech. Thesis: "Improving Efficiency of Comminution in Ball Mills"
Thesis Advisor: Devang V. Khakhar, Ph.D.

University of Calcutta, Kolkata, India
B.Tech. in Chemical Engineering, 2008 - 2011
B.Tech. Project: "Minimum Impeller Speed for Complete Liquid-Liquid Dispersion"
Project Advisor: Kaushik Ganguly

University of Calcutta, Kolkata, India
B.Sc. in Chemistry, 2005 - 2008

EXPERIENCE
RESEARCH EXPERIENCE
University of Illinois at Chicago (UIC), Chicago, IL
Ph.D. Student, 2013 - Present
Advisor: Brian P. Chaplin, Ph.D.

- Developed electrochemical sensors for the determination of antibiotic (Ciprofloxacin (CFX)) in natural water and wastewater effluent matrix with high sensitivity and selectivity. The design and fabrication of the sensor was accomplished by combining a layer of multi-walled carbon nanotubes (MWCNTs) dispersed in a porous Nafion film and dropcasted onto a boron-doped diamond (BDD) film electrode.

- Prepared fluorinated boron-doped diamond film (BDD) electrodes through electrochemical oxidation of perfluorooctanoic acid (PFOA), radio frequency (RF) plasma with H_2/CF_4 gas, and silanization for the minimization of perchlorate (carcinogenic) formation with significant organic oxidation and subsequent removal from water and wastewater matrix.
- Incorporated catalyst (Bi doped SnO_2) on sub-stoichiometric TiO_2 ceramic membrane through pulsed laser deposition (PLD), electrodeposition/thermal oxidation, and electrosorption/thermal oxidation to achieve higher reaction and removal rate of organics from water matrix by increasing surface area, hydroxyl radical production and potential window.
- Performed electrocatalytic nitrate reduction to remove nitrate with high N_2 selectivity from natural water matrix using different catalyst (Pd-In and Pd-Cu alloy) loaded sub-stoichiometric TiO_2 membrane as nitrate is a serious health hazard for human being especially for infant (blue-baby syndrome).
- Created vertically aligned multi-walled carbon nanotubes (VAMWCNT) for the sensor application.
- Removed dimethyl methylphosphonate (DMMP) which is a surrogate of a chemical weapon named Sarin from water matrix through electrochemical oxidation using sub-stoichiometric TiO_2 membrane.

Indian Institute of Technology Bombay, Mumbai, India
M.Tech. Student, 2011 - 2013
Advisor: Devang V. Khakhar, Ph.D.

- Batch grinding test was applied on limestone in a ball mill to identify the effect of feed size, feed mass, ball diameter and mixed ball size usage on grinding rate constant. Developed and modified correlation among grinding rate constant, feed size and ball diameter.

University of Calcutta, Kolkata, India
B.Tech. Student, 2008 - 2011
Advisor: Kaushik Ganguly

- Obtained minimum impeller speed for complete liquid-liquid (organic and aqueous) dispersion and interpreted the effect of impeller position, volume fraction of individual phase, impeller speed and liquid height on minimum impeller speed by light attenuation method. Evaluated and validated correlation (model) to fit all the parameters with experimental data.

Development Consultants Private Limited, Kolkata, India
Intern, May 2010 - July 2010

- Designed process block diagram of ore processing project.
- Calculated pump head and power requirement for the project.

TEACHING EXPERIENCE

Teaching Assistant, UIC, Chicago, IL

Chemical Engineering Lab I (CHE 381), Department of Chemical Engineering, Fall 2013 (lab), Fall 2014 (lab)

- Assisted conducting lab experiments, delivered a brief demonstration before each lab, explained and clarified student queries, organized lab presentations, diagnosed and solved any operational problem. Checked prelab, final lab and presentation reports of around 50 students, uploaded and documented the grades in UIC blackboard.

Chemical Engineering Lab II (CHE 382), Department of Chemical Engineering, Spring 2015 (lab), Spring 2014 (lab)

- Assisted conducting lab experiments different than Fall, delivered a brief demonstration before each lab, answered student queries and troubleshoot any operational problem. Graded prelab, final lab and presentation reports of around 50 students and uploaded the grades in UIC blackboard.

Transport Phenomena I (CHE 311), Department of Chemical Engineering, Fall 2016 (class)

- Conducted office hours to solve any question from the students related to the course material, homework and exam. Graded homework and exam, supervised exams, distributed graded exam papers, recorded the grades and uploaded the grades in UIC blackboard.

Teaching Assistant, IIT Bombay, Mumbai, India

Chemical Engineering Lab IV (CL 433), Department of Chemical Engineering, IIT Bombay, Spring 2012 (lab), Spring 2013 (lab)

- Discussed the experiment and the governing principle to 100 undergraduate students. Helped students in performing CTRL 1 (Matlab simulation), CTRL 2 (Open loop interacting system), CTRL 3 (Closed loop interacting system), solved any operational problem and graded the exam papers.

Chemical Engineering Lab III (CL 335), Department of Chemical Engineering, IIT Bombay, Fall 2011 (lab), Fall 2012 (lab)

- Demonstrated the experiment (Metal recovery from a dilute solution by an electrochemical method), solved any operational problem and illustrated the governing principle to 100 undergraduate students and graded the exam papers.

AWARDS AND HONORS

- Awarded **Best High Impact Publication and Best High Research Productivity** award in the Department of Chemical Engineering at UIC.
- Reviewer at **ACS Sustainable Chemistry & Engineering, International Journal of Environmental Analytical Chemistry** and **Applied Catalysis B: Environmental**.
- Placed among the top 1% of the candidate (**All India Rank - 99**) in Graduate Aptitude Test in Engineering (GATE) 2011.
- Received scholarship in **National Scholarship Examination** of the secondary stage for the talented children in rural areas (at the end of class VIII), organized by Directorate of School Education, Government of West Bengal, India.

SKILLS

- **Laboratory Skills**: Electrochemistry, Catalyst Deposition (incipient wetness, electrodeposition etc.), Surface Modification (e.g. fluorination, silanization etc.) Techniques, Cleanroom, CNT growth, COD, RF Plasma, Wet Chemistry, Potentiostat, UV/VIS, HPLC, HPTLC, GC, IC, FTIR, Rheometer, Surface Tensiometer, Rapid Thermal Processing (RTP), pH/Conductivity Meter, SEM, EDS, TEM, XPS, XRD, SAXS, Raman Spectroscopy, e-beam Deposition, Reactive Ion Etching, ALD, PLD, CVD, Ellipsometer and AFM.
- **Computer Skills:** Microsoft Word, Excel and Power point, C/C^{++}, Aspen, AutoCAD, Comsol Multiphysics, XPSPEAK 4.1, MDI Jade, Mendeley, Origin and Matlab.
- **Language Skills:** Fluent in English, Hindi and Bengali.

PEER-REVIEWED PUBLICATIONS

- **Gayen, P.**, and Chaplin, B. P. "Fluorination of Boron-doped Diamond Film Electrodes for Minimization of Perchlorate Formation" *ACS Applied Materials & Interfaces* 9 (2017): 27638-27648
- **Gayen, P.**, and Chaplin, B. P. "Selective Electrochemical Detection of Ciprofloxacin with a Porous Nafion/Multiwalled Carbon Nanotube Composite Film Electrode." *ACS Applied Materials & Interfaces* 8 (2016): 1615-1626.
- Jawando, W., **Gayen, P.**, and Chaplin, B. P. "The effects of surface oxidation and fluorination of boron-doped diamond anodes on perchlorate formation and organic compound oxidation." *Electrochimica Acta* 174 (2015): 1067-1078.
- **Gayen, P.**, and Chaplin, B. P. "Electrocatalytic Reduction of Nitrate Using Magnéli Phase TiO_2 Reactive Electrochemical Membranes Doped with Pd-based Catalysts" *Work in progress.*
- **Gayen, P.**, and Chaplin, B. P. "Preparation, Characterization and Application of Highly Reactive Bismuth-Doped Tin Oxide Deposited TiO_2 Magnéli Phase Reactive Electrochemical Membranes." *Work in progress.*

- **Gayen, P.**, and Chaplin, B. P. "Removal of DMMP, a Surrogate of Sarin from Water Matrix through Electrochemical Oxidation Using Sub-stoichiometric TiO_2 Membranes" *Work in progress.*

ORAL PRESENTATIONS

- **Gayen, P.**, and Chaplin, B. P. "Fluorination of Boron-doped Diamond Film Electrodes for Minimization of Perchlorate Formation." 254th ACS National Meeting, Washington, D.C., MD, August 2017
- **Gayen, P.**, and Chaplin, B. P. "Fluorination of Boron-doped Diamond Film Electrodes for Minimization of Perchlorate Formation." Diamond and Carbon 2017, Chicago, IL, July 2017
- **Gayen, P.**, and Chaplin, B. P. "Fluorination of Boron-doped Diamond Film Electrodes for Minimization of Perchlorate Formation." AIChE 9th Annual Midwest Regional Conference, Chicago, IL, March 2017
- **Gayen, P.**, and Chaplin, B. P. "Selective Electrochemical Detection of Ciprofloxacin with a Porous Nafion/Multi-Walled Carbon Nanotube Composite Film Electrode." AIChE 8th Annual Midwest Regional Conference, Chicago, IL, March 2016
- **Gayen, P.**, and Chaplin, B. P. "Electrochemical detection of ciprofloxacin with a boron-doped diamond electrode modified with nafion-coated multi-walled carbon nanotubes." 250th ACS National Meeting, Boston, MA, August 2015
- **Gayen, P.**, and Chaplin, B. P. "Electrochemical Detection of Antibiotics in Environmental Matrices Using Functionalized Boron-Doped Diamond Electrodes." 227th ECS Meeting, Chicago, IL, May 2015

POSTER PRESENTATIONS

- **Gayen, P.**, and Chaplin, B. P. "Functionalized Boron-doped diamond electrode as electrochemical sensor for antibiotics." AIChE 7th Annual Midwest Regional Conference, Chicago, IL, March 2015

MEMBERSHIPS AND SOCIETIES

- American Institute of Chemical Engineers
- Electrochemical Society
- American Chemical Society